Cultivate Quantitative Magnetic Resonance Imaging Methods to Measure Markers of Health and Translate to Large Scale Cohort Studies

Julie Anne Fitzpatrick

Ph.D. by Published Works

School of Health and Society

University of Salford

2023

Table of Contents

List of Figures ..... **ix**

Acknowledgements ..... ***x***

Abbreviations ..... ***xi***

Abstract ..... ***xiii***

Introduction ***1***

Review of Literature ***3***

Introduction 3

Longitudinal vs Cross Sectional Studies 3

Large Cohort Study 4

History of Large-Scale Cohort Studies 5

Magnetic Resonance Imaging ***7***

Why Choose MRI? 7

How does MRI work? 8

Limitations of MRI 11

Image Quality **12**

Signal-to-Noise Ratio 12

Low Contrast Resolution 13

Spatial Resolution 13

Artefacts 15

Noise 15

Portfolio ***17***

Papers submitted for consideration. **17**

Supporting Evidence **18**

Paper 1 ..... ***19***

Cardiac T2* and lipid measurement at 3.0 T-initial experience **19**

Abstract 19

Introduction 19

Materials and methods 20

Results 23

Discussion....25
Conclusion....28
References....28

Paper 2 ....***32***

Liver Fat Content and T2*: Simultaneous Measurement by Using Breath-hold Multiecho MR Imaging at 3.0 T-Feasibility[1] **32**

Abstract....32
Introduction....32
Advances in Knowledge....33
Materials and Methods....33
Implication for patient care....34
Human Participants....34
Multiecho Sequence....34
Data Analysis: Modeling of Fat and Water Phase Interference....35
Image Analysis....37
Reference Standard Liver Spectroscopy....38
Statistical Analysis....39
Results....39
Discussion....41
References....46

Paper 3 ....***50***

Reduction of total lung capacity in obese men: comparison of total intrathoracic and gas volumes....**50**

Abstract....50
Introduction....51
Methods....52
Results....54
Discussion....59
Grants....65
Disclosures....65
References....65

Paper 4 ....***68***

Whole body fat: Content and distribution....**68**

Abstract....68

Introduction 68
Indirect methods for body-fat measurements....70
Direct Methods for body fat measurements....71
Whole body versus regional body assessment 73
Abdominal MRI scanning....81
Multi-slice abdominal MRI scanning 82
Single-slice MRI abdominal scanning 83
Image Analysis....84
Application of MRI measurement of adipose tissue 85
Potential future areas of interest in MRI adipose tissue research....87
Ectopic Fat....87
Techniques to measure ectopic fat....88
MRI-based methods....89
Ectopic fat in skeletal muscle 92
Ectopic fat in the liver 95
Ectopic fat in the pancreas....98
Bone marrow....102
Conclusion....104
Acknowledgments....105
References....105

Paper 5 132

Validation of a fast method for quantification of intra-abdominal and subcutaneous adipose tissue for large-scale human studies 132

Abstract....132
Introduction 133
Materials and Methods....134
Image Analysis....136
Results....138
Discussion....140
Acknowledgements....144
Conflict of Interest 145
References....145

Paper 6 149

Changes in Liver Volume in Patients with Chronic Hepatitis C Undergoing Antiviral Therapy 149

Abstract 149
Introduction 149
Methods 151
Results 153
Discussion 155
Conflicts of Interest 157
Acknowledgments 157
References 157

Paper 7 160

Psoas Major Crosssectional Area: A Potential Marker of Cardiorespiratory Fitness 160

Abstract 160
Introduction 160
Materials and Methods 161
Results 163
Discussion 166
Limitations of the Study 167
Conclusion 168
Financial support and sponsorship 168
Conflicts of Interest 168
References 168

Paper 8 171

Advancing Pancreas Segmentation in Multi-protocol MRI Volumes using Hausdorff-Sine Loss Function 171

Abstract 171
Introduction 171
Materials and methods 173
Experimental Results and Analysis 175
Conclusion 179
References 179

Paper 9 182

Largescale analysis of iliopsoas muscle volumes in the UK Biobank 182

Abstract 182
Introduction 182
Materials and methods 185

Results 189
Discussion 192
Code availability 196
References 196
Author contributions 200
Competing interests 200

Evaluation of Papers 201

Paper 1 (P1): Cardiac T2* and lipid measurement at 3.0 T-initial experience 201
Influence 201
Personal Contribution 202

Paper 2 (P2) 204

Liver fat content and T2*: Simultaneous measurement by using breath-hold multiecho MR imaging at 3.0 T – Feasibility 204
Influence 204
Personal Contribution 205

Paper 3 (P3) 207

Reduction of total lung capacity in obese men: Comparison of total intrathoracic and gas volume 207
Influence 207
Personal Contribution 208

Paper 4 (P4) 210

Whole body fat: Content and distribution 210
Influence 210
Personal Contribution 211

Paper 5 (P5) 213

Validation of a fast method for quantification of intra-abdominal and subcutaneous adipose tissue for large-scale human studies 213
Influence 213
Personal Contribution 214

Paper 6 (P6) 216

Changes in Liver Volume in Patients with Chronic Hepatitis C Undergoing Antiviral Therapy ... 216

Influence 216
Personal Contribution 216
Paper 7 (P7) 217
Psoas major cross-sectional area: A potential marker of cardiorespiratory fitness 217
Influence 217
Personal Contribution 217
Paper 8 (P8) 219
Advancing Pancreas Segmentation in Multi-protocol MRI Volumes using Hausdorff-Sine Loss Function 219
Influence 219
Personal Contribution 219
Paper 9 (P9) 221
Large-scale analysis of iliopsoas muscle volumes in the UK Biobank....221
Impact and Reach....221
Personal Contribution 222
Aims 223
Aim 1 223
Aim 2 223
Aim 3 223
Aim 4 223
Objectives 223
Feasibility and Acquisition 224
Optimisation....224
Analysis 224
Quality Control 225
Translate 225
Critical Appraisal....226
Chapter 1 227

Feasibility and Acquisition 227
Introduction 227
Field Strength 227
Ethics and Safety 228
Cardiac MRI (CMRI) 229
Liver MRI 230
Patient Experience 231
Data 233
DIRECT and UKBB 234
Chapter 2 236
Optimisation 236
Introduction 236
Lung Volume 236
Translate Multi-Echo to Pancreas 239
Pancreas Volume 240
Fast Whole-Body Protocol Validation 241
Chapter 3 243
Analysis 243
Introduction 243
In-House Software 243
Open-Source Software 244
Viewing Conditions 245
Reliability 245
Measuring Psoas 246
Chapter 4 249
Quality Control 249
Introduction 249
Pancreas Segmentation 250
Machine Learning 251
Quality in Large Scale Studies 251
Dissemination of Imaging Protocol 252
Fat Phantom 254
Chapter 5 256

Translate 256
Introduction 256
Large Scale Studies-Patient Perspective 256
Upscaling Body Composition Protocol 257
QA in Large Scale Studies 257
Psoas Muscle in Large Scale Studies 258
Future Work 260
Career Aspirations 261
Conclusion 262
Appendix 264
A. Supporting Evidence-Poster Presentations 265
Ai. Quantifying hepatic lipid content and T2* decay using breath-hold mutiecho imaging at 3.0 tesla 265
Aii. Measurement of Pancreatic Fat Using Muti Echo MRI 266
Aiii. Comparing Multi Echo and MRS to Measure Pancreatic Fat 267
Aiv. Psoas Muscle Cross Sectional Area: A Novel Marker of Physical Fitness 268
B. DIRECT Training Presentation 269
C. Biobank Letter 274
D. Current/Future Work 275
Bibliography 276
Curriculum Vitae 311

List of Figures

Figure 1: Different Imaging Modalities 7
Figure 2: Selection of Image Contrast in MRI. 8
Figure 3: Diagram of MRI scanner (Hornak, 2020) 9
Figure 4: Pulse Sequences (Ebrahim, Mohamed, 2023) 10
Figure 5: Example of Coronal T1 weighted image of the thorax 238
Figure 6 FOV in different MRI equipment 253

Acknowledgements

"*A lot of people have gone further than they thought they could because someone else thought they could*" – Unknown

I wish to acknowledge and extend my gratitude and appreciation to the following who all thought I could go further than I thought I could:

Dr. Katy Szczepura
Dr. Andrew Tootell
Dr. Samantha Bird
Professor Jimmy D. Bell
Professor E. Louise Tomas
Scott Howard
Dr. Peter Lally
and
Iván Solovey: First and last and always.

Abbreviations

2D	Two Dimensional
3D	Three Dimensional
AI	Artificial Intelligence
B0	Field Strength
BH	Breath Hold
CMRI	Cardiac Magnetic Resonance Imaging
CNR	Contrast to Noise Ratio
CSA	Cross-Sectional Area
CT	Computerised Tomography
dB	Decibel
DE	Dual Echo
DIRECT	DIabetes REsearCh on patient straTification
DQ	Data Quality
DSV	Diameter of Spherical Volume
ECG	Electrocardiogram
FID	Free Induction Decay
FLAIR	Fluid Attenuated Inversion Recovery
fMRI	functional Magnetic Resonance Imaging
FOV	Field of View
GCP	Good Clinical Practice
Gd	Gadolinium
GE	Gradient Echo
GNC	German National Cohort
IHD	Ischemic heart disease
IMI	Innovative Medicines Initiative
IQ	Information Quality
ISMRM	International Society of Magnetic Resonance in Medicine
ME	Multi Echo
MHRA	Medicines and Healthcare Products Regulatory Agency
MITK	The Medical Imaging Interaction Toolkit
MR	Magnetic Resonance Imaging
MRA	Magnetic Resonance Angiography
MRC	Medical Research Council
MRI	Magnetic Resonance Imaging
MRS	Magnetic Resonance Spectroscopy
MSK	Musculoskeletal

ms	millisecond
mT	milli Tesla
P	Paper
PhD	Doctor of Philosophy
PHSG	Population Health Sciences Group
PM	Psoas Muscle
PNAS	Proceeding of the Academy of Sciences
PNS	Peripheral Nerve Stimulation
QA	Quality Assurance
QC	Quality Control
qMRI	Quantitative Magnetic Resonance Imaging
RA	Rectus Abdominus Muscle
RF	Radio Frequency
RFOV	Rectangular Field of View
SAR	Specific Absorbsion Rate
SE	Spin Echo
SNR	Signal to Noise Ratio
ST	Slice Thickness
T	Tesla
T1D	Type One Diabetes
T2D	Type Two Diabetes
TE	Time to Echo
TR	Time to Repeat
UK	United Kingdom
UKBB	United Kingdom Bio Bank
UKRI	UK Research and Innovation
VCG	Vector Cardiogram
VR	Virtual Reality
WHO	World Health Organisation

Abstract

Magnetic Resonance Imaging (MRI) is an indispensable tool in healthcare and research, with a growing demand for its services. The appeal of MRI stems from its non-ionizing radiation nature, ability to generate high-resolution images of internal organs and structures without invasive procedures, and capacity to provide quantitative assessments of tissue properties such as ectopic fat, body composition, and organ volume. All without long term side effects. Nine published papers are submitted which show the cultivation of quantitative measures of ectopic fat within the liver and pancreas using MRI, and the process of validating whole-body composition and organ volume measurements. All these techniques have been translated into large-scale studies to improve health measurements in large population cohorts. Translating this work into large-scale studies, including the use of artificial intelligence, is included. Additionally, an evaluation accompanies these published studies, appraising the evolution of these quantitative MRI techniques from the conception to their application in large cohort studies. Finally, this appraisal provides a summary of future work on crowdsourcing of ground truth training data to facilitate its use in wider applications of artificial intelligence. In conclusion, this body of work presents a portfolio of evidence to fulfil the requirements of a PhD by published works at the University of Salford.

Introduction

Medical Imaging plays a significant role in clinical care and research trials (Munn & Jordan, 2011). Everyday millions of medical images are produced, which are used for the diagnosis of disease and response to treatment (Mohamed Y. Abdallah & Alqahtani, 2019). With medical imaging moving from qualitative to quantitative (Hosny et al., 2018), immense amounts of electronic imaging data need storage but also hold additional untapped information, which could contribute to evidence-based practice and patient care (Canvasser et al., 2014). An example is organ segmentation to measure volume, which can help quantify disease states, function, and response to treatment (Geraghty et al., 2004). Technological advances and an ageing population mean that demand for imaging services will increase (Board of the Faculty of Clinical Radiology, 2019; Care Quality Commission, 2018). However, high vacancy rates for Radiologists and Radiographers mean demand outstrips the supply of imaging services.

In addition to increased demand for clinical imaging, it is becoming more common to perform large cohort studies, thus creating large amounts of data available to researchers (*About UK Biobank | UK Biobank*, 2022; German National Cohort (GNC) Consortium, 2014). Although not all large-scale cohort studies include imaging, the advantages are well recognised (MRC Population Health Sciences Group (PHSG), 2014). No matter how large, an imaging protocol for a research study requires it to be safe, applicable, feasible, robust, reliable, and repeatable. MRI has the advantage of not using ionising radiation and is an obvious choice when undertaking the imaging portion of a large-scale study. Furthermore, MRI can investigate tissue properties non-invasively. MRI opens the possibility of gaining insight into markers of health which may have previously only been possible using biopsy, post-surgery or at post-mortem.

The advent of artificial intelligence (AI) has the potential to play a significant role in several areas of radiology problem-solving, where its impact has been described as profound (*SELECT COMMITTEE ON ARTIFICIAL INTELLIGENCE. COLLATED WRITTEN EVIDENCE*

VOLUME, 2017). However, due to algorithm development and training, the performance of an AI system is only as good as the training data, sometimes referred to as "ground truth", which should be comprehensive and of high quality. Robust methods of acquiring and analysing medical images are required to provide high-quality data for the development and training of artificial intelligence systems. When data becomes available, it comes with a financial and time investment to analyse and annotate. So, extracting meaningful results worthy of publication and translation into improved clinical care will only be achieved on the required scale with additional resources. That is, skilled staff such as radiographers who can perform annotation and analysis, in other words, the production of robust and fully validated ground-truth cohorts. To ensure good quality data for AI development and training, it is essential that the data is accurately, reliably, and consistently acquired. The role of the radiographer in this process is essential in ensuring as they are acquiring consistently high quality data whilst still ensuring participant safety and comfort (Scheek et al., 2021). More recently, radiographers are beginning to play a pivotal role in the use of artificial intelligence in radiology, especially around ground-truth production and validation.

This thesis presents nine papers and supporting evidence to fulfil the requirement PhD by publications. The papers are evidence of the cultivation of new qualitative MRI (qMRI) techniques and their translation into large-scale cohort studies. The submitted papers covers a journey of learning and development after entering a research environment. Gaining skills and understanding of research principles and how trials are conducted, including how quantitative data are acquired. Evolving by participating and assuming more responsibility for performing the analysis to produce viable results, including ground truth, how this process occurs, and the choices that determine the methods that are selected. This evolution also includes creating and optimizing imaging techniques that produce viable data before initiating independent ideas for unique and novel investigations. Finally, this is a commentary on how the portfolio demonstrates original and unique contributions while discussing the detailed understanding required to render qMRI techniques suitable for larger imaging research studies.

Review of Literature

Introduction

When undertaking any form of research, a strategy is required to tackle the research question, which outlines a plan to collect, interpret, analyse, interpret, and draw conclusions from the data. According to the research design, there are various types and subtypes that can be further divided into groups, but the overarching approach falls into quantitative, qualitative, and mixed methods (Creswell & Guetterman, 2018)

In recent years there has been an increase in large-scale research studies in response to the need to understand the mechanisms underpinning non-inheritable disease, epidemiology and thus inform government policy regarding health and spending. Cohort studies collect vast amounts of data from population groups who share a common characteristic, with some following participants for decades or even several generations (Barrett & Noble, 2019). Notable in these studies is that there is no intervention and control group, and data can be collected either retrospectively or prospectively. However, little is documented about including imaging in such large-scale studies. Thus, the literature has been examined to establish the background and history of large-scale studies and how imaging is incorporated.

Longitudinal vs Cross Sectional Studies

In 2016 the Proceedings of the Academy of Sciences (PNAS), a highly regarded peer-reviewed scientific journal, published an article by Chaleckis et al. (2016) entitled “Individual Variability in Human Blood Metabolites Identifies Age-Related Differences” (Chaleckis et al., 2016). The authors presented a robust investigation into the differences in blood metabolites in two different age groups-young (15 young (29 ± 4y of age) and old (15 elderly (81 ± 7y of age). Makinen et al. (2016) responded by writing to the editor of PNAS, criticising the conclusions. Attention was drawn to the causal and mechanistic claims from two groups containing only fifteen participants and how cross-sectional studies should be interpreted cautiously (Mäkinen & Ala-Korpela, 2016). Confounding factors such as lifestyle and socioeconomic status can lead to distorted associations and misleading claims (Smith et al., 2007) .

The year before Chaleckis was published, Belsky et al. (2015) had already highlighted the need to study human ageing in the first part of life when ageing trajectories start to diverge. In addition, longitudinal studies are required as age-related diseases start manifesting and accelerated ageing can be identified. Thus, advocating the need for both cross-sectional and longitudinal studies (Belsky et al., 2015). Case-controlled studies can consider many variables when there is a lengthy period between exposure and the emergence of a disease (Mann, 2003). However, the outcome is either the presence of disease or not, and many influencing factors can be missed. Nevertheless, case-controlled studies can help generate hypotheses for further investigation.

Large Cohort Study

A large cohort study is the best way to study the hundreds, maybe thousands of variables and interactions with environmental factors (Manolio & Collins, 2010). Selection bias can be minimised by including a random sample of the population and minimising 'lost' participants. Belsky et al. included over 1037 participants in their study, which leads to the question of how many participants amounts to a large-scale study? For example, in a functional MRI (fMRI) study, Desmond and Glover (2002) concluded that twelve was enough to identify a statistically significant effect. However, this publication was about signal changes in the brain in a single population and the authors acknowledge that different parameters may be required when observing different populations, for example young and old. Nevertheless, there has also been a rise in large-scale imaging studies in psychiatry, with the number of participants expanding to thousands with the "*statistical mantra is that more subjects means more power*" (Turner, 2014).

In 2014, the Medical Research Council (MRC) published 'Maximising the value of UK population cohorts', a review of the most significant UK population cohort studies 34 cohorts was identified, 17 of which include longitudinal data. In this review, one of the inclusion criteria was that the initial sample size at recruitment was >1000 (MRC Population Health Sciences Group (PHSG), 2014). Without any firm definition, 1000 was suggested as an acceptable figure but there is always the possibility that significance could be achieved with smaller numbers or reduced by the utilisation of more accurate and reproducible techniques use if the assessment of the variables of interest. Moreover, there is scope to achieve a large cohort by combining smaller studies, combining the data, and performing a meta-analysis.

However, researchers can be reluctant to share data (Molloy, 2011), and there will be complications with standardisation due to widely varying protocols (Turner, 2014).

History of Large-Scale Cohort Studies

There is evidence that Sir James McKenzie attempted a longitudinal study of the health residents of St. Andres in the 1890 and early 1900s at the Mackenzie Institute of Clinical Research (Mccormick, 1981). 92 cases were included and 42 showed evidence of ischemic heart disease (IHD). Thus, McKenzie concluded that IHD was common at the time. Several long-term studies were established in the 1940s in the USA, including the Framington Heart Study (Mahmood et al., 2014), with the first cohort consisting of 5209 participants. This has expanded over the last 74 years to include offspring of the original cohort and more diverse ethnicities. Now including 7 cohorts of 15,448 total participants the study has identified common factors which contribute to cardiovascular disease (*About FHS | Framingham Heart Study*, 2022).

Perhaps the best known large longitudinal studies is the British Doctors Study which started sending questionnaires about smoking habits to doctors in 1951. Collecting data from 58,761 respondents a link between smoking and lung cancer was established (Doll & Hill, 1954, 1964). Follow up of this cohort continued until 2001. These studies have resulted in new understanding of disease prevalence and contributory factors.

One of the challenges facing researchers is finding and recruiting a representative sample of the population. When devising a study to investigate the side effect of contraception, researchers required a group who are intelligent, cooperative, health conscious and would be easy to follow. Registered nurses were identified, and the Nurses Cohort Study was founded in 1976. In 2002 the third cohort was enlisted and participants now number 280,000. The study has expanded beyond contraception and yielded many exciting findings, for example, '*Nuts may protect against heart disease*.' (Guasch-Ferré et al., 2017). A further large-scale study is the 45 and Up Study in Australia, which started recruiting in 2006 and now comprises of a huge cohort of 250,000 normal participants (‘Australia’s Largest Ongoing Study of Health and Ageing | 45 and Up Study | Sax Institute’, 2023). The studies undertaken with this cohort includes questionnaires or interviews and some biological samples, such as blood and urine but there is no imaging of this cohort.

More recently, the German National Cohort has included imaging in 56,971 of 205,415 normal participants recruited between 2014 and 2019 (German National Cohort (GNC) Consortium, 2014). While all participants have collected interviews, medical examinations and samples, the MRI programme sub-set includes whole-body, brain, and cardiac imaging. In 2014, one in thirty people were enrolled in cohorts in the UK and linking to primary health records creates an invaluable national resource (Pell et al., 2014). A current directory of cohort studies in the UK can be found on the UK Research and Innovation (UKRI) website (*Cohort Directory*, 2023). The Medical Research Council (MRC), a council of UKRI, encourages the more extensive use of imaging modalities to add value and enhance understanding of disease in cohort studies (MRC Population Health Sciences Group (PHSG), 2014). Nevertheless, there is little in the literature regarding how imaging can and should be introduced to a cohort study. Undeniably, acquisition parameters and protocols are documented, but the details of developing and implementing an imaging protocol are often unseen.

Magnetic Resonance Imaging

Although there is some debate about who invented human magnetic resonance imaging (MRI) machines (Matthews, 2022), there is no doubt that it is a versatile piece of technology which has revolutionized medical imaging. The soft tissue image contrast produced by MRI is superior to other imaging modalities, and as it does not use ionising radiation has become widely used in both clinical and research fields. Many parameters can be manipulated to influence the final image, meaning MRI is an adaptable imaging modality (Bornert & Norris, 2020). Thus, the notion that 'one size fits all' is not applicable to MRI, and the operator has a lot of opportunities to exploit, such as time to repeat (TR), echo time (TE), matrix, slice thickness (ST) and field of view (FOV) among others. MRI is about compromise and striking a fine balance between the final image's requirements and maximizing image quality. This process is often referred to as optimisation and is an essential process in the design and implementation of imaging protocols.

Why Choose MRI?

There is often uncertainty regarding why MRI may be chosen instead of other imaging modalities.

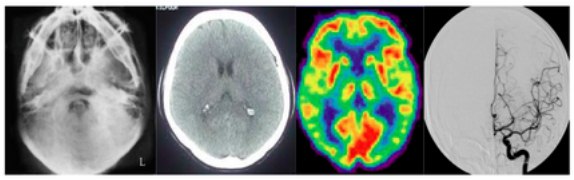

Figure 1: Different Imaging Modalities

From left to right, plain radiograph of the skull base, computerised tomography (CT) of the head, positron emission tomography (PET) of the brain and contrast-enhanced (CE) angiography of the cerebral arteries.

All the above images contain and convey clinically relevant information but do this by using ionising radiation. This type of radiation in the form of X-Rays or gamma rays carries enough energy to liberate electrons and is considered a carcinogen by the World Health Organisation (*Ionizing Radiation, Health Effects and Protective Measures*, 2016). In contrast, MRI does not use electromagnetic radiation in the ionising spectrum. Although there are short-term effects of MRI scanning, and limitations in terms of tolerance, there is currently no compelling evidence of any long-term harm (Herate et al., 2022).

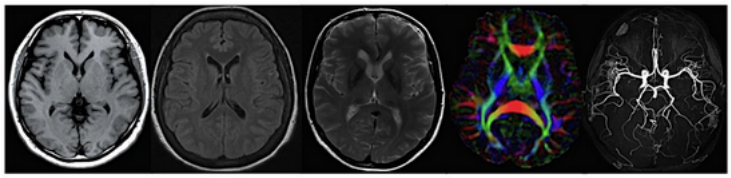

Figure 2: Selection of Image Contrast in MRI.

From left to right, T1-weighted, fluid-attenuated inversion recovery (FLAIR), T2-weighted, diffusion-weighted, and magnetic resonance angiography (MRA).

In a single MRI image acquisition examination, many different tissue contrasts can be obtained non-invasively, in any orientation and without the need for the administration of iodine-based contrast media. The superior tissue contrast and lack of ionising radiation mean that MRI is often the imaging modality of choice in research studies where serial imaging is necessary.

However, there are limitations that need to be considered when selecting MRI as the imaging modality. Safety is fundamental, and all individuals entering the MR environment should be carefully screened and free of any contraindications, such as ferromagnetic metallic implants. Furthermore, some implants, although non-magnetic, can heat up during imaging, are MR conditional, and are only safe under certain limited scanning conditions. The international standard for the safe use of MRI has been published by the International Electrotechnical Commission (IEC) (*IEC 60601-2-33:2022 Medical Electrical Equipment- Part 2-33*, 2022), and the UK has its own safety guidelines published by the Medicines and Healthcare Products Regulatory Agency (MHRA) (*Magnetic Resonance Imaging Equipment in Clinical Use*, 2022).

How does MRI work?

MRI is based on the natural magnetisation of hydrogen nuclei when placed in an external magnetic field. Other elements can be imaged, such as oxygen, sodium, nitrogen, carbon, and fluorine, but only hydrogen is of an adequate quantity and concentration in the human body to provide conventional images. These elements are utilized because of their angular momentum, which is a result of an odd mass number/atomic weight and is known as MR-active nuclei.

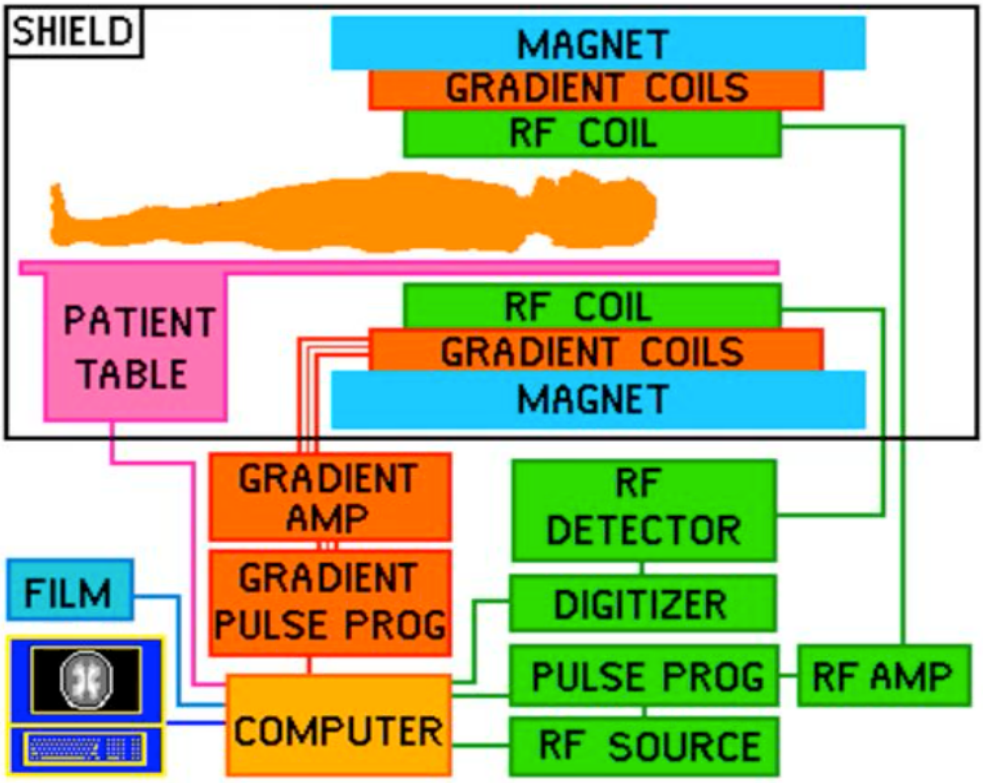

Figure 3: Diagram of MRI scanner (Hornak, 2020)

Placing the body in a strong magnetic field causes the hydrogen proton axis to line up along the scanner longitudinal axis and creates a magnetic vector. Extra energy is introduced in the form of a radio wave pulse that is specific to the element and field strength, and the magnetic vector is deflected from the longitudinal to the transverse plane.

When the radio wave is switched off, the magnetic vector returns to its original resting state, which is variable for different tissues and is measured in two ways. Longitudinal relaxation is referred to as T1 recovery, whereas axial relaxation is T2 decay and occurs in the transverse plane when the axial spin dephases and loses its phase coherence. T1 and T2 are time constants measured in milliseconds (ms) and are specific to different tissues in the body. As relaxation occurs, a signal is generated, which is called free induction decay (FID).

Pulse Sequences

To produce useful images, a series of events involving RF pulses and switching gradient fields are followed by the collection of the signal. These events are determined by the required image contrast and type of pathology required for detection. Collectively, this series of events is called a pulse sequence and falls broadly into two categories: spine echo or gradient echo.

The spin echo uses a second RF pulse to rephase and create an echo, whereas a gradient echo applies switching gradients to create an echo event after the initial RF pulse. By applying additional gradients, the local magnetic field can be altered in small increments; thus, different parts of the body resonate at different frequencies and spatial encoding is achieved. The signal emitted from the subject is gathered on receiver coils, built up in k-space-the spatial frequency information in two or three dimensions and becomes an image via Fourier transformation.

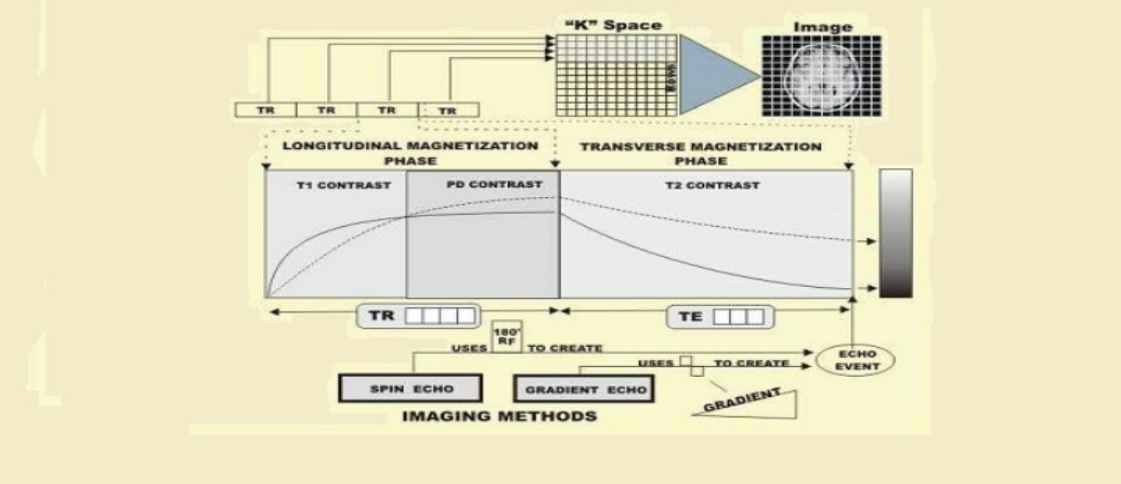

Figure 4: Pulse Sequences (Ebrahim, Mohamed, 2023)

Field Strength

A factor not manipulated by the operator is static field strength (B0) which refers to the power of the operating magnetic field measured in Tesla (T). It is proportional to the nuclear magnetic signals produced by magnetic resonance and is a major factor in image quality. It affects the signal-to-noise ratio (SNR) and T1 of tissue, but poor homogeneity leads to inadequate image quality, something which blighted early systems (Bornert & Norris, 2020). Field homogeneity describes the uniformity of the magnetic field within the bore (isocentre). It is measured in parts per million (ppm) over the diameter of a spherical volume (DSV). SNR is supralinearly proportional to B0, so using the highest field strength available is logical. However, many imaging departments may not have a choice of field strength, and access can be limited depending on demand.

Is bigger always better though? Higher field strengths, especially when first introduced, were prone to inhomogeneity, resulting in special distortion and inadequate fat suppression. This is corrected by improved shimming, the act of making small adjustments to the main magnetic field.

Artefacts in the form of magnetic susceptibility increase at higher field strength (Huang et al., 2015). Another consideration is safety which is influenced by B0. An object or implant which is mildly affected at 0.5T can turn into a dangerous projectile at 3T (Shellock & Crues, 2022) Combined with increased risk of heating, specific absorption rate (SAR) and limits of occupational exposure (Medecines and Healthcare products Regulatory Agency, 2022) there is now increasing interest in exploiting lower field strengths (Sheth et al., 2021).

Limitations of MRI

There is no doubt that MRI is a remarkable imaging modality, but there are limitations to be considered. The most obvious is the static magnetic field, which determines the location and limits those who can enter the MRI environment. Thus, some willing research participants and patients are excluded owing to the presence of metallic implants. Further complications of implants are that some can heat up during scanning due to the time-varying magnetic fields inducing electrical currents in the implant. These time-varying magnetic fields can also induce peripheral nerve stimulation (PNS), which manifests as twitching and discomfort in the extremities. Further heating is created by the deposition of RF energy in both implants and human tissue, which can cause discomfort and can be dangerous for vulnerable members of the population who cannot regulate their temperature.

From a patient perspective, MRI is often poorly tolerated, with the acoustic noise being reported as at least a nuisance and at most '*intolerable*.' Noise levels can exceed permitted safe levels of 85 decibel (dB) and ear protection is required to protect hearing and improve comfort (MHRA, 2021).

Claustrophobia is another difficulty, with the restricted space inside the scanner causing anxiety, which can be so severe that some people cannot endure the procedure at all, and so are excluded unless anaesthesia is administered.

In addition, long scan times can be difficult to deal with and contribute to motion artifacts during imaging, as patients become restless and uncomfortable.

Despite good tissue contrast, it is still appropriate to administer gadolinium (Gd) contrast medium, which was previously considered safe. However, recent evidence suggests Gd retention after repeated administration and the possibility of nephrogenic systemic fibrosis in patients with impaired kidney function (Do et al., 2020).

Image Quality

When referring to quality, it is important to differentiate between a quality assurance (QA) program and the subjective assessment of image quality. QA is a 'process to ensure that any product or service meets a required standard" (Koller et al., 2006), and a recommended set of tests specifically for MRI is included in The Institute of Physics and Engineering in Medicine guidelines (*Quality Control and Artefacts in Magnetic Resonance Imaging*, 2017).
In contrast, image quality is subjective and best described as enabling the observer to extract information from the image and make an exact diagnosis (Holmes & Griffiths, 2016). In an ideal situation, an image will have a high signal, contrast resolution, spatial resolution, and have low levels of noise and be free of artefacts. When considering participants and equipment usage, images also need to be acquired within a concise scan time. Unfortunately, it is not possible to have all of these, and trade-offs always need to be made when optimising pulse sequences. Therefore, the operator requires a good understanding of MRI parameters and the impact on the images and participants when manipulating any of these parameters.

Signal-to-Noise Ratio

The magnetic resonance (MR) signal is a term which is frequently referred to and is defined as '*the voltage induced in the receiver coil by the precession of net magnetic vector in the transverse plane*' (Westbrook et al., 2011) and corresponds to the brightness of any pixel and/or voxel in the image (McRobbie et al., 2006) and so is a key factor in the final image. Sadly, noise is also generated by the system and the presence of the patient/subject in the main magnetic field occurring at all frequencies and random in time. In contrast, signal is variable and relative to noise, so the signal-to-noise ratio (SNR) is a major consideration when manipulating parameters. According to Westbrook et al. (2011), the factors which affect SNR are proton density, voxel volume, repetition time (TR), echo time (TE), flip angle, number of excitations, receiver bandwidth and coil type. However, other factors have been recognised, such as the use of multi-element surface coils, parallel imaging and different reconstruction filters (Dietrich et al., 2007).

Low Contrast Resolution

As already mentioned, MRI produces images with superior soft tissue contrast compared to other imaging modalities (Bryan, 2009). This can be exploited to image all organs, including those previously unattainable by imaging such as the pituitary gland (Bradley et al., 2001). Low contrast resolution refers to the MRI system's ability to distinguish between two structures with similar signal intensities. The type of MRI sequence used affects contrast resolution, as different sequences are sensitive to different tissue properties.

The contrast mechanisms can be divided into intrinsic and extrinsic. Intrinsic qualities are T1, T2 and proton density (PD). Scanning parameters are manipulated by the operator to 'weight' the image towards the desired contrast. The choice of sequence, either spin echo or gradient echo, will then determine which parameters are at the disposal of the operator, which includes TR, TE and, in the case of gradient echo, flip angle. Since these parameters are time-dependent, manipulation can change the timing of the scan and limit choices related to slice number to ensure scan times remain optimised.

Extrinsic contrast mechanisms, however, include flow, the introduction of contrast media, fat suppression techniques including inversion recovery (IR), refocusing pulses, slice thickness and field strength contribute to the image contrast to varying degrees. The impact on the image will vary between body parts and the structure under examination.

It is acknowledged that MRI examinations are longer than other imaging. Indeed, the very first image of a human performed by Damadian and his team took five hours on a machine named the Indomitable (Damadian, 1972). Since then, much progress has been made with stronger gradients, faster rise times and slew rates; however, motion is always a problem. Along with hardware improvements, developing under-sampling techniques using the fact that k-space is symmetrical reduces scan time but at the expense of image quality (Moratal et al., 2008). The introduction of parallel imaging techniques has seen scan times reduced further, though with a new type of artefact (Pruessmann et al., 1999). More recently, this technique has been developed further to include under-sampling (Candes et al., 2004) and is now commercially available as compressed SENSE (Geerts-Ossevoort et al., 2018).

Spatial Resolution

In MRI, spatial resolution refers to the ability of the imaging system to distinguish between two adjacent structures or features in an image. It is a measure of the smallest distance

between two objects that can be reliably resolved by the MRI scanner. Resolutions come in various forms, and all of them impact the overall resolution in some way. Contrast was discussed in the previous section.

The spatial resolution is limited by the size of the imaging voxels, which are three-dimensional rectangular solids, resulting in a different resolution in the three directions. The size of the imaging voxel is governed by the matrix, field of view (FOV) and slice thickness (ST) (Allisy-Roberts, Penelope & Williams, Jerry, 2008). Variations in any of these three parameters will result in changing the size of the voxel and, thus, the spatial resolution. However, changes to the phase encoding direction of the FOV will also impact the time of the scan, so a balance between scan length and the required spatial resolution is vital. In contrast, though, reducing phase encoding steps can be used to reduce the scan time if the shape of the anatomy allows it by selecting a rectangular FOV(RFOV) (Westbrook et al., 2011).

A significant influence on spatial resolution is the choice of slice thickness, as this determines the depth of the voxel. The scanner hardware will determine the minimum slice thickness possible while using two dimensional 2D (2D) imaging though thinner slices can be achieved by utilising three-dimensional (3D) imaging techniques but with a time penalty.

Selecting the minimum slice thickness and gap appears to be a logical choice. However, since the voxel represents the signal from a small volume of tissue, reducing the slice thickness will reduce the amount of signal which can be measured, which has an impact on the overall image quality (McRobbie et al., 2006). But a larger voxel, although improving the signal, can cause partial voluming where individual signal intensities are averaged together and not distinct within the vowel.

All the parameters which influence spatial resolution are controlled by the operator. Again, a judgment is required to balance all the requirements of the image and the capabilities of the scanner and subject.

Temporal Resolution

Temporal resolution is the ability of the imaging system to capture images rapidly over time, allowing for the visualisation of dynamic processes in real-time or near real-time. Examples are cardiac MRI and flow measurements.

Artefacts

Artefacts on the MR image can degrade the quality and are broadly defined as "*any feature on an image which misrepresents the object in the field of view*" (McRobbie et al., 2006). The most common fall into three categories: motion, inhomogeneity, or digital imaging. Motion is predominately caused by involuntary movement or physiological motion caused by normal bodily functions, such as respiration. Inhomogeneous artifacts are due to imperfections in the main magnetic field and the susceptibility of tissue-air interfaces. Finally, a variety of artifacts are caused by the digital imaging processes and Fourier Transform. Some artefacts are inevitable and can only be minimised while some can be illuminated completely. Being able to recognise artefacts, along with a thorough understanding of causes and remedies is imperative to maximise image quality.

Noise

Electrical noise exists in all conductors and materialises as a grainy and mottled appearance on the MR image. However, further noise arises mainly from naturally occurring electrical currents within the human body, which create fluctuating magnetic fields. Thus, random noise is induced in the coil by the electronically charged particles such as sodium and potassium during nerve conduction (McRobbie et al., 2006). Noise and the relationship with signal and contrast are expressed as a ratio and calculated mathematically.

This succinct overview of MRI parameters has displayed many options available to the operator, none without an impact. Therefore, it is essential that the reason for imaging is specified, the operator is knowledgeable and uses a judicious choice of all the parameters.

Imaging Parameters and Terminology

The control of the events in a pulse sequence is chosen by the operator by manipulating parameters. Some of the most common included in this text are:

Field of View	Area included in the imaging
Inversion Recovery	Pulse sequence beginning with 180-degree inverting pulse resulting in heavy T1 weighting.
Multi Echo (ME)	Repeated gradient reversal to produce multiple echo events.

Flip Angle	Amount of rotation the net magnatraction experiences upon application of RF pulse.
In and Out of Phase	Imaging during phase coherence and again out of phase coherence.
k-space	Part of the processor where spatial frequencies are stored.
Parallel Imaging	Using multiple coils to fill segments of k-space
Phase	Position of the magnetic moment on its precessional path.
Phase Encoding	Location of a signal based on phase.
Shimming	Optimising the homogeneity of the main magnetic field.
Slice Thickness (ST)	The depth of the selected slice
Echo Time (TE)	Time from 90-degree pulse to the echo.
Repetition Time (TR)	Time between successive 90-degree radio frequency (RF) pulses.

Portfolio

Papers submitted for consideration.

The following papers are unformatted versions that were accepted for publication (2008-2020). Therefore, the referencing styles used are consistent with the respective journals' guide for authors, and figure and tabled legends apply to the respective publication.

1. Cardiac T2* and lipid measurement at 3.0 T-initial experience (O'Regan, Callaghan, Fitzpatrick, et al., 2008)

2. Liver fat content and T2*: Simultaneous measurement by using breath-hold multiecho MR imaging at 3.0 T – Feasibility (O'Regan, Callaghan, Wylezinska-Arridge, et al., 2008)

3. Reduction of total lung capacity in obese men: Comparison of total intrathoracic and gas volumes (Watson et al., 2010)

4. Whole body fat: Content and distribution (Thomas et al., 2013)

5. Validation of a fast method for quantification of intra-abdominal and subcutaneous adipose tissue for large-scale human studies (Borga et al., 2015)

6. Changes in Liver Volume in Patients with Chronic Hepatitis C Undergoing Antiviral Therapy (J. A. Fitzpatrick et al., 2015)

7. Psoas major cross-sectional area: A potential marker of cardiorespiratory fitness (J. A. Fitzpatrick et al., 2013)

8. Advancing Pancreas Segmentation in Multi-protocol MRI Volumes using Hausdorff-Sine Loss Function (Asaturyan et al., 2019a, 2019b)

9. Large-scale analysis of iliopsoas muscle volumes in the UK Biobank (J. A. Fitzpatrick et al., 2020)

Supporting Evidence

I. Quantifying hepatic lipid content and T2* decay using breath-hold multiecho imaging at 3.0 tesla (O'Regan et al., 2006)

II. Measurement of Pancreatic Fat Using Multi Echo MRI (J. Fitzpatrick, Thomas, Durighel, O'Regan, et al., 2010)

III. Comparing Multi Echo MRI and MRS to Measure Pancreatic (J. Fitzpatrick et al., 2012)

IV. Psoas Muscle Cross Sectional Area: A Novel Marker of Physical Fitness (J. A. Fitzpatrick et al., 2013)

Paper 1

Cardiac T2* and lipid measurement at 3.0 T-initial experience

Declan P. O ʼRegan, Martina F. Callaghan, ***Julie Fitzpatrick*****,** Rossi P. Naoumova, Joseph V. Hajnal, Stephan A. Schmitz

Abstract This study was designed to assess whether breath-hold cardiac multiecho imaging at 3.0 T is achievable without significant image artefacts and if fat/water phase interference modulates the exponential T2* signal decay. Twelve healthy volunteers (mean age 39) were imaged on a Philips Intera 3.0 T MRI scanner. Multiecho imaging was performed with a breath-hold spoiled gradient echo sequence with a seven echo readout (echo times 1.15–8.05 ms, repetition time 11 ms) using a black-blood prepulse and volume shimming. T2* values were calculated with both mono- and biexponential fits from the mean signal intensity of the interventricular septum. The global mean T2* was 27.3 ms±6.4. The mean signal-to-noise ratio (SNR) of the septum was 22.8±9.9, and the contrast-to-noise ratio (CNR) of the septum to the left ventricular cavity 20.3±9.4. A better fit was obtained with a biexponential model and the mean fat fraction derived was 3.7%. Cardiac functional parameters were in the normal range and showed no correlation with T2*. Cardiac T2* estimation with gradient multiecho imaging at 3.0 T can be achieved with minimal artefact and modelling the signal decay with a biexponential function allows estimation of myocardial lipid content as well as T2* decay.

Introduction

Transfusional iron overload is a frequent cause of heart failure in patients with thalassaemia [1, 2]. Biochemical measures of iron overload are inconsistent predictors of myocardial iron deposition [3] and so an accurate non-invasive assessment of iron overload may guide diagnosis, treatment and response. Iron deposition complexes such as ferritin, haemosiderin and low molecular weight cytosol iron cause a shortening of T2* largely due to paramagnetic effects [4]. Gradient echo sequences with readouts at multiple echo times can be used to rapidly acquire a set of increasingly T2*-weighted images. The fitting of an exponential curve to the magnitude signal intensity of these images allows the measurement of T2* in a defined

anatomical region. The inverse correlation of T2* with liver iron concentration, as obtained by biopsy, has been used to validate this technique [5]. Cardiac-triggered gradient-echo sequences may be used to obtain T2* measurements of the heart to estimate the severity of myocardial iron deposition as well as assessing systolic and diastolic function. This technique has shown good inter-study and inter-scanner reproducibility [5, 6], correlates with invasive biopsy [3, 7] and can monitor response to chelation therapy [8–10].

Cardiac imaging at 3.0 T may offer significant advantages over previous techniques for measuring myocardial T2*. The higher field strength has the advantage of potentially doubling the signal-to-noise ratio (SNR) compared to conventional 1.5 T systems and this may allow imaging at greater spatial or temporal resolution. Higher SNR may also allow the interference effects of fat and water signals within the myocardium to be detected [11]. The greater susceptibility effects at high field strength might also result in improved sensitivity to lower concentrations of tissue iron. However, there are several technical issues which remain problematic for high-field cardiac T2* imaging such as susceptibility artefact and poor shimming [12].

This study was designed to assess whether breath-hold cardiac multiecho imaging at 3.0 T is achievable without significant image artefacts and if fat/water phase interference modulates the exponential T2* signal decay.

Materials and methods

Subjects

Imaging was performed on 12 subjects (9 male, 3 female) with a mean age of 39 (range 27–49). No subjects had a history of iron overload or cardiac disease. Ethical approval was granted for the study and all participants gave written informed consent. Specific absorption rate (SAR) limits were 4.0 W/kg.

MR sequences

The MRI studies were performed on a 3.0 T Philips Intera system (Best, The Netherlands). The maximum gradient strength was 31 mT/m and the maximum slew rate 200 mT/m/ms. A six-element cardiac phased array receiver coil was used and a vector-ECG system used for R-wave detection. Scout images were obtained and used to plan an axial stack of cine balanced-steady state free precession images in the left ventricular short axis from base to apex.

Sequence parameters for the cine sequence were matrix 176×256, flip angle 45°, field of view 350 mm, slice thickness 8 mm with a 2-mm gap, TE 1.8 ms, TR 3.7 ms and 20 cardiac phases. Velocity-encoded imaging was performed across the mitral valve to assess diastolic function with a through plane velocity encoding parameter of 80 cm/s.
Multiecho imaging was performed with a breath-hold spoiled gradient echo sequence with a seven echo readout. A single acquisition was made through the mid cavity of the left ventricular short axis. The multiecho sequence parameters were matrix 128×256, flip angle 20°, field of view 320 mm, slice thickness 10 mm, turbo field echo factor 6 and TR 11 ms. The echo times chosen were when the signals from fat and water are alternately in-phase and out-of-phase with respect to each other. Proton spectroscopy studies have determined that the chemical shift of intrahepatic lipid relative to water is 3.4 ppm [13] and so the first TE chosen was 1.15 ms with a ΔTE of 1.15 ms (TEs-1.15, 2.30, 3.45, 4.60, 5.75, 6.90 and 8.05 ms). Cardiac triggering was set for mid-diastole to reduce motion artefact. Localised higher-order shimming was used with a volume placed over the whole heart. A black- blood double inversion prepulse was used for suppression of ghosting artefact from the blood pool. Images were acquired in held expiration.

Quantitative analysis

Quantitative image analysis was performed by a cardiac radiologist (DPO'R). The cine sequences were analysed using Philips (Best, The Netherlands) ViewForum software release 4.1. The endo- and epicardial borders were defined on the left ventricular cine images using a standard methodology [14] to derive left ventricular mass, ejection fraction, end diastolic volume (LVEDV), end systolic volume (LVESV), peak filling rate (PFR) and time to PFR. On the velocity-encoded images a region of interest was defined across the mitral valve orifice and flux rates calculated and an E:A ratio derived. Multivariate linear regression analysis was performed on these functional indices with myocardial T2* as a dependent variable using SPSS software (SPSS Inc, Chicago, IL) assuming significance at $p < 0.05$. T2* analysis was performed using ImageJ software (U.S. National Institutes of Health, Bethesda, MD) and SigmaPlot (Systat software Inc, San Jose, CA). Polygonal regions of interest were drawn around the interventricular septum. The endocardial boundary was excluded to avoid contamination with the blood pool signal. Curve fitting was performed with a single process exponential decay model using the following equation:

$$|S(t)| = \left|S_0 e^{-t/T2^*}\right| + c$$

where $|S_0|$ is the initial magnitude signal intensity and $|S(t)|$ the magnitude signal intensity at echo time t and T2* the global decay constant. An offset correction (c) was included to model the effect of noise bias in the data [15]. Parametric colour maps of global T2* were obtained with a pixel-by-pixel analysis using Matlab 7.0 (Mathworks, Natick, MA).

A biexponential curve-fitting equation was used to model the chemical shift interference effects of fat and water components as a function of echo time [11]:

$$|S(t)| = \left|S_W e^{-t/T2^*_W} + S_F e^{-t/T2^*_F + i\Delta\omega t}\right| + c$$

where S_w and S_f are the components of the magnitude signal ($|S(t)|$) due to water and fat, respectively, $T2^*_w$ and $T2^*_f$ their respective decay constants, t the time after excitation, and $\Delta\omega$ the difference in frequency between fat and water. To reduce the number of degrees of freedom in the model the frequency difference between fat and water was taken to be 3.4 ppm. The signal components due to water (S_w) and fat (S_f), as well as their respective T2* decay constants ($T2^*_w$ and $T2^*_f$), were modeled with an iterative curve-fitting technique using the Levenberg- Marquardt algorithm [16] (SigmaPlot version 10, SPSS Inc, Chicago, IL). A comparison between the two models, which have different degrees of freedom, was made with an F-test assuming significance at $p<0.05$. The goodness of fit of the two models was described by the r2 statistic.

SNR and CNR measurements were obtained from the mean signal intensity of the interventricular septum (SISeptum) and the left ventricular cavity (SICavity). The myocardial septum was manually segmented with a polygonal region of interest. A circular region of interest was placed within the left ventricular cavity avoiding the papillary muscles. Background noise (N) was assessed from the standard deviation of the signal intensity of a rectangular region of interest placed in the background and orientated in the phase encoding direction. The standard deviation of the noise was multiplied by the Rayleigh factor (1.53) to account for the non-Gaussian distribution of noise in magnitude images [17]. SNR was calculated as:

$$mean\left(SI_{Septum}\right) / Standard\ deviation(N) \times 1.53$$

and the CNR as -

$$mean\left(SI_{Septum}\right) - mean\left(SI_{Cavity}\right) / Standard\ deviation(N) \times 1.53$$

Results

All subjects tolerated the study and images of diagnostic quality were obtained. Image quality was maintained throughout the multiecho acquisition, although at the longest echo times signal loss was observed at the inferolateral wall of the LV (Fig. 1). Parametric colour maps were obtained showing the regional variation in global T2* values (Fig. 2).

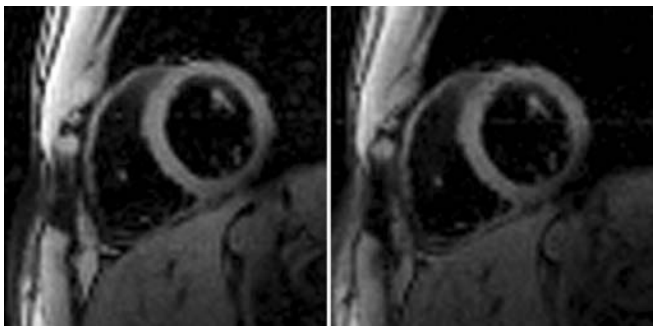

Fig. 1 Two images from a black-blood multiecho sequence of the left ventricle. The first echo at 1.15 ms is shown on the left and the last echo at 8.05 ms on the right. Image quality is maintained with only minor susceptibility effect in the inferolateral wall at the longer echo times

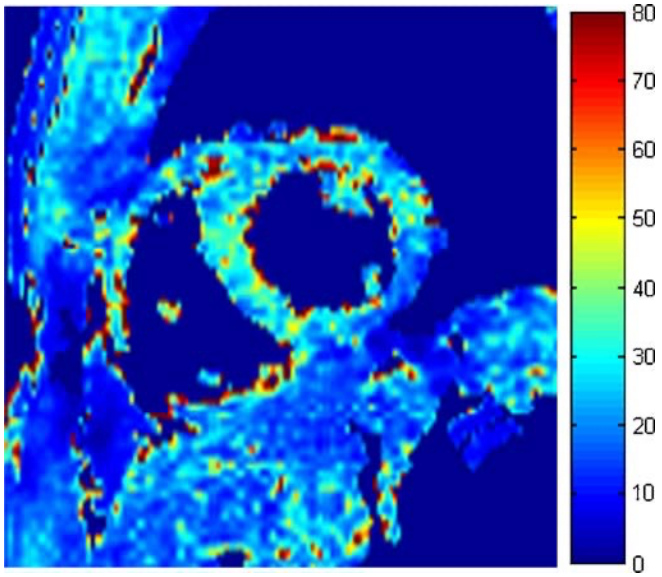

Fig. 2 A parametic colour map of the global T2 values (ms) within the heart*

Results are expressed as a mean ± 1 SD. The mean T2* of the myocardial septum was 27.3 ms ± 6.4. Using r2 as a measure of goodness-of-fit, the single process decay model (r2 = 0.979) (Fig. 3) was inferior to the fat/water chemical shift biexponential model (r2=0.998) (Fig. 4). The F-test indicated that the higher-order biexponential model provided a better fit ($p < 0.05$). The model indicated a fat fraction of 3.7%, a T2* (water) of 26 ms and T2* (fat) of 2 ms. The mean SNR of the septum was 22.8±9.9, and the CNR of the septum to the left ventricular cavity 20.3 ± 9.4 (Table 1). The mean LV mass was 88.9 g ± 32.0, LVEDV 148.8 ml ± 46.3, LVESV 59.8 ml ± 25.4, ejection fraction 60.3% ± 7.5, cardiac output 6.0 l/min ± 1.7, E:A ratio 1.8 ±

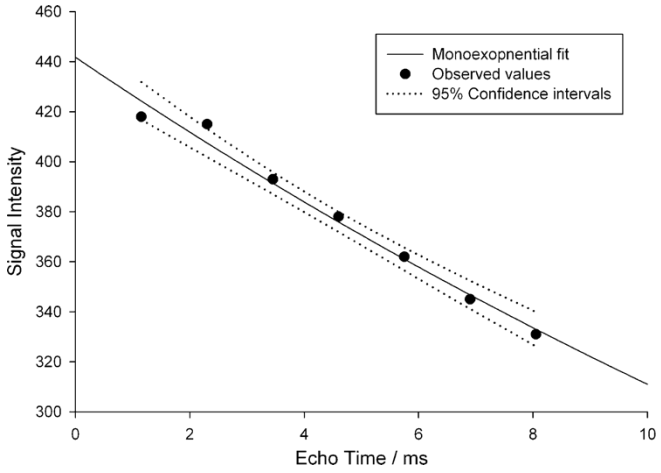

Fig. 3 A plot to show the variation in mean signal intensity with echo time for the interventricular septum (n=12) using a trendline with a single process exponential decay

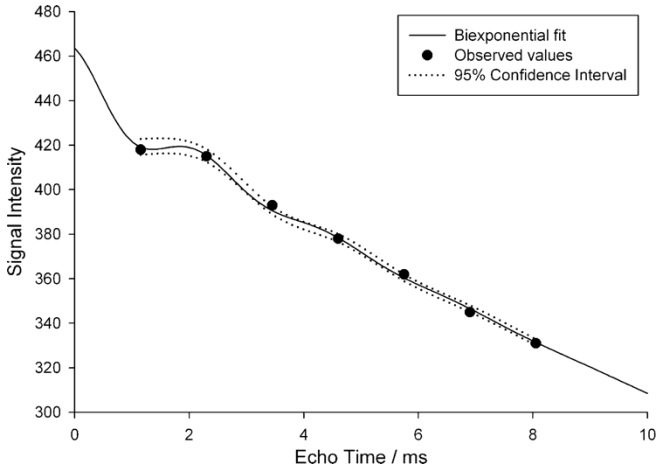

Fig. 4 The same data are plotted as in Fig. 3, but an improved fit is obtained with a biexponential decay model to account for fat/water phase interference within the myocardium

0.6, PFR 467 ml/s±103.4, and the time to PFR 124.6 ms± 40.3. There was no correlation between T2* values in these healthy subjects and the measured parameters of systolic and diastolic function.

Discussion

This pilot study demonstrates that black blood breath-hold multiecho cardiac T2* measurement is achievable at 3.0 T field strength with minimal image artefacts. The phase interference between fat and water signals modulates the signal intensity as a function of echo time and a better fit is obtained with a biexponential model. This technique allows both the myocardial fat content and the T2* decays of fat and water to be determined.

Table 1 The values for each participant undergoing multiecho imaging

	Global T2*	SNR	CNR
1	29.0	25.9	23.6
2	28.8	17.9	15.8
3	18.2	13.0	11.0
4	21.4	40.0	37.2
5	23.9	34.4	32.7
6	28.2	17.6	13.0
7	25.0	27.6	25.1
8	21.5	24.2	22.3
9	28.0	13.6	11.8
10	43.5	6.6	6.0
11	30.9	19.8	17.6
12	28.5	33.0	28.1

The principle of cardiac multiecho imaging is that myocardial iron concentration has a predictable relation- ship with tissue relaxivity. The T2* decay can be expressed as:

$$\frac{1}{T2^*} = \frac{1}{T2} + \frac{1}{2}\gamma\Delta B$$

and will be dependent on the tissue T2, the variation in magnetic field (ΔB) and the gyromagnetic ratio (γ). Iron deposition complexes, such as ferritin and other iron nanoparticles, have complex properties of ferromagnetism, antiferromagnetism and paramagnetism [18]. They appear unique in that their 1/T2 shows a linear dependence on field strength [19]. Field-dependent change in 1/T2 may there- fore be highly specific for changes in ferritin levels [18]. The difference in T2-relaxation times for the heart has not been reported, but the T2 of the solid abdominal viscera is slightly shorter at 3.0 T than 1.5 T using spin-echo techniques [20]. Gradient echo sequences are also sensitive to local field inhomogeneities caused by the microscopic field gradients of iron particles leading to a shortening of T2*. Empirically 1/T2* at 3 T is twice that at 1.5 T in subjects with iron overload with a small offset depending on the non-iron component of the tissue [12]. Therefore extrapolation to 3.0 T of biopsy-validated T2* data obtained at 1.5 T [5] should be feasible.

In this study the mean cardiac T2* values are derived from a relatively early range of echo times between 1.15 ms and 8.05 ms. In patients with iron overload with a very short T2* it is important to sample the signal decay curve as early as possible to avoid underestimation of iron con- tent. Furthermore, the short echo times used in this study limit artefact due to cardiac motion, flow effects and blood oxygenation level dependent effects [15]. Normal values of myocardial T2* using a breath-hold multiecho sequence at 1.5 T have been reported as 33.3 ms±7.8 with eight readouts between 2.6 and 16.7 ms and a TR of 20 ms [21]. A combination of single and multiecho T2* measurement at 3.0 T has reported myocardial T2* values in healthy volunteers (excluding outliers) of 33.3 ms ± 8.3 with eight readouts between 1.6 and 12.8 ms and a TR of 13 ms [12]. Our study addressed potential sources of artefact by using localized volume shimming and a black blood prepulse. Our findings at 3 T show a myocardial T2* of 27.3 ms ± 6.4 with seven readouts between 1.15 and 8.05 ms and a TR of 11 ms. The similar relaxation values at 3.0 T compared to lower field strengths may reflect the absence of measurable quantities of ferritin in the myocardium of normal volunteers. In the healthy subjects that were imaged, with no history of iron overload, there does not appear to be any significant correlation of myocardial T2* with the measured parameters of systolic

or diastolic function. Our study examined a small number of normal volunteers and a larger cohort may be needed to define normal ranges for T2* at 3 T. Myocardial T2* measurement has shown good inter-study and inter-scanner reproducibility at 1.5 T [5, 6], but this has yet to be determined at 3 T.

A deviation from a simple exponential T2* decay in myocardium due to fat and water phase interference has been noted previously [15]. The use of in-phase and out- of-phase echo times and fitting to a biexponential model allows an estimate of myocardial lipid content to be made [11]. In volunteers the lipid content is small but introduces a time dependency to the signal decay. Cardiac steatosis can be measured with proton spectroscopy and is detectable in diabetic patients [22] and may have a role in cardiac failure [23]. However, the amount of fat detected was small and the variation in signal intensity would be lessened in T2* protocols using intermediate echo time intervals.

Cardiac imaging at 3.0 T has demonstrated the potential for significant improvement in signal-to-noise ratios (SNR) and image quality [24, 25], but may be associated with greater B1 and B0 field inhomogeneities, longer T1 relaxation and power deposition limitations [26]. Multi- echo imaging of the heart therefore poses a number of challenges at high field strength. Radio frequency power deposition was reduced by using a shallower flip angle (20°) than that typically used at 1.5 T field strength (35°). The potential loss of SNR may be compensated for by using a shorter TR although this will depend on the longest echo time in the multiecho acquisition. Susceptibility artefact appeared relatively minor and was limited to signal loss of the inferolateral epicardial left ventricle at longer echo times. This effect has been observed at lower field strength and may be due to deoxygenated blood in the posterior vein of the left ventricle causing local field inhomogeneity [27]. Motion artifact was minimized by imaging during suspended respiration and limiting the acquisition window to mid-diastole. A double inversion- recovery black blood prepulse was employed to further reduce ghosting artifact from the blood pool and localized higher-order volume shimming was used to improve B homogeneity.

When quantifying magnitude MR images there is a potential for noise bias when the SNR falls below 2 [28]. However, the high SNR offered by 3.0 T imaging limits the potential error introduced by structural noise variation. As the signal decay was being measured in normal volunteers with no iron overload, a signal plateau was not reached. However an offset

correction was included in the models for consistency as significant underestimation of T2* may occur in severe iron overload due to noise bias [15].

The most appropriate measurement of SNR and CNR is controversial, and a standard approach has been taken in this study using a “noise-only” region in the field of view [24, 25, 29]. However, the noise is not evenly distributed in an image formed by a phased array coil and apparently noise-free areas in the background may be contaminated by artefact [30]. Nevertheless, our method serves as an appropriate indicator of image noise and contrast. An advantage of the good SNR achievable at 3.0 T is that it may be traded for higher spatial or temporal resolution with the use of parallel imaging techniques. Breath-hold multi-slice imaging may become feasible, and smaller voxels may allow better differentiation of endocardial and epicardial variation in T2*[31].

Conclusion

Cardiac T2* estimation with gradient multiecho imaging at 3.0 T can be achieved with minimal artefact by the use of localised shimming and black blood imaging. Modelling the signal decay with a biexponential function allows estimation of myocardial lipid content as well as T2* decay.

References

1. Olivieri NF, Nathan DG, MacMillan JH et al (1994) Survival in medically treated patients with homozygous beta- thalassemia. N Engl J Med 331(9): 574–578

2. Zurlo MG, De Stefano P, Borgna- Pignatti C et al (1989) Survival and causes of death in thalassaemia major. Lancet 2(8653):27–30

3. Mavrogeni SI, Markussis V, Kaklamanis L et al (2005) A comparison of magnetic resonance imaging and cardiac biopsy in the evaluation of heart iron overload in patients with beta-thalassemia major. Eur J Haematol 75(3):241–247

4. Stark D (1991) Hepatic iron overload: paramagnetic pathology. Radiology 179(2):333–335

5. Anderson LJ, Holden S, Davis B et al (2001) Cardiovascular T2-star (T2*) magnetic resonance for the early diag- nosis of myocardial iron overload. Eur Heart J 22(23):2171–2179

6. Westwood MA, Anderson LJ, Firmin DN et al (2003) Interscanner repro- ducibility of cardiovascular magnetic resonance T2* measurements of tissue iron in thalassemia. J Magn Reson Imaging 18(5):616–620
7. Westwood MA, Sheppard MN, Awogbade M et al (2005) Myocardial biopsy and T2* magnetic resonance in heart failure due to thalassaemia.
Br J Haematol 128(1):2
8. Anderson LJ, Westwood MA, Holden S et al (2004) Myocardial iron clearance during reversal of siderotic cardio- myopathy with intravenous desferrio- xamine: a prospective study using T2* cardiovascular magnetic resonance.
Br J Haematol 127(3):348–355
9. Pepe A, Lombardi M, Positano V et al
(2006) Evaluation of the efficacy of oral deferiprone in beta-thalassemia major by multislice multiecho T2*. Eur J Haematol 76(3):183–192
10. Christoforidis A, Haritandi A, Tsatra I et al (2007) Four-year evaluation of myocardial and liver iron assessed prospectively with serial MRI scans in young patients with beta-thalassaemia major: comparison between different chelation regimens. Eur J Haematol 78 (1):52–57
11. Derby K, Kramer DM, Kaufman L (1993) A technique for assessment of bone marrow composition using mag- netic resonance phase interference at low field. Magn Reson Med 29(4): 465–469
12. Storey P, Thompson AA, Carqueville CL et al (2007) R2* imaging of transfusional iron burden at 3 T and comparison with 1.5T. J Magn Reson Imaging 25(3):540–547
13. Szczepaniak LS, Babcock EE, Schick F et al (1999) Measurement of intracel- lular triglyceride stores by H spectros- copy: validation in vivo. Am J Physiol Endocrinol Metab 276(5):E977–E989
14. Alfakih K, Plein S, Thiele H et al (2003) Normal human left and right ventricular dimensions for MRI as assessed by turbo gradient echo and steady-state free precession imaging sequences. J Magn Reson Imaging 17 (3):323–329
15. Ghugre NR, Enriquez CM, Coates TD, Nelson MD Jr, Wood JC (2006) Improved R2* measurements in myo- cardial iron overload. J Magn Reson Imaging 23(1):9–16
16. Marquardt DW (1963) An Algorithm for Least Squares Estimation of Parameters. J Soc Ind Appl Math 11:431–441

17. Kaufman L, Kramer DM, Crooks LE, Ortendahl DA (1989) Measuring signal-to-noise ratios in MR imaging. Radiology 173(1):265–267
18. Bartzokis G, Aravagiri M, Oldendorf WH, Mintz J, Marder SR (1993) Field dependent transverse relaxation rate increase may be a specific measure of tissue iron stores. Magn Reson Med 29 (4):459–464
19. Vymazal J, Brooks RA, Zak O et al (1992) T1 and T2 of ferritin at different field strengths: effect on MRI. Magn Reson Med 27(2):368–374
20. de Bazelaire CMJ, Duhamel GD, Rofsky NM, Alsop DC (2004) MR imaging relaxation times of abdominal and pelvic tissues measured in vivo at 3.0 T: Preliminary results. Radiology 230(3):652–659
21. Westwood M, Anderson LJ, Firmin DN et al (2003) A single breath-hold multiecho T2* cardiovascular magnetic resonance technique for diagnosis of myocardial iron overload. J Magn Reson Imaging 18(1):33–39
22. McGavock JM, Lingvay I, Zib I et al (2007) Cardiac steatosis in diabetes mellitus. A 1H-magnetic resonance spectroscopy study. Circulation 116 (10):1170–1175
23. Sharma S, Adrogue JV, Golfman L et al (2004) Intramyocardial lipid accumu- lation in the failing human heart resembles the lipotoxic rat heart. Faseb J 18(14):1692–1700
24. Hinton DP, Wald LL, Pitts J, Schmitt F (2003) Comparison of cardiac MRI on 1.5 and 3.0 Tesla clinical whole body systems. Invest Radiol 38(7):436–442
25. Gutberlet M, Spors B, Grothoff M et al (2004) Comparison of different cardiac MRI sequences at 1.5 T/3.0 T with respect to signal-to-noise and contrast- to-noise ratios-initial experience. Rofo 176(6):801–808
26. Schar M, Kozerke S, Fischer SE, Boesiger P (2004) Cardiac SSFP imaging at 3 Tesla. Magn Reson Med 51(4):799–806
27. Reeder SB, Faranesh AZ, Boxerman JL, McVeigh ER (1998) In vivo measurement of T*2 and field inho- mogeneity maps in the human heart at 1.5 T. Magn Reson Med 39(6): 988–998
28. Gudbjartsson H, Patz S (1995) The Rician distribution of noisy MRI data. Magn Reson Med 34(6):910–914
29. Pijl MEJ, Doornbos J, Wasser MNJM et al (2004) Quantitative analysis of focal masses at MR imaging: A plea for standardization. Radiology 231 (3):737–744

30. Kellman P, McVeigh ER (2005) Image reconstruction in SNR units: a general method for SNR measurement. Magn Reson Med 54(6):1439–1447
31. Positano V, Pepe A, Santarelli MF et al (2007) Standardized T(2)* map of normal human heart in vivo to correct T (2)* segmental artefacts. NMR Biomed 20(6):578–590

Paper 2

Liver Fat Content and T2*: Simultaneous Measurement by Using Breath-hold Multiecho MR Imaging at 3.0 T-Feasibility[1]

Declan O'Regan, Martina Callaghan, Marzena Wylezinska-Arridge, ***Julie Fitzpatrick***, Rossi Naoumova, Joseph Hajnal, Stephan Schmitz

Abstract

Research ethics committee approval was obtained for this study, and written informed consent was obtained from all participants. The purpose was to prospectively evaluate the feasibility of breath-hold multiecho in- and out -of- phase magnetic resonance (MR) imaging for simultaneous lipid quantification and T2* measurement. A spoiled gradient-echo sequence with seven echo times alternately in phase and out of phase was used at 3.0 T. Imaging was performed in a lipid phantom, in five healthy volunteers (all men; mean age, 37 years), and in five obese individuals with hyperlipidemia or diabetes (four men, one woman; mean age, 53 years). A biexponential curve-fitting model was used to derive the relative signal contributions from fat and water, and these results were compared with results of liver proton MR spectroscopy, the reference standard. There was a significant correlation between multi-echo and spectroscopic measurements of hepatic lipid concentration ($r^2 = 0.99$, $P < .001$). In vivo, the T2* of water was consistently longer than that of fat and reliably enabled the signal components to be correctly assigned. In the lipid phantom, the multiecho method could be used to determine the fat-to-water ratio and the T2* values of fat and water throughout the entire range of fat concentrations. Multiecho imaging shows promise as a method of simultaneous fat and T2* quantification.

Introduction

Accurate noninvasive assessment of liver fat content is an important tool in the evaluation of patients with hepatic steatosis [1]. Lipid quantification with magnetic resonance (MR) imaging relies on the difference in resonant frequency between fat and water molecules. With gradient-echo sequences, the signal intensity is at a maximum when the transverse

magnetization vectors of fat and water within the voxel are in phase and at a minimum when the vectors are out of phase [2]. Single and dual-echo techniques have previously been used to estimate lipid content within the liver [2-9] and adrenal glands [10]. However, signal intensity loss on in-phase images caused by the presence of liver iron is a potential pit fall in the determination of liver fat percentage by using dual-echo imaging [11]. A separate sequence is therefore required to correct for global T2* effects. A further limitation is that dual-echo methods do not enable differentiation of whether the dominant component is fat or water, so an additional sequence with either gradient-echo imaging or breath-hold spectroscopy is required to resolve this [12,13]. In contrast, multiecho imaging has the potential to enable more accurate and efficient measurement of tissue fat content in a single sequence. The signal intensity variation in a multiecho acquisition would be expected to depend on the individual T2* decays of the fat and water components, as well as a periodic oscillation of signal intensity between in-phase and out-of-phase echo times dependent on the fat-to-water ratio [14-17]. A rapid single sequence allowing accurate tissue fat quantification as well as T2* measurement would be of potential value in lipid deposition disorders. Thus, the aim of our study was to prospectively evaluate the feasibility of breath-hold multiecho in- and out of phase MR imaging for simultaneous lipid quantification and T2* measurement.

Advances in Knowledge

- Unlike with dual-echo methods, with multiecho MR imaging, fat measurement can be performed without the need to acquire a separate T2* map, and the signal components may be correctly assigned to fat and water on the basis of their different T2* values.
- Results of fat quantification in the liver by using a multiecho technique correlate highly ($r^2 = 0.99$, $P < .001$) with those of T2-corrected proton MR spectroscopy.

Materials and Methods

Financial support was given by Bayer Schering Pharma (Newbury, Berkshire,England) and Philips Medical Systems (Best, the Netherlands). The authors had control of the data and information submitted for publication.

Lipid Phantom Study

A phantom was constructed by pouring equal volumes of mineral oil (liquid petrolatum; Johnson and Johnson, New Brunswick, NJ) and water into a cylindric container [6]. The water was doped with 10mmol/L copper sulfate solution to shorten its T2. An oblique imaging plane was chosen that passed through the boundary of the two immiscible layers. Therefore, the oil-to-water ratio within a voxel at a given point in the image varied along a continuous gradient from pure oil to pure water (Fig 1). The oil percentage at a given point was determined through cross reference to a coronal high-spatial resolution T1-weighted gradient-echo MR image obtained perpendicular to the plane of the fluid layers. The sequence parameters were as follows: flip angle, 80°; field of view, 3320 mm; section thickness, 4 mm; receiver band width, 1930 Hz/pixel; acquired voxel size, 0.5 x 0.5 x 4 mm; repetition time msec/echo time msec, 16/2.3; number of signal averages, two; and a frequency encoding direction oriented parallel to the oil and water interface.

Implication for patient care

- Multiecho MR imaging shows promise as a method for simultaneous fat and T2* quantification in the liver.

Human Participants

The study was undertaken with the approval of the Hammersmith Hospital research ethics committee, and written informed consent was obtained from all study participants. Five obese individuals with a history of hyperlipidemia or diabetes (four men, one woman; mean age, 53} years; range, 35-67 years; mean body mass index, 36.2 kg/m² range, 33-40 kg/m²) were enrolled. The control group consisted of five healthy volunteers with no history of excess alcohol use (<30 g per day) or diabetes (five men; mean age, 37 years; range, 32-44 years; mean body mass index, 25.0 kg/m²; range, 22-30 kg/m²).

Multiecho Sequence

The MR imaging studies were performed with a 3.0-T MR imaging system (ltera; Philips) operating with Release 1.7 software. A software patch was installed to enable multiecho imaging. The same scaling factors were applied to each image in the multiecho acquisition.

The maximum gradient strength was 31 mT/m, and the maximum slew rate was 200 mT/m/msec. Imaging was performed by using a breath-hold spoiled gradient-echo sequence with a seven-echo readout, resulting in a total acquisition time of 4 seconds for a single section. The multiecho sequence parameters were as follows: flip angle, 20°; field of view, 320 mm; section thickness, 10 mm; receiver bandwidth, 780 Hz/pixel; acquired voxel size, 2.5 x 2.5 x 10 mm; repetition time, I7 msec; and number of signal averages, two. Proton spectroscopy studies have revealed that the chemical shift of intrahepatic lipid relative to water is 3.4 ppm (I8); hence, in vivo, the first echo time (TE) chosen was 1.15 msec, with a ΔTE of 1.15 msec (TEs: 1.15, 2.30, 3.45, 4.60, 5.75, 6.90, and 8.053 msec). The chemical shift in the oil phantom was determined as 3.5 ppm, and the ΔTE was reduced to 1.12 msec (TEs: 1.12, 2.24, 3.36, 4.48. 5.60, 6.72. and 7.84 msec) for these experiments. Body imaging was performed by one technologist (J.F., with I0 years of experience in MR imaging). A six-channel phased-array receiver coil was used, and images were acquired in held expiration, A single-section multiecho sequence was performed in a transverse plane passing through the liver and spleen, superior to the main portal vein. Higher-order shimming was used, with a volume manually placed over the liver. Participant tolerance of the examination, signs of peripheral nerve stimulation, and image quality were monitored. Liver spectroscopy was performed by one operator (M.W., with IO years of experience in spectroscopy). Spectroscopy was performed during the same study as multiecho imaging. Single-voxel spectroscopic measurement of intrahepatic fat levels was performed according to a protocol previously validated at 1.5T [19]. An 8-cm^3 cubic volume of interest was placed over the right lobe of the liver, avoiding intrahepatic blood vessels. The Q-body coil was used to transmit and receive. A point -resolved spectroscopy sequence [20] without water suppression was used for spatial localization and spectra acquisition. To correct for T2 decay, three consecutive spectra were acquired with echo times of 40, 60, and 135 msec. The repetition time was 2000 msec, and 32 signals were acquired.

Data Analysis: Modeling of Fat and Water Phase Interference

In tissues containing lipid and water, there will be oscillation in signal intensity as a function of echo time. The signal intensity of each component will also show T2* decay, The magnitude signal intensity (|S|) may therefore be modeled with the following equation:

$$|S| = |S_w e^{-t/T2^*_w} + S_f e^{-t/T2^*_f + i\Delta\omega t}|$$

where S_w and S_f, are the components of the signal from water and fat, respectively, and $T2^*_w$ and $T2^*_f$ are their respective decay constants, while t is the time after excitation and Δ_ω is the difference in frequency between fat and water. To reduce the number of degrees of freedom in the model, the frequency difference between fat and water was considered to be 3.4 ppm. The signal components from water (S_w) and fat (S_f), as well as their respective T2* decay constants ($T2^*_w$ and $T2^*_f$), were modeled with an iterative curve-fitting technique by using the Levenberg-Marquardt algorithm (21) and software (SigmaPlot, version 10; SPSS, Chicago,III). For the purpose of comparison with results of MR spectroscopy, the lipid content was expressed as a percentage of the total signal as follows: lipid content percentage = 100%· [S_f/ (S_w)+ S_f)]. A comparison was made with fat estimation performed by using a conventional dual-echo method by analyzing only the first pair of in-phase and out-of-phase echoes with the following equation: lipid content percentage= [(S_{IP} - S_{op})· 100%| /(2·S_{IP}), where S_{IP} and S_{op} are the signal intensities on the in-phase and out of phase images, respectively [6].

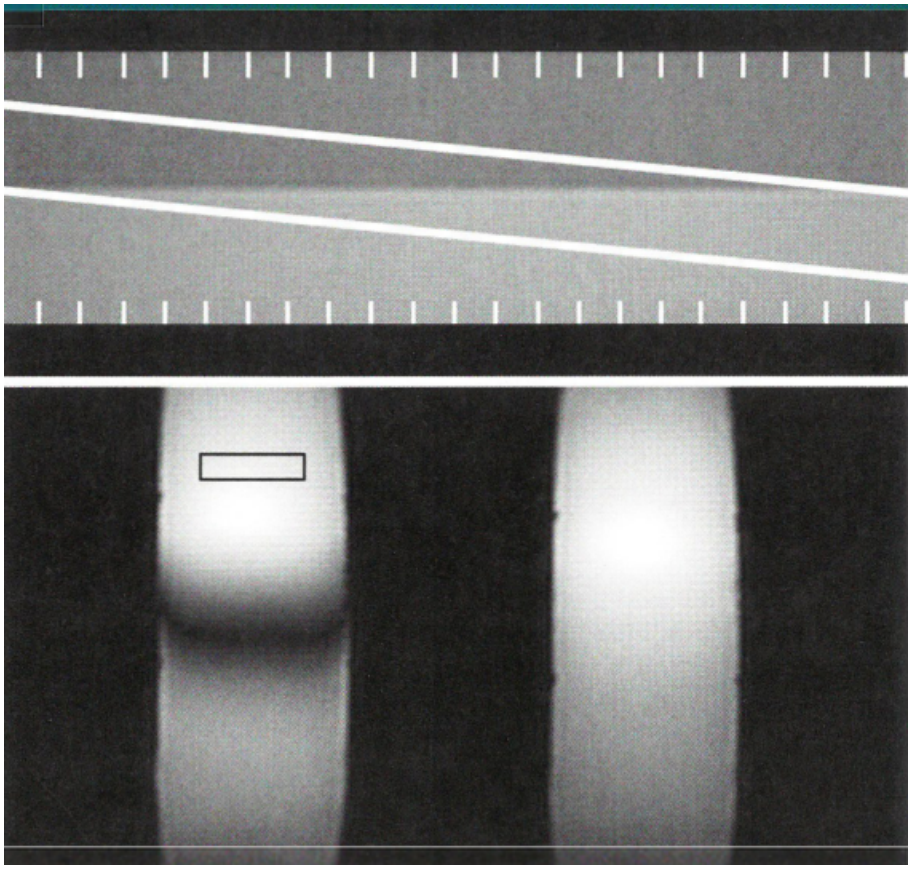

Fig. 1 Oil and water phantom: immiscible layers of mineral oil and water were used to simulate a range of oil-to-water ratios. Top: An oblique MR imaging section (16/2.3; flip angle, 80°; frequency encoding direction, left to right) was positioned across the interface of the two layers, and 11 points along this gradient from 0% to 100% oil were used to position the regions of interest (ROIs) on the multiecho images Bottom left: Out-of-phase image (17/1.15; flip angle, 20°) shows position of first rectangular ROI and demonstrates signal cancellation in voxels containing fat and water. Bottom right: In-phase image (17 /2.3; flip angle, 20°) is shown for comparison.

Image Analysis

The raw image data were exported from the imaging unit for off-line re-construction and were converted to "Analyze" format by using software (Matlab, version 7.0; Mathworks, Natick, Mass). Analysis of multiecho imaging studies was performed by one operator (D.P.O., with 6 years of experience in MR imaging) with a Pentium 4 3.0-GHz computer by using software (ImageJ; National Institutes of Health, Bethesda, Md). The coronal TI-weighted image of the oil and water phantom was used to identify the relative proportions of

fat and water along the oblique imaging section. Eleven equally spaced divisions along this gradient, from 0% to 100% oil, were cross-referenced to a position on the multiecho images. Each ROI placed on the multiecho images measured 40 x 10 pixels. On the liver images, a circular ROI (30 mm in diameter) was placed in the same location as the spectroscopy voxel, avoiding vascular structures. In each case, the mean signal intensity was measured at each echo time. 'The curve fitting algorithm using the biexponential model was used to derive the fat fraction, as well as the component T2* decays for fat and water. An automated pixel-by-pixel analysis was performed to obtain color-coded parametric maps of liver fat and water percentages, also by using the Matlab software.

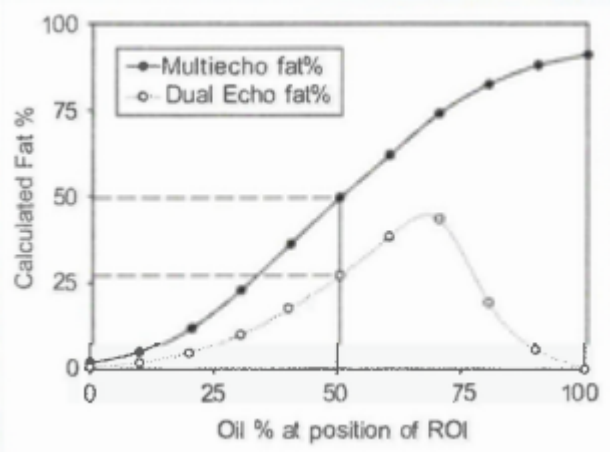

Fig. 2 Graph shows results of fat percentage estimation across range of oil-to-water ratios in the oil and water phantom by using the dual-echo and multiecho sequences. The component with the longer T2 has been assigned to water in the multiecho analysis. The dual-echo plot assumes that water is the dominant component. Dotted lines=calculated fat percentage at 50:50 oil-to-water ratio for each method.*

Reference Standard Liver Spectroscopy

The phase-corrected spectra were analyzed in the time domain by using the AMARES algorithm included in the MRUI software package [22]. Resonance fitting was performed by M.W. to obtain signal intensities for lipid (S_f) and water (S_w). Exponential regression analysis of the peak amplitudes at each echo time was used for T2 decay correction. Lipid fraction was derived from S_f and $S_w$in the same manner as that used with the multiecho technique.

Statistical Analysis

Statistical analysis was performed by using software (SPSS, version 12, SPSS; and MedCale, version 9, MedCale Software, Mariakerke, Belgium). Results are presented as mean values ± 1 standard deviation. Bland-Altman plots [23] were used to analyze the agreement between multiecho and MR spectroscopic estimations of liver fat content and between multiecho and dual-echo estimations of liver fat content, The correlation between liver fat concentration as determined with multiecho imaging and concentration as determined with MR spectroscopy was assessed by using linear least-squares regression. The means of the in vivo $T2^*_w$ and $T2^*_f$ values were compared by using a paired-samples t test. $P < .05$ was considered to indicate a significant difference.

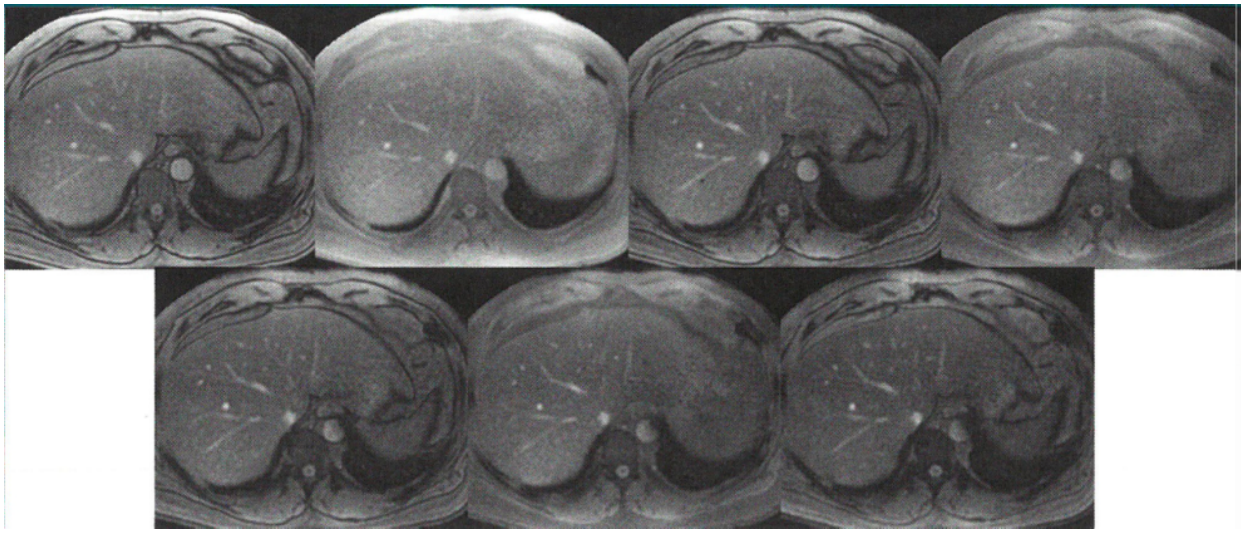

Fig. 3 Transverse breath-hold multiecho MR imaging acquisition (17/1.15--8.05; flip angle, 20°; field of view, 320 mm; section thickness, 10 mm) in liver with seven readouts. Images are alternately out of phase and in phase from left to right in each row. Image quality is maintained throughout the range of echo times.

Results

Oil and Water Phantom

The multiecho sequence modeling derived the two signal intensity components and their respective T2* values throughout the range of oil-to-water ratios. The two signal intensity components (oil and water) had mean T2* values of 94.4 msec ± 11.6 and 5.1 msec ± 2.3 respectively. The correct interpretation of the oil-to-water ratio at each position along the

phantom was obtained if the component with the longer T2* value was assumed to be water. The dual-echo method does not allow a determination of the dominant component, and, accordingly, less signal cancellation was seen at each end of the oil concentration gradient. At the midpoint of the phantom, with a 50:50 oil-to-water ratio, the multiecho method derived a fat content of 49%; the dual-echo method derived a fat content of 27% (Fig 2).

In Vivo Multiecho Sequence and MR Spectroscopy

MR imaging was well tolerated by all participants; there was good image quality throughout the range of echo times (Fig 3). Specific absorption rates were within specified limits (4.0 W/kg), and no peripheral nerve stimulation was reported. The proton spectra demonstrated satisfactory line widths, with water and lipid peaks at 4.7 and 1.3ppm, respectively. The multiecho sequence modeling converged on a fit for S_w and S_f and the individual $T2^*_w$ and $T2^*_f$ components in all subjects but one (Table). This healthy volunteer had a fat content of only 1.3% at multiecho imaging, and the $T2^*_f$, could not be derived. In the patient group, the mean hepatic fat fraction determined with multiecho imaging was 17.7% ± 7.3, while the mean water T2* value was 16.0 msec ± 4.1 and the mean lipid T2* value was 7.4 msec ± 2.1. In the volunteer group, the mean hepatic fat fraction was 2.7% ± 1.4, while the mean water T2* value was 21.8 msec ± 11.7 and the mean lipid T2* value was 4.6 msec ± 1.8. Among all subjects, there was a significant difference between the mean $T2^*_w$, and $T2^*_f$ values (P <.05), and the $T2^*_w$ value was consistently greater than the $T2^*_f$ value (Figs 4, 5).

Bland-Altman analysis revealed a systematic underestimation of fat content with the dual-echo method compared with the multiecho method, with the mean limits of agreement being -2.6% ± 2.4 (1.96 times the standard deviation) (Fig 6). Results of least-squares analysis

Results of MR Spectroscopy, Dual-Echo Modeling, and Multiecho Modeling of Liver Fat Content in Healthy Volunteers and Obese Individuals

Group and Participant No.	Fat Percentage at MR Spectroscopy	Fat Percentage with Dual-Echo Modeling	Fat Percentage with Multiecho Modeling	$T2^*_w$ with Multiecho Modeling (msec)	$T2^*_f$ with Multiecho Modeling (msec)
Healthy volunteers					
1	1.1	<0	1.3	11.8	—
2	1.6	<0	2.0	16.0	6.0
3	2.6	<0	3.1	19.2	6.1
4	1.3	<0	2.0	41.8	2.6
5	3.7	0.5	4.8	20.0	3.6
Obese individuals					
6	11.0	7.2	10.7	20.0	7.0
7	10.6	7.0	10.2	17.7	5.0
8	20.3	16.5	20.5	11.2	6.5
9	20.7	19.3	19.7	19.0	10.6
10	28.7	25.1	27.5	12.1	8.0

indicated a significant correlation between multiecho and spectroscopic measurements of hepatic lipid ($y = 0.94x + 0.63$, $r^2 = 0.99$, $P < .001$) (Fig 7). A Bland-Altman analysis revealed that the mean limits of agreement of fat quantification with the multiecho method compared with quantification with MR spectroscopy was 0.03% ± 1.5 (1.96 times the standard deviation) (Fig 8). A computer simulation was used to measure the expected error in fat estimation with the dual-echo method in a system with biexponential decay. Representative values for the T2* of fat and water obtained in this group of subjects were used in the simulation (Fig 9). For instance, this demonstrated that at 30% fat, the dual-echo method would be expected to produce a 6% (uncorrected for T2*) or 4% (with global T2* correction) underestimation of true fat content.

Note – In participants 1-4, the first out-of-phase image had higher signal intensity than the in-phase image for the dual-echo analysis

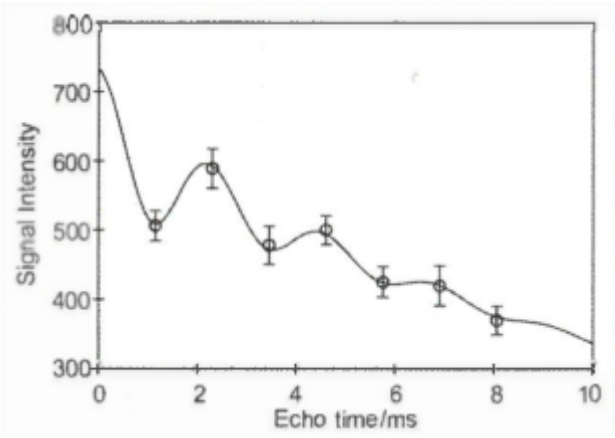

Fig. 4 Plot of mean signal intensity in ROI in steatolic liver with the multiecho sequence shows the bi exponential model's convergence on a best fit curve.

Discussion

Our results demonstrate the feasibility of using in-phase and out-of-phase multiecho imaging to quantify liver fat content and T2* with one sequence. Coregistered pixel maps of liver fat content and T2* values may be automatically generated. The technique shows excellent agreement with T2-corrected single-voxel spectroscopy, and each set of images is obtained in a short breath hold. Multiexponential analysis of fat-water systems has been shown to be feasible with spin-echo sequences in phantoms [15], and gradient-echo sequences have been used to assess bone marrow composition at 1.5 T [16] and lower field strengths [17].

However, to our knowledge, there are no published reports of the use of multiecho phase interference techniques to quantify liver fat content. Dual-echo imaging is in routine clinical use for the semiquantitative assessment of liver fat content. However, multiecho sequences overcome a number of limitations of conventional dual-echo techniques for fat quantification. First, the method allows a determination of the fat-to-water ratio that is corrected for T2* effects without the need for additional mapping sequences and potential image misregistration. This may be a substantial limitation of dual-echo imaging in patients with cirrhosis because of the T2*-shortening effects of iron deposition [11]. Dual-echo quantification also fails at low fat fractions when T effects predominate over fat-water signal cancellation. The multiecho technique also allows a further correction to be made for the differential T2* decays of fat and water, although the effect on fat estimation is expected to be only approximately 5% in vivo. However, the ability to distinguish between the water and fat signal components over comes an important limitation of dual echo fat estimation. The dual-echo approach requires an additional gradient echo sequence with different T1 weighting [12] or visual inspection of results of breath-hold spectroscopy [13] to confirm whether fat or water is the majority component. Despite these steps, there remains ambiguity between 45% and 55% fat content [6], and spectroscopic results that are uncorrected for T2 decay may have similar limitations. Our findings indicate that in the liver, the T2* of water is consistently longer than that of fat at 3.0 T, and this allows the signals to be correctly assigned if the liver fat content is a least 2%. Below this level, noise within the image prevents the signal contribution of fat from being modeled. In this study, the multiecho sequence was optimized for the quantification of tissue fat. However, as the sequence also inherently measures tissue T2*, it has the potential to provide coregistered information on hepatic iron content. Gradient multiecho techniques, with an arbitrary echo time interval, have been histologically validated in the assessment of hepatic iron overload at 1.5 T [24] and enable a reliable assessment of global tissue T2* [25-27]. However, the echo times chosen must allow adequate sampling of the T2* decay curve, and this will depend on the severity of the iron overloading being investigated. Multiecho imaging with biexponential analysis has the advantage over simple relaxometry of being able to model the effects of both T2* decay and fat-water phase interference on signal intensity. Our study had limitations. MR spectroscopy was chosen as a reference standard for the multiecho technique because it has been validated at 1.5 T [18,28-30]. Early experience in liver MR spectroscopy at 3.0 T

demonstrated it to be a promising technique [31,32], and it has the potential to achieve improved signal-to-noise characteristics and greater spectral resolution. However, these advantages may be offset by increased line widths due to increased field inhomogeneities and decreased T2 relaxation times [33]. No histologic correlation of hepatic steatosis was made in our study because the patients in the study group did not have an indication for liver biopsy. Furthermore, the measurement of lipid in histologic samples relies on semiquantitative methods [34,35]. The ratio calculated with the multiecho sequence reflects the molar concentrations of resonating hydrogen nuclei in fat and water, but this may be readily converted into fat content by liver weight or volume for comparison with biopsy data [19]. The biexponential model was not extended to include T1 decay constants for fat and water. To reduce the TI weighting of the sequence while maintaining an adequate signal-to-noise ratio, a shallow flip angle of 20°was chosen, the tissue T1 relaxation time of the liver is also significantly longer at 3.0 T than at 1.5 T (36), and this may also reduce the effects of T1 contrast on fat quantification. The chemical shift was also chosen as a fixed parameter in the model and was used to determine the optimum echo times for maximum and minimum phase cancellation. A potential under-estimation of lipid concentration would be obtained if the actual chemical shift differed from this value, The model also assumed that there was a single lipid resonance and did not allow for the effects of separate methyl and methylene groups, for instance. The accuracy of the curve-fitting algorithm will also depend on the metric used to measure goodness of fit, as well as the effects of noise in the data. The oil phantom demonstrated the behavior of the multiecho sequence over a wide range of oil concentrations. Chemical shift will displace the fat and water voxels, but these errors were minimized by the choice of frequency encoding direction and by not including the edges of the phantom in our ROI measurements. The radiofrequency excitation pulse is a sine function, and the shape of the section profile may modulate the transition from oil to water voxels. Flip angle inhomogeneity and susceptibility effects at the boundary of the layers may also affect the linearity between the calculated and the measured oil concentration. The difference in T2* of the oil and water components was also greater than that seen in vivo. In conclusion, results of our feasibility study show that multiecho MR imaging provides a technique for quantifying liver fat content that is highly correlated with T2-corrected proton spectroscopy. In contrast to dual-echo methods, multiecho imaging overcomes the potential errors due to T2* effects and enables the correct assignment of the fat and water signal components in a sequence

performed during a single breath hold. This technique also allows the simultaneous acquisition of coregistered fat and T2* maps of the liver.

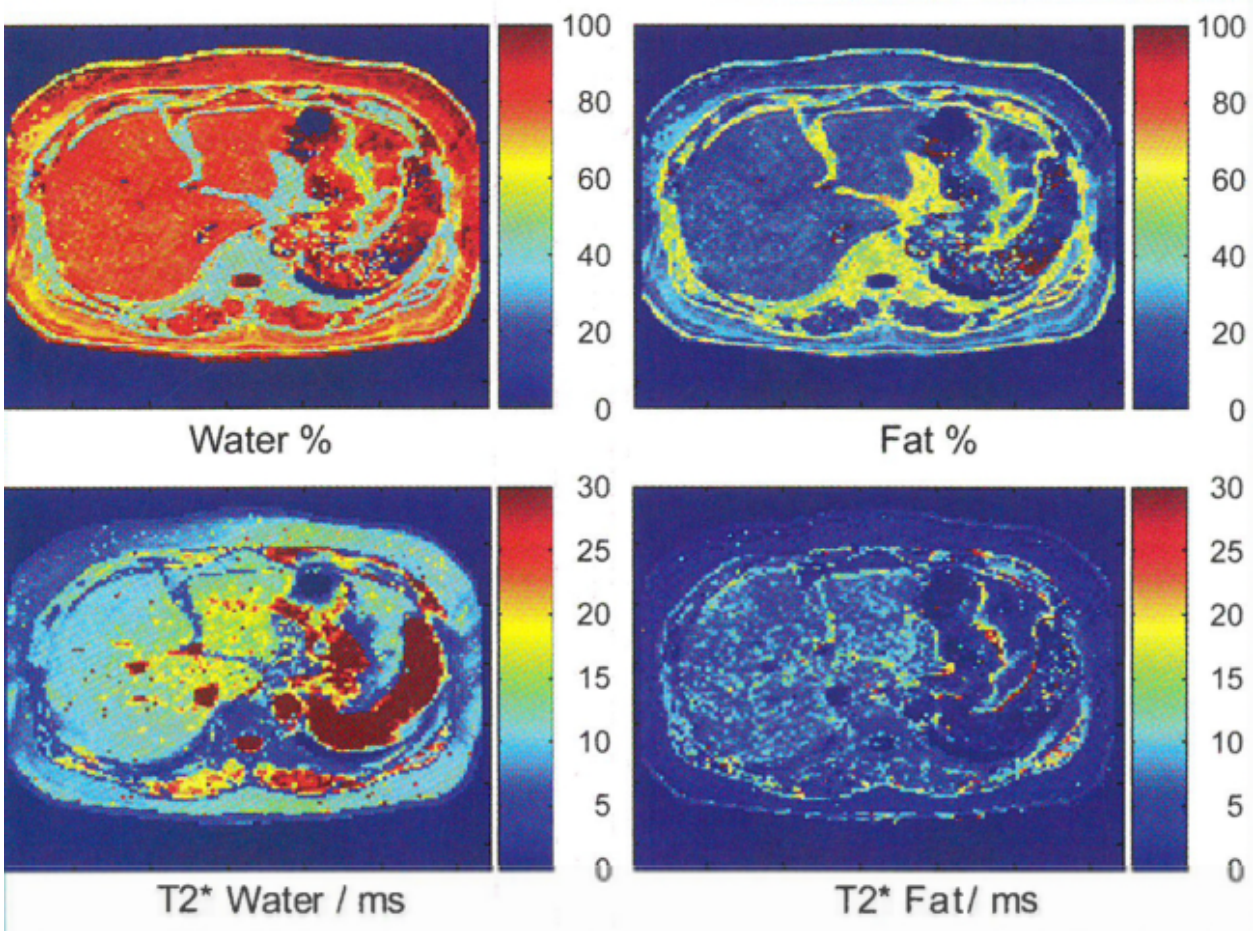

Fig.5 Color-coded parametric maps of multiecho data in patient with hepatic steatosis. Coregistered images of water and fat percentage, as well as their respective T2 values (in milliseconds), were derived from a single multiecho acquisition. Color bars and numbers in top row= percentages; those in bottom row= milliseconds.*

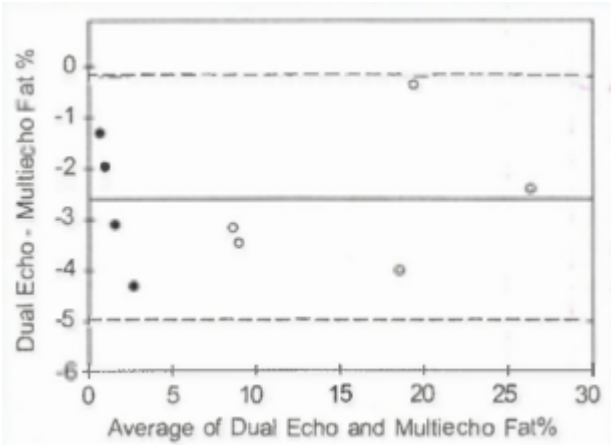

Fig. 6 Bland-Altman plot of agreement of liver fat assessment in vivo between dual-echo and multiecho MR imaging. The mean of each pair of measurements is plotted against their difference. Dashed lines= 95% confidence intervals, solid line = mean value, ●= healthy volunteers, ○= obese individuals.

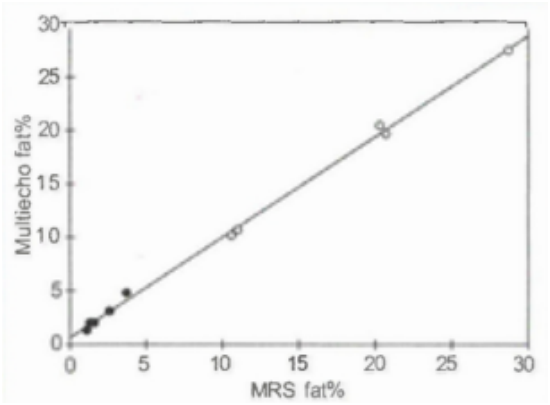

Fig. 7 Graph shows relationship between fat estimation in the liver performed by using multiecho MR imaging technique and that performed by using MR spectroscopy (MRS) (y = 0.94x+ 0.63, r^2= 0.99, P < .001). ● = Healthy volunteers, ○ = obese individuals.

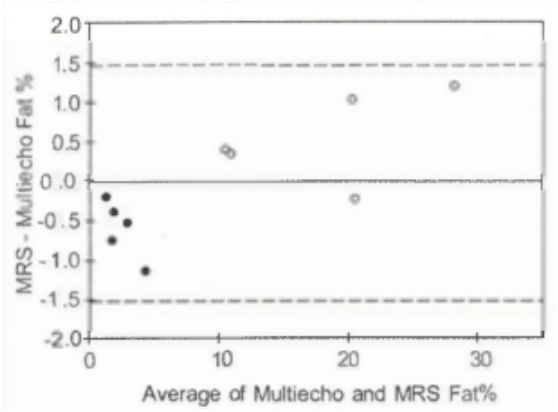

Fig. 8 Bland-Altman plot of agreement of liver fat assessment in vivo between MR spectroscopy and multiecho imaging. The mean of each pair of measurements is plotted

against their difference. Dashed lines= 95% confidence intervals, solid line = mean value, ● = healthy volunteers, ○ = obese individuals.

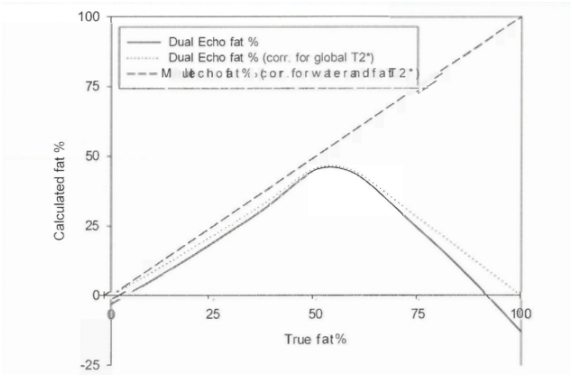

Fig. 9 Graph shows simulation of expected differences in fat percentage calculation by using three methods. The bi exponential model was used to simulate in- and out-of-phase signal intensities throughout the entire range of fat-to-water ratios. Physiologic T2 values ($T2^*_w$, 20 msec; T2*, 5 msec) estimated from in vivo data have been used in the model. For this comparison, T1 effects were not included in the model. The ideal correlation was assumed to be given by the multiecho method, which corrects for the individual T2* decays of fat and water. The first in-phase and out-of-phase echo times from the simulation were used for fat quantification with the dual-echo method, with water assumed to be the dominant component. These values were then corrected (corr.) for global T2* decay by using regression analysis of the in-phase echo times.*

References

1. Clark JM. Brancati FL, Diehl AM. Non-alcoholic fatty liver disease. Gastroenterology 2002:122:1649-1657.

2. Fishbein MIH. Gardner KG, Potter CJ, Schmalbrock P, Smith MA. Introduction of fast MR imaging in the assessment of hepatic steatosis. Magn Reson Imaging 1997:15:287-293.

3. Javor ED, Ghany MG, Cochran E, et al. Leptin reverses nonalcoholic steat0hepatitis in patients with severe lipodystrophy. Hepatology 2005:41:753-760.

4. Kawamitsu H, Kaji Y, Ohara T, Sugimura K. Feasibility of quantitative intrahepatic lipid imaging applied to the magnetic resonance dual gradient echo sequence. Magn eson Med Sci 2003; 2; 47-50.

5. Rinella ME, McCarthy R, Thakrar K, et al. Dual-echo, chemical shift gradient-echo magnetic resonance imaging to quantify hepatic steatosis: implications for living liver donation. Liver Transpl 2003:9:851-856.
6. Hussain HK, Chenevert TL, Londy Fl, et al. Hepatic fat fraction: MR imaging for quantita-five measurement and display early experience. Radiology 2005:237:1048-1055.
7. Pilleul F, Chave G, Dumortier J, Scoazec JY, Valette PJ. Fatty infiltration of the liver: detection and grading using dual Tl gradient echo nsequences on clinical MR system. Gastroenterol Clin Biol 2005:29:1143-1147.
8. Chan DC, Watts GF, Ng TW, Hua J, Song S, Barret PH. Measurement of liver fat by magnetie resonance imaging: relationships with bodv fat distribution, insulin sensitivity and plasma lipids in healthy men. Diabetes Obes Metal 2006:8:698-702.
9. Qayyum A, Goh JS, Kakar S, Yeh BM, Merriman RB. Coakley V, Accuracy of liver fat quantification at MR imaging: comparison of out-of-phase gradient-echo and fat-saturated fast spin-echo techniques initial experience. Radiology 2005:237:507--511.
I0. Namimoto T, Yamashita Y, Mitsuzaki K. et al. Adrenal masses: quantification of fat content with double-echo chemical shift in-phase and opposed-phase FLASH MR images for differentiation of adrenal adenomas. Radiology 2001:218:642-646.
II. Westphalen AC, Qayyum A, Yeh BM, et al. Liver fat: effect of hepatic iron deposition on evaluation with opposed-phase MR imaging. Radiology 2007:242:450 -455.
I2. Hollingsworth KG, Abubacker MZ, Joubert I, Allison ME, Lomas DJ. Low-carbohydrate diet induced reduction of hepatic lipid content observed with a rapid non-invasive MRI technique. Br J Radiol 2006:79:712--715.
13. Chang JS, Taouli B, Salibi N, Hecht EM, Chin DG, Lee VS. Opposed-phase MRI for fat quantification in fat-water phantoms with 1H MR spectroscopy to resolve ambiguity of fat or water dominance. AIR Am J Roentgenol 2006;187:W103-W106.
14. Haacke EM.Magnetic resonance imaging: physical principles and sequence design. New York, NY: Wiley-Liss, 1999.
I5. Kamman RL, Bakker CJ, van Dijk P, Stomp (P,Heiner AP, Berendsen HJ. Multi-exponential relaxation analysis with MR imaging and NMR spectroscopy using fat-water systems. Magn Reson Imaging 1987:5:381-392.
I6. Wehrli FW, Ford JC, Attie M, Kressel HY, Kaplan FS, Trabecular structure: preliminary application of MR interferometry, Radiology 1991:179:615-621.

17. Derby K. Kramer DM. Kaufman L. A technique for assessment of bone marrow composition using magnetic resonance phase interference at low field. Magn Reson Med 1993:29:4653- 469.
I8. Szczepaniak LS, Babcock EE, Schick F, et al. Measurement of intracellular triglyceride stores by H spectroscopy: validation in vivo. Am J Physiol 1999:276(5 pt I):E977--E989.
I9. Szczepaniak LS, Nurenberg P, Leonard D, et al. Magnetic resonance spectroscopy to measure hepatic triglyceride content: prevalene of hepatic steatosis in the general population. Am J Physiol Endocrinol Metab 20053: 288: E462-E468.
20. Bottomley PA. Spatial localization in NMR spectroscopy in vivo. Ann N Y Aead Sci 1987; 508:333-348.
21. Marquardt DW. An algorithm for least squares estimation of parameters. J Soc Ind Appl Math 1963:11:431- 441
22. Vanhamme L, van den Boogaart A, Van Huffel S. Improved method for accurate and efficient quantification of MRS data with use of prior knowledge. J Magn eson 1997:129:35--43.
knowledge. J Magn eson 1997:129:35--43.
23. Bland JM, Alman DG. Statistical methods for assessing agreement between two methods of clinical measurement. Lancet 1986:E:307 -310.
24. Anderson LI, Holden S, Davis B, et al. Cardio-vascular T-star (T) magnetic resonance for the early diagnosis of myocardial iron over-load. Eur Heart J 2001;22: 2171-2179.
25.Bonkovsky HL, Rubin RB, Cable EE, Davidoff A. Bijeken TH, Stark DD. Hepatic iron concentration: noninvasive estimation by means of MR imaging techniques. Radiology 1999:212:227 234.
26. Westwood MA, Anderson LI, Firmin DN, et al. Interscanner reproducibility of cardiovascular magnetic resonance T measurements of tissue iron in thalassemia. J Magneson Imaging 2003:18:616--620.
27. Wood JC, Enriquez C, Ghugre N, et al. MRI R2 and R mapping accurately estimates hepatie iron concentration in transfusion-dependent thalassemia and sickle cell disease patients.Blood 2005;106: 1460--1463.
28. Longo R, PollesselloP. Ricci C. et al. Proton MR spectroscopy n quantitative in vivo determination of fat content in human liver steatosis. J Magn Heson Imaging 1995:5:281--285.

29, Thomsen C, Becker U, Winkler K Christoffersen P, Jensen M, Henriksen O. Quantification of liver fat using magnetic resonance spectroscopy. lagn Reson Imaging 1994:12:487 --495.
30. Longo R. Ricci C, MasuttiF, et al. Fatty infiltration of the liver: quantification by IHH localized
magnetic resonance spectroscopy and comparison with computed tomography. Invest Radiol 1993;28:297--302.
3I. Ishii M. Yoshioka Y, Ishida \W, et al. Liver fat content measured by magnetic resonance spectroscopy at 33.0 tesla independently correlates with plasminogen activator inhibitor-I and body mass index in type 2 diabetic subjects. Tohoku J Exp Med 2005 206:23-30.
32. Fischbach F, Thormann M, Ricke J. (I)H magnetic resonance spectroscopy (MRS) of the liver and hepatic malignant tumors at 33.0 Tesla [in German]. Radiologe 2004:44:1192-1196.
33.Barker PB, Hearshen DO, Boska MD. Single-voxel proton MRS of the human brain at 1.3T and 3.0T. Magn Reson Med 2001:45:765--769.
34. Sanyal AJ. AGA technical review on nonalcoholic fatty liver disease. Gastroenterology 2002:123:1705-1725.
35. Franzen LE, Ekstedt M. Kechagias S, Bodin L. Semiquantitative evaluation overestimates the degree of steatosis in liver biopsies: a comparison to stereological point counting. Mod Pathol 20053: 18:912-916.
36. de Bazelaire CM, Duhamel GD, Rofsk NM, Alsop DC. MR imaging relaxation times of ab- dominal and pelvic tissues measured in vivo at 3.0 T: preliminary results. Radiology 2004; 230:652-659.

Paper 3

Reduction of total lung capacity in obese men: comparison of total intrathoracic and gas volumes

R. Watson[1], N. Pride[1], E. Louise Thomas[2], ***J. Fitzpatrick[2]***, G. Durighel[2], J. McCarthy[2], S. Morin[2], P. Ind[1], and J. Bell[2]

Abstract

Reduction of total lung capacity in obese men: comparison of total intrathoracic and gas volumes. *J Appl Physiol* 108: 1605–1612, 2010. First published March 18, 2010; doi:10.1152/japplphysiol.01267.2009. - Restriction of total lung capacity (TLC) is found in some obese subjects, but the mechanism is unclear. Two hypotheses are as follows: *1*) increased abdominal volume prevents full descent of the diaphragm; and *2*) increased intrathoracic fat reduces space for full lung expansion. We have measured total intrathoracic volume at full inflation using magnetic resonance imaging (MRI) in 14 asymptomatic obese men [mean age 52 yr, body mass index (BMI) 35–45 kg/m²] and 7 control men (mean age 50 yr, BMI 22–27 kg/m²). MRI volumes were compared with gas volumes at TLC. All measurements were made with subjects' supine. Obese men had smaller functional residual capacity (FRC) and FRC-to-TLC ratio than control men. There was a 12% predicted difference in mean TLC between obese (84% predicted) and control men (96% predicted). In contrast, differences in total intrathoracic volume (MRI) at full inflation were only 4% predicted TLC (obese 116% predicted TLC, control 120% predicted TLC), because mediastinal volume was larger in obese than in control [heart and major vessels (obese 1.10 liter, control 0.87 liter, *P* 0.016) and intrathoracic fat (obese 0.68 liter, control 0.23 liter, $P < 0.0001$)]. As a consequence of increased mediastinal volume, intrathoracic volume at FRC in obese men was considerably larger than indicated by the gas volume at FRC. The difference in gas volume at TLC between the six obese men with restriction, TLC 80% predicted (OR), and the eight obese men with TLC 80% predicted (ON) was 26% predicted TLC. Mediastinal volume was similar in OR (1.84 liter) and ON (1.73 liter), but total intrathoracic volume was 19% predicted TLC smaller

in OR than in ON. We conclude that the major factor restricting TLC in some obese men was reduced thoracic expansion at full inflation.

Introduction

About 50 years ago it was established that functional residual capacity (FRC) and expiratory reserve volume (ERV) are reduced in most seated obese subjects [14, 32]. More recently, reduction in total lung capacity (TLC), formerly thought only to occur in massively obese subjects [28], has been found in some subjects with less severe obesity [17]. Consistent with the development of a restrictive pattern of lung function in some obese subjects, prospective studies have shown that weight gain is associated with loss of vital capacity (VC) [6, 7, 34], while weight loss is associated with increase in VC [22, 28, 29, 31]. The mechanical factors reducing VC and TLC in obesity are uncertain, but it has been speculated that increased abdominal volume in some way reduces inspiratory descent of the diaphragm and consequent expansion of the thorax. Recent studies of induced ascites in dogs have shown that, at FRC, the lung-expanding action of the diaphragm was reduced. The mechanism was an increase in abdominal elastance combined with an expansion of the ring of insertion of the diaphragm to the lower rib cage [19, 20]. A further possible cause of reduction in TLC is an increase in intrathoracic fat competing for space with the lungs within the intrathoracic cavity. This mechanism would be analogous to that proposed for the re- strictive pattern associated with chronic heart failure, which is much improved after cardiac transplantation [16, 23].

We are not aware of studies measuring total intrathoracic volume and its major compartments at full inflation in either normal weight or obese subjects. Such measurements would define the contribution of any increase in intrathoracic fat to the restrictive pattern in obesity and also allow an estimate of intrathoracic volume at all other gas volumes, including FRC.

In the present exploratory study, we have measured total intrathoracic volume at full inflation using magnetic resonance imaging (MRI) and compared these results with measurements of TLC and subdivisions in 7 control and 14 obese men. Both measurements were made in the supine position. These measurements were made as part of a study that also measured abdominal volumes and visceral and subcutaneous fat in all the subjects; these results will be the subject of a separate report.

Methods

Subjects

All subjects were healthy, middle-aged men without significant symptoms, in particular, no history of cardiac or respiratory disease, sleep disturbance, breathlessness, or reduced effort tolerance. Control men were normal weight or slightly overweight, with the highest body mass index (BMI) being 27.5 kg/m^2. Obese subjects were seen on a preliminary occasion to establish that their BMI was between 35 and 45 kg/m^2 (grade 2 or 3 obesity) and that spirometry showed no obstructive features. Written, informed consent was obtained from all subjects, and the protocol was approved by the Hammersmith Research Ethics Committee.

Anthropometry

Height without shoes and weight wearing light clothing were measured on a stadiometer. Hip circumference was taken at the level of the trochanters. Waist circumference (standing with arrested normal breathing) was measured at the midlevel between lowest rib and iliac crest. Four skinfold thicknesses (triceps, biceps, subscapular, suprailiac) were measured, as recommended by Cotes et al. [8] and Durnin and Womersley [9]. In some men with a large amount of subcutaneous fat, it was not possible to measure a skinfold with the skin calliper, which was then recorded as 45 mm.

Lung Function

Spirometry was measured seated using a portable Vitalograph flowhead (Vitalograph Maids Moreton, Bucks, UK). Subjects were asked to perform slow vital capacities (SVC) and then forced expirations to obtain forced expiratory volume in 1s (FEV). The best of at least three readings of each was taken.

TLC and subdivisions were measured in duplicate in the supine position using the multibreath helium dilution (MBHe) technique (Morgan Benchmark) [4]. Subjects were positioned comfortably on the mouth- piece and, when relaxed and breathing regularly, were turned into the circuit at the end of a tidal expiration. Occasional deep inhalations were made by the subject, and helium equilibrium was reached in 3 min. The subject was then asked to take a full inspiration [inspiratory capacity (IC)] to TLC, followed by a SVC. TLC was taken as the sum of the gas volume at which the subject was turned into the circuit (FRC) and IC. The residual volume (RV) was TLC-SVC. Two repeatable measurements of FRC were obtained and averaged. European

reference values [27] were used for spirometry, TLC, VC, and RV. After these measurements and while attached to a recording spirometer and remaining supine, the subjects were trained to take a repeatable full inspiration followed by breath holding for 17s; this maneuver would be used and repeated several times during the (immediately subsequent) MRI scans.

MRI Acquisition

With the use of a Philips Achieva 1.5-T MRI scanner with a Q-Body Coil (Philips Medical System, Best, NL) a T1-weighted turbo spin echo sequence, which covered the entire thoracic cavity, was acquired. Subjects lay supine with arms by their side and hips and knees slightly flexed and were instructed to make a full inflation and then breath hold for 17s while images were acquired in the coronal plane. Typical parameters: field of view 530 x 300 mm; repetition time 400 ms; echo time 17 ms; number of slices 50/stack; slice thickness 6 mm; interslice gap 1 mm; reconstructed voxel 1.56 x 1.56 mm; and 5 breath holds. During scanning, a marker was placed on the midsternum to indicate sternal displacement and monitored during the breath hold to ensure inspired volume was maintained. In addition, the definition of the lung border was checked visually to ensure that there was no motion artifact during a breath hold. Total MRI scan time was 20 min.

Analysis and Identification of Fat, Lungs, Heart, and Main Vessels

Each coronal slice was segmented into six tissue types on the basis of pixel density using commercial imaging software (Slicomatic 4.2; Tomovision, Montreal, Canada). Adipose tissue has a high signal intensity compared with most other tissues, but an experienced operator (VardisGroup, London, UK), who was unaware of the objectives of the study, coded tissue compartments using expert anatomical knowledge, as previously reported [30].

Calculation of Intrathoracic Volumes

See Fig.1. The intrathoracic cavity at full inflation was well defined by the pleural border of the lungs over almost all of its surface. The cavity was bounded by the rib cage, anteriorly by the sternum, posteriorly by the vertebral column, caudally by the diaphragm, and cranially at the level of the lung apices. The total intrathoracic cavity volume was subdivided into three volumes. *1)* The first is total lung volume (TLV). In addition to gas volume, TLV includes the volume of intrapulmonary tissue, blood, and fluid. Because the cranial boundary of TLV was at the apex of the lungs, air in the intrathoracic trachea was included. When comparing TLV with

TLC measured by MBHe, 0.07 liter was deducted from TLC to allow for the volume of air in the extrathoracic airway (TLC*) (24). 2) The second volume is intrathoracic fat. *3*) The third volume is heart and major blood vessels (aorta, superior vena cava, and major hilar extrapulmonary vessels) and other mediastinal structures (e.g., esophagus). We refer to the sum of the second and third volumes as mediastinal volume. To estimate intrathoracic volume at FRC or RV, IC or VC was subtracted from the measured value of total intrathoracic volume at full inflation. The difference between gas volume and intrathoracic volume at any level of lung inflation then equals (mediastinal volume plus lung tissue volume). This ignores any change in intrathoracic blood volume (heart, major extrapulmonary vessels, intrapulmonary blood vessels) that may occur with lung deflation.

All lung gas volumes and all MRI volumes were measured as liters. To allow for differences in height between individuals, we also expressed gas volumes (TLC and subdivisions) as a percentage of predicted values (%pred) (27). Because we required a height-corrected unit of volume to compare gas and MRI volumes, we also empirically expressed all MRI volumes as a percentage of predicted TLC. We are not aware of any data relating heart and/or mediastinal volume to height or to TLC.

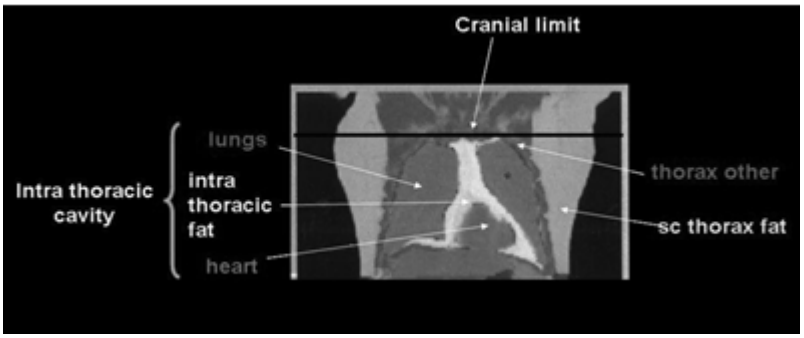

Fig. 1. Coronal section of magnetic resonance imaging (MRI) scan of thorax in an obese man, shaded to show lungs, heart, and intrathoracic fat (mainly pericardial). For clarity, this scan was acquired with the subject supine, but with his arms ex- tended above his head.sc, Subcutaneous

Results

Anthropometry

See Table 1. Control and obese men were well matched for age, but control men were, on average, 5 cm taller than the obese men ($P = 0.07$). Obese men had highly significant increases in BMI and standard markers of obesity.

Lung Function Results: Spirometry

See Table 2. The obese men had some reduction in seated FEV_1 and VC (both as absolute volumes and %pred), but FEV_1/VC was normal.

					Obese Subdivisions	
	Controls	Obese	*P*	80%predicted TLC (ON)	80%predicted TLC (OR)
n	7	14		8	6
Age, yr	50.1 9.3	52.4 6.3	NS	53.1 6.3	51.3 6.9
Height, m	1.82 0.04	1.77 0.07	0.07	1.77 0.1	1.76 0.1
Weight, kg	82.4 8.0	121.0 11.2	0.0001	122.2 11.5	119.3 11.7
Body mass index, kg/m²	25.0 2.2	38.8 2.2	0.0001	38.9 2.2	38.7 2.4
Waist circumference, cm	92.2 4	127.3 8.4	0.001	128.3 9.4	126.0 7.6
Waist/hip	0.93 0.05	1.02 0.05	0.002	1.03 0.06	1.00 0.03
Skinfolds, mm	53.2 22.0	119.7 13.2	0.001	115.8 15.1	124.3 9.7

Table 1. *Anthropometry of subjects*

Values are means SD; *n*, no. of subjects. TLC, total lung capacity; ON, obese nonrestrictive; OR, obese restrictive; waist/hip, ratio of waist to hip. *P* values: controls vs. obese. Nonsignificant (NS) *P* 0.2.

Supine TLC and Subdivisions

The most striking and consistent abnormalities in the obese men were a small FRC and FRC-to-TLC ratio (FRC/TLC), leading to a small ERV. As a further consequence of the low FRC/TLC, mean IC was identical in the obese and control men. Differences in mean TLC, VC, RV, and FEV_1 between obese and control men were not statistically significant. There was no relation between FRC or FRC/TLC and BMI within either group. A principal objective of this study was to examine factors that might be responsible for a reduced TLC, so we have subdivided the obese men into those with a restrictive disorder (TLC < 80%pred; group OR; $n = 6$) and those with TLC 80%pred (group ON; $n = 8$). This arbitrary but commonly used subdivision (2 men in the ON subgroup had TLC 82%pred) is used to facilitate presentation of the results in Tables 2 and 3. In Figs. 2–4, individual results for all 21 men that we studied are shown with ON and OR subgroups identified by different symbols.

Comparison of Obese Men With TLC ≤ 80%pred (OR) and with TLC ≥ 80%pred (ON)

There were no differences in mean values of any of the anthropometric features between the two obese subgroups (Table1). The OR subgroup with TLC < 80%pred also had smaller mean values of all subdivisions of TLC (VC, RV, FRC, IC; $P < 0.03$ in all cases), except ERV ($P = 0.51$). The ON subgroup had similar values of TLC, VC, RV, and FEV_1 as the control men (P values > 0.15 in all cases), but differed from the control men in having a smaller FRC ($P = 0.036$) and ERV ($P = 0.014$).

Intrathoracic Volumes at Full Inflation Measured by MRI

See Table 3. Total intrathoracic volume at full inflation was, on average, 0.71 liter larger in control than obese men; ex- pressing total intrathoracic volume as %pred TLC, mean control and obese values were 120 and 116%pred TLC, respectively (Table 3). This 4% difference compared with a 12%difference in TLC %pred measured by MBHe dilution (Table 2). These mean results conceal great between-individual variability within both groups (Figs. 2–4). Each of the three compartments of total intrathoracic volume differed between control and obese men. By far, the largest compartment was TLV, which occupied, on average, 88% of the total intrathoracic volume in control men. Mean TLV (%pred TLC) was smaller in the obese men than in the control men (P = 0.016). Mean values of both mediastinal components of intrathoracic volume were larger in the obese men than in the control men (Fig. 2): mean heart and major blood vessel volume was 1.10 liter in obese vs. 0.87 liter in control men (P = 0.016), while mean volume of intrathoracic fat (mainly pericardiac and mediastinal, but sometimes also extending over the adjacent pleural surface of the diaphragm, Fig. 1) was 0.68 liter in obese and 0.23 liter in control men ($P < 0.0001$). Because of the increased mediastinal volume, the inflated lungs only occupied, on average, 78% of the total intrathoracic cavity volume in obese men. Thus increased mediastinal volume might contribute to re- duction in TLC in some of the obese men. However, mean mediastinal volume was similar in the obese subgroups with (OR 1.84 liter) and without (ON 1.73 liter) reduced TLC (P = 0.56). The relation between TLV and total intrathoracic volume in all 21 men is shown in Fig. 3. In the ON men, whose values of TLV overlapped those of the control men, mean total intrathoracic volume was actually slightly greater (124%pred TLC) than in the control group (120%pred TLC). In contrast, total intrathoracic volume was only 105%pred TLC in the OR subgroup. This 19%pred TLC difference in mean total intrathoracic volume between ON and OR (P = 0.005) was the major factor accounting for the smaller TLC MBHe in the OR subgroup

Table 2. *Spirometry and lung volumes*

	Controls	Obese	*P*	Obese Subdivisions >80%predicted TLC (ON)	Obese Subdivisions <80%predicted TLC (OR)
n	7	14		8	6
			Seated		
FEV_1					
Liters	4.12 ± 0.8	3.45 ± 0.8	0.07	3.81 ± 0.8	2.97 ± 0.4
%Predicted	106 ± 14	96 ± 15	0.155	105.5 ± 12.9	83.2 ± 4.8
FEV_1/VC, %	76 ± 7	81 ± 6	NS	80 ± 7	82 ± 4
			Supine		
TLC					
Liters	7.15 ± 0.8	5.96 ± 1.3	0.04	6.83 ± 0.9	4.81 ± 0.6
%Predicted*	96 ± 8	84 ± 15	0.08	95 ± 10	69 ± 4
VC					
Liters	5.23 ± 0.8	4.43 ± 0.9	0.063	4.98 ± 0.7	3.71 ± 0.6
%Predicted*	108.1 ± 11.8	99.3 ± 17.1	NS	111.1 ± 0.5	83.6 ± 9.3
RV					
Liters	1.91 ± 0.5	1.53 ± 0.6	NS	1.85 ± 0.7	1.11 ± 0.2
%Predicted*	84 ± 17	68 ± 25	NS	81 ± 26	50 ± 8
FRC, liters	3.32 ± 0.5	2.13 ± 0.7	0.001	2.51 ± 0.8	1.61 ± 0.3
FRC/TLC, %	46.4 ± 6.1	35.0 ± 5.9	0.0005	36.1 ± 7.2	33.5 ± 3.3
ERV, liters	1.40 ± 0.5	0.60 ± 0.4	0.006	0.66 ± 0.5	0.51 ± 0.3
IC, liters	3.84 ± 0.69	3.84 ± 0.69	NS	4.32 ± 0.4	3.20 ± 0.4

*Values are means ± SD; n, no. of subjects. FEV_1, forced expiratory volume in 1s; VC, vital capacity; RV, residual volume; FRC, functional residual capacity; ERV, expiratory reserve volume; IC, inspiratory capacity. *Predicted values are for upright TLC and subdivisions. P values: controls vs. obese. NS = P > 0.2*

Table 3. *Total intrathoracic volumes at full inflation measured by magnetic resonance imaging*

	Control	Obese	*P*	Obese Subdivisions 80%predicted TLC (ON)	Obese Subdivisions 80%predicted TLC (OR)
n	7	14		8	6
Total intrathoracic volume					
Liters	8.92 0.9	8.21 1.3	NS	8.87 1.0	7.32 1.1
%Predicted TLC	120 8	116 13	NS	124 10	105 11
Heart and vessels, liters	0.87 0.2	1.10 0.2	0.016	1.04 0.2	1.18 0.2
Fat, liters	0.23 0.1	0.68 0.2	0.0001	0.69 0.2	0.66 0.3
Lungs (TLV)					
Liters	7.82 0.8	6.43 1.3	0.004	7.14 0.8	5.48 0.8
%Predicted TLC	105 7	90.8 13	0.016	99.9 8	78.6 8
Lungs (TLV)/total intrathoracic volume, %	88 1.5	78 4.2	0.0001	80 1.81	75 4.5

Values are means ± SD; *n*, no. of subjects. *P* values: controls vs. obese. NS = *P* >0.2.

Comparison of Lung Volume at Full Inflation Measured by MRI and MBHe Dilution

Individual values of TLV measured by MRI were closely related to, but slightly greater than, TLC* measured by MBHe dilution (Fig. 4). The mean volume difference (TLV-TLC*), which reflects the volume of intrapulmonary tissue and fluid, was 0.74 liter in control and 0.54 liter in obese men (difference nonsignificant, P = 0.61).

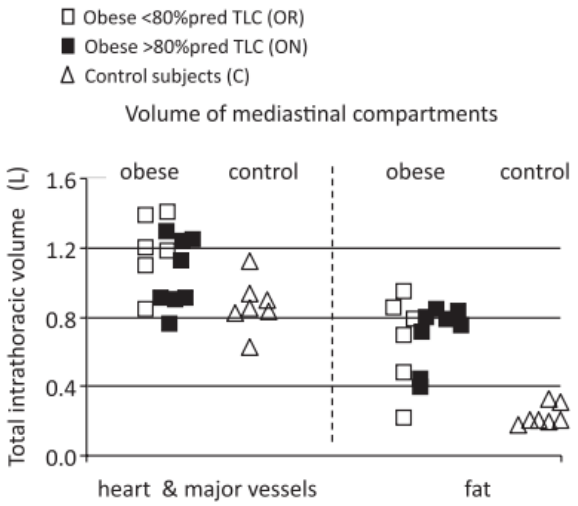

Fig. 2. Contributions of volumes of heart and major blood vessels (left) and intrathoracic fat (right) to total intrathoracic volume in control and obese men. Symbols distinguish control men from obese restrictive (OR) and obese nonrestrictive (ON) subgroups. TLC, total lung capacity.

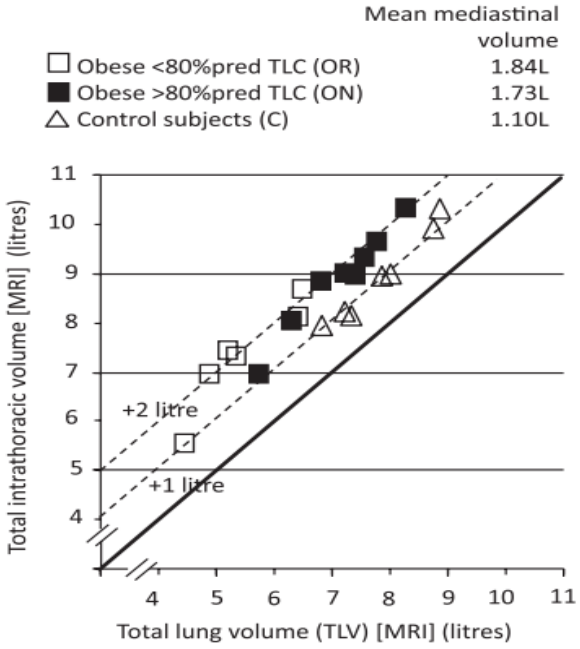

Fig. 3. Total lung volume (TLV) at full inflation plotted against total intrathoracic volume in control and obese men. The thick diagonal line is the line of identity, and the dashed lines indicate when the total intrathoracic volume is 1 or 2 liters greater than TLV. Note that many values of TLV in ON subgroup and in control men overlap.

Comparison of Gas volumes and Estimates of Intrathoracic Volumes When the Lungs are Deflated

Because mediastinal volume was, on average, 0.68 liter larger in obese than control men, differences between control and obese men in all intrathoracic volumes were smaller than the difference in corresponding gas volumes. For example, while mean FRC gas volume was 45%pred TLC in control and 30%pred TLC in obese men, mean intrathoracic volume at FRC was 69%pred TLC in control and 62%pred TLC in obese men (Fig. 5).

Discussion

In this exploratory study, in obese middle-aged men, we measured total intrathoracic volume and its components at full inflation to investigate the features of restrictive lung disease (TLC < 80%pred). A restrictive pattern was found in 6 of the 14 men and was associated with a smaller total intrathoracic volume. Mediastinal volume was 0.68 liter larger in obese than control men due to increase in volumes occupied by the heart and major blood vessels and by intrathoracic fat, but was similar in obese men with and without restrictive lung disease.

Methodology

Subjects. We chose men for this exploratory study of restrictive lung disease associated with obesity, because two prospective studies [6, 34] have shown that loss of VC with increase in weight is greater in men than in women. Possibly this is because men have a more central pattern of obesity than women; in our department, visceral abdominal fat measured by MRI averages 14.8% of total body fat in obese men and 8.9% in obese women (E. L. Thomas, unpublished observations). *MRI scanning technique*. The pleural edges of the lungs were well defined during breath holding, allowing an accurate measurement of TLV. Intrathoracic fat was also clearly visualized by its characteristic density. The heart and major blood vessels, including the extrapulmonary hilar vessels, were the major contributors to the remaining mediastinal compartment, which includes organs such as the esophagus. This nonvascular volume should be small and similar in control and obese men. The close correspondence between values of TLV and TLC (Fig. 4) in an individual supports the effectiveness of the "training" in breath holding at full inflation; furthermore, it suggests that helium equilibrated with true total gas volume in the obese men, even though they were supine with a very low FRC/TLC, and so probably had some airway closure during tidal breathing [15]. Frequent deep

inspirations were made during helium equilibration so as to allow access of helium to lung beyond any closed airways. TLV measured by imaging includes intrapulmonary tissue, fluid, and blood, as well as gas, so (TLV-TLC*) potentially estimates lung tissue and fluid volume, albeit with limited accuracy because of the following. 1) TLV and TLC were measured in separate maneuvers, during which esophageal pressure was not measured. Hence we do not know if a comparable lung recoil pressure was achieved in all full-inflation maneuvers, nor whether glottal closure occurred during breath holding. 2) These estimates depend on the difference between two volumes, which are 8 –10 times larger. Nevertheless, our mean estimate of lung tissue and fluid volume for the 21 men of 0.61 liter (0.74 liter in control men, 0.54 liter in obese men) is similar to previous estimates in healthy subjects using gas uptake of 0.61 liter [5], or by comparing volumes measured by chest radiographs at full inflation with body plethysmography of 0.72 liter [26]. We had expected lung tissue volume to be larger in the obese than the control men, because, in obesity, intrapulmonary blood volume is probably larger [2, 18, 29], particularly when supine. *Differences between supine* and seated gas volumes. There is no consistent supine change in RV, but supine values of TLC and VC in normal subjects are, on average, slightly lower (200 ml or less) than seated values [3, 21, 32, 33, 35], with the reduction being attributed to an increase in central blood volume when supine. Similar small reductions in supine TLC and VC have been shown in obese subjects [3, 32, 33, 35]; indeed, previously our laboratory found that supine TLC in obese subjects, some of whom had lung restriction, was, on average, only 80 ml smaller than seated values [33]. Hence we believe our results for TLC, VC, and RV also apply to seated subjects. This is not the case for FRC. Whereas in normal subjects, FRC falls by 700 – 800 ml on going from the seated to the supine position [3, 21, 32, 33, 35], in severely obese subjects our laboratory [33, 35] and others [3, 32] have shown that supine falls in FRC are much smaller and may even be absent. The difference in values of FRC, FRC/TLC, and ERV between control and obese subjects shown in Table 2, therefore, would be even larger if the subjects were seated.

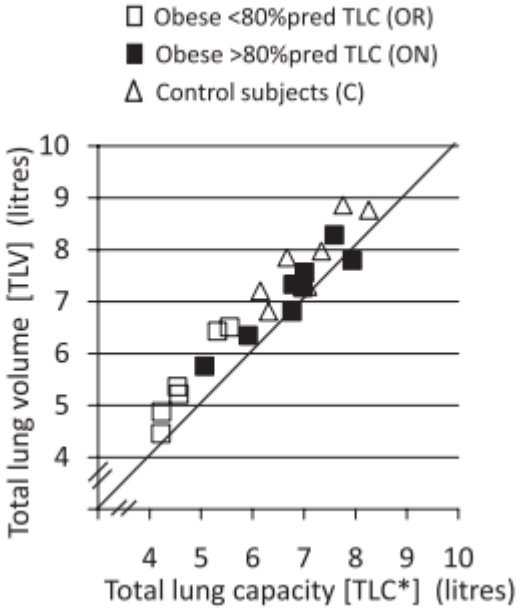

Fig. 4. Comparison of TLC measured by multibreath helium dilution (TLC) and TLV measured by MRI in control men. The diagonal line is the line of identity. In this comparison, measured TLC has been reduced by the estimated volume of the extrathoracic airway (see METHODS).*

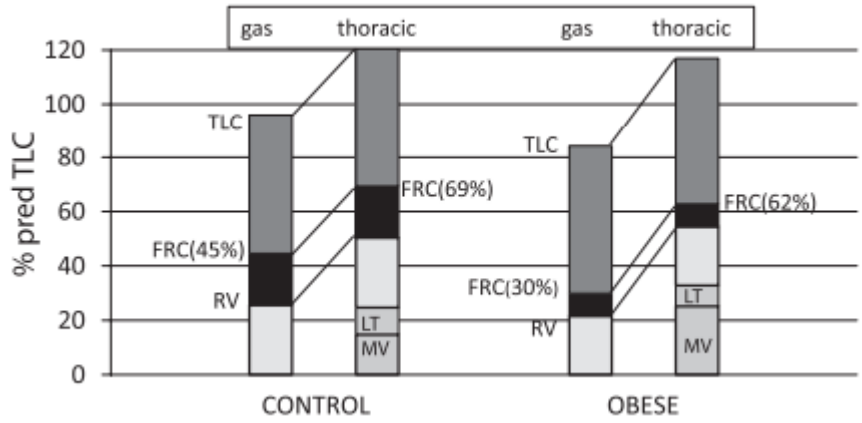

Fig. 5. Comparison of mean gas volumes and estimates of mean intrathoracic volumes (all expressed as %predicted TLC) in control and obese men. LT, lung tissue volume; MV, mediastinal volume; FRC, functional residual capacity; RV, residual volume. Increased mediastinal volume in the obese men results in the differences in intrathoracic volumes between obese and control men being smaller than the corresponding differences in gas volumes.

Comparison of Supine Lung Gas Volumes in Obese Men with and without Restriction

Obese men had highly significant reductions in supine FRC, FRC/TLC, and ERV compared with control men. Reduction in TLC in the obese men was more variable and, when results were corrected for height differences between control and obese men, did not quite reach

statistical significance vs. control subjects. In early studies of individual patients with “morbid” obesity with hypercapnia (“Pickwickian”, or obesity hypoventilation syndrome), reduction in TLC was a prominent feature [14, 29], but was often not found in later, less selected studies of obesity [28]. Recently, the relation of BMI to seated TLC and subdivisions has been clarified by Jones and Nzekwu [17], who studied 373 men and women (their results were not distinguished) whose BMI ranged from 20 to 58 kg/m². Mean values of seated TLC, FRC, VC, ERV, and RV all declined progressively with increasing BMI, but at very different rates and with a wide scatter of results, especially for ERV and RV. The largest and most consistent reductions were in FRC and, consequently, also in ERV, which were found in mild obesity. At a BMI of 30 –35 kg/m². mean FRC was 75% and mean ERV 47% of values at BMI of 20 kg/m² ; values of ERV as small as 20%pred or less were common, limiting the possibility of any further reduction at higher BMI. As a result, an exponential curve was fitted to these data. In contrast mean reductions in TLC, VC, and RV with increase in BMI were much smaller, so that group mean values remained within the normal range (TLC and VC both 88%pred, RV 90%pred), even in subjects with BMI 40 kg/m². Our finding that obese men had large reductions in FRC, whether or not they were in the ON or the OR group, is, therefore, consistent with Jones and Nzekwu’s findings. Total intrathoracic volume in obesity. In control men, the fully inflated lungs occupied, on average, 88% of the total intrathoracic volume, but in obese men only 78% because of their larger mediastinal volume, which, in the obese men, averaged 1.78 liter (25.2%pred TLC) compared with 1.10 liter (14.8%pred TLC) in the control men. We are not aware of earlier measurements of intrathoracic fat, but an increase in central blood volume was consistently noted in early studies of obesity hypoventilation syndrome, even in the absence of overt heart failure [18, 29], and has been confirmed more recently in obese subjects without any symptoms to suggest clinical heart disease [2]. The mean 10% pred TLC increase of mediastinal volume in the obese compared with the control men hardly contributed to the large difference in TLC between the ON and OR groups, because mean mediastinal volume was only 0.11 liter larger in the OR than in the ON subgroup. Indeed, Fig. 3 shows that, whereas individual values of TLV largely overlap in the ON and control groups, total intrathoracic volume at a given TLV tends to be larger in the ON individuals, perhaps suggesting the thoracic wall has “accommodated” to the larger mediastinal volume. The major contributor to restriction of TLC in the OR group was that, while the eight ON men had a mean total intrathoracic volume at full inflation slightly larger (124%pred TLC) than the control men

(120%pred), in the six OR men, mean total intrathoracic volume at full inflation was 105%pred TLC. Possibly, therefore, in some obese men, the large abdomen limits caudal movement of the diaphragm at full inflation. Recent experiments inducing acute ascites in dogs have shown that the load on the diaphragm was increased by an increase in abdominal elastance, but, in addition, the lung-expanding action of the diaphragm was impaired by reduction in its pressure-generating ability [19, 20]. We are not aware of comparable studies of diaphragm function and load in human obesity. The immediate cause of reduction in TLC is a reduction in VC (changes in RV are small and inconsistent). Reductions in VC with increase in weight have been shown in men in three prospective studies over 5–7 yr, with mean losses of forced VC (FVC) of 26 ml [6], 21 ml [7] and 17 ml [34] for each kg of weight gained. Two of these studies also studied women [6, 34] in whom losses of FVC per kg weight gain were considerably smaller. Conversely, rises in VC following reductions in weight were first reported in small studies many years ago [29, 31]. In the last decade gastric surgery has become a popular method to induce large and rapid reductions in weight; so far only a few studies have reported the effects on spirometry, but in them mean FVC has consistently increased 6 mo or more after operation [22]. The precise mechanism by which VC is reduced by increase in weight, why this loss of VC is larger in men than in women, and why reduction in TLC is very variable among obese men of similar age and BMI all remain uncertain. Reduction in FRC and RV. The reduction in FRC and ERV in healthy subjects when lying supine is attributed to a rightward displacement of the PV curve of the relaxed chest wall, increasing its pressure at a given gas volume, and reducing relaxation volume (Vr) [1]. A comparable supine decrease in Vr would be expected in obesity. In practice, in severe obesity when supine FRC hardly falls below seated values, FRC is probably maintained above Vr as a response to expiratory flow limitation [25, 35]. Our finding of an increase in mediastinal volume in obesity potentially alters the interaction between elasticity of the chest wall and of the lungs. Classically, this interaction is related to a common volume, defined by the volume of gas contained in the lungs. When considering the pleural cavities, this convention obscures the normal difference between the volume enclosed by the parietal pleura and intrapulmonary gas volume, which arises from the tissue and fluid content (including blood) within the lungs. In intrathoracic disease, the difference between total intrapleural volume and intrapulmonary gas volume may be increased, as originally analyzed by Fenn [11] for pneumothorax, or for both pleural cavities with increase in intrapulmonary fluid, blood, or tissue volume in conditions such as interstitial lung fibrosis [12]. FRC, TLC,

and RV all are partly determined by active or passive characteristics of the chest wall and respiratory muscles, so their values in thoracic diseases can be fully interpreted only if chest wall volume is known or can be inferred [13]. Previously, two papers have suggested that restriction of TLC may be partially reversed by heart transplantation, due to the effects of increased heart volume in chronic heart failure [16, 23]; one of these studies [16] estimated the change in heart volume following heart transplantation from chest radiographs. In the present study, we have measured mediastinal volume in a few healthy middle-aged men. This volume, when combined with lung tissue and fluid volume, is responsible for the "normal" difference between total intrathoracic volume and total gas volume. So far, despite the wide availability of three-dimensional imaging techniques that could measure simultaneously total intrathoracic volume and TLV, we have not found any published estimates of mediastinal volume to check against our value of 1.10 liter. The acquired increase in mediastinal volume in obesity implies that the difference between intrathoracic volume and the corresponding gas volume has increased on average by 0.68 liter in adult life. In middle-aged healthy men, chest wall compliance in the operating tidal range close to FRC averages 0.176 l/cmH_2O seated and 0.161 l/cmH_2O supine [10]. Hence an acute increase of 0.68 liter in mediastinal volume could increase pressure exerted by the relaxed chest wall by as much as 4 cmH_2O, which would have a large effect on Vr. However, with a chronic increase in mediastinal volume, the elastic properties of the chest wall may show partial or even complete adaptation. Increase in mediastinal volume may also influence the value of RV, at least in younger obese adults in whom RV is determined by a static balance between the maximum muscle pressure and the outward recoil of the passive structures of the chest wall as its volume is reduced [1]. The minimum gas volume of the lung at RV may be reduced if there is an increase in indistensible volume within the thoracic cavity. This may explain that, while gas volume at RV was smaller in the obese men than in the control men, intrathoracic volume at RV was slightly larger in the obese men than in the control men (see Fig. 5). Thus it seems possible that increase in mediastinal volume may influence the values of FRC and RV in obesity, even if it is not important in restricting TLC in obesity. In conclusion, we found that reduction in TLC in obese men was associated with reduced expansion of the thoracic cage. Both intrathoracic fat volume and the volume of heart and major blood vessels were larger in the obese than the control men, but these volumes did not differ between obese men with and without lung restriction. Further

studies are required to determine the factors impairing full expansion of the thorax in some obese men.

Grants

The authors are grateful to the United Kingdom Medical Research Council for financial support. We acknowledge infrastructure support from the National Institute for Health Research Biomedical Research Centre funding scheme.

Disclosures

No conflicts of interest, financial or otherwise, are declared by the author(s).

References

1. Agostoni E, Hyatt RE. Static behaviour of the respiratory system. In: Handbook of Physiology. The Respiratory System. Mechanics of Breathing. Bethesda, MD: Am. Physiol. Soc., 1986, sect. 3, vol. III, pt. 1, chapt. 9, p. 113–130.

2. Alpert MA. Obesity cardiomyopathy: pathophysiology and evolution of the clinical syndrome. Am J Med Sci 321: 225–236, 2001.

3. Bae J, Ting EY, Giuffrida JG. The effect of changes in the body position of obese patients on pulmonary volume and ventilatory function. Bull NY Acad Med 52: 830 –837, 1976.

4. Brown R, Leith DE, Enright PL. Multiple breath helium dilution measurement of lung volumes in adults. Eur Respir J 11: 246 –255, 1998.

5. Cander L, Forster RE. Determination of pulmonary parenchymal tissue volume and pulmonary capillary blood flow in man. J Appl Physiol 14: 541–551, 1959.

6. Chen Y, Horne SL, Dosman JA. Body weight and weight gain related to pulmonary function decline in adults: a six-year follow up study. Thorax 48: 375–380, 1993.

7. Chinn DJ, Cotes JE, Reed JW. Longitudinal effects of change in body mass on measurements of ventilatory capacity. Thorax 51: 699 –704, 1996.

8. Cotes JE, Chinn DJ, Miller MR. Body size and anthropometric measurements. In: Lung Function (6th ed.). Oxford, UK: Blackwell, 2006, p. 31–41.

9. Durnin JVGA, Womersley J. Body fat assessed from total body density and its estimation from skinfold thickness: measurements on 481 men and women aged from 16 to 72 years. Br J Nutr 32: 77–97, 1974.
10. Estenne M, Yernault JC, De Troyer A. Rib cage and diaphragmabdomen compliance in humans: effects of age and posture. J Appl Physiol 59: 1842–1848, 1985.
11. Fenn WO. The pressure-volume diaphragm of the breathing mechanism. In: Respiratory Physiology in Aviation, edited by Boothby WM. Randolph Field, TX: USAF School of Aviation Medicine, 1954, p. 19 –27.
12. Gibson GJ, Pride NB. Pulmonary mechanics in fibrosing alveolitis: the effects of lung shrinkage. Am Rev Respir Dis 116: 637–647, 1977.
13. Gibson GJ, Pride NB. Pleural, alveolar and systemic diseases affecting chest wall function. In: The Thorax. Part C: Disease (2nd ed.), edited by Roussos C. New York: Dekker, 1995, vol. 85, chapt. 72, p. 2101–2133. (Lung Biol. Health Dis Ser.)
14. Hackney JD, Crane MG, Collier CC, Rokaw S, Griggs DE. Syndrome of extreme obesity and hypoventilation: studies of aetiology. Ann Intern Med 51: 541–52, 1959.
15. Hedenstierna G, Santessen J. Breathing mechanics, dead space, and gas exchange in the extremely obese, breathing spontaneously and during anaesthesia with intermittent positive pressure ventilation. Acta Anaesthesiol Scand 20: 248 –254, 1976.
16. Hosenpud JD, Stibolt TA, Atwal K, Shelley D. Abnormal pulmonary function specifically related to congestive heart failure: comparison of patients before and after cardiac transplantation. Am J Med 88: 493–496,1990.
17. Jones RL, Nzekwu MM. The effects of body mass index on lung volumes. Chest 130: 827–833, 2006.
18. Kaltman AJ, Goldring RM. Role of circulatory congestion in the cardiorespiratory failure of obesity. Am J Med 60: 645–653, 1976.
19. Leduc D, Capello M, Gevenois PA, De Troyer A. Mechanics of the canine diaphragm in ascites: a CT study. J Appl Physiol 104: 423–428, 2008.
20. Leduc D, De Troyer A. Dysfunction of the canine respiratory muscle pump in ascites. J Appl Physiol 102: 650 –657, 2007.
21. Navajas D, Farre R, Rotger MM, Milic-Emili J, Sanchis J. Effect of body posture on respiratory impedance. J Appl Physiol 64: 194 –199, 1988.

22. Nguyen NT, Hinojosa MW, Smith BR, Gray J, Varela E. Improvement of restrictive and obstructive pulmonary mechanics following bariatric surgery. Surg Endosc 23: 808 –812, 2009.
23. Niset G, Ninane V, Antoine M, Yernault JC. Respiratory dysfunction in congestive heart failure: correction after heart transplantation. Eur Respir J 6: 1197–1201, 1993.
24. Nunn JF, Campbell EJM, Peckett BW. Anatomical subdivisions of the volume of respiratory deadspace and effect of position of the jaw. J Appl Physiol 14: 174 –176, 1959.
25. Pankow W, Podszus T, Gutheil T, Penzel T, Peter JH, von Wichert P. Expiratory flow limitation and intrinsic positive end-expiatory pressure in obesity. J Appl Physiol 85: 1236 – 1243, 1998.
26. Pierce RJ, Brown DJ, Holmes M, Cumming G, Denison DM. Estimation of lung volumes from chest radiographs using shape information.Thorax 34: 726 –734, 1979.
27. Quanjer PH. Standardised lung function testing. Bull Eur Physiopath Respir 19, Suppl 5: 7–10, 1983.
28. Ray CS, Sue DY, Bray G, Hanson JE, Wasserman K. Effects of obesity on respiratory function. Am Rev Respir Dis 128: 501–506, 1983.
29. Rochester DF, Enson Y. Current concepts in the pathogenesis of the obesity-hypoventilation syndrome. Mechanical and circulatory factors. Am J Med 57: 402–420, 1974.
30. Thomas EL, Saeed N, Hajnal JV, Brynes A, Goldstone AP, Frost G, Bell JD. Magnetic resonance imaging of total body fat. J Appl Physiol 85: 1778 –1785, 1998.
31. Thomas PS, Cowen ERT, Hulands G, Milledge JS. Respiratory function in the morbidly obese before and after weight loss. Thorax 44: 382–386, 1989.
32. Tucker DH, Sieker HO. The effect of change in body position on lung volumes and intrapulmonary gas mixing in patients with obesity, heart failure and emphysema. Am Rev Respir Dis 82: 787–791, 1960.
33. Watson RA, Pride NB. Postural changes in lung volumes and respiratory resistance in subjects with obesity. J Appl Physiol 98: 512–517, 2005.
34. Wise RA, Enright PL, Connett JE, Anthonisen NR, Kanner RE, Lindgren P, O'Hara P, Owens GR, Rand CS, Tashkin DP. Effect of weight gain on pulmonary function after smoking cessation in the Lung Health Study. Am J Respir Crit Care Med 157: 866 –872, 1998.
35. Yap JC, Watson RA, Gilbey S, Pride NB. Effects of posture on respiratory mechanics in obesity. J Appl Physiol 79: 1199 –1205, 1995.

Paper 4

Whole body fat: Content and distribution

E. Thomas[1], ***J. Fitzpatrick***[1], S. Malik[2], S. Taylor-Robinson[3], J. Bell[1]

Abstract

Obesity and its co-morbidities, including type II diabetes, insulin resistance and cardiovascular diseases, have become one of the biggest health issues of present times. The impact of obesity goes well beyond the individual and is so far-reaching that, if it continues unabated, it will cause havoc with the economies of most countries. In order to be able to fully understand the relationship between increased adiposity (obesity) and its co-morbidity, it has been necessary to develop proper methodology to accurately and reproducibly determine both body fat content and distribution, including ectopic fat depots. Magnetic Resonance Imaging (MRI) and Spectroscopy (MRS) have recently emerged as the gold-standard for accomplishing this task. Here, we will review the use of different MRI techniques currently being used to determine body fat content and distribution. We also discuss the pros and cons of MRS to determine ectopic fat depots in liver, muscle, pancreas and heart and compare these to emerging MRI techniques currently being put forward to create ectopic fat maps. Finally, we will discuss how MRI/MRS techniques are helping in changing the perception of what is healthy and what is normal and desirable body-fat content and distribution.

Introduction

Obesity has become one of the major health concerns of modern times. It is estimated that over 700 million people across the world are currently either overweight or obese [1]. In the UK alone, latest studies show that over 60% of the adult population is either over weight (with a body mass index (BMI) between 25–30 kg/m^2) or obese (with a BMI between 30–40 kg/m^2), while 30.3% of children (aged 2–15) are overweight or obese. This increase in body adiposity is closely associated with a number of non-communicable diseases, including type-2 diabetes, hypertension, cardiovascular disorders and some forms of cancer. Indeed, type-2 diabetes is today a major worldwide problem, with more than 346,000,000 diabetics across the planet

and these figures may double by 2030 [1]. In some countries, levels of diabetes now affect over 20% of the adult population. The social and economic impact of the obesity pandemic, and its co-morbidities, cannot be overstated, and at this rate is likely to have a severe impact on healthcare provision in many economies [2]. Adipose tissue (or body-fat) is a multifaceted and complex organ [3]. Besides functioning as a system for excess energy deposition, protection from the cold and everyday hazards, adipose tissue produces an assortment of molecular messengers (adipokines), which influence a diverse array of functions, including appetite, fertility, neuronal development and plasticity, inflammatory responses, and the action of other hormones, including insulin [4]. Yet, despite these positive functions, a close association between excess body adiposity and the development of non-communicable diseases has been reported in many epidemiological studies [5]. Moreover, these associations are further strengthened if age and physical activity (or the lack of it) are included in the paradigm. Detailed studies of adipose tissue content and distribution suggest that the latter plays an important part in these associations [6]. Indeed, a number of adipose-tissue related sub-phenotypes have now been identified, including 'thin on the outside fat on the inside' (TOFI) and 'fat-fit' subjects, which indicate the importance of having accurate and reproducible measurements of both the total body-fat and its distribution [7]. For example, in the case of TOFI, subjects with normal BMI (<24.9 kg/m^2) but increased abdominal obesity, have increased risk of developing insulin resistance and type II diabetes, while the "fat-fit", subjects with BMI > 30 kg/m^2 appear metabolically normal despite their elevated body adiposity [8]. In order to understand these somehow paradoxical findings, it is important to get a better definition of the different concepts/ words involved in many of these associations, including 'adipose tissue', 'body-fat' and 'ectopic fat'. The use of the words 'fat' or 'body-fat' has become synonymous with obesity, and in general refers to the fat found immediately under the skin covering substantial parts of the surface of the body. Strictly speaking, this fat layer is actually 'subcutaneous adipose tissue' and is part of a larger organ: adipose tissue, which makes up a significant part of our bodies. Adipose tissue can also be found surrounding organs such as the liver, pancreas, kidneys and the heart, to some degree. It is also found in muscles and other areas of the body including part of the orbital cavities. All these fat depots, which in many instances are not in direct physical contact with each other, appear to work in a coordinated manner, and are normally referred to as 'total adipose tissue'. Besides these fat depots, fat can also be accumulated within certain organs and tissue, including liver, pancreas,

heart and muscle, and these deposits are technically known as ‘ectopic fat depots’. Some of these depots have recently been shown to be important independent risk factors for disease development and clearly deserve closer scrutiny if the underlying mechanism that underpins the associations between increased body adiposity is to be unravelled [9]. The need for an accurate and reproducible method to determine levels of different fat depots, including ectopic fat, has driven the scientific community to investigate the potential use of imaging technologies, including CT, magnetic resonance imaging and spectroscopy (MRI/MRS). Thus, in the last two decades MRI/MRS have become the gold-standard for such studies, especially as the scientific community moves into the post-genomic era and an understanding is sought of the gene-environment interactions that contribute to the determination of fat content and distribution in different subjects and their role in the reported gender and ethnic differences. With this in mind, we will review the use of MRI and MRS in the study of adipose tissue and ectopic fat and how these techniques are helping us to get a better understanding of the role of body fat not only in disease development, but also in the process of achieving optimal health.

Indirect methods for body-fat measurements

A number of techniques are currently available to assess body fat content. Indirect methods include: body-mass-index (BMI), skinfold anthropometry, bioelectrical impedance, underwater weighing, and body water dilution [10]. While there are pros and cons for all of these methodologies, the one thing they have in common is that they give little or no information concerning adipose tissue distribution. Moreover, most of these techniques are based on indirect measurements of either body water or body volume and necessitate equations to convert these into total fat measurements. While these methodologies do provide valuable information, particularly at a population level, they are not always applicable to all ethnic groups or to subjects with extremes of body types. This is mainly due to the fact that they were derived from specific populations, generally Caucasian. More importantly, they say nothing about intra-abdominal (also known as ‘visceral fat’) or ectopic fat levels, two crucial factors in the association between body adiposity and disease development. We will therefore not discuss these methods further.

Direct Methods for body fat measurements

CT and MRI to measure adipose tissue content and distribution

The fact that different fat depots within the body appear to contribute, to a differing extent, to the risk of developing non-communicable diseases, has made it clear that measuring total body fat content alone was not sufficient. This has necessitated the development and implementation of new techniques that could accurately measure body fat content and distribution and which could be applicable to all populations and body types. The first technique used which appeared to meet all of these criteria was CT scanning. Total adipose tissue content could be measured as well as individual adipose tissue depots, particularly intra-abdominal adipose tissue depot [11–14]. However, a major drawback of CT scanning is the radiation dose it delivers, which greatly limits its application, particularly for longitudinal studies and in paediatric populations. With the advent of in vivo magnetic resonance techniques, MRI was seen as an ideal alternative. The first studies applying MRI to measure adipose tissue content and distribution in humans were published in the mid-1980s [15– 17]. MRI has since been fully validated against both animal and human post-mortem dissection studies [18–21], showing that this technique gives extremely accurate and reproducible measurements of adipose tissue content and distribution. Since then, this area of research has grown beyond recognition. Fig.1 shows a graphical representation of papers published in the last 30 years using MRI techniques to measure adipose tissue content and distribution and in particular, visceral fat. It is likely that this graph underestimates the number of papers in this area, particularly those published in recent years. Initially, the use of MRI for adipose tissue assessment was driven mainly by research groups based in radiology departments or MR research units, with the development of MR methodologies being the primary focus of the research. However, since then, MRI has become the gold-standard for overall clinical phenotyping, and is now routinely used by many research groups. As such, MRI is often not included as a keyword in many papers and therefore cannot be readily found in Medline searches.

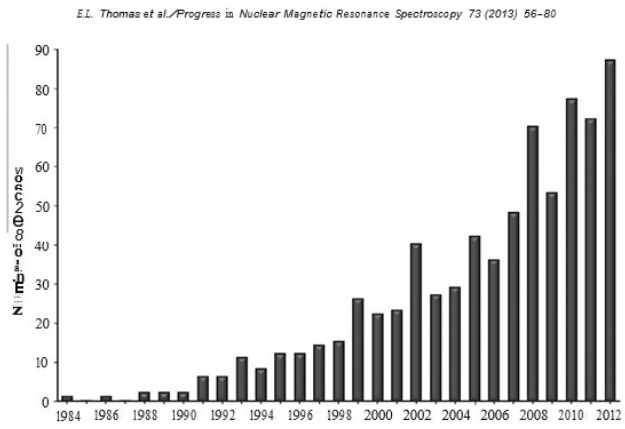

Fig. 1 Number of publications between 1989 and 2012 found on Pubmed using MRI adipose tissue content. distribution and visceral adipose tissue in various combinations as key word searches.

Development and application of different MRI sequences to assess adipose tissue

A number of MRI sequences have been developed and applied in order to measure body fat content and distribution in humans and animals. In one of the first reports on the potential use of MRI to measure adipose tissue, the group from Aberdeen, working at 0.08T, tested a variety of sequences to differentiate between fat and lean tissue, including proton density, T_1-weighted, inversion recovery and saturation recovery sequences [15]. They found the greatest degree of tissue contrast with the inversion recovery (IR) pulse sequence (TR 370 ms, interval of 170 ms), which they employed in subsequent publications [22]. An inversion recovery sequence, with transverse images, was also used in the seminal paper by Seidell et al. working at 1.5T (TR 820 ms, TE 20 ms, interval of 300 ms) [14]. This IR sequence has now been largely replaced by the more robust T_1-weighted spin-echo sequence (Table 1). A typical image example obtained with this sequence is shown in Fig.2, with fat appearing as high signal (white), showing good differentiation from muscle, fluid, bone and internal organs (grey). However, this technique is not without problems, since it is relatively slow and is susceptible to respiratory motions, factors that can be important when dealing with older population or newborn babies. Variations of this sequence have been proposed, including a gradient-echo sequence, which produces very similar looking images, but allows faster acquisition time, since it only requires a single radiofrequency pulse, and fast-switching gradients. There are some disadvantages to this approach, however, including loss of signal from static magnetic field inhomogeneity. This can result in gradient-echo acquisitions being more affected by magnetic susceptibility artefacts compared with spin-echo sequences. There have been many attempts to

produce dedicated MRI sequences which allow more rapid acquisition, overcome breathing/motion induced artefacts, and enable faster and automated image analysis, (a major bottleneck in most studies using MRI or CT to measure adipose tissue content and distribution) (Table 1). One technique that appears to be gaining great favour with researchers is the use of water-suppressed sequences to produce fat and water only images. (For a typical example of this technique refer to Fig.9, Section 3.1.2). Although this sequence is an attractive alternative to T_1-weighted spin-echo sequences, it does not come without problems. It is far more sensitive to motion/respiratory artefacts and highly susceptible to misidentification of non-adipose tissue fat (e.g. bowel fat)

Whole body versus regional body assessment

As well as different MRI sequences for data acquisition, researchers have used a variety of approaches to the number of images they acquire and at which anatomical location. The initial impetus to accurately measure and map total and regional adipose tissue necessitated protocols in which images were obtained throughout the body (whole-body imaging). Subsequently single-slice and region-specific multi-slice protocols were developed (Fig. 3). Table 1 illustrates the variety of MR approaches to measuring whole body or abdominal adipose tissue used by different research groups around the world. It is not possible to make this list fully comprehensive, given the sheer number of different groups now applying these techniques. Groups where a predominantly single-slice acquisition approach is used have not been included for reasons of space

Table 1
sdfsadfds.

Group	Key, authors	Year	Approx. number relevant papers	Coverage	Slice thickness	Slice gap	Subject Position	Sequence	Analysis	Scanner	Image time	Ref.
Sweden												
The Karolinska Institute, Stockholm Sweden	Sohlstrom, Forsum	1993–1997	3	30 slices	20 mm	Various, average 40 mm	Supine, arms beside body	Saturation Recovery	MIS 100	0.02T Acut	2.5 h	[23]
Uppsala University Hospital, Uppsala, Sweden	Kullberg, Johansson	2006	16	Whole body (12 stacks of 25 slices), body scanned in 2 halves	8 mm	None	Supine, arms extended above head	Spoiled T_1-weighted gradient-echo	In-house software	1.5T Philips	45 min	[24]
Germany												
University of Tubingen, Tubingen, Germany	Machann, Schick	2004–2012	60	Whole body, fingertips to toes 100–130 slices, patient turned half-way	10 mm	10 mm	Prone arms extended above head	T_1-weighted fast spin-echo	Customised MATLAB	1.5T Siemens	20–25 min	[25]
Christian-Albrechts University, Kiel, Germany	Bosy-Westphal, Muller	2008–2012	20	Whole body, wrists to ankles	10 mm	None	Supine, arms extended above head	T_1-weighted gradient-echo	SliceOmatic	1.5T Siemens		[26]
University of Ulm, Ulm, Germany	Muller, Kassubek	2010	1	Whole body 6–8 volumes composed of 36 2D slices	5 mm	NA	Not specified	T_1-weighted turbo spin-echo	In-house software	1.5T Siemens	27–36 min	[27]
German Cancer Research Center, Heidelberg, Germany	Wald, Heimann	2012	1	Whole body	3 mm	1 mm	Supine, arms beside body	2-point Dixon with 3D gradient echo	In-house software	1.5T Siemens	<15mins	[28]
The Netherlands												
Utrecht, The Netherlands	Seidell, Bakker, Elbers, Koppeschaar	1990–2003	10	Lower rib to iliac crest, 6 slices	12 mm	50 mm gaps	Supine	Inversion Recovery	Philips software	1.5T Philips		[29,30]
UK												
Hammersmith Hospital, London, UK	Thomas, Bell	1996–2012	50	Whole body, fingertips to toe ~113 slices	10 mm	10 mm gaps between slices	Prone, arms above head	T_1-weighted spin-echo	SliceOmatic	1.5T Philips	20–25 min	[31]
Aberdeen, Scotland	Fowler, Fuller and Foster	1984–1991	5	28 slices from sternum to ankle	12 mm	Various	Not specified	Inversion Recovery	Aberdeen Imager	0.08T		[22]
University of Liverpool, Liverpool, UK	Cuthbertson, Kemp	2012	3	Whole body	10 mm	10 mm	Prone, arms above head	T_1-weighted spin-echo	SliceOmatic	1.5T Siemens		[32]
Newcastle University, Newcastle-upon-Tyne, UK	Hayes, Taylor	2008–2011	3	Lower sternum to the mid thigh	10 mm	30 mm	Supine	T_1-weighted spin-echo	In-house software	1.5T Philips		[33]
Ireland												
Cork, Ireland	McLaughlin, Maher	2012	1	Whole body coronal and selected axial	11 mm	Not specified	Not specified	T_1-weighted spin-echo and gradient-echo	Osirix	1.5T Siemens		[34]
Finland												
Helsinki, Finland	Tiikkainen, Yki-Jarvinen	2002–2012	30	From 8 cm above to 8 cm below L4/L5	10 mm	None	Prone	T_1-weighted spin-echo	Alice 3.0	1.5T Siemens		[35]
University of Turku, Turku, Finland	Virtanen, Nuutila	2002–2011	8	Abdominal and femoral regions	Not Specified	Not specified	Not specified	T_1-weighted field-echo	Not Specified	0.23T Marconi		[36]
Iceland												
Landspitali University Hospital Fossvogi,	Arnardottir, Maislin	2012	3	Abdomen from xiphoid process to L5/S1	10 mm	None	Not specified	Gradient echo	Amira	1.5T Siemens		[37]

(*continued on next page*)

Table 1 (*continued*)

Group	Key, authors	Year	Approx. number relevant papers	Coverage	Slice thickness	Slice gap	Subject Position	Sequence	Analysis	Scanner	Image time	Ref.
Reykjavik, Iceland												
Italy												
Padova, Italy	Busetto, Enzi	2000–2002	2	From L4/L5 as origin to hand then foot, 41 slices in total	10 mm	50 mm	Arms above head	T_1-weighted spin-echo	NIH Image	1.5T Philips		[38]
Spain												
Navarra, Spain	Idoate, Izquierdo	2010–2012	3	Abdomen, 2 stacks of 10 contiguous slices	10 mm	None	Supine, arms beside body	Spoiled T_1-weighted gradient-echo	SliceOmatic	1.0T Siemens		[39]
Canada												
Queen's University, Ontario, Canada	Ross	1992–2012	60	41 slices, head to toe	10 mm	50 mm gaps	Prone, arms above head	T_1-weighted spin-echo	In-house software	1.5T Siemens	30 min	[40]
USA												
Southwestern Medical Centre, Dallas, Texas, USA	Abate, Garg, Grundy	1994–2012	15	Entire abdomen contiguous slices	10 mm	None	Supine, arms beside body	T_1-weighted spin-echo	Toshiba software	0.35T Toshiba		[20]
University of Texas Health Science Center, San Antonio, Texas, USA	Bonora, DeFronzo	1991–2011	10	Abdomen 4 slices, centered at l4	5 mm	15 mm	Not specified	T_1-weighted spin-echo	In-house software	1.5T GE	<5mins	[41]
University of Wisconsin, Wisconsin, USA	Poonawalla, Reeder	2012	1	Liver dome to pelvic floor	Unclear – volume acquired?		Supine, arms extended above head	3D multiecho spoiled gradient-echo	SliceOmatic	3T GE		[42]
University of Pittsburg School of Medicine, Pittsburg, USA	Lee, Arslanian	2010–2012	4	From l4/l5 as origin to hand then foot, 41 slices in total	10 mm	50 mm	Prone, arms above head	T_1-weighted spin-echo	SliceOmatic	3T Siemens		[43]
Vanderbilt University School of Medicine, Nashville, Tennessee, USA	Silver, Welch	2012	1	Whole body 17 stacks of 12 slices	8 mm	None	Supine, arms bent above head	Multiple fast field ech0	In-house software	3T Philips	20–25 min	[44]
Washington University School of Medicine, St Louis, Missouri, USA	Staten, Totty, Kohrt	1989	1	Chest, abdomen and midthigh, unclear how many slices at each site	10 mm	Various	Not specified	Spin-echo	Siemens software	0.5T Siemens		[17]
Washington University School of Medicine, St Louis, Missouri, USA	Siegel, White	2007	1	Entire abdomen	10 mm	None	Not specified	Fast Imaging with steady-state precession (FISP)	Analyze	1.5T Siemens	5 min	[45]
Columbia University, New York, USA	Albu, Pi-Sunyer, Heymsfield, Shen, Punyanitya, Gallagher	1997–2012	>50	Whole body ~40 slices, fingertips to toe	10 mm	40 mm	Arms above head	T_1-weighted spin-echo	SliceOmatic	1.5T GE		[46,47]
Georgia Prevention Institute, Augusta, USA	Gutin, Litaker	1998–2012	17	5 slices from l5 upwards	10 mm	2 mm	Not specified	T_1-weighted spin-echo	Not Specified	1.5T GE		[48]
Yale, Connecticut, USA	Caprio, Shulman, Pierpont	1995–2012	15	Abdomen and pelvis	10 mm	5 mm	Not specified	T_1-weighted spin-echo	GE software	1.5T GE		[49]
Winston-Salem, USA	Crouse, Cefalu, Anderson	1991–1998	6	Abdomen 4 slices, centered on l3	10 mm	5 mm gaps	Not specified	Inversion Recovery	Not specified	1.5T Picker		[50]
Pennington Biomedical Research Center, Baton Rouge, USA	Katzmarzyk, Ravussin	2011–2012	5	Top of liver to bottom of right kidney	Not specified	47.8 mm	Not specified	Not specified	Analyze	3T GE		[51]

Wright State University, Dayton, Ohio, USA	Demerath, Lee	2007–2012	7	From t9 to s1	10 mm	None	Not specified	T_1-weighted fast spin-echo	SliceOmatic	1.5T Siemens	[52]
University of Southern California, Los Angeles, CA, USA	Goran, Hu	2002–2012	22	19 axial images from dome of the liver to l2–l3	10 mm	None	Not specified	Dixon method	SliceOmatic	1.5T Siemens	[53]
Japan											
Tsukuba Medical Center Hospital, Tsukuba, Japan	So, Matsuo, Tanaka	2012	3	Bottom of t10 to top of s1	10 mm	None	Supine, arms extended above head	T_1-weighted spin-echo	SliceOmatic	1.5T Siemens	[54]
Kyoto University, Kyoto, Japan	Nakai, Tsutsumi	2010	1	15 abdominal slices	10 mm	Not specified	Supine	T_1-weighted breath-hold Fast Low Angle Shot (FLASH) fat-excitation sequence	In-house software	1.5T Siemens	[55]
Wakakusa Daiichi Hospital, Osaka, Japan	Tanaka, Inoue	2006–2007	2	Abdomen and pelvis	2 mm	None	Supine	T(1) high-resolution isotropic volume examination (THRIVE)	Aze Virtual Place	1.5T Philips	[56]
Tottori University, Yonago, Japan	Masahiko, Murawaki	2007	1	Xiphoid process to knee joint	10 mm	10 mm	Not specified	T_1-weighted spin-echo	Photoshop	1.5T Siemens	[57]
Singapore											
Singapore General Hospital, Singapore	Tai, Tan	2000–2011	2	Dome of diaphragm to symphysis pubis	8 mm	2 mm	Supine, arms beside body	T_1-weighted gradient echo	Siemens software	1.5T Siemens	[58]
Australia											
Garvan Institute of Medical Research, Sydney, Australia	Thompson, Chisholm, Campbell	2002–2006	9	16 slices between t12/l1 and l4/5	5 mm	5 mm	Not specified	T_1-weighted spin-echo	NIH Image	1.5T GE	[59]
Monash University, Clayton, Australia	Allan, Strauss, McLachlan	1996–2012	6	Abdomen (12 cm above the femoral head and extending superiorly (5 slices) and thigh	10 mm	50 mm	Not specified	T_1-weighted spin-echo	SliceOmatic	Siemens/ GE	[60]
University of Sydney at Westmead Hospital, NSW, Australia	Vongsuvanh, van der Poorten	2008–2012	2	19 slices upwards from l5/s1	10 mm	2.5 mm	Not specified	T_1-weighted and T_2-weighted images	Hippo Fat	1.5T Siemens	[61]

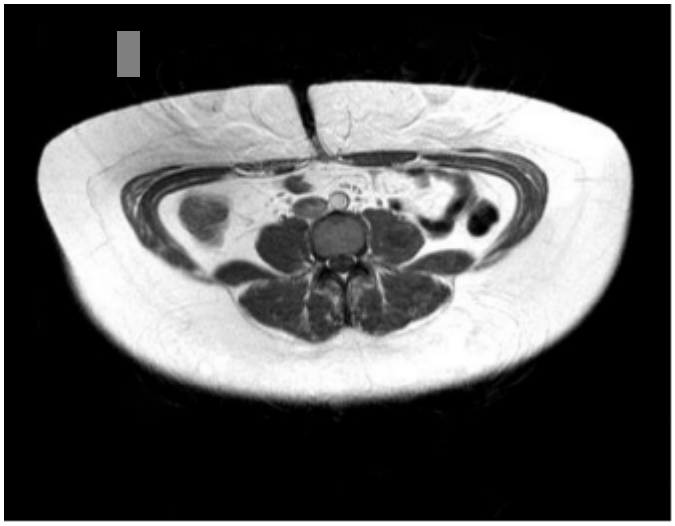

Fig. 2. Spin-echo image acquired in the abdomen at the level of the umbilicus, showing high signal arising from adipose tissue.

Whole body versus regional body assessment

For a detailed quantitative map of adipose tissue content and distribution, whole-body scanning is the most accurate and reproducible protocol available to researchers. However, this technique is also the most time-consuming, both in terms of MRI data acquisition (between 5 and 10 min) and image analysis (between 3 and 12 h). This protocol was originally published by Ross and colleagues and involved the acquisition of ca. 41 transverse slices (10 mm thick, with 40 mm gaps in-between), from the head to toe of subjects lying, with their arms extended above their head, in a prone position in the magnet [62]. Others, including Thomas et al. and Machann et al. have used a similar protocol, but with a smaller inter-slice gap of 10 mm, which results in a larger dataset (>110 slices), but better delineation of the intra-abdominal fat depots and internal organs [31,25]. Shen and colleagues suggested accuracy could be further improved by further reducing the slice thickness and obtaining contiguous data, particularly in datasets from infants and children [63]. In adults this is generally not very practical, particularly if a manual or semi-automatic approach is used to analyse the resulting datasets. Interestingly, Shen et al. also studies the effect of slice thickness on the volume of adipose tissue measured; providing the slice gap was less than 40 mm the difference between the measured and the true volumes is within 5% [64]. Furthermore Thomas et al. showed the coefficient of variation for measurement of abdominal adipose tissue increased in relation to the size of the interslice gap at a rate of 1.16%/cm [31]. A typical whole-body dataset obtained from a healthy volunteer, containing 113 transverse T_1-weighted images, is shown in Fig. 4. The images start in the toes

and end in the fingertips. While adipose tissue is clearly visible and can be quantified throughout the body, it should be noted that a significant degree of anatomy can also be observed. Hence, with the use of whole-body phenotyping, incidental findings of unexpected pathology can become a significant issue, particularly in older and more overweight populations [65]. Indeed, we and others have reported that up to 25% of volunteers from the general population, none of whom had any known medical conditions, were found to show abnormalities in their images, including hepatic and kidney cysts, missing kidneys and other relatively benign conditions. However, up to 5% of volunteers had clinically significant findings, many requiring some sort of clinical intervention. Thus, the possibility of incidental findings is something that must be considered in whole body MRI research, since dealing with unexpected pathology has ethical and financial implications as procedures have to be in place to ensure suitable follow-up for volunteers in whom abnormalities have been detected during the course of imaging studies. Despite its ability to give the most accurate quantitative measurements of adipose tissue, whole-body imaging approaches are currently used by a relatively small minority of groups world-wide. One of the main reasons for this is scanner design. Many MRI scanners do not currently have full computer-controlled table movement, which normally enables a subject to be moved through the magnet for a head-to-foot whole-body imaging; others may not have multiple coil-array systems for full body coverage. These factors are particularly important for obese subjects; the bore size (tunnel) of most clinical MR scanners is relatively small, making it difficult to accommodate very obese subjects. This problem is illustrated in Fig. 5. In this case, despite the patient fitting within the bore, at the maximum field-of-view (c.a. 530 mm, which is close to the maximum field-of-view that most clinical scanners allow) there is insufficient coverage to image the entire width of this subject's abdomen. Furthermore, despite some manufacturers producing MRI scanners with a sufficiently large bore (and even some open-side magnets) to accommodate very obese patients, the usable field-of-view is sometimes small relative to overall bore size, making adipose tissue measurement extremely challenging. For scanners without computer-controlled full table movement (or whole-body coil arrays), alternative approaches have been developed, including scanning subjects in two halves. First, subjects are scanned from head-to-abdomen and then repositioned to cover the lower part of the body. However, considerable care is required to ensure that the images from both halves of the body are correctly combined; otherwise undersampling or oversampling of the adjoining areas can occur. This is an important issue

since this area corresponds to the abdomen, the very anatomical point with the highest impact on health and disease. Regardless of the protocol used to obtain whole-body fat images, this scanning approach allows researchers to obtain quantitative information from at least 11 adipose tissue depots (including total adipose tissue content). These are summarised in Fig. 6. Clearly, imaging only part of the body, such as the abdomen as some researchers have proposed, would make it impossible to measure some of these fat depots, in particular inter-muscular adipose tissue, which is thought to be an independent risk factor for cardiovascular disease [66,67]. Moreover, whole-body imaging has other potential benefits; depending on sequence of choice and number of slices acquired, it may also be possible to measure other tissues and organ volumes including skeletal muscle, liver, kidney, heart, pancreas and bone marrow volumes [43,68–70]. Whole-body imaging approaches are also extremely useful in the study of patient groups where changes in overall fat distribution need to be assessed, as for example subjects with lipodystrophy (acquired or congenital), and patients with genetic mutations known to affect fat distribution. In these cases, *coronal images* (Fig. 7) are a valuable adjunct to the standard *transverse images* [71].

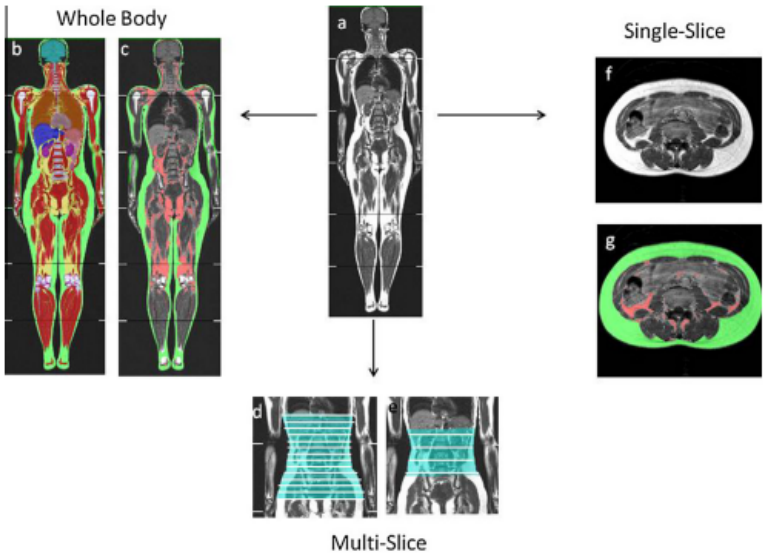

Fig. 3. Various imaging strategies for imaging adipose tissue. (a) T1-weighted whole body coronal image, for visual purposes this image has been segmented into (b) showing all major organs separately coded, allowing the volume of each organ to be measured. (c) The same image is segmented into subcutaneous (green) and internal (red) adipose tissue. Using a multi-slice approach the abdomen only is scanned, in (d) from the femoral heads to the slice containing the top of the liver/bottom of the lungs, approximate slice positions shown. This is also the area used to define visceral and abdominal subcutaneous adipose tissue in many whole body data sets [31]. (e), a more limited multi-slice acquisition, with images centred on vertebral bodies. Finally the single slice approach where just one image is obtained from a fixed point in the abdomen showing the (f) black&white and (g) segmented

images. (For interpretation of the references to colour in this figure legend, the reader is referred to the web version of this article.)

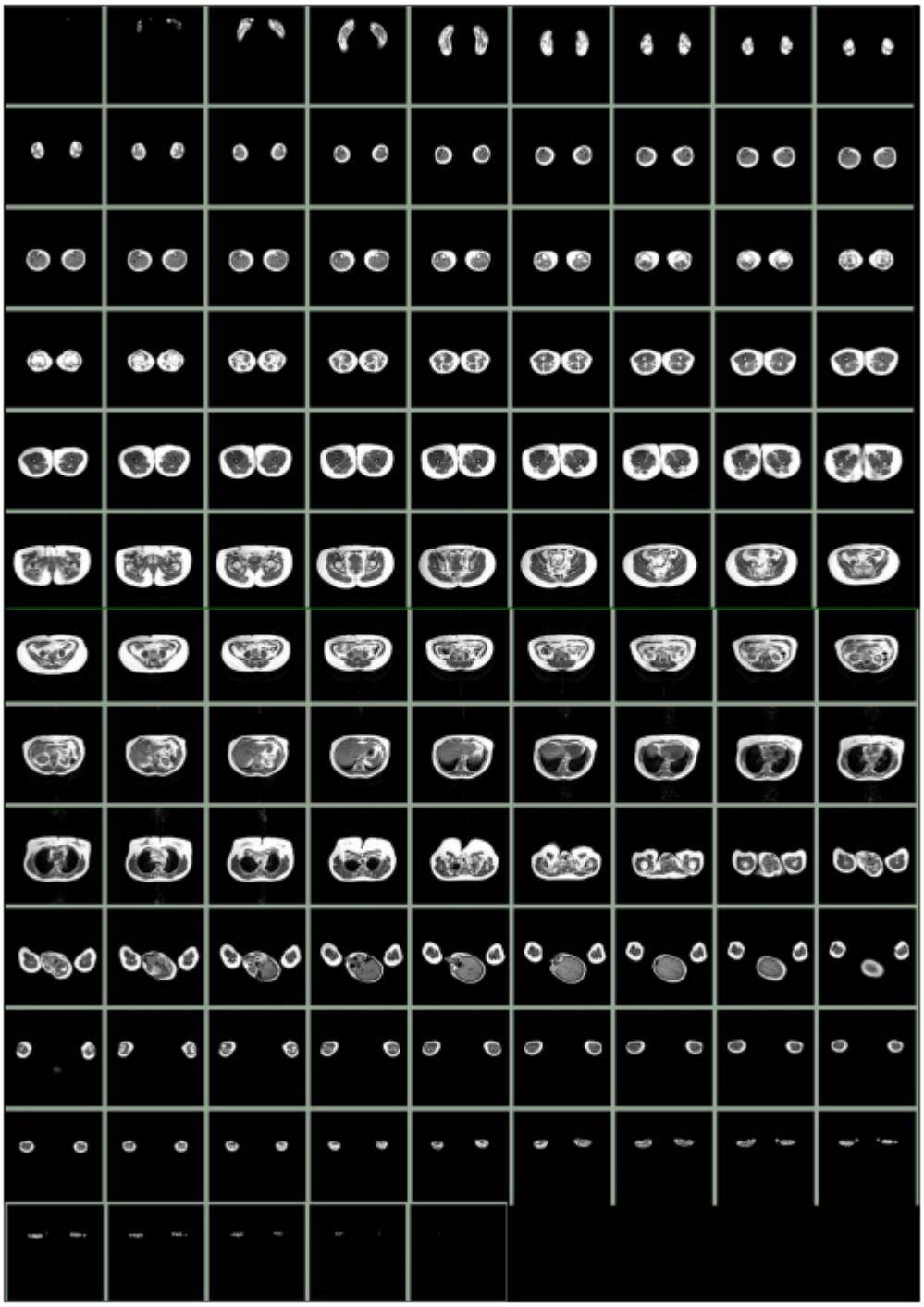

Fig. 4. Whole body MRI dataset from a healthy volunteer obtained at 1.5T. Fat appears as high intensity signal (white).

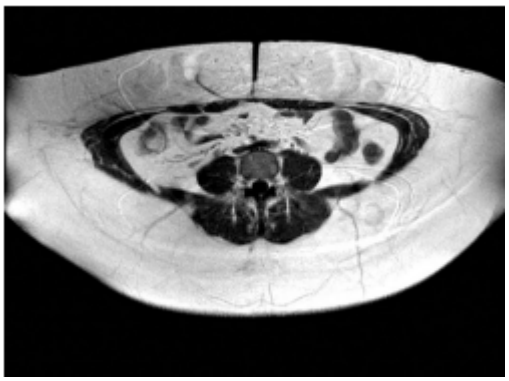

Fig. 5. Abdominal MR image from a volunteer too large to be fully imaged with a maximum available field-of-view of a standard 1.5T clinical scanner.

Abdominal MRI scanning

Several alternatives to whole-body imaging have been proposed, either to overcome the technical short-comings of scanners and/or to shorten examination/analysis time. These methodologies centred on acquiring images from the abdominal region of the body, which contains some of the main risk-factors associated with excess body adiposity, principally visceral adipose tissue and hepatic ectopic fat. As can be seen from Table 1, there is significant disparity in both the number of slices and the total abdominal area covered by these protocols. However, one can broadly group these protocols into two main approaches, multi-slice and single-slice acquisitions (Fig. 3).

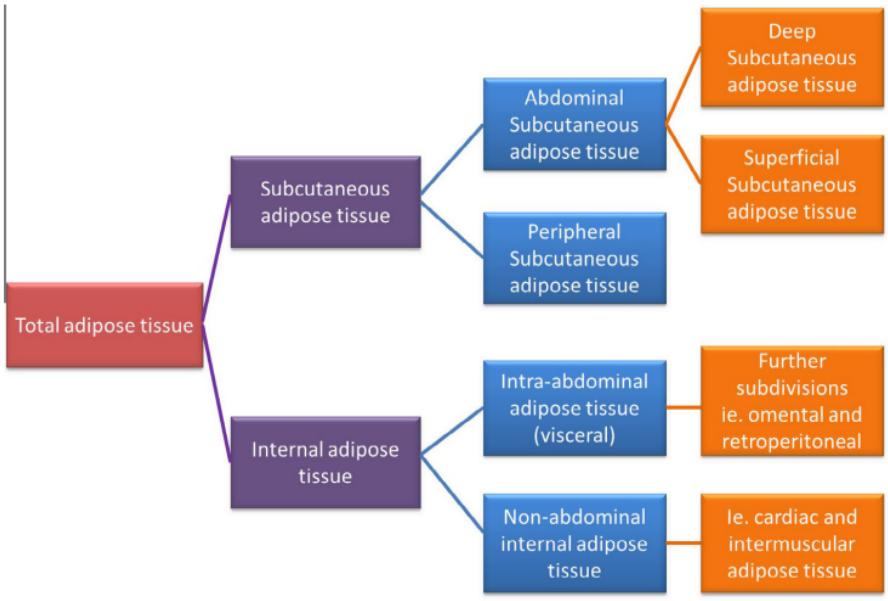

Fig. 6. Schematic showing adipose tissue measurements that can be made from a whole body MRI dataset.

Fig. 7. Coronal images allowing a qualitative assessment of adipose tissue deposition

Multi-slice abdominal MRI scanning

As the name points out, multi-slice protocols, applying similar MRI sequences to those utilised in whole-body scanning, aim to map part or the whole of the abdominal cavity. In general, these protocols use a variable number of slices, either contiguous or with fixed gaps, covering from the top of the liver down to the top of the head of the femoral bone (Fig. 3). These protocols are currently in use at many research centers as they have the advantage of being less time-consuming than whole-body imaging, requiring less time for scanning and data analysis, while still giving full information about abdominal adiposity. Recently, the multi-slice protocols have become the method of choice for large population studies, including biobanks. Often biobank phenotyping protocols require a large battery of detailed imaging procedures, including brain and cardiac anatomical and functional assessment, in addition to measures of abdominal and ectopic fat (usually liver); hence there is pressure to reduce scanning time, which abdominal imaging readily provides.

Single-slice MRI abdominal scanning

A number of studies have shown that there is a strong correlation between visceral adipose tissue measurements obtained from a single abdominal slice and total adipose tissue volume. This has led some groups to propose single-slice imaging as an alternative to both multi-slice and whole-body scanning for assessing abdominal adiposity. Several factors drive this trend, including cost of both scanner and analysis time. For example, it is possible to scan at least five volunteers with a single-slice protocol in the time it would take to obtain a whole-body dataset from a single individual. Moreover, given that image analysis can be extremely time consuming, a single slice reduces this to a bare minimum. However, this methodology is not without problems, not least the choice of anatomical landmark from which to acquire the single-slice image. This is not a minor issue as whole-body studies have shown that the distribution of adipose tissue within the abdominal cavity is highly heterogeneous [72,73]. The simplest proposed solution to this dilemma has been the use of the umbilicus, as this anatomical landmark can be easily located during patient positioning on the MR bed, without the need for pilot scans in coronal or sagittal planes. The main drawback with this approach is the fact that the relative position of the umbilicus differs considerably between subjects, especially in overweight and obese volunteers. More robust solutions have been investigated, including acquiring single-slice images at various vertebral landmarks, most notably at L4–L5, L3–L4, L2–L3, or at known distances away from these landmarks and comparing these with whole volume acquisitions [37,73–81]. The most commonly reported anatomical landmark for single-slice imaging tends to be at the level of L4–L5. However, while no complete consensus exists at present, and some authors state that a single slice at L4–L5 is a good predictor of the entire visceral adipose tissue depot [74,82], the majority of literature agrees that a slice 5–10 cm higher than L4–L5, close to L2–L3, is a preferable site [37,75,79–81]. However, the ability to predict total adipose tissue from a single-slice appears to vary, depending on gender and overall body adiposity, with different findings reported in lean and obese men and women [37,73,75]. Moreover, reliance on single-slice imaging can, in many circumstances, lead to an over- or underestimation of the true levels of visceral adipose tissue. This is of particular importance in weight loss/gain interventional studies, where adipose tissue reduction is known to be differentially affected across the abdominal cavity. For instance Thomas and colleagues showed a greater reduction in visceral adipose tissue at L2–L3 compared with L4–L5 in a cohort of overweight women following an exercise intervention [73]. Indeed, recent studies

have shown that changes in visceral adipose tissue cannot be predicted accurately using single-slice MRI, suggesting that multiple-slice protocols may be essential to detect such changes accurately [78,76]. Furthermore, using a multiple slice protocol in interventional studies over a single-slice approach significantly reduces the number of participants necessary to detect small changes [78]

Image Analysis

Image analysis is an important consideration when using MR techniques to assess body fat content and distribution. Indeed, in many cases it can become the bottleneck for large studies. From Table 1, it can see that there is considerable variation in not only the type of data obtained to measure adipose tissue content, but also in the way in which it is analysed. Whilst there are several commercially available packages, including Analyze (Mayo Clinic, Rochester, MN, USA), slice-O-matic™ (Tomovision, Montreal, Canada) NIH Image and ImageJ (National Institutes of Health, Bethesda, MD, USA), Hippo Fat™, and Matlab (The Mathworks, Inc.), many investigators use in-house written software, reflecting the growing need for a robust and reproducible automated method for adipose tissue analysis, particularly for large whole body datasets. Currently, the most used dedicated program is SliceOmatic (Tomovision, Montreal, Canada). The majority of analysis programmes work in two stages; the first step, a threshold, is determined manually or automatically based on the image intensity differences between adipose and lean tissues. Following this, the areas of SAT and VAT are delineated. More semi-automatic packages have additional refinements to assist the identification of adipose tissue including boundary enhancement, histogram-based region growing, clustering or mathematical morphology to define regions or pixels as fat or non-fat. There are also fully automated approaches [83,84] which have used a variety of methods incorporating various algorithms and masks. Some of these methods contain prior anatomical knowledge, but many of these still lack the ability to accurately differentiate between adipose tissue compartments, and to comprehensively exclude high signal from bone marrow, as well as motion-induced artefacts arising from peristalsis, respiration, and flow in lean and obese subjects [85–87]. Indeed, Bonekamp et al. identified approximately 16 different software packages, of which only five were available for testing since the others were either written in-house, discontinued, or part of the scanning software [87]. Since that paper was written there have been many publications reporting new automated methods, but in general these are not commercial and therefore not

readily available for testing. One of the main considerations when analysing adipose tissue images, particularly those from the chest or abdomen, is accurate identification of visceral fat. Fatty intestinal content, bone marrow, and artefact arising from motion will all produce pixels with a similar intensity to adipose tissue. Separating these out is essential, particularly in very lean individuals where they may contribute to a significant proportion of overall adipose tissue. The manual editing required for this form of process can introduce errors, unless the operator has sufficient expertise to identify and remove non-adipose signals. Some of these issues have led to the development and implementation of scanning protocols which attempt to minimise these factors, such as breath-hold, cardiac/respiratory gating, ultra-fast scanning of the abdomen and chest and/or scanning subjects in a prone position to minimise respiratory motion. An alternative approach is to obtain fat-only-images, which in theory should improve analysis accuracy. However, this can introduce its own uncertainty, due to lack of anatomical detail on images; hence a second anatomical dataset is sometimes included as an analysis reference.

Application of MRI measurement of adipose tissue

Since its initial development, the applications of MRI to measurements of adipose tissue content and distribution in relation to health and disease have been numerous. Whilst MRI is accepted as a gold standard methodology for measuring adipose tissue, its limitation as a field-based method for population studies and its relative cost precludes many investigators from using it in their research. Consequently, it often applied to validate and improve cheaper portable field methods of measuring body composition [88–92]. MRI has been used extensively to map unusual distributions of adipose tissue - this has been applied to populations of patients with HIV-related lipodystrophies [93], and acquired/congenital generalised and partial lipodystrophies [34,71]. It has been used to show reduced visceral adiposity in patients with Prader Willi Syndrome [94], and elevated visceral adiposity in women with Turner's syndrome [95,96], PCOS [32,97] and Cushing's disease [47]. Increased visceral adipose tissue has also been shown in adults and children with growth hormone deficiency; this has also been shown to reduce following therapy with growth hormone [30,95]. Several gene mutations and polymorphisms have been investigated, with some showing significant effects on adipose tissue distribution, and with others having little effect [98,99]. Other factors which have been shown to alter adipose tissue distribution include preterm birth. MRI has been applied to this population; it was found that the increased levels of visceral adipose tissue observed in infancy

persist into adulthood [100,101]. Numerous cross-sectional studies have used MRI to measure adipose tissue, reporting differences in both content and distribution as a result of age, gender, and ethnicity [31,102,103]. There have also been extensive studies measuring differences in adiposity between lean, overweight and obese populations. Changes in adipose tissue distribution have been described as a result of the menopause, which is thought to result in a preferential accumulation of visceral fat [104]. There have also been many interventional studies performed using MRI (for reviews see [104–106]), quantifying the impact of diet (restriction, overfeeding, composition modulation and supple mentation) and exercise [107–109]. Both long [110] and short term calorie restriction have been shown to result in loss of visceral adipose tissue [111], and overfeeding conversely causes an increase in this fat depot [112]. Changes in response to aerobic and resistance exercise have been compared, as well as gender differences in the response to an exercise programme, with men being shown to lose more visceral adipose tissue, but less subcutaneous adipose tissue in response to exercise than women [113]. Other interventions have been investigated; these include the effect of weight loss induced by drugs including orlistat, metformin, rosiglitazone, pioglitazone, and dexfenfluramine [114–117], as well as following obesity surgery [118]. Of particular interest is the trajectory of adipose tissue changes during weight gain or loss. Indeed, studies monitoring weight regain in women following anorexia nervosa show an interesting pattern of body fat redistribution with an initial increase in visceral adipose tissue, which does normalise with time [119]. There have also been extensive studies mapping depot-specific differences such as visceral compared to subcutaneous adipose tissues. Visceral fat is now recognised as a stronger and independent predictor of the metabolic syndrome compared with subcutaneous adipose tissue [120]. Similarly MRI has been used to unravel the inter-relationship between ‘deep’ and ‘superficial’ subcutaneous adipose tissue, gluteal and femoral subcutaneous adipose tissue, as well as regional differences within the visceral fat depot [121–127]. More recently, enhanced phenotyping methods have used MRI to classify subjects according to their adipose tissue distribution, and these have been shown to identify a number of sub-phenotypes in the general population whose metabolic risk factors are not proportionate with their overall size and adiposity (Fig. 8). There is mounting evidence to support the notion of ‘metabolically normal obesity’, in which subjects are metabolically healthy despite their substantially elevated body adiposity [128,129]. A similar phenotype is found in obese individuals described as ‘fat-fit’ [130]. In both of these groups MRI has been used to show that the metabolic ‘health’ is

related to fat distribution, in particular reduced visceral adipose tissue [7,7,120,128]. Conversely a phenotype has also been reported, in which normal-weight subjects have an elevated risk of metabolic disease, at odds with their apparently normal body size. This is commonly referred to as 'metabolically obese but normal-weight' [131]. Again this phenotype has been further refined using MRI to show a disproportionate accumulation of visceral fat in these individuals, now commonly referred to as TOFI (**T**hin **O**utside, **F**at **I**nside) [7,120,132].

Potential future areas of interest in MRI adipose tissue research

There are several topics that are receiving increasing attention within the research community, including the role of hypoxia and blood supply in adipose tissue function, detection of macrophage infiltration within adipose tissue, assessment of regional differences in fatty acid composition and mobilisation (fatty acid uptake and storage) and the development of fibrosis within adipose tissue. Whether there is the potential for MRI to inform these areas of research remains to be seen.

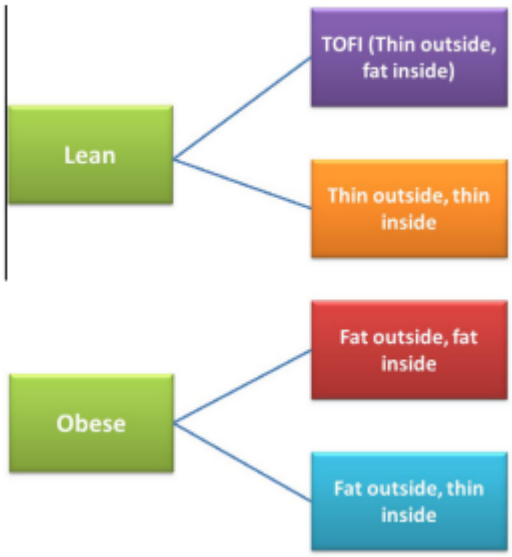

Fig. 8. Phenotypic variation in adipose tissue distribution.

Ectopic Fat

There is increasing interest in the potential role of ectopic fat in the development and impact of non-communicable disease. Ectopic, from Greek *ektopos* meaning out of position, refers to the storage of fat in non-adipose tissue depots such as skeletal muscle, liver, pancreas and

heart. The mechanisms by which ectopic fat accumulates are not fully understood, but one theory, the so called 'overflow hypothesis', suggests that under some circumstances adipocytes may lose their ability to expand to store excess energy, leading to an 'overspill' of triglycerides into other organs [133]. The implications of ectopic fat accumulation are considerable; ectopic fats are closely linked with the development of insulin resistance and the metabolic syndrome [134]. Until the advent of MR techniques, research into ectopic fat was somewhat limited by the need to obtain tissue biopsies, and although muscle (and sometime the liver) biopsies could be obtained for research purposes, research into ectopic fat accumulation in the heart and pancreas was clearly impractical. The development and application of MRI and MRS has resulted therefore in a significant increase in our understanding of the relationship between adipose tissue and various ectopic fat depots.

Techniques to measure ectopic fat

^{1}H MR spectropy-based methods

In *vivo* proton magnetic resonance spectroscopy (^{1}H MRS) is now routinely used to detect and quantify ectopic fat deposition in skeletal muscle (in the form of intra- and extra-myocellular lipids – IMCL and EMCL, respectively) [135–137] and liver (known as intra-hepatocellular lipid – IHCL) [138,139]. It is also used to measure both cardiac [140] and pancreatic [141] fat deposition. However, measurement of ectopic fat in these organs is more technically demanding, due to motion in the case of the heart, and its size and location in the case of the pancreas. As such, there are fewer publications regarding the non-invasive measurement of ectopic fat in these organs. Indeed, pancreatic fat assessment by MRS, although feasible, has been in part replaced by the use of MRI-based techniques, as these are less susceptible to contamination from surrounding adipose tissue signals. In most published studies of ectopic fat, the MRS localisation technique of choice appears to be the **PRESS** sequence (point-resolved-spectroscopy) developed in the early 1980s [142]. Some groups use a **STEAM** sequence (stimulated echo acquisition mode) instead, but this does tend to be more susceptible to motion, diffusion, and quantum effects (such as homonuclear coupling, which can result in difficulty in phasing and baseline correcting the spectra) and possibly a lower SNR [143]. An alternative MRS sequence used mainly in the liver is **Chemical Shift Imaging (CSI)** [144]. This allows spectra from across a 2D or 3D plane to be acquired in a single acquisition. In this sequence, the spatial location is phase-encoded with a spectrum recorded at each phase

encoding step. Multiple spectra from across the liver are collected, providing measurements of potential regional differences in ectopic fat deposition. Thus, as in *vivo* MRS allows for accurate and reproducible acquisition of metabolic data, in a localised and region specific manner, from almost any organ of the body, it has become the gold-standard for ectopic measurements in skeletal muscle, liver and heart.

MRI-based methods

An alternative to *in vivo* MRS for assessing ectopic fat is the use of MRI-based techniques. Recently, there have been an increasing number of publications, describing a variety of MRI–based sequences to measure liver fat deposition, exploiting the natural chemical shift differences between fat and water [145–149]. While the MRS-based techniques limit themselves mainly to single voxel [150] these methods allow for very high resolution assessment of regional variations of fat content. However, it should be mentioned that these techniques do involve the use of breath-holds during the scan, which may not be appropriate for many patient groups. It remains to be seen whether in future these techniques will be equally or more prevalently used than MRS. MRI-based techniques to assess ectopic fat fall broadly into two categories: those based on differences in the signal phase of fat and water, and those that make use of the chemical shift differences between the fat and water resonances, allowing for selective saturation of resonances. The former tend to be based on the so-called ‘‘**DIXON**’’ sequences, which are sequences designed to generate images containing only fat or water [151]. To achieve this separation, images are acquired in which the signals from fat and water are both ‘‘in phase’’ and ‘‘out of phase’’, subtracted and summed, resulting in water- and fat-only images. In this way fat content of any tissue can be readily measured. Typical water-only and fat-only images obtained with a DIXON-based technique can be seen in Fig. 9. The original sequence, referred to as a ‘two-point DIXON’, has since evolved to include a third echo, which helps to overcome some of the problems associated with field inhomogeneities [152,153]. The term ‘DIXON’ is now commonly used to encompass all chemical-shift based sequences to obtain separate water and fat images. These methods are today used both for obtaining fat-only images to quantify adipose tissue, as well as for detecting ectopic fat accumulation, principally in the liver. A further refinement of the DIXON technique is the so-called ‘**3D IDEAL’** (Iterative Decomposition with Echo Asymmetry and Least squares estimation) imaging and reconstruction method [153]. The advantage of this method is the fact that the data is obtained

as a volume, and is therefore more representative of the organ under investigation. It has also been reported to result in improved fat-to-water ratios, by correcting for transverse relaxation, as well as intravoxel dephasing, and can overcome field inhomogeneity problems. Its measurement of liver fat content has been reported to be comparable with ^{1}H MRS. However, it does requires prior knowledge of the chemical-shift spectral frequency and amplitude, which are measured in subcutaneous adipose tissue and then applied to the measurement of ectopic organ fat [147]. Significant differences in the fatty acid composition between different fat depots could therefore be a potential source of error. More recently, a **multi-echo (ME) MRI** sequence has been developed and applied to measure ectopic fat, reportedly being more accurate and robust than the DIXON-based methods, while at the same time providing an accurate measurement of T^*_2 [149]. This method has been most commonly applied in the liver and pancreas. It has the advantage over single voxel MRS in that regional differences in ectopic fat distribution can be measured. Furthermore, it is often possible to obtain a single slice containing the liver and pancreas, allowing simultaneous measurement of fat within two separate organs (see Fig. 10), thereby considerably reducing scanning time. A further benefit of using this method is the T^*_2 value; since changes in T^*_2 are indicative of elevated iron content, it provides a useful and clinically relevant additional measurement [154]. Thus, from the many images normally obtained with the ME sequence, decay curves are generated which show the change in signal intensity at each of the acquired echo times. In tissues containing lipid and water, there will be oscillation in signal intensity as a function of echo time. At some echo times the fat and water signals are in phase (higher signal) and at others they are out of phase (lower signal), this gives rise to the oscillations in the decay curve. An organ with very little fat infiltration will generate a very smooth decay curve (without obvious oscillations in the decay), whereas one containing a higher level of fat shows significant oscillations throughout the decay. From these data, 'heat-maps' can be generated to visualise regional differences in fat deposition. For instance, Fig. 10 shows the heat maps from four individuals with varying levels of fat in their liver and pancreas. Clearly, this kind of resolution in regional fat distribution could not be achieved by the use of MRS sequences. In addition, the use of multi-slice acquisition allows researchers to map fat content across the entire liver. An example of this can be seen in Fig. 11, which shows the large variation in fat throughout the entire liver of a volunteer.

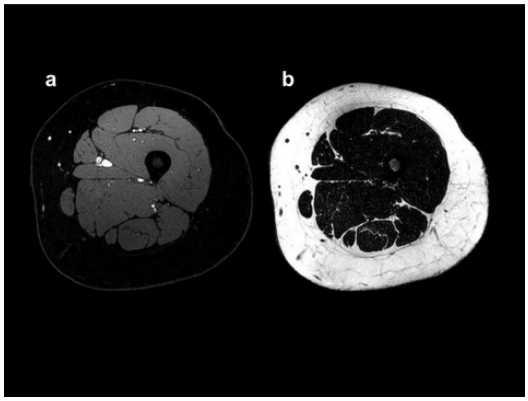

Fig. 9. Water (a) and fat (b) only MR images of the thigh of an overweight volunteer

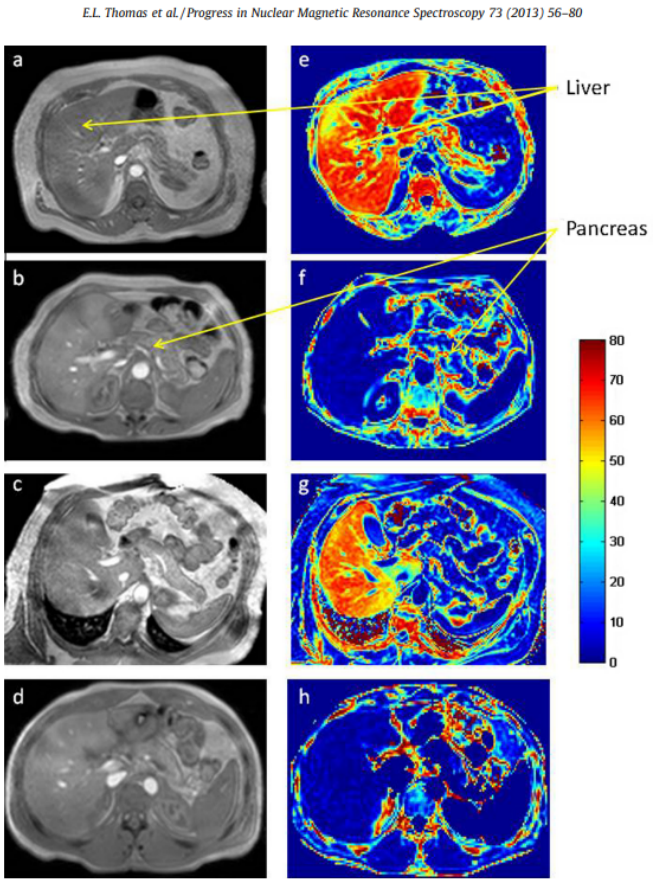

Fig. 10. A series of multi-echo (a–d) and corresponding heat-map images (e–f) from four volunteers with varying levels of ectopic fat in both the liver and pancreas. A scale reflecting fat content from blue (low) to red (high) is also shown. Images (a) + (e) show high liver and high pancreatic fat. Images (b) + (f) show low liver and with fat infiltrating into the pancreas. Images (c) + (g) show high liver and low pancreatic fat. Images (d) + (h) show

low liver and low pancreatic fat. The heat-map values were localised to the liver, hence the lack of relationship between the levels of fat in the adipose tissue and its colour. (For interpretation of the references to colour in this figure legend, the reader is referred to the web version of this article.)

Ectopic fat in skeletal muscle

The relationship between elevated triglyceride within muscle cells (known as intra-myocellular lipids or IMCL) and insulin resistance was initially established using muscle biopsies or ex-vivo tissue samples, in combination with electron microscopy and oil staining [155]. Elevated IMCL have been observed in diabetes and are inversely related to insulin action [156,157]. This area of research was changed completely in 1993, when Schick and colleagues demonstrated that it was possible to differentiate between triglycerides stored within muscle cells (IMCL) and the inter-muscular adipose tissue stored between muscle cells (referred to in the MRS community as extra-myocellular lipids or EMCL) using *in vivo* ^{1}H MRS [135]. A typical MRS spectrum obtained from the soleus muscle of a healthy volunteer can be seen in Fig. 12. Resonances arising from IMCL, EMCL, total creatine and choline-containing groups can be readily observed. Most studies using ^{1}H MRS to measure IMCL use a PRESS sequence with a voxel size ranging from 1.8 to 8 cm^{3}. A minority have used CSI, which enables simultaneous acquisition of multiple small voxels (MRSI) [158,159]. Most work has been published at 1.5T, but there are studies at 3T [160], 4T [161] and 7T [162]. Measurements are commonly made in the muscles of the lower calf – soleus, tibialis and occasionally, the gastrocnemius muscle. This differs from most biopsy studies where measurements are usually taken from the vastus lateralis located in the thigh. This is mainly due to practical scanning considerations rather than specific scientific reasons. However, there have additionally been reports of IMCL measurements by ^{1}H MRS in the thigh, arms [163], psoas [164] and paraspinal muscles [165]. As can be seen in Fig. 12, despite the fact that the four separate resonances arising from IMCL and EMCL can be readily observed, there is a significant degree of overlap between the four peaks. This can be an issue for analysis, necessitating the use of software with a degree of sophistication, generally requiring a degree of prior knowledge to accurately fit the peaks. This overlap can be more of a problem in

subjects with elevated EMCL, which increases as a result of aging, as well as in conditions including obesity, diabetes and also in patients with muscle disease such as polymyositis. Interestingly, it has been reported that the separation between the IMCL and EMCL resonances is muscle-dependent. This appears to be related to the alignment of muscle fibres, the greater the number of fibres in the muscle running parallel to the magnetic field, the greater the separation between peaks. In the tibialis, where the fibres are mostly parallel, the separation between IMCL and EMCL signals is greater than in the soleus muscle where the fibres are found in a more oblique orientation [136]. While there have been a few publications that measured absolute concentrations of IMCL, expressing results in mmol/kg wet weight, most studies present the IMCL data either as a ratio or as a percentage of the total water or creatine in the spectrum. The development of *in vivo* ^{1}H MRS has made it possible to study many different patient groups, as well as paediatric populations, and has also enabled longitudinal and interventional studies that would not have been possible using a biopsy approach. IMCL levels have been shown to vary according to muscle fibre type, with the highest levels found in oxidative muscles (such as the soleus muscle) and lower levels in glycolytic muscles (such as the tibialis muscle) [158,166]. IMCL levels have also been shown to be elevated in obesity [167] and reduced following weight loss [168,169]. The earlier observations of the relationship between IMCL and insulin resistance were confirmed [170–172], and it was proposed that the composition, not just the overall amount of triglyceride present may be a factor in the development of insulin resistance [173]. However, the relationship between IMCL and insulin resistance is by no means clear cut. For instance there have been reports of populations in whom there is a disassociation between insulin sensitivity and IMCL levels, for example populations of South Asian origin [174] or low birth weight subjects [175]. Furthermore it is possible to manipulate insulin sensitivity, independent of changes in IMCL [176] and several groups have reported that endurance trained athletes have high IMCL levels, despite high insulin sensitivity [177–179]. While trained athletes rapidly deplete their IMCL reserves during endurance exercise [180], there is evidence to suggest that IMCL can be increased following moderate exercise training [181]. It is thought that the muscles of endurance trained athletes possess a high oxidative capacity, enabling efficient use of IMCL as an energy source during exercise. This apparent contradiction has necessitated a rethink regarding whether elevated IMCL actually causes insulin resistance, or is a secondary effect [182]. Further research will be needed to unravel this complex relationship. More

recently, diffusion weighted imaging has been proposed as a potential method to differentiate between IMCL and EMCL in vivo, based on the observation that EMCL has a higher apparent diffusion coefficient compared with IMCL. As yet these are just *ex vivo* and animal studies, but it will be interesting to see this approach find significant application in human research [183]. MRI has also been used to measure muscle fat infiltration. As previously mentioned, Gallagher et al. have measured total body IMAT (also known as EMCL) using whole body MRI. Multi-echo imaging has also been used to measure muscle fat content [184]. However, with current technology MRI is unable to fully differentiate IMCL and EMCL; as such MRS will continue to be regarded as the technique of choice in this area of research.

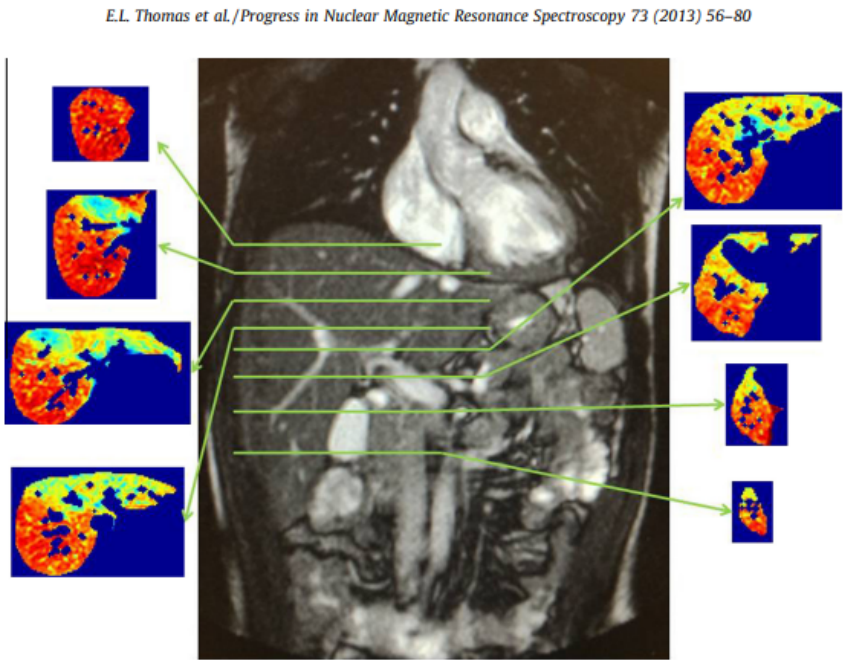

Fig. 11. Heat maps generated from multi-echo images acquired at various positions throughout the liver showing variations in hepatic fat content.

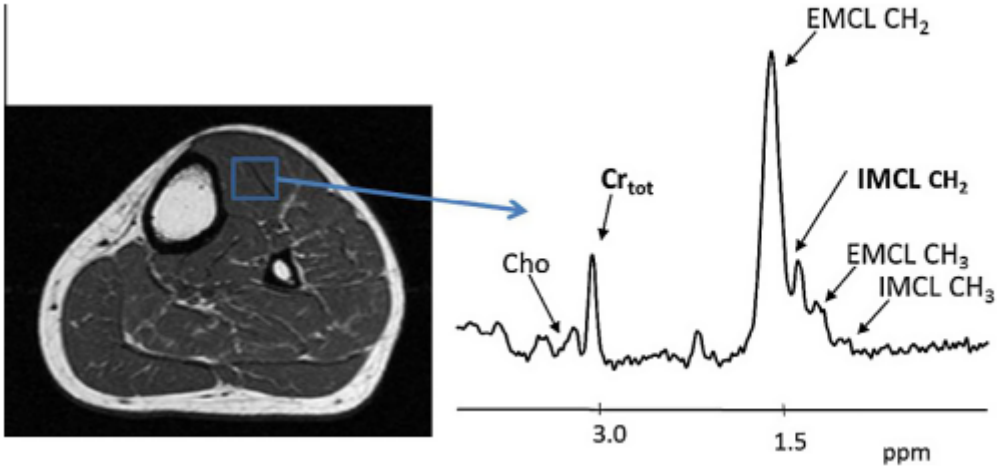

Fig. 12. Calf image and resulting ¹ H MR spectrum from a 2 x 2 x 2 cm³ PRESS voxel positioned in the tibialis muscle. Resonances from choline (Cho), total Creatine (comprising both creatine and phosphocreatine) (Cr_{tot}), and the CH_2 and CH_3 parts of the triglyceride for both EMCL and IMCL can be identified. IMCL content is calculated as the ratio of IMCL to Cr.

Ectopic fat in the liver

The study of fat deposition in the liver has a considerably long history, and indeed even some of Leonardo Da Vinci's drawings depict fatty liver. Many studies in the past have demonstrated that fat accumulates in the liver following excessive alcohol intake, and as a consequence of obesity and diabetes [185–187]. Ectopic fat deposited within the liver is commonly referred to as non-alcoholic fatty liver disease (NAFLD) or non-alcoholic steatohepatitis [188]. However, despite its long clinical history, NAFLD was, until relatively recently, considered as a relatively benign condition. It is now understood that excess fat deposited in the liver can cause hepatic inflammation, which in some individuals leads to fibrosis, which may in turn slowly progress to cirrhosis and may ultimately result in hepatocellular carcinoma [189,190]. Moreover ectopic liver fat has been, more recently, closely and independently associated with insulin resistance [191,192], a key stage in the subsequent development of type II diabetes. Thus, understanding the mechanism by which hepatic fat accumulates, and developing effective strategies to reduce it, is critically important, given that NAFLD prevalence is estimated at 30–40% in the US population, for example [139]. In addition to needle-biopsy which had been regularly used in

a clinical setting, there are a wide variety of non-invasive techniques to detect and quantify fat infiltration in the liver, including ultrasound, CT and MRI [193,194]. Ultrasound is perhaps the most frequently used, particularly in a clinical setting as it is cheap and widely available. However, it tends not to be quantitative and levels of fat infiltration are somewhat subjectively classified as absent, mild, moderate or severe [194]. CT indirectly assess liver fat content by measuring the ratio of liver density to that of the spleen, but the associated radiation somewhat limits its longitudinal application and use in paediatric studies. In the research setting, ^{1}H MRS measurement of hepatic fat content is becoming increasingly routine and widespread. Quantitative MRI measurement of hepatic fat is also becoming more common, with a wide variety of sequences available; for reviews of the different available methods see [145–148]. The practical details for the ^{1}H MRS of liver are quite similar to those discussed previously for muscle. Again, the vast majority of studies have been performed at 1.5T using a PRESS sequence, although some groups use chemical shift imaging, which allows regional changes to be observed across the liver, without the need to acquire repeated PRESS voxels. Fig. 13 shows typical spectra from subjects with low and high fat infiltration in the liver. A 2 x 2 x 2 cm^3 voxel is carefully positioned in the liver avoiding obvious blood vessels, fatty tissue and the gall bladder. The resulting spectrum contains resonances arising from water at 4.7 ppm, and the CH_2 and CH_3 parts of the triglyceride backbone at 1.3 and 0.9 ppm respectively. Liver fat data obtained by ^{1}H MRS are normally presented as a ratio or as a percentage of the total water in the spectrum, although some authors present liver fat in mmol/kg, assuming a hepatic water content of 71.1%. There are a variety of approaches to calculating this ratio, and as a result levels of IHCL may vary between different papers depending on the formula used. The most commonly used are described below:

i	ii	iii
$\frac{CH_2}{water}$	$\frac{CH_2}{Water+CH_2}$	$\frac{CH_2+CH_3}{Water+CH_2+CH_3}$

Most researchers use one of the above methods; others do not separate the CH_2 from CH_3 signal and present IHCL as fat/water ratio or the (fat/water + fat) ratio. At low levels of fat deposition the various methods produce similar results, but at higher levels of fat infiltration there can be considerable differences. For instance using the three different approaches, a very low fat infiltration would result in IHCL values (i) 0.71%, (ii) 0.70%, (iii) 0.81%; moderate fat

infiltration (i) 14.28%, (ii) 12.00%, (iii) 12.82%; and finally high fat infiltration (i) 56.72%, (ii) 32.33%, (iii) 34.77%. In essence, this is only an issue when comparing data from different research groups. The validation and application of ^{1}H MRS to assess ectopic fat in the liver has been extensively reviewed [120,146,195]. Liver fat has been shown to be a key risk factor for the development of insulin resistance and type-2 diabetes [35,196]. We now know, through this in vivo work, that liver fat is increased in conditions including obesity [138], type-2 diabetes [197], polycystic ovarian syndrome (PCOS) [32], and Turner's syndrome [96], as well as being modulated by age [7,198], diet [199,200], physical activity and fitness [8,199,201–203], and gender with women having reduced levels of liver fat compared with men [7,204]. It also varies between different ethnic groups with individuals of Afro-Caribbean origin having lower levels, compared to Caucasian or Hispanic populations [205,206]. Ectopic liver fat is also elevated in congenital partial and generalised lipodystrophy, as well as antiretroviral therapy-associated lipodystrophy, found in some treated HIV patients [207,208]. Furthermore, leptin replacement has been shown to reduce liver fat content in subjects with lipodystrophy [209,210]. Preterm birth has been shown to result in elevated liver fat in infancy, which persists into adulthood [211,100]. Elevated liver fat has consistently been shown to be effectively reduced following lifestyle interventions, which generally involve moderate calorie restriction and increased physical activity [169,212,213]. Liver fat has also been shown to be reduced using ^{1}H MRS following treatment with rosiglitazone [214], pioglitazone [215], metformin [216] and orlistat [116], as well as following weight loss induced by bariatric surgery [217]. While the development of ^{1}H MRS and its application to the study of liver fat has greatly increased the knowledge of the relationship between liver fat and other adipose tissue depots, and how levels can be modulated by various interventions, our understanding of this depot is still far from complete. Further technical development and applications are essential, particularly if we are to be able to differentiate non-invasively between those with 'benign' fatty infiltration and those with fatty infiltration that progresses to irreversible liver disease and established cirrhosis

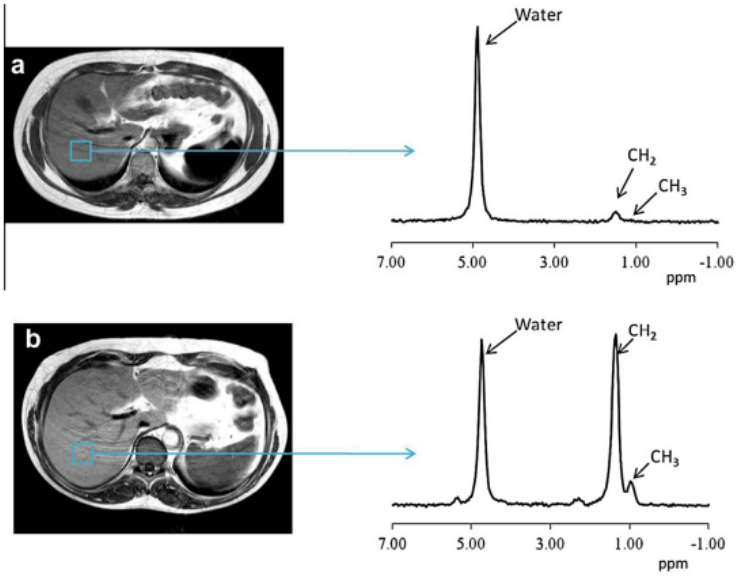

Fig. 13. Transverse image showing location of a 2 x 2 x 2 cm³ PRESS voxel positioned within the liver and corresponding ¹H MR spectra from volunteers with (a) low and (b) high levels of fat infiltration. Resonances can be seen arising from water, and the CH_2 and CH_3 parts of the triglyceride for hepatic fat. IHCL content is calculated as the ratio of CH_2 to water.

Ectopic fat in the pancreas

The pancreas has a dual function being both an endocrine and exocrine organ. Digestive enzymes are secreted into the small intestine by the exocrine portion to aid digestion. The endocrine portion of the pancreas is made up of clusters of cells called islets of Langerhans, distributed throughout the pancreas. There are four main types, classified by their secretions. The β cells are of particular interest, since they secrete insulin and are intimately involved with glucose homeostasis. It has been suggested that ectopic accumulation of triglycerides in pancreatic islets causes β-cell dysfunction, leading to pancreatic lipotoxicity [218–220], although it is unclear whether this is a direct consequence of triglyceride accumulation or a consequence of high levels of circulating lipids. These unresolved questions have driven the development of non-invasive techniques to study the pancreas. Until relatively recently, most studies have required *ex-vivo* tissue, cell cultures or rodent models, mainly due to the difficulty in assessing pancreatic fat *in vivo*. Needle biopsies are not practical due to the associated risk of developing pancreatitis. Ultrasound and CT have been applied to detect the presence of pancreatic steatosis, but as in the liver, this tends to be non-quantitative and is often regarded as a subjective measurement. Pancreatic fat was first measured non-invasively using ¹H MRS

by Tushuizen and colleagues in 2007; they showed that pancreatic fat content was elevated in subjects with type-2 diabetes, and that it was inversely associated with β-cell function [220]. Lingvay et al. comprehensively validated the use of ^{1}H MRS to quantify pancreatic triglyceride against biochemical measurements in rodents [141]. Furthermore, they demonstrated the reproducibility of the method in humans and showed in a relatively large cohort of subjects that pancreatic steatosis increases with BMI and impaired glycaemia. In a relatively short period of time, several other groups published studies using ^{1}H MRS to measure pancreatic fat content and were able to demonstrate that pancreatic fat content is related to both insulin resistance and liver fat content [203,221]. However, ^{1}H MRS of the pancreas is far more challenging, compared to ^{1}H MRS of the liver, due to the size, shape and location of the former. In some individuals, the pancreas has a smooth and well-defined shape, allowing relatively easy positioning of the voxel within the organ. However, in others, the pancreas has a more fragmented appearance, with the surrounding adipose tissue appearing to infiltrate the organ (Fig. 14). Positioning even a small voxel within the pancreas with this presentation is problematic, since the resulting spectra carry a risk of contamination from the surrounding adipose tissue. This has been one of the main factors that have driven development of MRI to quantitate pancreatic steatosis. Schwenzer and colleagues have extensively compared in/out-of phase sequences with spectral-spatial excitation imaging sequences [222], finding that both provided reliable estimates of pancreatic fat content, though it was more likely that fat-selective spectral-spatial methods would be utilised clinically, since they required fewer additional corrections to quantify fat content. In our own experience, we find excellent correlation between ^{1}H MRS and multi-echo imaging techniques, but since multi-echo avoids contamination from surrounding visceral adipose tissue, we find that it leads to a more successful examination in many cases. A further advantage of quantitative imaging methods is that regional variation in fat deposition throughout the pancreas can be measured using a single sequence. This appears to be particularly important in the pancreas since some studies have reported the pancreatic head contains less fat than the body and tail [222]. However, other studies have reported no regional variation [223]. Indeed, many of the recent papers measuring pancreatic fat content have used MRI-based methods [150,224–229]. Interestingly, in some publications liver fat is often measured using ^{1}H MRS, despite pancreatic fat being measured by MRI [224]. These studies have shown that pancreatic fat content increases with age [222,226] and can be predicted by visceral adipose tissue content

[226,228]. It has also been shown that there are ethnic differences in pancreatic fat content, with higher levels reported in Hispanic compared with African American subjects [226]. Furthermore, it has been shown that pancreatic fat can be reduced following a period of dietary restriction, which also resulted in normalisation of β -cell function [225]. Some studies have reported a significant correlation between hepatic and pancreatic fat content [226,227], while others have found no relationship between ectopic fat in these two organs [222,229]. Compared to other organs, non-invasive measurement of ectopic fat in the pancreas is very much in its infancy. However, this is a very rapidly expanding area of research, and it is likely that our understanding of fat in the pancreas and its consequences will increase substantially.

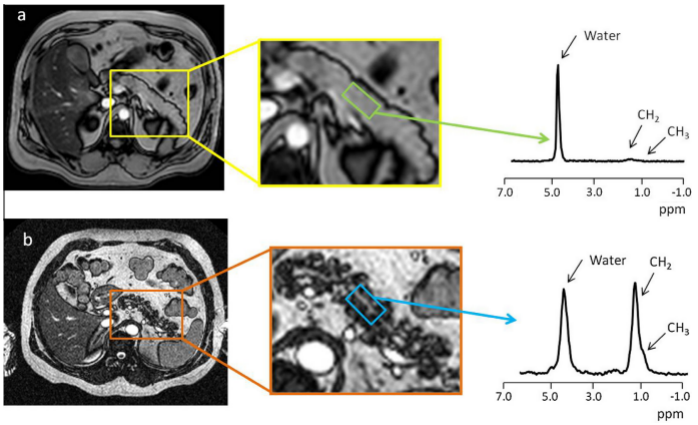

Fig. 14. Images through the abdomen showing the appearance of the pancreas in two individuals. Subject (a) has a well defined pancreas, as can be clearly seen in the expanded image with well-d4efined boundaries, in whom pancreatic spectra showing a low level of fat infiltration can be reproducibly obtained. Subjects (b) has an extremely irregularly shaped pancreas, making voxel placement difficult, the resulting spectrum has a high level fat as seen by the larger CH_2 resonance. It is difficult to be certain whether all or only some of this fat arises from ectopic fat within the pancreas.

Ectopic fat in the heart

Fat can be deposited and stored in several locations in and around the heart as intramyocardial, pericardial, epicardial, and paracardial adipose tissue (also referred to as mediastinal adipose tissue]. Adipose tissue in this location is essentially found on the epicardial surface, where it is in direct contact with the myocardium and vessels and serves as a source of energy. There is,

however, some degree of debate regarding the exact classification of each of these depots which seems in part to relate to the methodology used to measure these fat depots. Some authors describe pericardial and epicardial adipose tissue as distinctly different depots, with differences in adipocyte size and metabolism [230]. Others suggest that pericardial adipose tissue is the sum of both the epicardial and paracardial fat depots [231]. The different types of fat accumulation within the heart were described in detail by Richard Quain in an extensive article in 1850 [232]. Initial studies were conducted post-mortem, but the advent of fluoroscopy, which employs X-rays to obtain real-time moving images of the heart, enabled non-invasive studies to be conducted allowing the pericardial fat pad to be studied in living subjects [233,234]. More recently, echocardiography and CT and MRI have been used to measure this depot. The adipose tissue deposited around the heart has been shown to increase with age and level of obesity, in particular visceral adipose tissue content [235]. It is also increased in patients with diabetes and obstructive coronary artery disease. Fat is also found in other areas of the heart. Indeed, there are two different patterns of myocardial triglyceride deposition: the first involves infiltration of adipocytes, usually in the right ventricle interspersed between myocardial fibres, similar to the EMCL in skeletal muscle. Triglycerides also accumulate within the cytosol of cardiac myocytes. Here, their presence is referred to as 'cardiac steatosis'. Until the advent of ^{1}H MRS, this was only measurable at post-mortem or from biopsy samples. ^{1}H MRS has been used by several research groups to measure this steatosis [140,236–240]. ^{1}H MRS of the heart is technically more challenging than a similar acquisition in the liver or skeletal muscle, due to cardiac and respiratory motion, both of which have a significant impact on both shimming and water suppression. Spectral quality may be further compounded by the presence of epicardial fat which can cause spectral contamination. However, these difficulties may be overcome using cardiac and respiration triggering and gating [140,236]. Indeed, Felblinger et al. compared the effects of breath-hold vs combined ECG and respiratory gating, and they found spectral quality and reproducibility to be significantly improved using cardiac triggering [238]. More recent studies have combined ECG triggering with respiratory navigator echo–based motion compensation, which have been reported to reduce spectral linewidth, thereby improving spectral resolution and reproducibility [240]. ^{1}H MR spectra are generally obtained using a PRESS sequence with the voxel positioned within the septum of the heart (Fig. 15). Using ^{1}H MRS to measure myocardial fat, it has been shown that triglycerides can be detected within the cardiac myocytes of even very lean individuals, and in overweight subjects

in whom cardiac triglyceride levels are elevated. This fat depot is closely related to increased left ventricular mass [140]. Kankaanpää et al. have shown that cardiac triglycerides are elevated in obese compared with lean men [239,240]. However, the functional relevance of cardiac triglyceride accumulation is still unclear, in part due to the small number of papers published in this area. While cardiac triglycerides appear to be elevated in obesity, particularly in relation to visceral adipose tissue, no significant relationship between cardiac triglycerides and BMI or percentage body fat has been observed [235,242,243]. Furthermore, Gaborit et al. recently showed that while both cardiac triglycerides and epicardial adipose tissue were elevated in obese subjects, only epicardial adipose tissue was elevated in obese diabetic subjects, compared to obese non-diabetic subjects [241]. Furthermore, these authors also found that only the presence of epicardial adipose tissue was related to glucose tolerance, but they did find that cardiac triglycerides were independently associated with ventricular stroke volume, suggesting a specific interaction between cardiac steatosis and cardiac function [241]. There have been several interventional studies looking at the effect of dietary restriction, exercise, bariatric surgery and drugs on cardiac triglyceride content with conflicting results. Several papers have shown that cardiac triglyceride content can be reduced following a very low calorie diet [244] or exercise training in healthy overweight subjects [245]. Interestingly, the same group found that a similar exercise program did not reduce cardiac triglyceride content in patients with type-2 diabetes, despite improvements in cardiac function [246]. However, treatment with pioglitazone, which has been shown to reduce hepatic fat, did not affect cardiac steatosis [247]. Similarly, starvation studies have been shown to reduce hepatic steatosis while increasing cardiac steatosis [248]. Furthermore, weight loss following bariatric surgery has been shown to significantly decrease adiposity, particularly visceral adipose tissue and epicardial adipose tissue as well as hepatic fat content whilst having no effect on cardiac triglyceride content [249]. While there appear to be some contradictions in the published literature, overall these findings do indicate that the regulation of ectopic fat depots is organ-specific and that further studies are required to increase our understanding of the relevance of cardiac triglycerides and their relationship to adiposity.

Bone marrow

In addition to adipose tissue and ectopic fat, a significant quantity of fat is stored in the body in the form of bone marrow. The body contains two types of bone marrow: red bone marrow

consisting of hematopoietic cells, responsible for production of blood cells (this tends to be found in 'flat' bones such as the pelvis, sternum, ribs, and vertebrae); and yellow bone marrow, found mainly in the middle of long bones, and composed primarily of adipocytes. At birth, all bone marrow is red; the fat content of bone marrow progressively increases with age [250] and is considered to be a normal part of skeletal maturation and ageing. By adulthood almost 50% of bone marrow will have become yellow bone marrow. MRI and MRS have both been applied to measure the content, composition and distribution of bone marrow. Most studies have obtained PRESS spectra from the hematopoietic bone marrow located in the vertebral bodies. MRS has been proposed as a method of monitoring changes in response to treatment, as well as an aid to diagnosis in conditions including leukaemia, lymphoma, and plasmocytoma [251–253]. Changes in both the relative ratios of the lipid and water resonances, as well as the peak lineshapes and relaxation properties have been reported using ^{1}H MRS, following treatment for leukaemia and bone marrow transplant. Furthermore, age-related changes in bone marrow have been confirmed non-invasively using ^{1}H MRS [254–256]. Gender differences have also been reported with males having a higher bone marrow fat content compared with female subjects [255,256]; however this difference is reversed in older subjects (>60 years age) [257]. Bone marrow fat content has also been shown to increase with decreasing bone mineral density, making bone marrow fat content a potentially useful marker of osteoporosis [255,258–260]. Interestingly, Baum et al. have shown regional variation with bone mineral density decrease from L1 to L3, accompanied by a corresponding increase in bone marrow fat content [261] The composition of the fatty acids within the bone marrow may also be important; subjects with type-2 diabetes appear to have lower levels of unsaturated fatty acids within their vertebral bone marrow, compared to healthy controls [261]. The fat content of bone marrow has also been related to other adipose tissue depots, particularly visceral adipose tissue. Several authors have reported that subjects with a greater proportion of fat in their bone marrow have higher levels of visceral adipose tissue [258]. This may be an important finding, since previous studies have found a negative association between visceral adipose tissue and bone mineral density [262]. As well as measuring the fat content of bone marrow by MRS, the whole-body bone marrow volume has been measured using MRI. From these studies, it has been estimated that bone marrow comprises up to 7% of total adipose tissue [262]. However, these studies found no relationship between bone marrow volume and overall adiposity. Indeed, there are several indications that bone marrow does not function as a typical adipose tissue depot, one of which

being the paradoxical increase in bone marrow fat content following a period of starvation and also in anorexia [263].

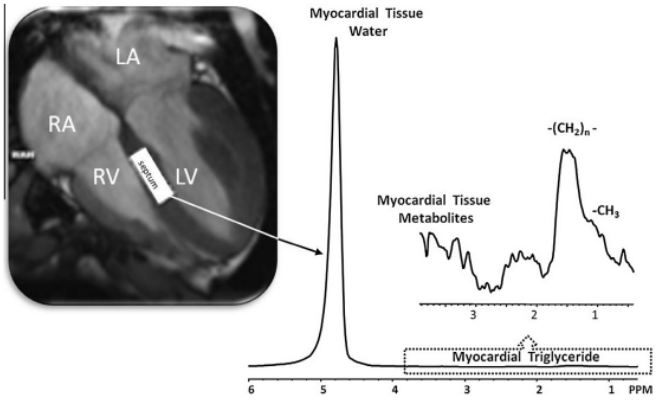

*Fig. 15. Image of the heart showing voxel positioned within the ventricular septum of the myocardium. The spectrum was collected using PRESS sequence on a Siemens Verio 3T system with PACE for breathing motion compensation in concert with near end of systole of the heart cycle. (Tr = 4s, Te = 40 ms, NA = 32, voxel = 8 * 18 * 26 mm). (Figure kindly supplied by Dr. L. Szczepaniak, Biomedical Imaging Research Institute of Cedars-Sinai Medical Centre.*

Conclusion

In conclusion, MRI and MRS have become the gold-standards for assessing body fat content and distribution. A variety of MRI sequences and scanning protocols are currently in use to determine the total and regional quantities of adipose tissue in human volunteers. The results from these studies point to the importance of abdominal adiposity in the development of non-transmittable diseases, including insulin resistance and type II diabetes. Ectopic fat, especially in liver and pancreas, appears to be another important independent risk factor for these disorders [264]. With the advent of *in vivo* MRS and fat-specific MRI sequences, this field of research is rapidly progressing as it no longer requires the use of needle biopsies to determine levels of fat infiltration in these and other organs. The use of MR-based techniques to measure adiposity is becoming increasingly common and is being utilised to assess body fat content and distribution *in utero*, at birth, during childhood as well as in the later stages of life, helping us to transform the way we view the function of this complex, yet essential, organ, adipose tissue.

Acknowledgments

All authors are grateful to the NIHR Biomedical Facility at Imperial College London for infrastructure support and the UK MRC for funding.

References

1. T. Scully, Diabetes in numbers, Nature 485 (2012) S2–S3.

2. A.D. Lopez, C.D. Mathers, M. Ezzati, D.T. Jamison, C.J.L. Murray, Global Burden of Disease and Risk Factors, World Bank, Washington, DC, 2006.

3. S. Cinti, The adipose organ at a glance, Dis. Model Mech. 5 (2012) 588–594.

4. N. Ouchi, J.L. Parker, J.J. Lugus, K. Walsh, Adipokines in inflammation and metabolic disease, Nat. Rev. Immunol. 11 (2011) 85–97.

5. A.H. Berg, P.E. Scherer, Adipose tissue, inflammation, and cardiovascular disease, Circ. Res. 96 (2005) 939–949.

6. M.J. Müller, M. Lagerpusch, J. Enderle, B. Schautz, M. Heller, A. Bosy-Westphal,

Beyond the body mass index: tracking body composition in the pathogenesis of obesity and the metabolic syndrome, Obes. Rev. 13 (2012) 6–13.

7. E.L. Thomas, J.R. Parkinson, G.S. Frost, A.P. Goldstone, C.J. Doré, J.P. McCarthy, A.L. Collins, J.A. Fitzpatrick, G. Durighel, S.D. Taylor-Robinson, J.D. Bell, The missing risk: MRI and MRS phenotyping of abdominal adiposity and ectopic fat, Obesity 20 (2012) 76–87.

8. G. O'Donovan, E.L. Thomas, J.P. McCarthy, J. Fitzpatrick, G. Durighel, S. Mehta, S.X. Morin, A.P. Goldstone, J.D. Bell, Fat distribution in men of different waist girth, fitness level and exercise habit, Int. J. Obes. 33 (2009) 1356–1362.

9. J.P. Després, Inflammation and cardiovascular disease: is abdominal obesity the missing link?, Int J. Obes. Relat. Metab. Disord. 3 (2003) S22–S24.

10. G. Williams, G. Frühbeck, Obesity: Science to Practice, Wiley-Blackwell, 1999.

11. G.A. Borkan, S.G. Gerzof, A.H. Robbins, D.E. Hults, C.K. Silbert, J.E. Silbert, Assessment of abdominal fat content by computed tomography, Am. J. Clin. Nutr. 36 (1982) 172–177.

12. H. Kvist, L. Sjöström, U. Tylén, Adipose tissue volume determinations in women by computed tomography: technical considerations, Int. J. Obes. 10

(1986) 53–67.

13. R.N. Baumgartner, S.B. Heymsfield, A.F. Roche, M. Bernardino, Abdominal composition quantified by computed tomography, Am. J. Clin. Nutr. 48 (1988)
936–945.

14. J.C. Seidell, A. Oosterlee, M.A. Thijssen, J. Burema, P. Deurenberg, J.G. Hautvast, J.H. Ruijs, Assessment of intra-abdominal and subcutaneous abdominal fat: relation between anthropometry and computed tomography, Am. J. Clin. Nutr. 45 (1987) 7–13.

15. M.A. Foster, J.M. Hutchison, J.R. Mallard, M. Fuller, Nuclear magnetic resonance pulse sequence and discrimination of high- and low-fat tissues, Magn. Reson. Imag. 2 (1984) 187–192.

16. M.F. Fuller, S.M. Stratton, D. Geddes, P.A. Fowler, M.A. Foster, A study of the
sites of adipose tissue loss by NMR imaging, in: K.J. Ellis, S.I. Yasumura, W.D. Morgan (Eds.), In Vivo Body Composition Studies, Institute of Physical Sciences in Medicine, London, 1987, pp. 55–59.

17. M.A. Staten, W.G. Totty, W.M. Kohrt, Measurement of fat distribution by magnetic resonance imaging, Invest. Radiol. 24 (1989) 345–349.

18. R. Ross, L. Léger, R. Guardo, J. De Guise, B.G. Pike, Adipose tissue volume measured by magnetic resonance imaging and computerized tomography in rats, J. Appl. Physiol. 70 (1991) 2164–2172.

19. P.A. Fowler, M.F. Fuller, C.A. Glasbey, G.G. Cameron, M.A. Foster, Validation of the in vivo measurement of adipose tissue by magnetic resonance imaging of lean and obese pigs Am, J. Clin. Nutr. 56 (1992) 7–13.

20. N. Abate, D. Burns, R.M. Peshock, A. Garg, S.M. Grundy, Estimation of adipose tissue mass by magnetic resonance imaging: validation against dissection in human cadavers, J. Lipid Res. 35 (1994) 1490–1496.

21. N. Mitsiopoulos, R.N. Baumgartner, S.B. Heymsfield, W. Lyons, D. Gallagher, R. Ross, Cadaver validation of skeletal muscle measurement by magnetic resonance imaging and computerized tomography, J. Appl. Physiol. 85 (1998) 115–122.

22. P.A. Fowler, M.F. Fuller, C.A. Glasbey, M.A. Foster, G.G. Cameron, G. McNeill, R.J. Maughan, Total and subcutaneous adipose tissue in women: the measurement of distribution an accurate prediction of quantity by using magnetic resonance imaging, Am. J. Clin. Nutr.

54 (1991) 18–25.

23. A. Sohlström, L.O. Wahlund, E. Forsum, Adipose tissue distribution as assessed by magnetic resonance imaging and total body fat by magneticresonance imaging, underwater weighing, and body-water dilution in healthy women, Am. J. Clin. Nutr. 58 (1993) 830–838.

24. J. Kullberg, J.E. Angelhed, L. Lönn, J. Brandberg, H. Ahlström, H. Frimmel, L. Johansson, Whole-body T1 mapping improves the definition of adipose tissue: consequences for automated image analysis, J. Magn. Reson. Imag. 24 (2) (2006 Aug) 394–401.

25. J. Machann, C. Thamer, B. Schnoedt, M. Haap, H.U. Haring, C.D. Claussen, M. Stumvoll, A. Fritsche, F. Schick, Standardized assessment of whole body adipose tissue topography by MRI, J. Magn. Reson. Imag. 21 (4) (2005 Apr) 455–462.

26. A. Bosy-Westphal, W. Later, B. Hitze, T. Sato, E. Kossel, C.C. Gluer, M. Heller, M.J. Muller, Accuracy of bioelectrical impedance consumer devices for measurement of body composition in comparison to whole body magnetic resonance imaging and dual X-ray absorptiometry, Obes. Facts 1 (2008) 319–324.

27. H.P. Müller, F. Raudies, A. Unrath, H. Neumann, A.C. Ludolph, J. Kassubek, Quantification of human body fat tissue percentage by MRI, NMR Biomed. 24 (2011) 17–24.

28. D. Wald, B. Teucher, J. Dinkel, R. Kaaks, S. Delorme, H. Boeing, K. Seidensaal, H.P. Meinzer, T. Heimann, Automatic quantification of subcutaneous and visceral adipose tissue from whole-body magnetic resonance images suitable for large cohort studies, J. Magn. Reson. Imag. 36 (2012) 1421–1434.

29. J.C. Seidell, C.J. Bakker, K. van der Kooy, Imaging techniques for measuring adipose-tissue distribution–a comparison between computed tomography and 1.5-T magnetic resonance, Am. J. Clin. Nutr. 51 (1990) 953–957.

30. Y.E. Snel, R.J. Brummer, M.E. Doerga, P.M. Zelissen, C.J. Bakker, M.J. Hendriks, H.P. Koppeschaar, Adipose tissue assessed by magnetic resonance imaging in growth hormone-deficient adults: the effect of growth hormone replacement and a comparison with control subjects, Am. J. Clin. Nutr. 61 (1995) 1290–1294.

31. E.L. Thomas, N. Saeed, J.V. Hajnal, A. Brynes, A.P. Goldstone, G. Frost, J.D. Bell, Magnetic resonance imaging of total body fat, J. Appl. Physiol. 85 (1998) 1778–1785.

32. H. Jones, V.S. Sprung, C.J. Pugh, C. Daousi, A. Irwin, N. Aziz, V.L. Adams, E.L. Thomas, J.D. Bell, G.J. Kemp, D.J. Cuthbertson, Polycystic ovary syndrome with hyperandrogenism

is characterized by an increased risk of hepatic steatosis compared to nonhyperandrogenic PCOS phenotypes and healthy controls, independent of obesity and insulin resistance, J. Clin. Endocrinol. Metab. 97(2012) 3709–3716.

33. L. Hayes, M.S. Pearce, M.J. Firbank, M. Walker, R. Taylor, N.C. Unwin, Do obese but metabolically normal women differ in intra-abdominal fat and physical activity levels from those with the expected metabolic abnormalities? A cross-sectional study, B.M.C. Public Health. 10 (2010) 723

34. P.D. McLaughlin, J. Ryan, P.A. Hodnett, D. O'Halloran, M.M. Maher, Quantitative whole-body MRI in familial partial lipodystrophy type 2: changes in adipose tissue distribution coincide with biochemical improvement, Am. J. Roentgenol. 199 (2012) W602–W606.

35. M. Tiikkainen, M. Tamminen, A.M. Häkkinen, R. Bergholm, S. Vehkavaara, J. Halavaara, K. Teramo, A. Rissanen, H. Yki-Järvinen, Liver-fat accumulation and insulin resistance in obese women with previous gestational diabetes, Obes. Res. 10 (2002) 859–867.

36. K.A. Virtanen, P. Lönnroth, R. Parkkola, P. Peltoniemi, M. Asola, T. Viljanen, T. Tolvanen, J. Knuuti, T. Rönnemaa, R. Huupponen, P. Nuutila, Glucose uptake and perfusion in subcutaneous and visceral adipose tissue during insulin stimulation in nonobese and obese humans, J. Clin. Endocrinol. Metab. 87 (2002) 3902–3910.

37. G. Maislin, M.M. Ahmed, N. Gooneratne, M. Thorne-Fitzgerald, C. Kim, K. Teff,

E.S. Arnardottir, B. Benediktsdottir, H. Einarsdottir, S. Juliusson, A.I. Pack, T. Gislason, R.J. Schwab, Single slice vs. volumetric MR assessment of visceral adipose tissue: reliability and validity among the overweight and obese, Obesity 20 (2012) 2124–2132.

38. L. Busetto, A. Tregnaghi, M. Bussolotto, G. Sergi, P. Benincà, A. Ceccon, V. Giantin, D. Fiore, G. Enzi, Visceral fat loss evaluated by total body magnetic resonance imaging in obese women operated with laparascopic adjustable silicone gastric banding, Int. J. Obes. Relat. Metab. Disord. 24 (2000) 60–69.

39. F. Idoate, J. Ibañez, E.M. Gorostiaga, M. García-Unciti, C. Martínez-Labari, M. Izquierdo, Weight-loss diet alone or combined with resistance training induces different regional visceral fat changes in obese women, Int. J. Obes. 35 (2011) 700–713.

40. R. Ross, J. Rissanen, H. Pedwell, J. Clifford, P. Shragge, Influence of diet and exercise on skeletal muscle and visceral adipose tissue in men, J. Appl. Physiol. 81 (1996) 2445–2455.

41. J.L. Lancaster, A.A. Ghiatas, A. Alyassin, R.F. Kilcoyne, E. Bonora, R.A. DeFronzo, Measurement of abdominal fat with T1-weighted MR images, J. Magn. Reson. Imag. 1 (1991) 363–369.

42. A.H. Poonawalla, B.P. Sjoberg, J.L. Rehm, D. Hernando, C.D. Hines, P. Irarrazaval, S.B. Reeder, Adipose tissue MRI for quantitative measurement of central obesity, J. Magn. Reson. Imag. 37 (2013) 707–716.

43. S. Lee, Y. Kim, J.L. Kuk, F.E. Boada, S. Arslanian, Whole-body MRI and ethnic differences in adipose tissue and skeletal muscle distribution in overweight black and white adolescent boys, J. Obes. 2011 (2011) 159373.

44. H.J. Silver, K.D. Niswender, J. Kullberg, J. Berglund, L. Johansson, M. Bruvold, M.J. Avison, E.B. Welch, Comparison of gross body fat-water magnetic resonance imaging at 3 tesla to dual-energy X-ray absorptiometry in obese women, Obesity (2012) (Epub ahead of print).

45. M.J. Siegel, C.F. Hildebolt, K.T. Bae, C. Hong, N.H. White, Total and intraabdominal fat distribution in preadolescents and adolescents: measurement with MR imaging, Radiology 242 (2007) 846–856.

46. J.B. Albu, L. Murphy, D.H. Frager, J.A. Johnson, F.X. Pi-Sunyer, Visceral fat and race-dependent health risks in obese nondiabetic premenopausal women, Diabetes 46 (1997) 456–462.

47. E.B. Geer, W. Shen, D. Gallagher, M. Punyanitya, H.C. Looker, K.D. Post, P.U. Freda, MRI assessment of lean and adipose tissue distribution in female patients with Cushing's disease, Clin. Endocrinol. 73 (2010) 469–475.

48. B. Gutin, P. Barbeau, S. Owens, C.R. Lemmon, M. Bauman, J. Allison, H.S. Kang, M.S. Litaker, Effects of exercise intensity on cardiovascular fitness, total body composition, and visceral adiposity of obese adolescents, Am. J. Clin. Nutr. 75 (2002).

49. S. Caprio, L.D. Hyman, C. Limb, S. McCarthy, R. Lange, R.S. Sherwin, G. Shulman, W.V. Tamborlane, Central adiposity and its metabolic correlates in obese adolescent girls, Am. J. Physiol. 269 (1995) E118–E126.

50. W.T. Cefalu, Z.Q. Wang, S. Werbel, A. Bell-Farrow, J.R. Crouse, W.H. Hinson, J.G. Terry, R. Anderson, Contribution of visceral fat mass to the insulin resistance of aging, Metabolism 44 (1995) 954–959.

51. D.M. Harrington, A.E. Staiano, S.T. Broyles, A.K. Gupta, P.T. Katzmarzyk, Waist circumference measurement site does not affect relationships with visceral adiposity and cardiometabolic risk factors in children, Pediatr Obes. (2012) (Epub ahead of print).

52. E.W. Demerath, S.S. Sun, N. Rogers, M. Lee, D. Reed, A.C. Choh, W. Couch, S.A. Czerwinski, W.C. Chumlea, R.M. Siervogel, B. Towne, Anatomical patterning of visceral adipose tissue: race, sex, and age variation, Obesity 15 (2007) 2984–2993.

53. K.A. Lê, S. Mahurkar, T.L. Alderete, R.E. Hasson, T.C. Adam, J.S. Kim, E. Beale, C. Xie, A.S. Greenberg, H. Allayee, M.I. Goran, Subcutaneous adipose tissue macrophage infiltration is associated with hepatic and visceral fat deposition, hyperinsulinemia, and stimulation of NF-jB stress pathway, Diabetes 60 (2011) 2802–2809.

54. R. So, T. Matsuo, H. Sasai, M. Eto, T. Tsujimoto, K. Saotome, K. Tanaka, Best single-slice measurement site for estimating visceral adipose tissue volume after weight loss in obese, Japanese men, Nutr. Metab. 14 (2012) 56.

55. R. Nakai, T. Azuma, T. Kishimoto, T. Hirata, O. Takizawa, S.H. Hyon, S. Tsutsumi, Development of a high-precision image-processing automatic measurement system for MRI visceral fat images acquired using a binomial RF-excitation pulse, Magn. Reson. Imag. 28 (2010) 520–526.

56. S. Tanaka, M. Yoshiyama, Y. Imanishi, M. Teragaki, N. Kasayuki, N. Shimizu, K. Nakahira, T. Hanaki, Y. Naito, M. Tanaka, Y. Inoue, Measuring visceral fat with water-selective suppression methods (SPIR, SPAIR) in patients with metabolic syndrome, Magn. Reson. Med. Sci. 6 (2007) 171–175.

57. M. Koda, M. Senda, M. Kamba, K. Kimura, Y. Murawaki, Sonographic subcutaneous and visceral fat indices represent the distribution of body fat volume, Abdom. Imag. 32 (2007) 387–392.

58. E.S. Tai, T.N. Lau, S.C. Ho, A.C. Fok, C.E. Tan, Body fat distribution and cardiovascular risk in normal weight women. Associations with insulin resistance, lipids and plasma leptin, Int. J. Obes. Relat. Metab. Disord. 24 (2000) 751–757.

59. S.K. Gan, A.D. Kriketos, B.A. Ellis, C.H. Thompson, E.W. Kraegen, D.J. Chisholm, Changes in aerobic capacity and visceral fat but not myocyte lipid levels predict increased insulin action after exercise in overweight and obese men, Diabetes Care 26 (2003) 1706–1713.

60. C.A. Allan, B.J. Strauss, H.G. Burger, E.A. Forbes, R.I. McLachlan, Testosterone therapy prevents gain in visceral adipose tissue and loss of skeletal muscle in nonobese aging men, J. Clin. Endocrinol. Metab. 93 (2008) 139–146.

61. R. Vongsuvanh, J. George, D. McLeod, D. van der Poorten, Visceral adiposity index is not a predictor of liver histology in patients with non-alcoholic fatty liver disease, J. Hepatol. (57) (2012) 392–398.

62. R. Ross, L. Léger, D. Morris, J. de Guise, R. Guardo, Quantification of adipose tissue by MRI: relationship with anthropometric variables, J. Appl. Physiol. 72 (1992) 787–795.

63. W. Shen, J. Chen, S. Kwak, M. Punyanitya, S.B. Heymsfield, Between-slice intervals in quantification of adipose tissue and muscle in children, Int. J. Pediatr. Obes. 6 (2011) 149–156.

64. W. Shen, Z. Wang, H. Tang, S. Heshka, M. Punyanitya, S. Zhu, J. Lei, S.B. Heymsfield, Volume estimates by imaging methods: model comparisons with visible woman as the reference, Obes. Res. 11 (2003) 217–225.

65. S.H. Morin, J.F. Cobbold, A.K. Lim, J. Eliahoo, E.L. Thomas, S.R. Mehta, G. Durighel, J. Fitzpatrick, J.D. Bell, S.D. Taylor-Robinson, Incidental findings in healthy control research subjects using whole-body MRI, Eur. J. Radiol. 72 (2009) 529–533.

66. D. Gallagher, P. Kuznia, S. Heshka, J. Albu, S.B. Heymsfield, B. Goodpaster, M. Visser, T.B. Harris, Adipose tissue in muscle: a novel depot similar in size to visceral adipose tissue, Am. J. Clin. Nutr. 81 (2005) 903–910.

67. J.E. Yim, S. Heshka, J. Albu, S. Heymsfield, P. Kuznia, T. Harris, D. Gallagher, Intermuscular adipose tissue rivals visceral adipose tissue in independent associations with cardiovascular risk, Int. J. Obes. 31 (2007) 1400–1405.

68. W. Shen, M. Punyanitya, Z. Wang, D. Gallagher, M.P. St-Onge, J. Albu, S.B. Heymsfield, S. Heshka, Total body skeletal muscle and adipose tissue volumes: estimation from a single abdominal cross-sectional image, J. Appl. Physiol. 97 (2004) 2333–2338.

69. A. Bosy-Westphal, E. Kossel, K. Goele, W. Later, B. Hitze, U. Settler, M. Heller, C.C. Glüer, S.B. Heymsfield, M.J. Müller, Contribution of individual organ mass loss to weight loss-associated decline in resting energy expenditure, Am. J. Clin. Nutr. 90 (2009) 993–1001.

70. R.A. Watson, N.B. Pride, E.L. Thomas, P.W. Ind, J.D. Bell, Relation between trunk fat volume and reduction of total lung capacity in obese men, J. Appl. Physiol. 112 (2012) 118–

126.

71. A. Garg, J.L. Fleckenstein, R.M. Peshock, S.M. Grundy, Peculiar distribution of adipose tissue in patients with congenital generalized lipodystrophy, J. Clin. Endocrinol. Metab. 75 (1992) 358–361.

72. J.R. Greenfield, K. Samaras, D.J. Chisholm, L.V. Campbell, Regional intrasubject variability in abdominal adiposity limits usefulness of computed tomography, Obes. Res. 10 (2002) 260–265.

73. E.L. Thomas, J.D. Bell, Influence of undersampling on magnetic resonance imaging measurements of intra-abdominal adipose tissue, Int. J. Obes. Relat. Metab. Disord. 27 (2003) 211–218.

74. R. Ross, K.D. Shaw, J. Rissanen, Y. Martel, J. de Guise, L. Avruch, Sex differences in lean and adipose tissue distribution by magnetic resonance imaging: anthropometric relationships, Am. J. Clin. Nutr. 59 (1994) 1277–1285.

75. N. Abate, A. Garg, R. Coleman, S.M. Grundy, R.M. Peshock, Prediction of total subcutaneous abdominal, intraperitoneal, and retroperitoneal adipose tissue masses in men by a single axial magnetic resonance imaging slice, Am. J. Clin. Nutr. 65 (1997) 403–408.

76. W. Shen, J. Chen, M. Gantz, G. Velasquez, M. Punyanitya, S.B. Heymsfield, A single MRI slice does not accurately predict visceral and subcutaneous adipose tissue changes during weight loss, Obesity 20 (2012) 2458–2463.

77. J.L. Kuk, T.S. Church, S.N. Blair, R. Ross, Does measurement site for visceral and abdominal subcutaneous adipose tissue alter associations with the metabolic syndrome?, Diabetes Care 29 (2006) 679–684

78. R. So, H. Sasai, T. Matsuo, T. Tsujimoto, M. Eto, K. Saotome, K. Tanaka, Multiple-slice magnetic resonance imaging can detect visceral adipose tissue reduction more accurately than single-slice imaging, Eur. J. Clin. Nutr. 66 (2012) 1351–1355.

79. T.S. Han, I.E. Kelly, K. Walsh, R.M. Greene, M.E. Lean, Relationship between volumes and areas from single transverse scans of intra-abdominal fat measured by magnetic resonance imaging, Int. J. Obes. Relat. Metab. Disord. 21 (1997) 1161–1166.

80. W. Shen, M. Punyanitya, Z. Wang, D. Gallagher, M.P. St-Onge, J. Albu, S.B. Heymsfield, S. Heshka, Visceral adipose tissue: relations between single-slice areas and total volume, Am. J. Clin. Nutr. 80 (2004) 271–278.

81. E.W. Demerath, W. Shen, M. Lee, A.C. Choh, S.A. Czerwinski, R.M. Siervogel, B. Towne, Approximation of total visceral adipose tissue with a single magnetic resonance image, Am. J. Clin. Nutr. 85 (2007) 362–368.

82. H. Kvist, B. Chowdhury, U. Grangård, U. Tylén, L. Sjöström, Total and visceral adipose-tissue volumes derived from measurements with computed tomography in adult men and women: predictive equations, Am. J. Clin. Nutr. 48 (1988) 1351–1361.

83. T.H. Liou, W.P. Chan, L.C. Pan, P.W. Lin, P. Chou, C.H. Chen, Fully automated large-scale assessment of visceral and subcutaneous abdominal adipose tissue by magnetic resonance imaging, Int. J. Obes. 30 (2006) 844–852.

84. V. Positano, A. Gastaldelli, A.M. Sironi, M.F. Santarelli, M. Lombardi, L. Landini, An accurate and robust method for unsupervised assessment of abdominal fat by MRI, J. Magn. Reson. Imag. 20 (2004) 684–689.

85. E.W. Demerath, K.J. Ritter, W.A. Couch, N.L. Rogers, G.M. Moreno, A. Choh, M. Lee, K. Remsberg, S.A. Czerwinski, W.C. Chumlea, R.M. Siervogel, B. Towne, Validity of a new automated software program for visceral adipose tissue estimation, Int. J. Obes. 31 (2007) 285–291.

86. H. Arif, S.B. Racette, D.T. Villareal, J.O. Holloszy, E.P. Weiss, Comparison of methods for assessing abdominal adipose tissue from magnetic resonance images, Obesity 15 (2007) 2240–2244.

87. S. Bonekamp, P. Ghosh, S. Crawford, S.F. Solga, A. Horska, F.L. Brancati, A.M. Diehl, S. Smith, J.M. Clark, Quantitative comparison and evaluation of software packages for assessment of abdominal adipose tissue distribution by magnetic resonance imaging, Int. J. Obes. 32 (2008) 100–111.

88. E.L. Thomas, A.L. Collins, J. McCarthy, J. Fitzpatrick, G. Durighel, A.P. Goldstone, J.D. Bell, Estimation of abdominal fat compartments by bioelectrical impedance: the validity of the ViScan measurement system in comparison with MRI, Eur. J. Clin. Nutr. 64 (2010) 525–533.

89. P. Brambilla, G. Bedogni, L.A. Moreno, M.I. Goran, B. Gutin, K.R. Fox, D.M. Peters, P. Barbeau, M. De Simone, A. Pietrobelli, Crossvalidation of anthropometry against magnetic resonance imaging for the assessment of visceral and subcutaneous adipose tissue in children, Int. J. Obes. 30 (2006) 23–30.

90. R.P. Stolk, O. Wink, P.M. Zelissen, R. Meijer, A.P. van Gils, D.E. Grobbee, Validity and reproducibility of ultrasonography for the measurement of intra-abdominal adipose tissue, Int. J. Obes. Relat. Metab. Disord. 25 (2001) 1346–1351.

91. E. Bonora, R. Micciolo, A.A. Ghiatas, J.L. Lancaster, A. Alyassin, M. Muggeo, R.A. DeFronzo, Is it possible to derive a reliable estimate of human visceral and subcutaneous abdominal adipose tissue from simple anthropometric measurements?, Metabolism 44 (1995) 1617–1625

92. R.J. Winsley, J. Fulford, K.M. MacLeod, N. Ramos-Ibanez, C.A. Williams, N. Armstrong, Prediction of visceral adipose tissue using air displacement plethysmography in children, Obes. Res. 13 (2005) 2048–2051.

93. C. Grunfeld, M. Saag, J. Cofrancesco, C.E. Lewis, R. Kronmal, S. Heymsfield, P.C. Tien, P. Bacchetti, M. Shlipak, R. Scherzer, Study of Fat Redistribution and Metabolic Change in HIV Infection (FRAM). Regional adipose tissue measured by MRI over 5 years in HIV-infected and control participants indicates persistence of HIV-associated lipoatrophy, AIDS 24 (2010) 1717–1726.

94. A.P. Goldstone, A.E. Brynes, E.L. Thomas, J.D. Bell, G. Frost, A. Holland, M.A. Ghatei, S.R. Bloom, Resting metabolic rate, plasma leptin concentrations, leptin receptor expression, and adipose tissue measured by whole-body magnetic resonance imaging in women with Prader-Willi syndrome, Am. J. Clin. Nutr. 75 (2002) 468–475.

95. J. Leger, C. Carel, I. Legrand, A. Paulsen, M. Hassan, P. Czernichow, Magnetic resonance imaging evaluation of adipose tissue and muscle tissue mass in children with growth hormone (GH) deficiency, Turner's syndrome, and intrauterine growth retardation during the first year of treatment with GH, J. Clin. Endocrinol. Metab. 78 (1994) 904–909.

96. J.E. Ostberg, E.L. Thomas, G. Hamilton, M.J. Attar, J.D. Bell, G.S. Conway, Excess visceral and hepatic adipose tissue in Turner syndrome determined by magnetic resonance imaging: estrogen deficiency associated with hepatic adipose content, J. Clin. Endocrinol. Metab. 90 (2005) 2631–2635.

97. J.G. Dolfing, C.M. Stassen, P.M. van Haard, B.H. Wolffenbuttel, D.H. Schweitzer, Comparison of MRI-assessed body fat content between lean women with polycystic ovary syndrome (PCOS) and matched controls: less visceral fat with PCOS, Hum. Reprod. 26 (2011) 1495–1500.

98. K. Müssig, H. Staiger, F. Machicao, C. Thamer, J. Machann, F. Schick, C.D. Claussen, N. Stefan, A. Fritsche, H.U. Häring, RARRES2, encoding the novel adipokine chemerin, is a genetic determinant of disproportionate regional body fat distribution: a comparative magnetic resonance imaging study, Metabolism 58 (2009) 519–524.

99. U. Lim, T. Ernst, L.R. Wilkens, C.L. Albright, A. Lum-Jones, A. Seifried, S.D. Buchthal, R. Novotny, L.N. Kolonel, L. Chang, I. Cheng, L. Le Marchand, Susceptibility variants for waist size in relation to abdominal, visceral, and hepatic adiposity in postmenopausal women, J. Acad. Nutr. Diet. 112 (2012) 1048–1055.

100. E.L. Thomas, J.R. Parkinson, M.J. Hyde, I.K. Yap, E. Holmes, C.J. Doré, J.D. Bell, N. Modi, Aberrant adiposity and ectopic lipid deposition characterize the adult phenotype of the preterm infant, Pediatr. Res. 70 (2011) 507–512.

101. S. Uthaya, E.L. Thomas, G. Hamilton, C.J. Doré, J.D. Bell, N. Modi, Altered adiposity after extremely preterm birth, Pediatr. Res. 57 (2005) 211–215.

102. E.L. Thomas, G. Frost, S.D. Taylor-Robinson, J.D. Bell, Excess body fat in obese and normal-weight subjects, Nutr. Res. Rev. 25 (2012) 150–161.

103. A.E. Staiano, P.T. Katzmarzyk, Ethnic and sex differences in body fat and visceral and subcutaneous adiposity in children and adolescents, Int. J. Obes. 36 (2012) 1261–1269.

104. M.J. Toth, A. Tchernof, C.K. Sites, E.T. Poehlman, Menopause-related changes in body fat distribution, Ann. N.Y. Acad. Sci. 904 (2000) 502–506.

105. S.R. Smith, J.J. Zachwieja, Visceral adipose tissue: a critical review of intervention strategies, Int. J. Obes. Relat. Metab. Disord. 23 (1999) 329–335.

106. T.B. Chaston, J.B. Dixon, Factors associated with percent change in visceral versus subcutaneous abdominal fat during weight loss: findings from a systematic review, Int. J. Obes. 32 (2008) 619–628.

107. R. Ross, I. Janssen, Is abdominal fat preferentially reduced in response to exercise-induced weight loss?, Med Sci. Sports Exerc. 31 (1999) S568–S572.

108. I. Ismail, S.E. Keating, M.K. Baker, N.A. Johnson, A systematic review and meta-analysis of the effect of aerobic vs. resistance exercise training on visceral fat, Obes. Rev. 13 (2012) 68–91.

109. T. Christiansen, S.K. Paulsen, J.M. Bruun, K. Overgaard, S. Ringgaard, S.B. Pedersen, V. Positano, B. Richelsen, Comparable reduction of the visceral adipose tissue depot after a

diet-induced weight loss with or without aerobic exercise in obese subjects: a 12-week randomized intervention study, Eur. J. Endocrinol. 160 (2009) 759–767.

110. S.B. Racette, E.P. Weiss, D.T. Villareal, H. Arif, K. Steger-May, K.B. Schechtman, L. Fontana, S. Klein, J.O. Holloszy, One year of caloric restriction in humans: feasibility and effects on body composition and abdominal adipose tissue, J. Gerontol. A: Biol. Sci. Med. Sci. 61 (2006) 943–950.

111. A.P. Viljanen, R. Lautamäki, M. Järvisalo, R. Parkkola, R. Huupponen, T. Lehtimäki, T. Rönnemaa, O.T. Raitakari, P. Iozzo, P. Nuutila, Effects of weight loss on visceral and abdominal subcutaneous adipose tissue blood-flow and insulin-mediated glucose uptake in healthy obese subjects, Ann. Med. 41 (2009) 152–160.

112. M. Maersk, A. Belza, H. Stødkilde-Jørgensen, S. Ringgaard, E. Chabanova, H. Thomsen, S.B. Pedersen, A. Astrup, B. Richelsen, Sucrose-sweetened beverages increase fat storage in the liver, muscle, and visceral fat depot: a 6-mo randomized intervention study, Am. J. Clin. Nutr. 95 (2012) 283–289.

113. J.L. Kuk, R. Ross, Influence of sex on total and regional fat loss in overweight and obese men and women, Int. J. Obes. 33 (2009) 629–634.

114. K.A. Virtanen, K. Hällsten, R. Parkkola, T. Janatuinen, F. Lönnqvist, T. Viljanen, T. Rönnemaa, J. Knuuti, R. Huupponen, P. Lönnroth, P. Nuutila, Differential effects of rosiglitazone and metformin on adipose tissue distribution and glucose uptake in type 2 diabetic subjects, Diabetes 52 (2003) 283–290.

115. Y. Miyazaki, A. Mahankali, M. Matsuda, S. Mahankali, J. Hardies, K. Cusi, L.J. Mandarino, R.A. DeFronzo, Effect of pioglitazone on abdominal fat distribution and insulin sensitivity in type 2 diabetic patients, J. Clin. Endocrinol. Metab. 87 (2002) 2784–2791.

116. E.L. Thomas, A. Makwana, R. Newbould, A.W. Rao, G. Gambarota, G. Frost, B. Delafont, R.G. Mishra, P.M. Matthews, E.S. Berk, S.M. Schwartz, J.D. Bell, J.D. Beaver, Pragmatic study of orlistat 60 mg on abdominal obesity, Eur. J. Clin. Nutr. 65 (2011) 1256–1262.

117. S.J. Marks, N.R. Moore, M.L. Clark, B.J. Strauss, T.D. Hockaday, Reduction of visceral adipose tissue and improvement of metabolic indices: effect of dexfenfluramine in NIDDM, Obes. Res. 4 (1996) 1–7.

118. L. Johansson, M. Roos, J. Kullberg, J. Weis, H. Ahlström, M. Sundbom, B. Edén

Engström, F.A. Karlsson, Lipid mobilization following Roux-en-Y gastric
bypass examined by magnetic resonance imaging and spectroscopy, Obes. Surg. 18 (2008) 1297–1304.

119. L. Mayer, B.T. Walsh, R.N. Pierson, S.B. Heymsfield, D. Gallagher, J. Wang, M.K. Parides, R.L. Leibel, M.P. Warren, E. Killory, D. Glasofer, Body fat redistribution after weight gain in women with anorexia nervosa, Am. J. Clin. Nutr. 81
(2005) 1286–1291.

120. E.W. Demerath, D. Reed, N. Rogers, S.S. Sun, M. Lee, A.C. Choh, W. Couch, S.A. Czerwinski, W.C. Chumlea, R.M. Siervogel, B. Towne, Visceral adiposity and its anatomical distribution as predictors of the metabolic syndrome and cardiometabolic risk factor levels, Am. J. Clin. Nutr. 88 (2008) 1263–1271.

121. S.R. Smith, J.C. Lovejoy, F. Greenway, D. Ryan, L. deJonge, J. de la Bretonne, J. Volafova, G.A. Bray, Contributions of total body fat, abdominal subcutaneous adipose tissue compartments, and visceral adipose tissue to the metabolic complications of obesity, Metabolism 50 (2001) 425–435.

122. Y. Miyazaki, L. Glass, C. Triplitt, E. Wajcberg, L.J. Mandarino, R.A. DeFronzo, Abdominal fat distribution and peripheral and hepatic insulin resistance in type 2 diabetes mellitus, Am. J. Physiol. Endocrinol. Metab. 283 (2002) E1135–E1143.

123. R. Ross, J. Aru, J. Freeman, R. Hudson, I. Janssen, Abdominal adiposity and insulin resistance in obese men, Am. J. Physiol. Endocrinol. Metab. 282 (2002) E657–E663.

124. R. Golan, I. Shelef, A. Rudich, Y. Gepner, E. Shemesh, Y. Chassidim, I. Harman-Boehm, Y. Henkin, D. Schwarzfuchs, S. Ben Avraham, S. Witkow, I.F. Liberty, O. Tangi-Rosental, B. Sarusi, M.J. Stampfer, I. Shai, Abdominal superficial subcutaneous fat: a putative distinct protective fat subdepot in type 2 diabetes, Diabetes Care 35 (2012) 640–647.

125. D.C. Chan, G.F. Watts, A.V. Sussekov, P.H. Barrett, Z. Yang, J. Hua, S Song, Adipose tissue compartments and insulin resistance in overweight-obese Caucasian men, Diabetes Res. Clin. Pract. 63 (2004) 77–85.

126. A. Misra, A. Garg, N. Abate, R.M. Peshock, J. Stray-Gundersen, S.M. Grundy, Relationship of anterior and posterior subcutaneous abdominal fat to insulin sensitivity in nondiabetic men, Obes. Res. 5 (1997) 93–99.

127. J.E. Yim, S. Heshka, J.B. Albu, S. Heymsfield, D. Gallagher, Femoral–gluteal

subcutaneous and intermuscular adipose tissues have independent and opposing relationships with CVD risk, J. Appl. Physiol. 104 (2008) 700–707.

128. N. Stefan, K. Kantartzis, J. Machann, F. Schick, C. Thamer, K. Rittig, B. Balletshofer, F. Machicao, A. Fritsche, H.U. Häring, Identification and characterization of metabolically benign obesity in humans, Arch. Intern. Med. 168 (2008) 1609–1616.

129. R.P. Wildman, P. Muntner, K. Reynolds, A.P. McGinn, S. Rajpathak, J. Wylie-Rosett, M.R. Sowers, The obese without cardiometabolic risk factor clustering E.L. Thomas et al. / Progress in Nuclear Magnetic Resonance Spectroscopy 73 (2013) 56–80 77

and the normal weight with cardiometabolic risk factor clustering: prevalence and correlates of 2 phenotypes among the US population (NHANES 1999–2004), Arch. Intern. Med. 11 (2008) 1617–1624.

130. P.A. McAuley, S.N. Blair, Obesity paradoxes, J. Sports Sci. 29 (2011) 773–782.

131. N.B. Ruderman, S.H. Schneider, P. Berchtold, The ‘‘metabolically-obese’’, normal-weight individual, Am. J. Clin. Nutr. 34 (1981) 1617–1621.

132. A. Katsuki, Y. Sumida, H. Urakawa, E.C. Gabazza, S. Murashima, N. Maruyama, K. Morioka, K. Nakatani, Y. Yano, Y. Adachi, Increased visceral fat and serum levels of triglyceride are associated with insulin resistance in Japanese metabolically obese, normal weight subjects with normal glucose tolerance, Diabetes Care 26 (2003) 2341–2344.

133. L. Heilbronn, S.R. Smith, E. Ravussin, Failure of fat cell proliferation, mitochondrial function and fat oxidation results in ectopic fat storage, insulin resistance and type II diabetes mellitus, Int. J. Obes. Relat. Metab. Disord. 28 (2004) S12–S21.

134. R.H. Unger, Minireview: weapons of lean body mass destruction: the role of ectopic lipids in the metabolic syndrome, Endocrinology 144 (2003) 5159–5165.

135. F. Schick, B. Eismann, W.I. Jung, H. Bongers, M. Bunse, O. Lutz, Comparison of localized proton NMR signals of skeletal muscle and fat tissue in vivo: two lipid compartments in muscle tissue, Magn. Reson. Med. 29 (1993) 158–167.

136. C. Boesch, J. Slotboom, H. Hoppeler, R. Kreis, In vivo determination of intra-myocellular lipids in human muscle by means of localized ^{1}H-MR-spectroscopy, Magn. Reson. Med. 37 (1997) 484–493.

137. L.S. Szczepaniak, E.E. Babcock, F. Schick, R.L. Dobbins, A. Garg, D.K. Burns, J.D. McGarry, D.T. Stein, Measurement of intracellular triglyceride stores by 1H spectroscopy:

validation in vivo, Am. J. Physiol. 276 (1999) E977–E989.

138. E.L. Thomas, G. Hamilton, N. Patel, R. O'Dwyer, C.J. Doré, R.D. Goldin, J.D. Bell, S.D. Taylor-Robinson, Hepatic triglyceride content and its relation to body adiposity: a magnetic resonance imaging and proton magnetic resonance spectroscopy study, Gut 54 (2005) 122–127.

139. L.S. Szczepaniak, P. Nurenberg, D. Leonard, J.D. Browning, J.S. Reingold, S. Grundy, H.H. Hobbs, R.L. Dobbins, Magnetic resonance spectroscopy to measure hepatic triglyceride content: prevalence of hepatic steatosis in the general population, Am. J. Physiol. Endocrinol. Metab. 288 (2005) E462–E468.

140. L.S. Szczepaniak, R.L. Dobbins, G.J. Metzger, G. Sartoni-D'Ambrosia, D. Arbique, W. Vongpatanasin, R. Unger, R.G. Victor, Myocardial triglycerides and systolic function in humans: in vivo evaluation by localized proton spectroscopy and cardiac imaging, Magn. Reson. Med. 49 (2003) 417–423.

141. I. Lingvay, V. Esser, J.L. Legendre, A.L. Price, K.M. Wertz, B. Adams-Huet, S. Zhang, R.H. Unger, L.S. Szczepaniak, Noninvasive quantification of pancreatic fat in humans, J. Clin. Endocrinol. Metab. 94 (2009) 4070–4076.

142. P.A. Bottomley, Spatial localization in NMR spectroscopy in vivo, Ann. N.Y. Acad. Sci. 508 (1987) 333–348.

143. A. Haase, J. Frahm, D. Matthaei, W. Hänicke, H. Bomsdorf, D. Kunz, R. Tischler, MR imaging using stimulated echoes (STEAM), Radiology 160 (1986) 787–790.

144. I.L. Pykett, B.R. Rosen, Nuclear magnetic resonance: in vivo proton chemical shift imaging. ****Work in progress, Radiology. 149 (1983) 197-201.

145. S.B. Reeder, I. Cruite, G. Hamilton, C.B. Sirlin, Quantitative assessment of liver fat with magnetic resonance imaging and spectroscopy, J. Magn. Reson. Imag. 34 (2011) 729–749.

146. F. Springer, J. Machann, C.D. Claussen, F. Schick, N.F. Schwenzer, Liver fat content determined by magnetic resonance imaging and spectroscopy, World J. Gastroenterol. 16 (2010) 1560–1566.

147. H.H. Hu, K.S. Nayak, M.I. Goran, Assessment of abdominal adipose tissue and organ fat content by magnetic resonance imaging, Obes. Rev. 12 (2011) 504–515.

148. K.D. Patel, K.W. Abeysekera, M. Marlais, M.J. McPhail, H.C. Thomas, J.A. Fitzpatrick, A.K. Lim, S.D. Taylor-Robinson, E.L. Thomas, Recent advances in imaging hepatic fibrosis

and steatosis, Expert Rev. Gastroenterol. Hepatol. 5 (2011) 91–104.

149. D.P. O'Regan, M.F. Callaghan, M. Wylezinska-Arridge, J. Fitzpatrick, R.P. Naoumova, J.V. Hajnal, S.A. Schmitz, Liver fat content and T2*: simultaneous measurement by using breath-hold multiecho MR imaging at 3.0 T—feasibility, Radiology 247 (2008) 550–557.

150. H.H. Hu, H.W. Kim, K.S. Nayak, M.I. Goran, Comparison of fat-water MRI and single-voxel MRS in the assessment of hepatic and pancreatic fat fractions in humans, Obesity 18 (2010) 841–847.

151. W.T. Dixon, Simple proton spectroscopic imaging, Radiology 153 (1984) 189–194.

152. G.H. Glover, E. Schneider, Three-point Dixon technique for true water/fat decomposition with B0 inhomogeneity correction, Magn. Reson. Med. 18 (1991) 371–383.

153. S.B. Reeder, A.R. Pineda, Z. Wen, A. Shimakawa, H. Yu, J.H. Brittai, G.E. Gold, C.H. Beaulieu, N.J. Pelc, Iterative decomposition of water and fat with echo asymmetry and least-squares estimation (IDEAL): application with fast spin-echo imaging, Magn. Reson. Med. 54 (2005) 636–644.

154. J.C. Wood, J.M. Tyszka, S. Carson, M.D. Nelson, T.D. Coates, Myocardial iron loading in transfusion-dependent thalassemia and sickle cell disease, Blood 103 (2004) 1934–1936.

155. E. Standl, N. Lotz, T. Dexel, H.U. Janka, H.J. Kolb, Muscle triglycerides in diabetic subjects. Effect of insulin deficiency and exercise, Diabetologia 18 (1980) 463–469.

156. L.H. Storlien, A.B. Jenkins, D.J. Chisholm, W.S. Pascoe, S. Khouri, E.W. Kraegen, Influence of dietary fat composition on development of insulin resistance in rats. Relationship to muscle triglyceride and omega-3 fatty acids in muscle phospholipid, Diabetes 40 (1991) 280–289.

157. E.W. Kraegen, P.W. Clark, A.B. Jenkins, E.A. Daley, D.J. Chisholm, L.H. Storlien, Development of muscle insulin resistance after liver insulin resistance in high-fat-fed rats, Diabetes 40 (1991) 1397–1403.

158. J.H. Hwang, J.W. Pan, S. Heydari, H.P. Hetherington, D.T. Stein, Regional differences in intramyocellular lipids in humans observed by in vivo ^{1}H-MR spectroscopic imaging, J. Appl. Physiol. 90 (2001) 1267–1274.

159. J. Hu, Q. Jiang, Y. Xia, C. Zuo, High spatial resolution in vivo 2D 1H magnetic resonance spectroscopic imaging of human muscles with a band-selective technique, Magn. Reson. Imag. 19 (2001) 1091–1096.

160. S.S. Velan, C. Durst, S.K. Lemieux, R.R. Raylman, R. Sridhar, R.G. Spencer, G.R. Hobbs, M.A. Thomas, Investigation of muscle lipid metabolism by localized one- and two-dimensional MRS techniques using a clinical 3T MRI/MRS scanner, J. Magn. Reson. Imag. 25 (2007) 192–199.

161. M.H. Cui, J.H. Hwang, V. Tomuta, Z. Dong, D.T. Stein, Cross contamination of intramyocellular lipid signals through loss of bulk magnetic susceptibility effect differences in human muscle using ^{1}H-MRSI at 4 T, J. Appl. Physiol. 103 (2007) 1290–1298.

162. A. Khuu, J. Ren, I. Dimitrov, D. Woessner, J. Murdoch, A.D. Sherry, C.R. Malloy, Orientation of lipid strands in the extracellular compartment of muscle: effect on quantitation of intramyocellular lipids, Magn. Reson. Med. 61 (2009) 16–21.

163. V.B. Schrauwen-Hinderling, L.J. van Loon, R. Koopman, K. Nicolay, W.H. Saris, M.E. Kooi, Intramyocellular lipid content is increased after exercise in nonexercising human skeletal muscle, J. Appl. Physiol. 95 (2003) 2328–2332.

164. C.E. Fonvig, D.S. Bille, E. Chabanova, T.R. Nielsen, H.S. Thomsen, J.C. Holm, Muscle fat content and abdominal adipose tissue distribution investigated by magnetic resonance spectroscopy and imaging in obese children and youths, Pediatr. Rep. 4 (2012) e11.

165. B. Mengiardi, M.R. Schmid, N. Boos, C.W. Pfirrmann, F. Brunner, A. Elfering, J. Hodler, Fat content of lumbar paraspinal muscles in patients with chronic low back pain and in asymptomatic volunteers: quantification with MR spectroscopy, Radiology 240 (2006) 786–792.

166. J. Rico-Sanz, E.L. Thomas, G. Jenkinson, S. Mierisová, R. Iles, J.D. Bell, Diversity in levels of intracellular total creatine and triglycerides in human skeletal muscles observed by ^{1}H-MRS, J. Appl. Physiol. 87 (1999) 2068–2072.

167. R. Sinha, S. Dufour, K.F. Petersen, V. LeBon, S. Enoksson, Y.Z. Ma, M. Savoye, D.L. Rothman, G.I. Shulman, S. Caprio, Assessment of skeletal muscle triglyceride content by ^{1}H nuclear magnetic resonance spectroscopy in lean and obese adolescents: relationships to insulin sensitivity, total body fat, and central adiposity, Diabetes 51 (2002) 1022–1027.

168. K.F. Petersen, S. Dufour, K. Morino, P.S. Yoo, G.W. Cline, G.I. Shulman, Reversal of muscle insulin resistance by weight reduction in young, lean, insulin-resistant offspring of parents with type 2 diabetes, Proc. Natl. Acad. Sci. USA 109 (2012) 8236–8240.

169. E.L. Thomas, A.E. Brynes, G. Hamilton, N. Patel, A. Spong, R.D. Goldin, G. Frost, J.D.

Bell, S.D. Taylor-Robinson, Effect of nutritional counselling on hepatic, muscle and adipose tissue fat content and distribution in non-alcoholic fatty liver disease, World J. Gastroenterol. 12 (2006) 5813–5819.

170. G. Perseghin, P. Scifo, F. De Cobelli, E. Pagliato, A. Battezzati, C. Arcelloni, A. Vanzulli, G. Testolin, G. Pozza, A. Del Maschio, L. Luzi, Intramyocellular triglyceride content is a determinant of in vivo insulin resistance in humans: a ^{1}H–^{13}C nuclear magnetic resonance spectroscopy assessment in offspring of type 2 diabetic parents, Diabetes 48 (1999) 1600–1606.

171. M. Krssak, K. Falk Petersen, A. Dresner, L. DiPietro, S.M. Vogel, D.L. Rothman, M. Roden, G.I. Shulman, Intramyocellular lipid concentrations are correlated with insulin sensitivity in humans: a 1H NMR spectroscopy study, Diabetologia 42 (1999) 113–116.

172. S. Jacob, J. Machann, K. Rett, K. Brechtel, A. Volk, W. Renn, E. Maerker, S. Matthaei, F. Schick, C.D. Claussen, H.U. Haring, Association of increased intramyocellular lipid content with insulin resistance in lean nondiabetic offspring of type 2 diabetic subjects, Diabetes 48 (1999) 1113–1119.

173. M. Borkman, L.H. Storlien, D.A. Pan, A.B. Jenkins, D.J. Chisholm, L.V. Campbell, The relation between insulin sensitivity and the fatty-acid composition of skeletal-muscle phospholipids, N. Engl. J. Med. 328 (1993) 238–244.

174. N.G. Forouhi, G. Jenkinson, E.L. Thomas, S. Mullick, S. Mierisova, U. Bhonsle, P.M. McKeigue, J.D. Bell, Relation of triglyceride stores in skeletal muscle cells to central obesity and insulin sensitivity in European and South Asian men, Diabetologia 42 (1999) 932–935.

175. S. Dufour, K.F. Petersen, Disassociation of liver and muscle insulin resistance from ectopic lipid accumulation in low-birth-weight individuals, J. Clin. Endocrinol. Metab. 96 (2011) 3873–3880.

176. L.M. Goff, G.S. Frost, G. Hamilton, E.L. Thomas, W.S. Dhillo, A. Dornhorst, J.D. Bell, Carbohydrate-induced manipulation of insulin sensitivity independently of intramyocellular lipids, Br. J. Nutr. 89 (2003) 365–375.

177. B.H. Goodpaster, J. He, S. Watkins, D.E. Kelley, Skeletal muscle lipid content and insulin resistance: evidence for a paradox in endurance-trained athletes, J. Clin. Endocrinol. Metab. 86 (2001) 5755–5761.

178. C. Thamer, J. Machann, O. Bachmann, M. Haap, D. Dahl, B. Wietek, O. Tschritter, A.

Niess, K. Brechtel, A. Fritsche, C. Claussen, S. Jacob, F. Schick, H.U. Haring, M. Stumvoll, Intramyocellular lipids: anthropometric determinants and relationships with maximal aerobic capacity and insulin sensitivity, J. Clin. Endocrinol. Metab. 88 (2003) 1785–1791.

179. L.J. van Loon, R. Koopman, R. Manders, W. van der Weegen, G.P. van Kranenburg, H.A. Keizer, Intramyocellular lipid content in type 2 diabetes 78 E.L. Thomas et al. / Progress in Nuclear Magnetic Resonance Spectroscopy 73 (2013) 56–80 patients compared with overweight sedentary men and highly trained endurance athletes, Am. J. Physiol. Endocrinol. Metab. 287 (2004) E558–E565.

180. J. Rico-Sanz, M. Moosavi, E.L. Thomas, J. McCarthy, G.A. Coutts, N. Saeed, J.D. Bell, In vivo evaluation of the effects of continuous exercise on skeletal muscle triglycerides in trained humans, Lipids 35 (2000) 1313–1318.

181. J.J. Dubé, F. Amati, M. Stefanovic-Racic, F.G. Toledo, S.E. Sauers, B.H. Goodpaster, Exercise-induced alterations in intramyocellular lipids and insulin resistance: the athlete's paradox revisited, Am. J. Physiol. Endocrinol. Metab. 294 (2008) E882–E888.

182. P.M. Coen, B.H. Goodpaster, Role of intramyocelluar lipids in human health, Trends Endocrinol. Metab. 23 (2012) 391–398.

183. L. Xiao, E.X. Wu, Diffusion-weighted magnetic resonance spectroscopy: a

novel approach to investigate intramyocellular lipids, Magn. Reson. Med. 66 (2011) 937–944.

184. M.A. Fischer, D. Nanz, A. Shimakawa, T. Schirmer, R. Guggenberger, A. Chhabra, J.A. Carrino, G. Andreisek, Quantification of muscle fat in patients with low back pain: comparison of multi-echo MR imaging with single-voxel MR spectroscopy, Radiology 266 (2013) 555–563.

185. T. Addison, Observations on fatty degeneration of the liver, Guy's Hosp. Rep. 1 (1836) 476.

186. C. Rokitansky, A Manual of Pathological Anatomy, vol. 2, Sydenham Society, London, 1849. pp. 117–145.

187. W. Pepper, Saccharine diabetes, M. Rec. 25 (1884) 9–12.

188. J. Ludwig, T.R. Viggiano, D.B. McGill, B.J. Oh, Nonalcoholic steatohepatitis: Mayo Clinic experiences with a hitherto unnamed disease, Mayo. Clin. Proc. 55 (1980) 434–438.

189. E.E. Powell, W.G. Cooksley, R. Hanson, J. Searle, J.W. Halliday, L.W. Powell, The natural history of non-alcoholic steatohepatitis: a follow-up study of fortytwo patients for up

to 21 years, Hepatology 11 (1990) 74–80.

190. C.A. Matteoni, Z.M. Younossi, T. Gramlich, N. Boparai, Y.C. Liu, A.J. McCullough, Nonalcoholic fatty liver disease: a spectrum of clinical and pathological severity, Gastroenterology 116 (1999) 1413–1419.

191. J.H. Hwang, D.T. Stein, N. Barzilai, M.H. Cui, J. Tonelli, P. Kishore, M. Hawkins, Increased intrahepatic triglyceride is associated with peripheral insulin resistance: in vivo MR imaging and spectroscopy studies, Am. J. Physiol. Endocrinol. Metab. 293 (2007) E1663–E1669.

192. E. Fabbrini, F. Magkos, B.S. Mohammed, T. Pietka, N.A. Abumrad, B.W. Patterson, A. Okunade, S. Klein, Intrahepatic fat, not visceral fat, is linked with metabolic complications of obesity, Proc. Natl. Acad. Sci. USA 106 (2009) 15430–15435.

193. S.R. Mehta, E.L. Thomas, J.D. Bell, D.G. Johnston, S.D. Taylor-Robinson, Noninvasive means of measuring hepatic fat content, World J. Gastroenterol. 14 (2008) 3476–3483.

194. S.R. Mehta, E.L. Thomas, N. Patel, M.E. Crofton, J. McCarthy, J. Eliahoo, S.X. Morin, J. Fitzpatrick, G. Durighel, A.P. Goldstone, D.G. Johnston, J.D. Bell, S.D. Taylor-Robinson, Proton magnetic resonance spectroscopy and ultrasound for hepatic fat quantification, Hepatol. Res. 40 (2010) 399–406.

195. N.F. Schwenzer, F. Springer, C. Schraml, N. Stefan, J. Machann, F. Schick, Noninvasive assessment and quantification of liver steatosis by ultrasound, computed tomography and magnetic resonance, J. Hepatol. 51 (2009) 433–445.

196. K.M. Korenblat, E. Fabbrini, B.S. Mohammed, S. Klein, Liver, muscle, and adipose tissue insulin action is directly related to intrahepatic triglyceride content in obese subjects, Gastroenterology 134 (2008) 1369–1375.

197. M. Krssak, A. Brehm, E. Bernroider, C. Anderwald, P. Nowotny, C. Dalla Man, C. Cobelli, G.W. Cline, G.I. Shulman, W. Waldhäusl, M. Roden, Alterations in postprandial hepatic glycogen metabolism in type 2 diabetes, Diabetes 53 (2004) 3048–3056.

198. M.G. Cree, B.R. Newcomer, C.S. Katsanos, M. Sheffield-Moore, D. Chinkes, A. Aarsland, R. Urban, R.R. Wolfe, Intramuscular and liver triglycerides are increased in the elderly, J. Clin. Endocrinol. Metab. 89 (2004) 3864–3871.

199. Y. Tamura, Y. Tanaka, F. Sato, J.B. Choi, H. Watada, M. Niwa, J. Kinoshita, A. Ooka, N. Kumashiro, Y. Igarashi, S. Kyogoku, T. Maehara, M. Kawasumi, T. Hirose, R. Kawamori,

Effects of diet and exercise on muscle and liver intracellular lipid contents and insulin sensitivity in type 2 diabetic patients, J. Clin. Endocrinol. Metab. 90 (2005) 3191–3196.

200. J. Westerbacka, K. Lammi, A.M. Häkkinen, A. Rissanen, I. Salminen, A. Aro, H. Yki-Järvinen, Dietary fat content modifies liver fat in overweight nondiabetic subjects, J. Clin. Endocrinol. Metab. 90 (2005) 2804–2809.

201. G. Perseghin, G. Lattuada, F. De Cobelli, F. Ragogna, G. Ntali, A. Esposito, E. Belloni, T. Canu T, I. Terruzzi, P. Scifo, A. Del Maschio, L. Luzi, Habitual physical activity is associated with intrahepatic fat content in humans, Diabetes Care 30 (2007) 683–688.

202. K. Kantartzis, C. Thamer, A. Peter, J. Machann, F. Schick, C. Schraml, A. Königsrainer, I. Königsrainer, S. Kröber, A. Niess, A. Fritsche, H.U. Häring, N. Stefan, High cardiorespiratory fitness is an independent predictor of the reduction in liver fat during a lifestyle intervention in non-alcoholic fatty liver disease, Gut 58 (2009) 1281–1288.

203. J.C. Hannukainen, R. Borra, K. Linderborg, H. Kallio, J. Kiss, V. Lepomäki, K.K. Kalliokoski, U.M. Kujala, J. Kaprio, O.J. Heinonen, M. Komu, R. Parkkola, M. Ahotupa, T. Lehtimäki, R. Huupponen, P. Iozzo, P. Nuutila, Liver and pancreatic fat content and metabolism in healthy monozygotic twins with discordant physical activity, J. Hepatol. 54 (2011) 545–552.

204. A. Kotronen, J. Westerbacka, R. Bergholm, K.H. Pietiläinen, H. Yki-Järvinen, Liver fat in the metabolic syndrome, J. Clin. Endocrinol. Metab. 92 (2007) 3490–3497.

205. D. Liska, S. Dufour, T.L. Zern, S. Taksali, A.M. Calí, J. Dziura, G.I. Shulman, B.M. Pierpont, S. Caprio, Interethnic differences in muscle, liver and abdominal fat partitioning in obese adolescents, PLoS One 2 (2007) e569.

206. E. D'Adamo, V. Northrup, R. Weiss, N. Santoro, B. Pierpont, M. Savoye, G. O'Malley, S. Caprio, Ethnic differences in lipoprotein subclasses in obese adolescents: importance of liver and intraabdominal fat accretion, Am. J. Clin. Nutr. 92 (2010) 500–508.

207. K. Brechtel, S. Jacob, J. Machann, B. Hauer, M. Nielsen, H.P. Meissner, S. Matthaei, H.U. Haering, C.D. Claussen, F. Schick, Acquired generalized lipoatrophy (AGL): highly selective MR lipid imaging and localized ^{1}H-MRS, J. Magn. Reson. Imag. 12 (2000) 306–310.

208. J. Sutinen, A.M. Häkkinen, J. Westerbacka, A. Seppälä-Lindroos, S. Vehkavaara, J. Halavaara, A. Järvinen, M. Ristola, H. Yki-Järvinen, Increased fat accumulation in the liver

in HIV-infected patients with antiretroviral therapy-associated lipodystrophy, AIDS 16 (2002) 2183–2193.

209. K.F. Petersen, E.A. Oral, S. Dufour, D. Befroy, C. Ariyan, C. Yu, G.W. Cline, A.M. DePaoli, S.I. Taylor, P. Gorden, G.I. Shulman, Leptin reverses insulin resistance and hepatic steatosis in patients with severe lipodystrophy, J. Clin. Invest. 109 (2002) 1345–1350.

210. V. Simha, L.S. Szczepaniak, A.J. Wagner, A.M. DePaoli, A. Garg, Effect of leptin replacement on intrahepatic and intramyocellular lipid content in patients with generalized lipodystrophy, Diabetes Care 26 (2003) 30–35.

211. E.L. Thomas, S. Uthaya, V. Vasu, J.P. McCarthy, P. McEwan, G. Hamilton, J.D. Bell, N. Modi, Neonatal intrahepatocellular lipid, Arch. Dis. Child Fetal Neonatal Ed. 93 (2008) F382–F383.

212. S. Schäfer, K. Kantartzis, J. Machann, C. Venter, A. Niess, F. Schick, F. Machicao, H.U. Häring, A. Fritsche, N. Stefan, Lifestyle intervention in individuals with normal versus impaired glucose tolerance, Eur. J. Clin. Invest. 37 (2007) 535–543.

213. K. Shah, A. Stufflebam, T.N. Hilton, D.R. Sinacore, S. Klein, D.T. Villareal, Diet and exercise interventions reduce intrahepatic fat content and improve insulin sensitivity in obese older adults, Obesity 17 (2009) 2162–2168.

214. A.B. Mayerson, R.S. Hundal, S. Dufour, V. Lebon, D. Befroy, G.W. Cline, S. Enocksson, S.E. Inzucchi, G.I. Shulman, K.F. Petersen, The effects of rosiglitazone on insulin sensitivity, lipolysis, and hepatic and skeletal muscle triglyceride content in patients with type 2 diabetes, Diabetes 51 (2002) 797–802.

215. R. Belfort, S.A. Harrison, K. Brown, C. Darland, J. Finch, J. Hardies, B. Balas, A. Gastaldelli, F. Tio, J. Pulcini, R. Berria, J.Z. Ma, S. Dwivedi, R. Havranek, C. Fincke, R. DeFronzo, G.A. Bannayan, S. Schenker, K. Cusi, A placebo-controlled trial of pioglitazone in subjects with nonalcoholic steatohepatitis, N. Engl. J. Med. 355 (2006) 2297–2307.

216. Y. Tamura, H. Watada, F. Sato, N. Kumashiro, Y. Sakurai, T. Hirose, Y. Tanaka, R. Kawamori, Effects of metformin on peripheral insulin sensitivity and intracellular lipid contents in muscle and liver of overweight Japanese subjects, Diabetes Obes. Metab. 10 (2008) 733–738.

217. M.L. Phillips, S. Boase, S. Wahlroos, M. Dugar, L. Kow, J. Stahl, J.P. Slavotinek, R. Valentine, J. Toouli, C.H. Thompson, Associates of change in liver fat content in the morbidly

obese after laparoscopic gastric banding surgery, Diabetes Obes. Metab. 10 (2008) 661–667.

218. Y. Lee, H. Hirose, M. Ohneda, J.H. Johnson, J.D. McGarry, R.H. Unger, Beta-cell lipotoxicity in the pathogenesis of non-insulin-dependent diabetes mellitus of obese rats: impairment in adipocyte-beta-cell relationships, Proc. Natl. Acad. Sci. USA 91 (1994) 10878–10882.

219. M. Dubois, J. Kerr-Conte, V. Gmyr, T. Bouckenooghe, G. Muharram, M. D'Herbomez, A. Martin-Ponthieu, M.C. Vantyghem, B. Vandewalle, F. Pattou, Non-esterified fatty acids are deleterious for human pancreatic islet function at physiological glucose concentration, Diabetologia 47 (2004) 463–469.

220. M.E. Tushuizen, M.C. Bunck, P.J. Pouwels, S. Bontemps, J.H. van Waesberghe, R.K. Schindhelm, A. Mari, R.J. Heine, M. Diamant, Pancreatic fat content and beta-cell function in men with and without type 2 diabetes, Diabetes Care 30 (2007) 2916–2921.

221. N.J. van der Zijl, G.H. Goossens, C.C. Moors, D.H. van Raalte, M.H. Muskiet, P.J. Pouwels, E.E. Blaak, M. Diamant, Ectopic fat storage in the pancreas, liver, and abdominal fat depots: impact on b-cell function in individuals with impaired glucose metabolism, J. Clin. Endocrinol. Metab. 96 (2011) 459–467.

222. N.F. Schwenzer, J. Machann, P. Martirosian, N. Stefan, C. Schraml, A. Fritsche, C.D. Claussen, F. Schick, Quantification of pancreatic lipomatosis and liver steatosis by MRI: comparison of in/opposed-phase and spectral-spatial excitation techniques, Invest. Radiol. 43 (2008) 330–337.

223. J. Li, Y. Xie, F. Yuan, B. Song, C. Tang, Noninvasive quantification of pancreatic fat in healthy male population using chemical shift magnetic resonance imaging: effect of aging on pancreatic fat content, Pancreas 40 (2011) 295–299.

224. M. Heni, J. Machann, H. Staiger, N.F. Schwenzer, A. Peter, F. Schick, C.D. Claussen, N. Stefan, H.U. Häring, A. Fritsche, Pancreatic fat is negatively associated with insulin secretion in individuals with impaired fasting glucose and/or impaired glucose tolerance: a nuclear magnetic resonance study, Diabetes Metab. Res. Rev. 26 (2010) 200–205.

225. E.L. Lim, K.G. Hollingsworth, B.S. Aribisala, M.J. Chen, J.C. Mathers, R. Taylor, Reversal of type 2 diabetes: normalisation of beta cell function in association with decreased pancreas and liver triacylglycerol, Diabetologia 54 (2011) 2506–2514.

226. K.A. Lê, E.E. Ventura, J.Q. Fisher, J.N. Davis, M.J. Weigensberg, M. Punyanitya, H.H.

Hu, K.S. Nayak, M.I. Goran, Ethnic differences in pancreatic fat E.L. Thomas et al. / Progress in Nuclear Magnetic Resonance Spectroscopy 73 (2013) 56–80 79 accumulation and its relationship with other fat depots and inflammatory markers, Diabetes Care 34 (2011) 485–490.

227. P.E. Sijens, M.A. Edens, S.J. Bakker, R.P. Stolk, MRI-determined fat content of human liver, pancreas and kidney, World J. Gastroenterol. 16 (2010) 1993–1998.

228. A.P. Rossi, F. Fantin, G.A. Zamboni, G. Mazzali, C.A. Rinaldi, M. Del Giglio, V. Di Francesco, M. Barillari, R. Pozzi Mucelli, M. Zamboni, Predictors of ectopic fat accumulation in liver and pancreas in obese men and women, Obesity 19 (2011) 1747–1754.

229. A.B. Maggio, P. Mueller, J. Wacker, M. Viallon, D.C. Belli, M. Beghetti, N.J. Farpour-Lambert, V.A. McLin, Increased pancreatic fat fraction is present in obese adolescents with metabolic syndrome, J. Pediatr. Gastroenterol. Nutr. 54 (2012) 720–726.

230. G. Iacobellis, Epicardial and pericardial fat: close, but very different, Obesity 17 (2009) 625.

231. H.S. Sacks, J.N. Fain, Human epicardial adipose tissue: a review, Am. Heart J. 153 (2007) 907–917.

232. R. Quain, On fatty diseases of the heart, Med. Chir. Trans. 33 (1850) 121–196.

233. J.F. Holt, Epipericardial fat shadows in differential diagnosis, Radiology 48 (1947) 472–479.

234. S.L. Cohen, The right pericardial fat pad, Radiology 60 (1953) 391–393.

235. G. Iacobellis, F. Assael, M.C. Ribaudo, A. Zappaterreno, G. Alessi, U. Di Mario, F. Leonetti, Epicardial fat from echocardiography: a new method for visceral adipose tissue prediction, Obes. Res. 11 (2003) 304–310.

236. J.A. den Hollander, W.T. Evanochko, G.M. Pohost, Observation of cardiac lipids in humans by localized 1H magnetic resonance spectroscopic imaging, Magn. Reson. Med. 32 (1994) 175–180.

237. R. Kreis, J. Felblinger, B. Jung, C. Boesch, In vivo 1H-MR spectroscopy of the human heart, MAGMA 6 (1998) 164–167.

238. J. Felblinger, B. Jung, J. Slotboom, C. Boesch, R. Kreis, Methods and reproducibility of cardiac/respiratory double-triggered 1H-MR spectroscopy of the human heart, Magn. Reson. Med. 42 (1999) 903–910.

239. M. Kankaanpää, H.R. Lehto, J.P. Pärkkä, M. Komu, A. Viljanen, E. Ferrannini, J. Knuuti, P. Nuutila, R. Parkkola, P. Iozzo, Myocardial triglyceride content andepicardial fat mass in human obesity: relationship to left ventricular function and serum free fatty acid levels, J. Clin. Endocrinol. Metab. 91 (2006) 4689–4695.

240. R.W. van der Meer, J. Doornbos, S. Kozerke, M. Schär, J.J. Bax, S. Hammer, J.W. Smit, J.A. Romijn, M. Diamant, L.J. Rijzewijk, A. de Roos, H.J. Lamb, Metabolic imaging of myocardial triglyceride content: reproducibility of ^{1}H MR spectroscopy with respiratory navigator gating in volunteers, Radiology 245 (2007) 251–257.

241. B. Gaborit, F. Kober, A. Jacquier, P.J. Moro, T. Cuisset, S. Boullu, F. Dadoun, M.C. Alessi, P. Morange, K. Clément, M. Bernard, A. Dutour, Assessment of epicardial fat volume and myocardial triglyceride content in severely obese subjects: relationship to metabolic profile, cardiac function and visceral fat, Int. J. Obes. 36 (2012) 422–430.

242. G. Iacobellis, M.C. Ribaudo, A. Zappaterreno, C.V. Iannucci, F. Leonetti, Relation between epicardial adipose tissue and left ventricular mass, Am. J. Cardiol. 94 (2004) 1084–1087.

243. F.L. Ruberg, Z. Chen, N. Hua, S. Bigornia, Z. Guo Z, K. Hallock, H. Jara, M. LaValley, A. Phinikaridou, Y. Qiao, J. Viereck, C.M. Apovian, J.A. Hamilton, The relationship of ectopic lipid accumulation to cardiac and vascular function in obesity and metabolic syndrome, Obesity 18 (2010) 1116–1121.

244. S. Hammer, R.W. van der Meer, H.J. Lamb, M. Schär, A. de Roos, J.W. Smit, J.A. Romijn, Progressive caloric restriction induces dose-dependent changes in myocardial triglyceride content and diastolic function in healthy men, J. Clin. Endocrinol. Metab. 93 (2008) 497–503.

245. V.B. Schrauwen-Hinderling, M.K. Hesselink, R. Meex, S. van der Made, M. Schär, H. Lamb, J.E. Wildberger, J. Glatz, G. Snoep, M.E. Kooi, P. Schrauwen, Improved ejection fraction after exercise training in obesity is accompanied by reduced cardiac lipid content, J. Clin. Endocrinol. Metab. 95 (2010) 1932–1938.

246. V.B. Schrauwen-Hinderling, R.C. Meex, M.K. Hesselink, T. van de Weijer, T. Leiner, M. Schär, H.J. Lamb, J.E. Wildberger, J.F. Glatz, P. Schrauwen, M.E. Kooi, Cardiac lipid content is unresponsive to a physical activity training intervention in type 2 diabetic patients, despite improved ejection fraction, Cardiovasc. Diabetol. 10 (2011) 47.

247. R.W. van der Meer, L.J. Rijzewijk, H.W. de Jong, H.J. Lamb, M. Lubberink, J.A. Romijn, J.J. Bax, A. de Roos, O. Kamp, W.J. Paulus, R.J. Heine, A.A. Lammertsma, J.W. Smit, M. Diamant, Pioglitazone improves cardiac function and alters myocardial substrate metabolism without affecting cardiac triglyceride accumulation and high-energy phosphate metabolism in patients with well-controlled type 2 diabetes mellitus, Circulation 119 (2009) 2069–2077.

248. S. Hammer, M. Snel, H.J. Lamb, I.M. Jazet, R.W. van der Meer, H. Pijl, E.A. Meinders, J.A. Romijn, A. de Roos, J.W. Smit, Prolonged caloric restriction in obese patients with type 2 diabetes mellitus decreases myocardial triglyceride content and improves myocardial function, J. Am. Coll. Cardiol. 52 (2008) 1006–1012.

249. B. Gaborit, A. Jacquier, F. Kober, I. Abdesselam, T. Cuisset, S. Boullu-Ciocca, O. Emungania, M.C. Alessi, K. Clément, M. Bernard, A. Dutour, Effects of bariatric surgery on cardiac ectopic fat: lesser decrease in epicardial fat compared to visceral fat loss and no change in myocardial triglyceride content, J. Am. Coll. Cardiol. 60 (2012) 1381–1389.

250. M.S. Dunnill, J.A. Anderson, R. Whitehead, Quantitative histolological studies on age changes in bone, J. Pathol. Bacteriol. 94 (1967) 275–291.

251. K.E. Jensen, M. Jensen, P. Grundtvig, C. Thomsen, H. Karle, O. Henriksen, Localized in vivo spectroscopy of the bone marrow in patients with leukemia, Magn. Reson. Imag. 8 (1990) 779–789.

252. D. Ballon, A. Jakubowski, J. Gabrilove, M.C. Graham, M. Zakowski, C. Sheridan, J.A. Koutcher, In vivo measurements of bone marrow cellularity using volume-localized proton NMR spectroscopy, Magn. Reson. Med. 19 (1991) 85–95.

253. F. Schick, H. Bongers, W.I. Jung, M. Skalej, O. Lutz, C.D. Claussen, Volumeselective proton MRS in vertebral bodies, Magn. Reson. Med. 26 (1992) 207–217.

254. D. Schellinger, C.S. Lin, D. Fertikh, J.S. Lee, W.C. Lauerman, F. Henderson, B. Davis, Normal lumbar vertebrae: anatomic, age, and sex variance in subjects at proton MR spectroscopy—initial experience, Radiology 215 (2000) 910–916.

255. D. Schellinger, C.S. Lin, H.G. Hatipoglu, D. Fertikh, Potential value of vertebral proton MR spectroscopy in determining bone weakness, Am. J. Neuroradiol. 22 (2001) 1620–1627.

256. H. Kugel, C. Jung, O. Schulte, W. Heindel, Age- and sex-specific differences in the ^{1}H-spectrum of vertebral bone marrow, J. Magn. Reson. Imag. 13 (2001) 263–268.

257. J.F. Griffith, D.K. Yeung, H.T. Ma, J.C. Leung, T.C. Kwok, P.C. Leung, Bone marrow

fat content in the elderly: a reversal of sex difference seen in younger subjects, J. Magn. Reson. Imag. 36 (2012) 225–230.

258. M.A. Bredella, M. Torriani, R.H. Ghomi, B.J. Thomas, D.J. Brick, A.V. Gerweck, C.J. Rosen, A. Klibanski, K.K. Miller, Vertebral bone marrow fat is positively associated with visceral fat and inversely associated with IGF-1 in obese women, Obesity 19 (2011) 49–53.

259. D.K. Yeung, J.F. Griffith, G.E. Antonio, F.K. Lee, J. Woo, P.C. Leung, Osteoporosis is associated with increased marrow fat content and decreased marrow fat unsaturation: a proton MR spectroscopy study, J. Magn. Reson. Imag. 22 (2005) 279–285.

260. J.F. Griffith, D.K. Yeung, G.E. Antonio, S.Y. Wong, T.C. Kwok, J. Woo, P.C. Leung, Vertebral marrow fat content and diffusion and perfusion indexes in women with varying bone density: MR evaluation, Radiology 241 (2006) 831–838.

261. T. Baum, S.P. Yap, D.C. Karampinos, L. Nardo, D. Kuo, A.J. Burghardt, U.B. Masharani, A.V. Schwartz, X. Li, T.M. Link, Does vertebral bone marrow fat content correlate with abdominal adipose tissue, lumbar spine bone mineral density, and blood biomarkers in women with type 2 diabetes mellitus?, J Magn. Reson. Imag. 35 (2012) 117–124.

262. W. Shen, J. Chen, M. Punyanitya, S. Shapses, S. Heshka, S.B. Heymsfield, MRImeasured bone marrow adipose tissue is inversely related to DXA-measured bone mineral in Caucasian women, Osteoporos. Int. 18 (2007) 641–647.

263. M.A. Bredella, P.K. Fazeli, K.K. Miller, M. Misra, M. Torriani, B.J. Thomas, R.H. Ghomi, C.J. Rosen, A. Klibanski, Increased bone marrow fat in anorexia nervosa, J. Clin. Endocrinol. Metab. 94 (2009) 2129–2136.

264. E.L. Thomas, J.D. Bell, Intra-cellular fat accumulation, mechanisms and implications for health, Int. J. Body Compos. Res. 4 (2006) 39–43.

Paper 5

Validation of a fast method for quantification of intra-abdominal and subcutaneous adipose tissue for large-scale human studies

Magnus Borga[123], E Louise Thomas[4], Thobias Romu[12], Johannes Rosander[3], ***Julie Fitzpatrick***[4], Olof Dahlqvist Leinhard[35] and Jimmy Bell[4]

Abstract

Central obesity is the hallmark of a number of non-inheritable disorders. The advent of imaging techniques such as MRI has allowed for a fast and accurate assessment of body fat content and distribution. However, image analysis continues to be one of the major obstacles to the use of MRI in large-scale studies. In this study we assess the validity of the recently proposed fat–muscle quantitation system (AMRA™ Profiler) for the quantification of intra-abdominal adipose tissue (IAAT) and abdominal subcutaneous adipose tissue (ASAT) from abdominal MR images. Abdominal MR images were acquired from 23 volunteers with a broad range of BMIs and analysed using sliceOmatic, the current gold-standard, and the AMRA™ Profiler based on a non-rigid image registration of a library of segmented atlases. The results show that there was a highly significant correlation between the fat volumes generated by the two analysis methods, (Pearson correlation $r = 0.97$, $p < 0.001$), with the AMRA™ Profiler analysis being significantly faster (~3 min) than the conventional sliceOmatic approach (~40 min). There was also excellent agreement between the methods for the quantification of IAAT (AMRA 4.73 ± 1.99 versus sliceOmatic 4.73 ± 1.75 l, $p = 0.97$). For the AMRA™ Profiler analysis, the intra-observer coefficient of variation was 1.6% for IAAT and 1.1% for ASAT, the inter-observer coefficient of variation was 1.4% for IAAT and 1.2% for ASAT, the intra-observer correlation was 0.998 for IAAT and 0.999 for ASAT, and the inter-observer correlation was 0.999 for both IAAT and ASAT. These results indicate that precise and accurate measures of body fat content and distribution can be obtained in a fast and reliable form by the AMRA™ Profiler, opening up the possibility of large-scale human phenotypic studies. Copyright © 2015 John Wiley & Sons, Ltd

Introduction

Today, it is generally recognized that central obesity is a key risk factor for the development of a number of metabolic disorders [1,2]. It has also been shown that indirect measures such as body-mass index (BMI), waist circumference, and bioimpedance are poor predictors of regional body fat distribution on an individual level [3–5]. The advent of tomographic imaging modalities such as computer tomography (CT) and MRI has greatly facilitated our ability to directly measure body fat content and distribution in an accurate and reproducible manner [6,7]. Currently, it is possible to obtain a whole-body MRI scan of an individual in less than 5 min, allowing total and regional fat depots to be measured in detail. However, scan costs and image analysis are still substantial obstacles for large population studies. Indeed, MRI measures of whole-body regional body fat distribution have up to now been limited to research studies in relatively small cohorts of subjects, for example 80 subjects in Reference 7 and fewer than 500 in Reference 5. In studies with larger cohorts such as the Dallas Heart Study [8], the Framingham Heart Study [9], and the Multi-Ethnic Study of Atherosclerosis (MESA) [10], very limited abdominal MR/CT imaging was carried out, with some studies using a single slice to define abdominal adiposity. This clearly puts considerable limitations on the total information available to researchers [11]. Furthermore, although cost per scan has reduced considerably in recent years, the time required to analyse these datasets continues to be a major limiting factor, mainly due to the lack of fast, reliable, and reproducible methodologies [12]

In the last few years, an increasing number of genome-wide association studies, using ever-larger cohorts, have been carried out in order to identify common genetic variants associated with complex diseases including obesity, diabetes, heart disease, and cancer [13]. In many of these studies, phenotyping of subjects was limited to either weight or BMI, with some using also waist circumference. More recently a number of large population studies have been initiated where more in-depth phenotyping is sought, including the use of MRI and dual-energy X-ray absorptiometry methodologies, for the purpose of measuring body-fat distribution. One example is the UK Biobank, where up to 100 000 individuals will be scanned using MRI, while in the German Cohort Biobank it is envisaged that 30 000 volunteers will be scanned, many of whom will be followed longitudinally. Besides the obvious demand for efficient scanning protocols, the resulting millions of images need to be analysed in a fast and reproducible manner and at a minimum cost. Although existing manual

and semi-automated systems can be used to analyse images from small cohorts (<100 subjects), they are not feasible for use in large population studies.

The aim of this study is to evaluate the performance of a rapid semi-automated tool for quantification of body fat, including intra-abdominal adipose tissue (IAAT) and abdominal subcutaneous adipose tissue (ASAT) volumes from MR images. Recently, a number of such methods have been proposed [14–20]. Most of these methods [14–19] rely on binary classification of adipose tissue, making them sensitive to partial volume effects [21], a problem that increases with lower spatial resolution. In contrast to these methods, a new method has been proposed, AMRA™ Profiler, based on quantitative fat imaging where the entire fat signal within a certain compartment is taken into account [22,23]. In addition to reducing the sensitivity to partial volume effects, this makes the method less sensitive to segmentation errors. Also in [19], a similar approach was used where fat fraction was integrated within the segmented regions. In the work of Würslin et al. [20] a fuzzy segmentation of T_1-weighted spin- echo images was used to alleviate the problem of partial volume effects. In both these approaches, however, the segmentation was based on a two-dimensional (2D) slice-by-slice analysis. The method used in this study is based on a true three- dimensional (3D) analysis using atlas-based segmentation.

The qualities of the proposed method make it an ideal tool for potential large-scale human studies. However, this tool has not been fully validated against the current gold-standard technique for fat quantitation of MR images. Here, the AMRA™ Profiler is assessed against the tool of choice for fat quantitation, the commercially available sliceOmatic. The results show excellent agreement between the methods across a range of BMI, with analysis using the AMRA™ Profiler taking up to 10 times less time than sliceOmatic. The speed and robustness of the AMRA™ Profiler make it the ideal tool for small- and large-scale human phenotypic studies.

Materials and Methods

Image Acquisition

Written, informed consent was obtained from all volunteers. Ethical permission for this study was obtained from the research ethics committee of Hammersmith and Queen Charlotte's and Chelsea Hospital, London (REC: 07Q04011/19). In total, 23 volunteers (12 male, 11 female) were recruited via advertisements in newspapers, websites, and academic newsletters,

inviting male and female volunteers from the general public. No age constraints were placed on recruitment in order to generate cross-sectional data. Average BMI was 31.7 ± 5.1 kg/m² (range 22–46 kg/m²); age 36–66 years. Each subject was scanned with two different protocols on a 1.5T multinuclear scanner (Achieva, Philips Medical Systems, Best, The Netherlands).

Scanning Protocol

Two different MRI acquisition protocol were used in this study in order to maximize the capabilities of each analysis tool.

Established T_1-weighted acquisition protocol for sliceOmatic

The first scan was obtained using a rapid T_1-weighted protocol as previously described [6]. Briefly, a whole-body axial T_1-weighted spin echo sequence was acquired using a body coil and no respiratory gating (typical parameters: repetition time 560 ms, echo time 18 ms, slice thickness 10 mm, inter-slice gap 10 mm, flip angle 90°, number of excitations 1). Images were acquired as nine equal stacks of 12 slices at the isocentre of the magnet with the subjects in prone position

3D Dixon acquisition for AMRATM profiler.

The second scan was carried out using a phase-sensitive multipoint 3D Dixon acquisition [24] with coverage from the neck to the knees using the integrated quadrature body coil. In this scan, the subjects were in a supine position. Seven image stacks were acquired, of which Stacks 2–5, covering the abdomen, were acquired during breath hold (17s). Parameters for the image acquisition were as follows: repetition time 5.86 ms (8.16 ms for Stacks 3 and 4 covering the liver), echo time n × 1.15 ms, n = 1–4 (n = 1–6 for Stacks 3 and 4), matrix size 172 × 158, slice thickness 4.2 mm (5 mm for stack 7 covering lower part of thigh), and flip angle 13°. Given that each acquisition protocol resulted in slightly different anatomical coverage, for a robust comparison it was therefore decided to extract the same area from both datasets, using the previously published definition of the abdominal area: ‘from the image containing the femoral heads, to the slice containing the top of the liver/bottom of the lungs’ [6].

Image Analysis

Reference Method

SliceOmatic

The T_1-weighted images were analysed as previously described using the semi-automated software sliceOmatic (TomoVision, Montreal, Quebec, Canada), which has become the leading tool for analysis of body fat in clinical and pre-clinical research [8]. Briefly, total and regional volumes were recorded in litres (l), comprising ASAT and IAAT [25]. As previously stated, the abdominal region was defined as the image slices from the slice containing the femoral heads to the slice containing the top of the liver/bottom of the lungs [6]; therefore, the measurement of IAAT contains a mixture of visceral, perirenal, and retroperitoneal adipose tissue. In order to gauge abdominal adiposity as a whole, 'trunk fat' (TF) was derived from the sum of IAAT and ASAT: TF = IAAT + ASAT. The total time for the abdominal segmentation was approximately 40–60 min per dataset. The sliceOmatic analysis of the T_1-weighted images was performed by an independent observer (Vardis Group, London, UK).

AMRA™ Profiler Image Analysis

Image analysis was performed using AMRA™ Profiler (Advanced MR Analytics, Linköping, Sweden) as previously described [22,23], with some modifications. Water and fat images were calculated using a two-step process. First, an initial set of water and fat images was calculated using the first set of opposite phase (T_E= 2.3 ms) and in-phase (T_E = 4.6 ms) images, using the inverse gradient method [26,27]. In order to correct for R_2* effects and the fat signal spectrum, a final set of water–fat images was then calculated using all echoes with an in-house implementation of the IDEAL reconstruction [28,29]. To obtain quantitative fat images, the water and fat image pairs were calibrated using the method described in References 20 and 30. In summary, a quantitative fat image is computed based on pure adipose tissue as an internal signal reference. Hence, the signal intensity level in a given fat image voxel is related to the intensity in pure adipose tissue, which is given the value 1, corresponding to 100% adipose tissue. The IAAT and ASAT compartments were automatically segmented using non-rigid image registration of a library of manually segmented atlases as described in Reference 22. A library of 10 atlases representing a range of body shapes with manually segmented labels for IAAT, arms, and internal non-visceral

adipose tissue was used. A combination of atlas-based segmentation and morphological operations was used to remove the arms. In order to limit variability due to breathing, AMRA™ Profiler uses the top of the femoral head and the top of vertebra T9 as lower and upper limits of the abdominal region in the segmentation of ASAT. In order to further improve the segmentation performance for a larger variation of body shapes, the result from the atlas-based registrations was interpreted as a probability map [31] for each fat compartment, where 1 means that all atlases agree on the classification of adipose tissue and 0 means that no atlas agrees. The final definition of each fat compartment was obtained by applying a threshold value to the probability map of each compartment label. A quick visual inspection of the segmentation of each compartment was performed. In this step, the operator can observe the automated segmentation suggested by the computer and, if necessary, locally adjust the default threshold of the probability map in order to interactively change the final segmentation. To assess inter- and intra-operator variability, the manual interaction was performed three times by three different operators. All operators were employees at AMRA and trained to perform this task. To enable a direct comparison with the conventional sliceOmatic analysis, the volumes were manually cropped at approximately the same levels as the uppermost and lowest slices used to define the abdominal region in the sliceOmatic analysis. Finally, the calibrated fat signal was integrated within each segmented compartment. A scaling with the voxel volume then gave the total volume of adipose tissue within each compartment.

Statistical Analysis

All data are presented as means ± SD. Statistical analysis was performed in Microsoft Excel 2011 (v. 14.2.4) and SPSS (v. 22) for the inter- and intra-observer variability intra-class correlation coefficient (ICC). The Shapiro–Wilk test was performed to test normal distribution of the difference between the two methods. Agreement between techniques was tested with the method of Bland and Altman. The significance of the difference was determined by a two-tailed paired Student t-test. The inter- and intra-observer variability were assessed using the coefficient of variation (CoV) and the ICC using a two-way mixed, absolute agreement model and single measures. Inter-observer CoV was computed for each observer as the quotient between the standard deviation of the three observations and the mean observation and then averaged over all 23 subjects. The intra-observer CoV was computed as the standard deviation of the three observers' mean observations divided by the

total mean and then averaged over all 23 subjects. The intra-observer ICC was computed for each operator separately. The inter-observer ICC was computed between the mean values of each operator.

Results

Typical MR images and their respective image analysis results from one of the volunteers can be seen in Fig. 1. Quantitative measurements of IAAT, ASAT, and total TF were extracted from such images, using the standard sliceOmatic and the AMRA™ Profiler (Table 1). On average it took over 40 min for the abdominal region from the whole-body dataset to be fully analysed by sliceOmatic, necessitating continuous manual input from an expert operator. The AMRA™ Profiler required less than 3 min of manual intervention. The automated intensity inhomogeneity correction and calibration of the fat image volume took approximately 10 min and the atlas-based segmentation took approximately 7 min per atlas on a standard PC. The Shapiro–Wilk test showed no significant deviation from a normal distribution for the differences in IAAT, ASAT, and TF measurements ($p = 0.077$, $p = 0.147$, and $p = 0.159$ respectively). There was no significant difference in the amount of IAAT measured using AMRATM Profiler compared with the conventional sliceOmatic analysis (AMRA™ Profiler 4.73 ± 1.99 versus sliceOmatic 4.73 ± 1.75 l, $p = 0.97$). The difference in quantification of ASAT was 10.39 ± 5.38 (AMRATM Profiler) versus 9.78 ± 5.36 l (sliceOmatic), $p < 0.001$, and for TF 15.12 ± 5.74 (AMRA™ Profiler) versus 14.50 ± 5.50 l (sliceOmatic), $p = 0.005$. Excellent agreement between the two methods was observed for all fat depots (Fig. 2). For IAAT the 95% limits of agreement were -1.06 to 1.07 (Fig. 2a). Similar findings were observed with ASAT, where the 95% limits of agreement were -0.36 to 1.60 (Fig. 2b). For TF, the linear regression coefficient was 1.03 with an offset of 0.19 l and the 95% limits of agreements were -1.26 to 2.50 l (Fig. 2c). However, on average the AMRA rapid semi-automated system volume estimates of ASAT and TF were numerically larger, though not significantly, than the sliceOmatic analysis (6.3% for ASAT and 4.3% for TF). The measurement of IAAT was very similar between the two methods (0.1% for IAAT). A linear regression analysis of the Bland–Altman plots showed a significant linear regression coefficient of 0.134 ($p = 0.029$) for IAAT. For ASAT and TF, there was no significant linear regression ($p = 0.834$ and $p = 0.248$ respectively). Neither of the errors in IAAT or ASAT

showed any significant correlation to the amount of TF ($p = 0.248$ and $p = 0.335$ respectively). The intra-observer CoV was 0.9%, 1.5%, and 2.4% for Operators 1–3 respectively (average 1.6%) for IAAT and 0.6%, 1.1%, and 1.6% respectively (average 1.1%) for ASAT (Table 2). The intra-observer ICC was 1.000, 0.999, and 0.996 for Operators 1–3 respectively (average 0.998) for IAAT and 1.000, 0.999, and 0.998 for Operators 1–3 respectively (average 0.999) for ASAT. The inter-observer CoV was 1.4% for IAAT and 1.2% for ASAT. The inter-observer ICC was 0.999 for both IAAT and ASAT.

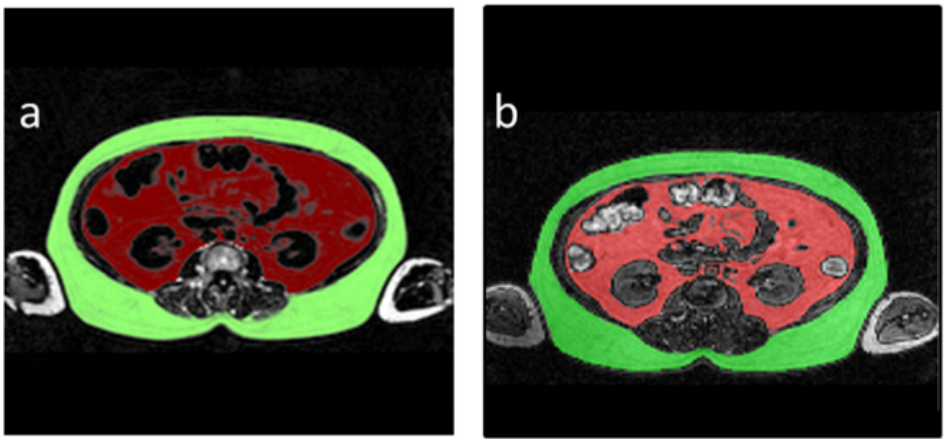

Fig 1. MR images from typical volunteer. (a) The calibrated fat image with intra-abdominal and subcutaneous segmentations made by the AMRA™ Profiler overlaid in red and green respectively. (b) The approximately corresponding transverse slice from the same subject analysed by sliceOmatic. In this example both images were acquired with the volunteer positioned in a supine position to make the images more readily comparable

Table 1. Measurements of IAAT, ASAT, and trunk AT with the two analysis methods

Subject no	IAAT (l)		ASAT (l)		Trunk AT (l)	
	sliceOmatic	AMRA	sliceOmatic	AMRA	sliceOmatic	AMRA
1	1.30	1.16	11.73	11.48	13.03	12.63
2	5.85	6.70	4.44	5.38	10.29	12.08
3	6.24	6.28	11.71	12.52	17.94	18.80
4	4.12	4.03	20.67	21.63	24.79	25.66
5	5.50	5.20	5.29	5.72	10.79	10.92
6	3.36	3.33	2.94	3.46	6.30	6.79
7	5.14	4.74	5.82	6.56	10.96	11.29
8	4.00	3.48	7.79	7.90	11.80	11.38
9	3.74	3.13	15.39	15.42	19.13	18.56
10	7.23	8.69	7.73	9.76	14.96	18.45
11	2.51	2.16	7.84	8.52	10.36	10.68
12	4.18	3.40	10.16	9.74	14.34	13.14
13	7.38	7.14	9.54	10.75	16.92	17.89
14	2.09	2.36	7.21	7.93	9.30	10.29
15	6.66	6.52	9.92	10.22	16.58	16.74
16	5.72	5.00	7.35	7.75	13.06	12.75
17	4.09	4.10	10.86	11.75	14.95	15.84
18	4.31	4.50	4.30	4.92	8.62	9.42
19	6.06	6.03	11.27	11.67	17.32	17.70
20	7.75	8.37	6.05	6.76	13.81	15.12
21	3.39	3.53	18.71	19.64	22.09	23.17
22	2.87	2.81	4.71	5.40	7.58	8.21
23	5.22	6.17	23.41	24.14	28.63	30.31

Volumes of intra-abdominal (IAAT), abdominal subcutaneous (ASAT), and total trunk adipose tissue measured in litres for each volunteer using sliceOmatic and AMRA™ Profiler.

Discussion

Rapid scanning protocols are well as automated image analysis are essential in large population studies where in vivo imaging modalities are becoming the norm. This study shows that quantification of central obesity, including IAAT ('visceral fat') and ASAT, can be done using a rapid semi-automated quantification method of MR images acquired with a very rapid multi-point Dixon protocol. Furthermore, the correlation to the current gold-standard semi-automated segmentation program (sliceOmatic) was extremely high for all fat depots. The agreement between the two methods of quantification was also extremely high. The design of the study was such that not only differences in analysis method were a factor, but also the MRI acquisition protocol. Whilst it might seem counter-intuitive to both acquire the data using different MRI sequences (T_1 versus 3D-Dixon) and have the patient in a different position (prone versus supine), it was decided that a true test of the standard versus the AMRA™ Profiler must ensure that the optimal and validated protocol should be used in each instance, so as to minimize potential bias for any given method. Given the variation in

acquisition and analysis, it is perhaps more impressive that the agreement in measurement particular of IAAT is so high. Indeed, the strong linear correlation and excellent agreement between the sliceOmatic and AMRA™ Profiler results indicates that the latter can be reliably used for quantification of IAAT, ASAT, and total TF. Moreover, given that the standard segmentation technique takes more than 40 min per subject for a trained operator, making it unfeasible for large population studies, the short analysis time of the AMRA™ Profiler, less than 3 min per subject, opens a realistic possibility for the analysis of MRI data sets from large cohort studies. The computation time for the automated processing, of course, depends on implementation and hardware. Parallel computing, e.g. using a GPU implementation or multi-core CPU, could of course reduce the current computation time. The linear regression coefficient was close to unity for both compartments, though the AMRA™ Profiler volume estimates were numerically larger for ASAT, though not significantly, than for sliceOmatic analysis. The differences between techniques were independent of the BMI and/or the total body fat content of the volunteers. Therefore, it is possible that the methods of defining which slices from the whole-body dataset to equate to the abdominal compartment generally used (the top of the liver to top of femoral head) could account for this difference rather than a difference between the analysis methods *per se*. There was, however, a positive linear correlation between the differences in IAAT measures and the IAAT volume, indicating that for subjects with more IAAT the AMRA™ Profiler tends to give smaller IAAT estimates than the reference method. The different acquisition approaches necessitated identifying the selecting matching top and bottom slices from an axial acquisition with relatively thick slices and inter-slice gaps and from a 3D dataset. A small mismatch, particularly in the lower slices containing the femoral heads, could have a significant impact of the amount of subcutaneous adipose tissue included (but not internal adipose tissue), since this covers the area where anatomically a small change in position can result in a substantial difference in subcutaneous fat content. A limitation with the AMRA™ Profiler is that it requires fat– water separated or complex-valued Dixon images, and cannot therefore be used for analysing already existing data acquired with, for example, a more traditional T_1-weighted protocol. However, the proposed rapid Dixon protocol has several advantages compared with the more traditional T_1-weighted protocol used as reference in this study. First of all, the close to isotropic image resolution, in combination with the breath-hold technique, gives a complete 3D data volume rather than a stack of more or less independent 2D image slices. This significantly simplifies

the use of 3D image processing, which also facilitates volumetric measurements of other anatomical structures and organs. Second, the calibrated fat image is specifically sensitive to fat, which is not the case for T_1-weighted images. A calibrated fat image also enables quantification of diffuse fat infiltration, e.g. in muscles and internal organs. It should also be stressed that the AMRA™ Profiler gives an objective, user-independent quantification of the fat signal. Only the anatomical definition of the compartment of interest is subject to segmentation as well as inspection and manual interaction. This is important, e.g., in the visceral compartment, where intestinal content easily can be mistaken for adipose tissue. The excellent inter- and intra-observer ICC and the very low interand intra-observer variability shown in this study confirm this. The CoV for the intra-observer comparison of 1.6% for IAAT and 1.1% for ASAT can be compared with values reported in an earlier study [32], where the investigated method (Hippo Fat) had a CoV of 7.25% for IAAT and 1.77% for ASAT and the sliceOmatic analysis had a CoV of 4.53% for IAAT and 1.85% for ASAT. The use of a quantitative fat image also means that, as opposed to methods based on classification of individual voxels into adipose or non-adipose tissue as in References 14–16, the method used here is much less affected by partial volume effects [21], since the fat in voxels containing a mix of adipose and nonadipose tissue will also be included. Estimation errors caused by partial volume effects increase with lower resolution, which is a consequence of rapid whole-body acquisition. Furthermore, the AMRA™ Profiler used in this study has also been used for compartmental muscle volume measurements [33], which is also a relevant factor in metabolic studies.

Table 2. Measurements of IAAT and ASAT using AMRA™ Profiler by three different operators

Subject no	IAAT (l)			ASAT (l)		
	Op. 1	Op. 2	Op. 3	Op. 1	Op. 2	Op. 3
1	7.58	7.67	7.66	12.59	12.67	12.72
2	7.31	7.36	7.32	12.15	12.22	12.26
3	3.68	3.78	3.88	9.43	9.39	9.54
4	2.53	2.60	2.56	8.40	8.38	8.60
5	1.32	1.29	1.29	11.08	10.98	11.22
6	5.73	5.77	5.73	5.95	5.83	6.05
7	9.28	9.41	9.23	7.72	7.75	7.79
8	3.84	3.94	3.91	3.63	3.57	3.56
9	6.73	6.86	6.73	5.39	5.26	5.36
10	7.05	7.18	7.04	11.51	11.44	11.59
11	6.78	6.95	6.79	13.25	13.24	13.23
12	4.45	4.45	4.39	21.63	21.67	22.10
13	4.35	4.53	4.49	19.39	18.86	19.03
14	3.15	3.18	3.11	15.80	15.74	15.70
15	9.61	9.76	9.50	10.61	10.51	10.52
16	4.36	4.39	4.47	13.66	13.65	13.87
17	3.34	3.40	3.37	5.56	5.57	5.61
18	2.35	2.43	2.54	9.35	9.35	9.58
19	4.98	5.07	5.02	4.88	4.84	4.94
20	5.38	5.45	5.28	7.44	7.34	7.38
21	4.43	4.52	4.56	12.93	12.91	13.12
22	6.96	7.38	7.14	24.23	23.38	22.92
23	5.11	5.18	5.30	6.50	6.44	6.42

Volumes of IAAT and ASAT measured three times by three different operators. The CoV for the intra-observer comparison was 1.6% for IAAT and 1.1% for ASAT. The inter-subject CoV for IAAT and ASAT was 1.6% and 1.1% respectively.

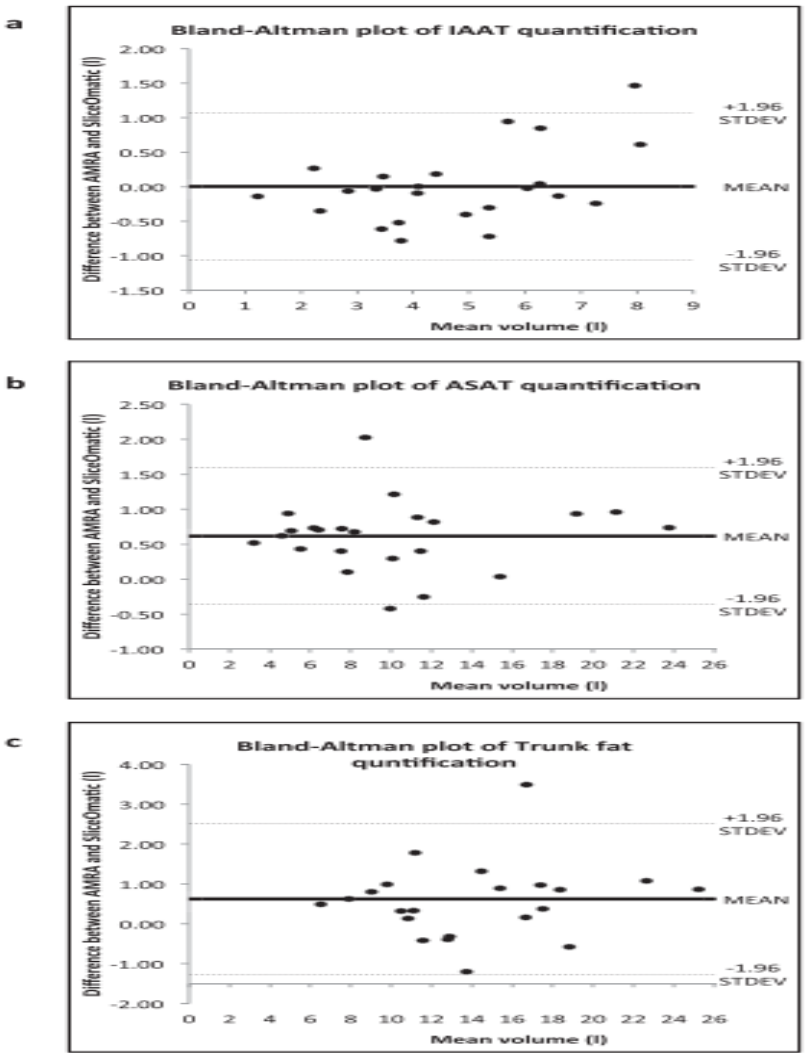

Fig 2. Bland–Altman plots describing agreement between fat volumes measured using sliceOmatic and the AMRA™ Profiler method for (a) IAAT, (b) ASAT, and (c) total trunk adipose tissue.

Acknowledgements

LT and JDB gratefully acknowledge funding from the UK Medical Research Council. We would like to thank Dr AP Goldstone and Giuliana Durighel for their contribution in the recruitment and scanning of volunteers.

Conflict of Interest

ELT, JF and JDB have no conflict of interest to declare. MB, TR, JR and ODL are stock holders in Advanced MR Analytics (AMRA).

References

1.Neeland IJ, Ayers CR, Rohatgi AK, Turer AT, Berry JD, Das SR, Vega GL, Khera A, McGuire DK, Grundy SM, de Lemos JA. Associations of visceral and abdominal subcutaneous adipose tissue with markers of cardiac and metabolic risk in obese adults. Obesity 2013; 21: E439–E47.

2. Cerhan JR, Moore SC, Jacobs EJ, Kitahara CM, Rosenberg PS, Adami H-O, Ebbert JO, English DR, Gapstur SM, Giles GG, Horn-Ross PL, Park Y, Patel AV, Robien K, Weiderpass E, Willett WC, Wolk A, Zeleniuch-Jacquotte A, Hartge P, Bernstein L, Berrington de Gonzalez A. A pooled analysis of waist circumference and mortality in 650,000 adults. Mayo Clin. Proc. 2014; 89: 335 345.

3. Prentice AM, Jebb SA. Beyond body mass index. Obes. Rev. 2001; 2: 141–147.

4. Thomas EL, Frost G, Taylor-Robinson SD, Bell JD. Excess body fat in obese and normal-weight subjects. Nutr. Res. Rev. 2012; 25: 150–161.

5. Thomas EL, Parkinson JR, Goldstone AP, McCarthy JP, Fitzpatrick JA, Durighel G, Taylor-Robinson SD, Bell JD. The missing risk: MRI and MRS phenotyping of abdominal adiposity and ectopic fat. Obesity 2012; 20: 76–87.

6. Thomas EL, Saeed N, Hajnal JV, Brynes A, Goldstone AP, Frost G, Bell JD. Magnetic resonance imaging of total body fat. J. Appl. Physiol. 1998; 85: 1778–1785.

7. Machann J, Schnoedt B, Schick F, Thamer C, Haap M, Haring HU, Claussen CD, Stumvoll M, Fritsche A, Schick F. Standardized assessment of whole body adipose tissue topography by MRI. J. Magn. Reson. Imaging 2005; 21: 455–462.

8. Chandra A, Neeland IJ, Berry JD, Ayers CR, Rohatgi A, Das SR, Khera A, McGuire DK, de Lemos JA, Turer AT. The relationship of body mass and fat distribution with incident hypertension: observations from the Dallas Heart Study. J. Am. Coll. Cardiol. 2014; 64: 997–1002.

9. Fox CS, Massaro JM, Hoffmann U, Pou KM, Maurovich-Horvat P, Liu CY, Vasan RS, Murabito JM, Meigs JB, Cupples LA, D'Agostino RB, Sr, O'Donnell CJ. Abdominal visceral

and subcutaneous adipose tissue compartments: association with metabolic risk factors in the Framingham Heart Study. Circulation 2007; 116: 39–48.
10. Shah RV, Murthy VL, Abbasi SA, Blankstein R, Kwong RY, Goldfine AB, Jerosch-Herold M, Lima JA, Ding J, Allison MA. Visceral adiposity and the risk of metabolic syndrome across body mass index: the MESA study. JACC Cardiovasc. Imaging 2014; 7(12): 1221–1235.
11. Thomas EL, Bell JD. Influence of undersampling on magnetic resonance imaging measurements of intra-abdominal adipose tissue. Int. J. Obes. Relat. Metab. Disord. 2003; 27: 211–218.
12. Bonekamp S, Ghosh P, Crawford S, Solga SF, Horska A, Brancati FL, Diehl AM, Smith S, Clark JM. Quantitative comparison and evaluation of software packages for assessment of abdominal adipose tissue distribution by magnetic resonance imaging. Int. J. Obes. 2008; 32: 100–111.
13. Fall T, Ingelsson E. Genome-wide association studies of obesity and metabolic syndrome. Mol. Cell. Endocrinol. 2014; 382: 740–757.
14. Kullberg J, Karlsson AK, Dahlgren J, Stokland E, Svensson PA. Adipose tissue distribution in children: automated quantification using water and fat MRI. J. Magn. Reson. Imaging 2010; 32: 204–210.
15. Poonawalla AH, Sjoberg BP, Rehm JL, Hernando D, Hines CD, Irarrazaval P, Reeder SB. Adipose tissue MRI for quantitative measurement of central obesity. J. Magn. Reson. Imaging 2013; 37: 707–716.
16. Thörmer G, Bertram HH, Garnov N, Peter V, Schütz T, Shang E, Blüher M, Kahn T, Busse H. Software for automated MRI-based quantification of abdominal fat and preliminary evaluation in morbidly obese patients. J. Magn. Reson. Imaging 2013; 37: 1144–1150.
17. Wald D, Teucher B, Dinkel J, Kaaks R, Delorme S, Boeing H, Seidensaal K, Meinzer HP, Heimann T. Automatic quantification of subcutaneous and visceral adipose tissue from whole-body magnetic resonance images suitable for large cohort studies. J. Magn. Reson. Imaging2012; 36: 1421–1434.
18. Müller HP, Raudies F, Unrath A, Neumann H, Ludolph AC, Kassubek J. Quantification of human body fat tissue percentage by MRI. NMR Biomed. 2011; 24: 17–24.
19. Addeman BT, Kutty S, Perkins TG, Soliman AS, Wiens CN, McCurdy CM, Beaton MD, Hegele RA, McKenzie CA. Validation of volumetric and single-slice MRI adipose analysis

using a novel fully automated segmentation method. J. Magn. Reson. Imaging 2015; 41: 233–241.
20. Würslin C, Machann J, Rempp H, Claussen C, Yang B, Schick F. Topography mapping of whole body adipose tissue using a fully automated and standardized procedure. J. Magn. Reson. Imaging 2010; 31: 430–439.
21. Ludwig UA, Klausmann F, Baumann S, Honal M, Hövener JB, König D, Deibert P, Büchert M. Whole-body MRI-based fat quantification: acomparison to air displacement plethysmography. J. Magn. Reson. Imaging 2014; 40: 1437–1444.
22. Leinhard OD, Johansson A, Rydell J, Smedby O, Nystrom F, Lundberg P. Quantitative abdominal fat estimation using MRI. Int. C. Patt Recog. 2008; 19: 2137–2140.
23. Erlingsson S, Herard S, Dahlqvist O, Lindström T, Länne T, Borga M, Nystrom FH, Group FFS. Men develop more intraabdominal obesity and signs of the metabolic syndrome after hyperalimentation than women. Metabolism 2009; 58: 995–1001.
24. Dixon W. Simple proton spectroscopic imaging. Radiology 1984; 153:189–194.
25. Ostberg JE, Thomas EL, Hamilton G, Attar MJH, Bell JD, Conway GS. Excess visceral and hepatic adipose tissue in Turner syndrome determined by magnetic resonance imaging: estrogen deficiency associated with hepatic adipose content. J. Clin. Endocrinol. Metab. 2005; 90: 2631–2635.
26. Rydell J, Knutsson H, Pettersson J, Johansson A, Farnebäck G, Dahlqvist O, Lundberg P, Nyström F, Borga M. Phase sensitive reconstruction for water/fat separation in MR imaging using inverse gradient. Med. Image Comput. Comput. Assist. Interv. 2007; 10: 210–218.
27. Rydell J, Johansson A, Leinard OD, Knutsson H, Farnebäck G, Lundberg P. Three dimensional phase sensitive reconstruction for water/fat separation in MR imaging using inverse gradient. Proc.Int. Soc. Magn. Reson. Med. 2008; 1519.
28. Reeder SB, Pineda AR, Wen Z, Shimakawa A, Yu H, Brittain JH, Gold GE, Beaulieu CH, Pelc NJ. Iterative decomposition of water and fat with echo asymmetry and least-squares estimation (IDEAL): application with fast spin-echo imaging. Magn. Reson. Med. 2005; 54: 636–644.
29. Hernando D, Hines CDG, Yu H, Reeder SB. Addressing phase errors in fat–water imaging using a mixed magnitude/complex fitting method. Magn. Reson. Med. 2012; 67: 638–644.

30. Romu T, Borga M, Dahlqvist Leinhard O. MANA – multi scale adaptive normalized averaging. In 2011 IEEE International Symposium on Biomedical Imaging: From Nano to Macro. IEEE,. Wright S, Pan X, Liebling M (eds). Chicago: 2011, 361–364.
31. Svarer C, Madsen K, Hasselbalch SG, Pinborg LH, Haugbøl S, Frøkjær VG, Holm S, Paulson OB, Knudsen GM. MR-based automatic delineation of volumes of interest in human brain PET images using probability maps. Neuroimage 2005; 24: 969–979.
32. Demerath EW, Ritter KJ, Couch WA et al. Validity of a new automated software program for visceral adipose tissue estimation. Int. J. Obes. 2007; 31: 285–291.
33. Thomas MS, Newman D, Leinhard OD, Kasmai B, Greenwood R, Malcolm PN, Karlsson A, Rosander J, Borga M, Toms AP. Test–retest reliability of automated whole body and compartmental muscle volume measurements on a wide bore 3T MR system. Eur. Radiol.2014; 24: 2279–2291.

Paper 6

Changes in Liver Volume in Patients with Chronic Hepatitis C Undergoing Antiviral Therapy

Julie Fitzpatrick, Jin Kim, Jeremy Cobbold, Mark McPhail, Mary Crossey, Aluel Bak-Bol, Ashraf Zaky, Simon Taylor-Robinson[1]

Abstract

Liver volumetric analysis has not been used to detect hepatic remodelling during antiviral therapy before. We measured liver volume (LV) changes on volumetric magnetic resonance imaging during hepatitis C antiviral therapy. Methods: 22 biopsy-staged patients (median [range] age 45^{19-65} years; 9F, 13M) with chronic hepatitis C virus infection were studied. LV was measured at the beginning, end of treatment and 6 months post-treatment using 3D T1-weighted acquisition, normalised to patient weight. Liver outlines were drawn manually on 4 mm thick image slices and LV calculated. Inter-observer agreement was analysed. Patients were also assessed longitudinally using biochemical parameters and liver stiffness using Fibroscan™. Results: Sustained viral response (SVR) was achieved in 13 patients with a mean baseline LV/kg of 0.022 (SD 0.004) L/kg. At the end of treatment, the mean LV/kg was 0.025 (SD 0.004, P = 0.024 cf baseline LV/kg) and 0.026 (SD 0.004, P = 0.008 cf baseline LV/kg) 6 months post-treatment (P = 0.030 cf baseline, P = 0.004). Body weight-corrected end of treatment LV change was significantly higher in patients with SVR compared to patients not attaining SVR (P = 0.050). End of treatment LV change was correlated to initial ALT (R^2 = 0.479, P = 0.037), but not APRI, AST, viral load or liver stiffness measurements. There was a correlation of 0.89 between observers for measured slice thickness. *Conclusions*: LV increased during anti-viral treatment, while the body weight-corrected LV increase persisted post-antiviral therapy and was larger in patients with SVR. (J Clin Exp Hepatol 2016;6:15–20)

Introduction

Hepatitis C virus (HCV) is a blood-borne hepatotrophic RNA virus of significant worldwide public health concern [1]. Currently estimates indicate that there are 270–300 million people

infected worldwide with the incidence of HCV expecting to peak in the next 10–20 years [1]. Treatment of HCV aims to improve outcome by slowing or halting progression to cirrhosis and hepatocellular carcinoma (HCC), but serial biopsy during or following treatment is not considered necessary or ethical at present. Non-invasive methods of assessing pathological changes in the liver are being assessed, but are often expensive, conceptually difficult or require specialist equipment [2]. At present, there is no accepted physiological description of any remodelling changes occurring during antiviral therapy, nor is there an accepted proxy to virological measurement to assess response to treatment. Patients with chronic liver disease (CLD) frequently undergo imaging studies using magnetic resonance imaging (MRI) scanning primarily for the assessment of focal lesions. Volumetric analysis of the liver by MRI [3,4] is applicable to many clinical settings [5-7]. In operative planning particularly for partial hepatectomy prior to surgery [3] for malignancy and for live-related liver donation, liver volume (LV) is useful in assessing the risk of inducing liver failure in the resection candidate [8] or ‘‘small-for-size’’ syndrome in the graft recipient [9]. Smaller LVs are seen in more advanced cases of fibrosis and in increasing Child–Pugh class of cirrhosis [10]. In patients with cirrhosis and portal hypertension, a LV of 75% can be expected, compared to age-matched controls. LV may also be related to pre-fibrotic metabolic processes such as steatosis or hepatitis B [11]. Patients with non-alcoholic fatty liver disease (NAFLD) have increased LV which has been shown to decrease on intensive weight loss programs [12]. Furthermore, NAFLD is associated with faster disease progression in HCV and may contribute to the baseline LV prior to treatment. Some authors have suggested that it is useful to assess changes in volume over time as an indicator of therapeutic effectiveness and or disease progression [13]. MRI is well established as an accurate means to measure LV [4, 14]. Unlike computed tomography (CT) scanning, MRI avoids the subject being exposed to ionising radiation, and the use of nephrotoxic contrast media is not necessary for volumetric analysis. CT volumetry has been employed in LV estimation in patients with acute liver failure [5, 15], although this is likely due to a pragmatic choice of rapid scanning modality in these critically ill patients. Longitudinal measurement of LV during treatment for chronic HCV infection has never been performed previously, and MR would be a preferred platform to perform this readily understood and exportable potential longitudinal marker. The purpose of this study was to measure and observe any changes in LV accurately in a cohort of patients undergoing therapy for chronic hepatitis C infection with pegylated interferon-alpha and ribavirin and assess the

correlation of volumetric change with biochemical, virological and ultrasound transient elastography (Fibroscan™, Echosens, Paris, France) indices of treatment response to help understand putative hepatic remodelling processes during successful viral eradication.

Methods

Patient Selection

Twenty-two patients with chronic hepatitis C (CHC) were prospectively recruited over a 2-year period from Imperial College Healthcare Trust with prior informed, written consent obtained from each subject. Ethical approval was obtained from the regional ethics committee in accordance with the 1975 Declaration of Helsinki, (ethics reference no. 06/Q041/10). Patients were studied at the beginning and 6 months after stopping treatment with pegylated interferon alpha 2a and ribavirin, the treatment time being genotype dependent with 24 weeks treatment given for genotypes 2 and 3, while genotypes 1 and 4 received 48 weeks treatment. Patients were included if they were aged 18–65 years, had evidence of replicating HCV infection on HCV RNA testing (Abbott Realtime HCV assay, Abbott Diagnostics, Illinois, USA), and had been referred for percutaneous liver biopsy for clinical indications. Patients were excluded if they consumed >20 g of alcohol per day; were obese (with a body mass index >30 kg/m²) or diabetic; if they were taking antiviral therapy; were co-infected with HIV or hepatitis B; were currently taking intravenous drugs, antihypertensive or lipidlowering medications; had ongoing illness or had evidence of hepatic decompensation. Histological grading was performed by an experienced histopathologist using standardised scoring criteria. Sustained virological response (SVR) was defined as no detectable virus on quantitative RNA testing 6 months post-treatment. Length of treatment was decided by genotype as per European Association for the Study of the Liver (EASL) guidelines [16]. All patients completed the study.

MRI

Patients were scanned using a Philips 1.5 T Achieva™ MRI (Philips Medical Systems, Best, Netherlands). Scans were performed at baseline, 3 months, end of treatment and 6 months post-treatment. Using a SENSE surface body coil, TFE 3D T_1-weighted DRIVe Equilibrium sequence were performed in a single breath-hold following hyperventilation. The parameters were FOV 375 260, TR 7, TE 3.4, FA 15, 50 slices 8 mm/4 mm, thus resulting in 4 mm slice thickness. All the data were sent to one workstation (Viewforum version R4.2V1L2 [Philips

Medical Systems, Best, The Netherlands]. The edge of the liver contour was manually drawn using the curser by an observer with 14 years' experience in MR imaging (JAF). This process was repeated for each slice; approximately 50 per examination, a total of 3500 contours were drawn in total (Figure 1). The ViewForum gives an area in mm [2], which was then multiplied by 4 to obtain a volume for the slice. These values were summed and divided by 1,000,000 to obtain a volume in litres. The LV was normalised to patient weight given the expected change in weight during antiviral therapy. An exercise in reproducibility was also undertaken for LV. Two observers (one experienced radiographer (JAF) and one hepatologist (AZ) analysed 46 randomised slices five times, over a disparate timeframe resulting in 230 liver areas being analysed. Further comparison was made by measuring and comparing the two observers drawing contours five times around five slices.

Non-invasive Markers of Liver Fibrosis

On the same day as MRI volume studies, all patients had serial standard blood liver biochemistry and both serum Enhanced Liver Fibrosis test (ELF™) (Siemens Healthcare Global, Erlangen, Germany) and hepatic liver stiffness measurements using Fibroscan™ (Echosens, Paris, France) as non-invasive markers of liver fibrosis.

Statistical Methods

Variables pre- and post-treatment were compared using paired t-testing and repeated measures ANOVA and % change in these variables was also assessed using oneway ANOVA. Coefficients of variability among measurements for the same patient were estimated and variability among observers was assessed using the intra-class correlation coefficient (ICC). Statistical significance was defined at the 95% level and all P-values calculated were two-tailed. Normality was assessed using the D'Agostino-Pearson test. Statistical analysis was performed using SPSS v 15 (SPSS, Chicago, USA) and MedCalc v 11.1 (MedCalc, Mariakerke, Belgium).

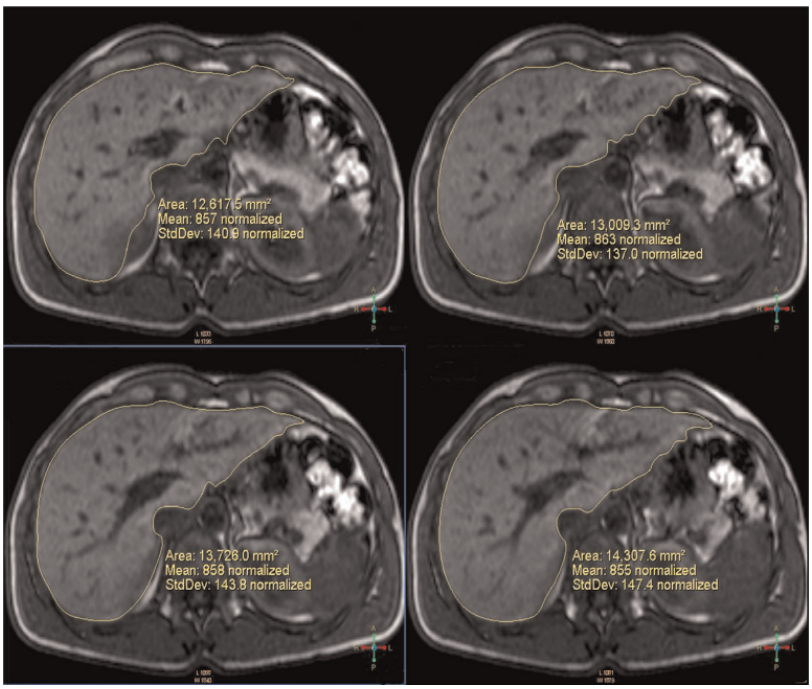

Fig 1. An example of liver contour drawing of 4 slices of a magnetic resonance imaging study

Results

Twenty-two patients (12M:10F) of median age 47 (19–65) years made up the study cohort. Eleven patients were current smokers and 7 patients were current alcohol users. The mean BMI was 25 (3.4) kg/m². The median fibrosis score on biopsy was 3 (1–6) and necroinflammatory (NI) score 4 (1–6) from biopsies of median length 26 (4–48) mm. Of these, only two patients had established cirrhosis and were well compensated with normal albumin levels and prothrombin times (Child grade A). The other 20 patients had pre-cirrhotic liver disease with good hepatic synthetic function. Twelve patients were genotype 1, two genotype 2, six genotype 3 and two genotype 4 with a median baseline viral load of 130417 (1404-3455391 copies/mL). The other baseline clinical and biochemical parameters are shown in Table 1 with their change during therapy

Volumetry

Thirteen of the participants achieved sustained viral response (SVR), 6 months after finishing treatment. The mean LV/kg at the start of treatment for all participants was 0.022 (SD 0.004) L/kg. Including all participants, the LV at the end of treatment was 0.025 (SD 0.004) L/kg (mean difference %, P = 0.024, Paired t test compared to baseline LV shown in Figure 2) and

further increased to 0.026 (0.004) L/kg 6 months after the conclusion of treatment (P = 0.008 compared to baseline, P = 0.034, repeat measures ANOVA, linear trend). The change in LV was more pronounced in those patients who achieved SVR (MD + 0.004, P = 0.008, one way ANOVA). Volume change was not related to treatment duration or genotype (P = 0.543, repeated measures ANOVA) and body-weight corrected LV change was dependent on virological response (P = 0.050, repeated measures ANOVA). Baseline LV was correlated to waist circumference (R = 0.496, P = 0.016). However, no further correlations were found with ALT, AST, APRI score, viral load, indices of necroinflammation or fibrosis, Fibroscan-measured liver stiffness or body mass index (BMI). However, the end of treatment LV was correlated to initial ALT (R = 0.479, P = 0.037), but not to initial APRI, AST or viral load. LV change was not dependent on the presence of cirrhosis at the start of therapy. There was no significant change in liver stiffness as measured by ultrasound transient elastography using Fibroscan™ over the course of therapy (10 (8) kPa to 11 (2) kPa, P = 0.778 Paired t test) and no correlation between Fibroscan™ change and LV change (R = 0.196, P = 0.487). However, significant change was noted with ELF™ serum testing (10 (1) to 10 (2), P = 0.0467, paired t test).

Table 1 Paired Change in Baseline Variables During Treatment Presented as Mean (SD). The Group Interaction was Assessed Using Repeated Measures ANOVA. ALT = alanine aminotransferase; GGT = gamma-glutamyl transpeptidase; Hb = haemoglobin; ELF™ = enhanced liver fibrosis score.

Variable	Pre-treatment	End of treatment	Paired *t* test	Group (SVR) Factor Interaction
ALT, iU/L	117 (103)	45 (39)	0.0018	0.297
GGT, iU/L	77 (65)	56 (40)	0.1393	0.821
Hb, g/L	140 (10)	120 (20)	<0.0001	0.074
AST, iU/L	79 (53)	48 (37)	0.0007	0.212
Platelets, $\times 10^9$/mL	195 (64)	170 (65)	0.0189	0.354
ELF™ score	10 (1)	10 (2)	0.0467	0.782
Triglycerides, mmol/L	1 (1)	2 (1)	0.0001	0.030
Low density lipoprotein, mmol/L	2 (1)	25 (64)	0.1631	0.952
Fibroscan™	10 (8)	11 (2)	0.7781	0.967
Liver volume, L	1.5 (0.3)	1.6 (0.3)	0.0276	0.115
Liver volume per kg body weight, L/kg	0.022 (0.004)	0.025 (0.004)	0.002	0.147

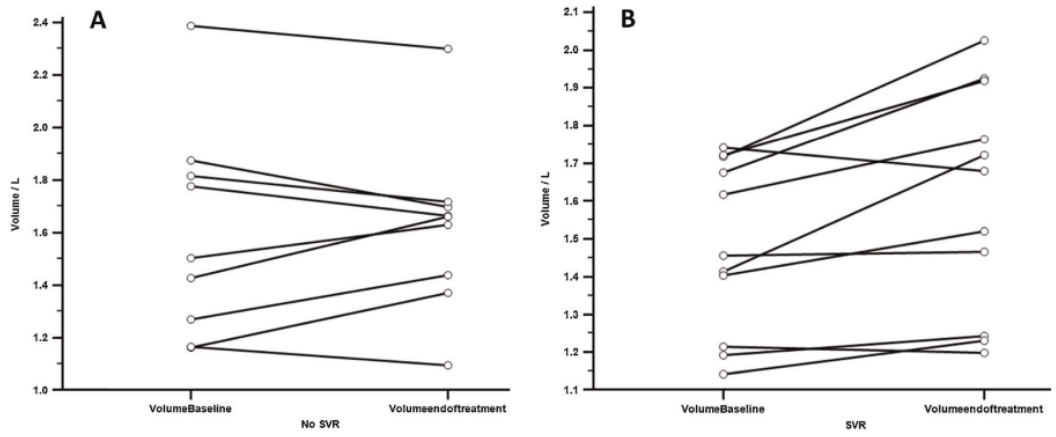

Fig 2. Comparison of liver volume in participants at baseline before the treatment and after 6 months of therapy. (A) Participants who did not achieve sustained viral response (P = 0.438); (B) Participants who achieved sustained viral response (P = 0.020).

Reproducibility

Comparison of LV measurements between the two observers showed a mean difference of 1% which is not statistically significant. The mean standard error/% slice area for the second observer was 2–1.5. The mean (SD) area/slice measurement was 9256 (116) mm^3 with the standard error over all the analysed slices 53 mm^3. Thus, the % standard error/slice measurement was measured at 1.02 (±0.18) % with only four slices having a % standard error greater than 2%. The intra-class correlation coefficient between observer 1 and 2 was 0.707 (95% CI: 0.331–0.867), suggesting good agreement. However, Passing and Bablock regression while demonstrating an intercept not significantly different from zero (8225 (-2492–12392)) did show a deviation from linearity in the slope (0.574 (0.363–1.1101)), suggesting there may be errors in agreement dependent on slice area.

Discussion

In this study, we have aimed to accurately measure and observe any variations in LV in a cohort of patients undergoing therapy for chronic hepatitis C infection with pegylated alpha interferon and ribavirin and assess the correlation of volumetric change with standard and novel indices of treatment response. For the first time, we have demonstrated that the LV rises during antiviral treatment and is more pronounced when measured over a 12-month period in patients, who achieve SVR. Volume increase could be interpreted as an indication of liver regeneration and/or recovery and this may be related to reduction in fibrotic load of the liver. Hepatic

fibrogenesis is dominantly orchestrated by hepatic stellate cell activation, which describes the conversion of the normally quiescent vitamin A storage cells to 'myofibroblasts', which contribute to both structural and dynamic hepatic fibrosis. Resolution of myofibroblast activity is regarded as an important step in the reversal of inflammatory damage, initiated by the expression of extracellular remodelling signals, which contribute to fibrotic load [17]. While the liver stiffness on Fibroscan™ did not decrease, this is not necessarily the best test to determine very small changes in fibrosis given that there are a number of false positives related to an abnormal Fibroscan™ including changes in liver perfusion [18]. Furthermore, changes in fibrotic load, as they require the reversal of myofibroblastic activation, are likely to resolve over a longer time frame than during the study period, so the Fibroscan technique may not detect any small reduction in fibrotic load of the liver in the face of any hepatic perfusion/inflammatory changes [2]. We observed a small, but significant increase in LV with SVR. This change is not related to baseline histological severity, suggesting that this is an effect of viral clearance. Furthermore, no positive correlation can be found in this study between the observed changes and Fibroscan™ or ELF score. Further studies assessing the changes in LV with MR-measured perfusion techniques are required. MRI is an expensive imaging modality and although commonplace in the developed world, demand on this particular resource is high. However, abdominal and liver studies are commonly performed on MRI due to its superior tissue contrast and lesion detection [19]. Therefore, the addition of another fast breath-hold sequence assessing LV in a larger population could be considered, particularly given the difficulty in performing serial liver biopsies in this population. Both performing and post-processing of MR images involve highly trained personnel, while manually defining liver contours is time consuming, and we have shown that bias can be introduced when non-imaging trained staff perform contour analysis. It would be advantageous to develop automated techniques to define LV both currently and prospectively on acquired data sets. Novel registration techniques [20] are currently in development and automated methods may soon be available, when the limitations of breath-hold acquisitions are overcome. Furthermore, we did not assess functional LV in this study, which is possible using SPECT-CT [21]. However, this is unlikely to be a source of bias, as no patients in this study had significant vascular abnormalities. A particular strength of our study was the reproducibility of MRI LV assessment. We would recommend that this assessment is done by trained staff, given the findings from Passing and Bablock regression. This is in agreement with previous studies [14], which

demonstrated that using MRI is a robust method for measuring LV and has the advantage of avoiding contrast media use and exposure of ionising radiation to participants. While multiple other modalities were employed to determine a potential mechanism of hepatic remodelling via non-invasive imaging our results were not conclusive in this regard. In future studies, it would be useful to measure LV changes during disease therapy, which in conjunction with the other imaging modalities discussed here, could further elucidate which mechanisms are involved hepatic remodelling of long-term fibro-inflammatory diseases.

Conflicts of Interest

The authors have none to declare.

Acknowledgments

All authors acknowledge the support of the United Kingdom National Institute for Health Research (NIHR) Biomedical Research Centre at Imperial College London for infrastructure support. The study was supported by a research grant from Pfizer Global Inc. (New York, USA). JFLC was supported by a grant from the Hammersmith Hospital Centenary Fund (London, United Kingdom); MJWM by a Fellowship from the Welcome Trust (London, United Kingdom) and MMEC by a research grant from Pfizer Global Inc. (New York, USA). MMEC and SDT-R hold grants from the United Kingdom Medical Research Council.

References

1. Wedemeyer H, Dore GJ, Ward JW. Estimates on HCV disease burden worldwide – filling the gaps. J Viral Hepat. 2015;22(suppl 1):1–5.

2. Cobbold JF, Patel D, Taylor-Robinson SD. Assessment of inflammation and fibrosis in non-alcoholic fatty liver disease by imagingbased techniques. J Gastroenterol Hepatol. 2012; 27:1281 1292.

3. Karlo C, Reiner CS, Stolzmann P, et al. CT- and MRI-based volumetry of resected liver specimen: comparison to intraoperative volume and weight measurements and calculation of conversion factors. Eur J Radiol. 2010; 75:e107–e111.

4. Reiner CS, Karlo C, Petrowsky H, Marincek B, Weishaupt D, Frauenfelder T. Preoperative liver volumetry: how does the slice thickness influence the multidetector computed

tomography- and magnetic resonance-liver volume measurements. J Comput Assist Tomogr. 2009; 33:390–397.
5. Yamagishi Y, Saito H, Ebinuma H, et al. A new prognostic formula for adult acute liver failure using computer tomography-derived hepatic volumetric analysis. J Gastroenterol. 2009; 44:615–623.
6. Kishi Y, Abdalla EK, Chun YS, et al. Three hundred and one consecutive extended right hepatectomies: evaluation of outcome based on systematic liver volumetry. Ann Surg. 2009; 250:540–548.
7. de Graaf W, van Lienden KP, Dinant S, et al. Assessment of future remnant liver function using hepatobiliary scintigraphy in patients undergoing major liver resection. J Gastrointest Surg. 2010;14: 369–378.
8. Paluszkiewicz R, Zieniewicz K, Kalinowski P, et al. Liver regeneration in 120 consecutive living-related liver donors. Transplant Proc. 2009; 41:2981–2984.
9. Simpson AL, Jarnagin WR, D'Angelica MI. Hepatic resection planning in the modern era: in reply to Mise and colleagues. J Am Coll Surg. 2014; 219:1195–1197.
10. Caldwell SH, de Lange EE, Gaffey MJ, et al. Accuracy and significance of pretransplant liver volume measured by magnetic resonance imaging. Liver Transpl Surg. 1996; 2:438–442.
11. Li WX, Zhao XT, Chai WM, et al. Hepatitis B virus-induced liver fibrosis and cirrhosis: the value of liver and spleen volumetry with multidetector spiral computed tomography.J Dig Dis. 2010;11:215–223.
12. Chen TY, Chen CL, Tsang LL, et al. Correlation between hepatic steatosis, hepatic volume, and spleen volume in live liver donors. Transplant Proc. 2008; 40:2481–2483.
13. Zoli M, Cordiani MR, Marchesini G, Abbati S, Bianchi G, Pisi E. Ultrasonographic follow-up of liver cirrhosis. J Clin Ultrasound. 1990;18:91–96.
14. Thomas EL, Hamilton G, Patel N, et al. Hepatic triglyceride content and its relation to body adiposity: a magnetic resonance imaging and proton magnetic resonance spectroscopy study. Gut. 2005;54:122–127.
15. Yamagishi Y, Saito H, Tada S, et al. Value of computed tomographyderived estimated liver volume/standard liver volume ratio for predicting the prognosis of adult fulminant hepatic failure in Japan. J Gastroenterol Hepatol. 2005; 20:1843–1849.
16. European Association for Study of Liver. EASL Clinical Practice Guidelines: management of hepatitis C virus infection. J Hepatol. 2014; 60:392–420.

17. Friedman SL, Bansal MB. Reversal of hepatic fibrosis—fact or fantasy? Hepatology. 2006; 43:S82–S88.
18. Cobbold JF, Taylor-Robinson SD. Transient elastography in acute hepatitis: all that's stiff is not fibrosis. Hepatology. 2008; 47: 370–372.
19. de Lange EE, Mugler 3rd JP, Gay SB, DeAngelis GA, Berr SS, Harris EK. Focal liver disease: comparison of breath-hold T1-weighted MP-GRE MR imaging and contrast-enhanced CT—lesion
detection, localization, and characterization. Radiology. 1996; 200:465–473.
20. Rajaraman S, Rodriguez JJ, Graff C, et al. Automated registration of sequential breath-hold dynamic contrast-enhanced MR images: a comparison of three techniques. Magn Reson Imaging. 2011; 29: 668–682.
21. Beppu T, Hayashi H, Okabe H, et al. Liver functional volumetry for portal vein embolization using a newly developed 99mTc-galactosyl human serum albumin scintigraphy SPECT-computed tomography fusion system. J Gastroenterol. 2011; 46:938–943.

Paper 7

Psoas Major Crosssectional Area: A Potential Marker of Cardiorespiratory Fitness

Julie Fitzpatrick, Edward S Chambers[1], James R C Parkinson, Gary Frost[1], Jimmy D Bell, E Louise Thomas

Abstract

Cardiorespiratory fitness is an important marker for overall health that significantly correlates with obesity-associated morbidities and mortality. Maximal oxygen uptake (VO_{2max}) recorded during an incremental exercise test is the gold standard assessment for aerobic fitness. However, its cost, chronic illness, and frailty often preclude its application. The cross-sectional area (CSA) of the abdominal psoas major muscle is a predictor of sarcopenia and surgery outcomes and represents a promising biomarker for cardiorespiratory health. Therefore, in the present study, we have planned to assess the relationship between psoas major CSA, anthropometry, and body composition in a UK-based cohort of 210 men and women. **Methods:** Body mass (kg), height (cm), waist circumference (cm), VO_{2max}, and blood pressure were measured in each participant. The CSA of psoas major, rectus abdominus, and another abdominal muscle of the core muscle group were assessed. **Results:** Following adjustment for height, psoas major CSA was found to be a significant predictor of percentage body fat (P = 0.02) in men, and body mass index (BMI) in both men (P = 0.015) and women (P = 0.004). We found psoas major CSA correlated more strongly with VO2max (r = 0.74, P < 0.01) than any other study outcome, including age and BMI. **Conclusion:** Psoas major muscle CSA represents an accurate, reproducible, and time-efficient surrogate for cardiorespiratory fitness and body composition.

Introduction

Physical inactivity significantly contributes to both morbidity and mortality, with public health organizations now increasingly promoting habitual exercise to reduce the negative impact of a sedentary lifestyle [1,2]. Improvements in cardiorespiratory fitness are a key target for intervention, with maximal oxygen uptake (VO_{2max}) recorded during an incremental exercise

test to exhaustion, being considered the gold standard [3,4]. Cardiorespiratory fitness is inversely related to fat mass [3], type 2 diabetes prevalence [5], and a more reliable predictor of mortality than other established markers, such as blood pressure or circulating cholesterol [6]. However, the time commitment and cost of performing these tests often make them impractical, and chronic illness or frailty in elderly patients precludes their application. Consequently, there is a need for accurate and reproducible biomarkers for use as surrogates of cardiorespiratory fitness. Morphometric analysis of core muscle cross-sectional area (CSA) is emerging as a strong indicator of health outcomes [7], with an increase in muscle fiber CSA as the main functional adaptation arising from aerobic and strength training.[8] The psoas major is a large muscle of the abdomen, forming part of the core muscle group, assisting lateral rotation and abduction of the hip joint.[9] Psoas major CSA has been used in a number of studies to predict the total body lean muscle mass[10], sarcopenia [11], and surgical outcomes in elderly patients [12,13]. It therefore represents a potential marker for cardiorespiratory fitness. In the present study, we would like to characterize how the CSA of psoas major and the rectus abdominus (RA), another Morphometric analysis of core muscle cross-sectional area (CSA) is emerging as a strong indicator of health outcomes [7], with an increase in muscle fiber CSA as the main functional adaptation arising from aerobic and strength training [8]. The psoas major is a large muscle of the abdomen, forming part of the core muscle group, assisting lateral rotation and abduction of the hip joint [9]. Psoas major CSA has been used in a number of studies to predict the total body lean muscle mass [10], sarcopenia [11], and surgical outcomes in elderly patients [12,13]. It therefore represents a potential marker for cardiorespiratory fitness. In the present study, we would like to characterize how the CSA of psoas major and the rectus abdominus (RA), another abdominal muscle of the core muscle group, vary with age, gender, and BMI in a cross-sectional population. Second, in a subset of our cohort, we have assessed the relationship between these muscles CSA and VO_{2max} to gauge their potential as a surrogate marker for overall physical health.

Materials and Methods

Ethical Approval

Written informed consent was acquired from all volunteers. Ethical approval for this study was obtained from the Brent National Research Ethics Committee (Rec: 12/LO/0139). All studies were carried out in accordance with the Declaration of Helsinki. In total, 210 participants were

recruited through advertisements in newspapers, websites, academic newsletters, and inviting male and female volunteers of Caucasian ethnicity from the general public. Participants presented with no history of chronic disease or excess alcohol intake were included in the study. Individuals on prescribed medication and pregnant women were excluded from the study.

Anthropometry, blood pressure, and clinical biochemistry

Body mass (kg), height (cm), and waist circumference (cm) were measured in each participant by a single experienced observer. Fasting glucose, total cholesterol, triglycerides, high-density lipoprotein, low-density lipoprotein, and insulin were measured by standard methods by the Department of Chemical Pathology, Imperial College Healthcare National Health Service Trust. Blood pressure of the participants was measured by trained clinician using an automatic sphygmomanometer after 5 min of rest in supine position.

Scanning

Individuals underwent magnetic resonance imaging (MRI) at 1.5T (Archiva, Philips Medical Systems, The Netherlands) following an overnight fast. Participants were in prone position, and T1-weighted axial images of the whole body were obtained as described previously [14]. During the same scanning session, ^{1}H MR spectra were also acquired at 1.5T. Using a surface coil, intrahepatocellular lipid (IHCL) was measured relative to liver water content [15].

Psoas major and rectus abdominus

Using the open source image processing program Image-J (NIH, USA), the CSA of the psoas major was manually isolated at lumbar point L3/L4. The CSA of the rectus abdominis (RA), which can also be clearly observed within the same axial slice, was measured from the same MRI images to provide a comparison core muscle. The CSA values for each muscle group in this study correspond to the sum of the CSA of the right- and left-hand sides [Supplementary Figure 1]. Due to the strong correlation between psoas major muscle and height, values are also presented as CSA/height^2 (mm^2 /m^2) [16].

Reproducibility

To test the reproducibility of the manual analysis of psoas major and RA CSA, two separate exercises were undertaken. In test 1, left and right muscle CSA [Supplementary Figure 1] were assessed three times in a row by the same observer; psoas: (Average [standard deviation [SD]) 4165.1 ± 24.37 mm^2, coefficient of variation (CoV): 0.59%; RA: 1826.0 ± 9.2 mm^2, and CoV:

0.50%. In test 2, the same axial slice was measured on three separate occasions, at 1 week intervals; average (SD): 4117.3 ± 61.92 mm² and CoV: 1.5%. In test 2, the analysis was repeated three times on a single, randomly chosen image, 1 week apart by the same observer; psoas CoV: 2.9% and RA: 3.7%.

VO_{2max} Assessment

An incremental cycling test to exhaustion [4] was carried out on the same study day as the MRI scan to obtain VO_{2max} in a subset of the cohort (99 individuals [67 male, 32 female]).

Statistical Analysis

Student's t-test and Spearman's rank correlations were performed on variables; psoas major CSA, RA CSA, and VO_{2max}. Linear regression was performed in GraphPad Prism version 6.0 (GraphPad Software, USA). IHCL values were log transformed after adding + 1 to their values due to the nonnormally distributed nature of the outcome [14]. Correlation was performed in SPSS 23 (IBM SPSS Statistics for Windows, USA) and linear regression in GraphPad Prism. $P < 0.05$ was considered significant. All data were presented as mean ± SD.

Results

A total of 210 participants (97F, 113M) took part in the initial study to characterize psoas major and RA muscles, both raw and adjusted for height, are summarized in Table 1. Average psoas CSA/height² and RA CSA/height² measurements for the entire cohort were 942 + 93 and 436 ± 141, respectively. Women presented with significantly smaller psoas and RA when compared to men (psoas CSA/height²: female 741+167 mm² /m², male 1114 + 266 mm² /h², $P < 0.001$; RA CSA/height²: female 324 ± 73 mm² /h², male 491 ± 134 mm² /h², $P < 0.001$).

Table 1: Characteristics of baseline cohort n = 210 (113 male, 97 female)

	Mean±SD	Range
Age (year)	43.8±14.5	18-67
Weight (kg)	79.8±18.1	40.7-146.6
Height (m)	1.7±0.1	1.5-2.0
BMI (kg/h^2)	26.6±5.1	15.5-47.5
Waist (cm)	90.2±15.7	56.5-131
Hip (cm)	103.6±9.5	76-136
WHR	0.87±0.1	0.67-1.09
Psoas major CSA (mm^2/m^2)	2857±1051	718-7458
Psoas major CSA/height^2	942±293	231-2312
RA CSA (mm^2/m^2)	1333±515	554-3217
RA/height^2	436141	198-998
S-IMCL	13.4±7	2.28-50.4
T-IMCL	6.4±3.5	0.25-30.5
IHCL	3.7±9.8	0.0-108.7
Total fat (kg)	24.3±11.1	5.4-67.0
Subcutaneous (kg)	19.3±9.2	3.79-57.3
Internal (kg)	5.0±2.8	0.88-14.7
Subcutaneous abdominal (kg)	5.5±3.2	0.65-18.2
Subcutaneous peripheral (kg)	13.8±6.1	3.14-39.7
Visceral (kg)	2.7±1.9	0.31-10.4
Nonvisceral internal (kg)	2.3±1.0	0.53-6.2

Data presented as mean ± SD. WHR: Waist to hip ratio, BMI: Body mass index, CSA: Cross-sectional area, RA: Rectus abdominis, S-IMCL: Soleus intramyocellular lipid, T-IMCL: Tibialis intramyocellular lipid, IHCL: Intrahepatocellular lipid, SD: Standard deviation

Figure 1 shows how muscle CSA, adjusted for height, varied by gender, age, BMI, and percentage body fat. Linear regression analysis revealed a significant inverse relationship between psoas CSA/height2 and age in men [r = 0.13; P = 0.016, Figure 1a] with no effect in women [Figure 1b]. Both psoas major CSA/height² (r = 0.28; P = 0.004) and RA CSA/height² (r = 0.46; P < 0.001) were significant predictors of BMI in women [Figure 1d], while only psoas major CSA/height² predicted BMI in men (r = 0.22, P = 0.015). Lastly, psoas major CSA/height² was a significant inverse predictor of body fat percentage in men [r = 0.22; P = 0.02, Figure 1e]. Examination of the relationship between psoas and RA with metabolically adverse fat depots, visceral fat and IHCL, can be found in Figure 2. Psoas major CSA/height² inversely predicted visceral fat in men [r = 0.20; P = 0.02, Figure 2a], while RA CSA/height² was a significant predictor of IHCL in women [r = 0.22; P = 0.02, Figure 2b]. A comparison of how psoas major and RA muscles (after adjustment for height) correlate with study outcomes is shown in Supplementary Figure 2. Both psoas major CSA/height² and RA/height² were inversely correlated with age (r = −0.49, P < 0.01, r = −0.50, P < 0.01). RA/height2 was significantly associated with visceral (r = 0.28, P < 0.01) and nonvisceral adipose tissue (r = 0.20, P < 0.05) with no correlation observed with psoas major CSA/height² (P = NS).

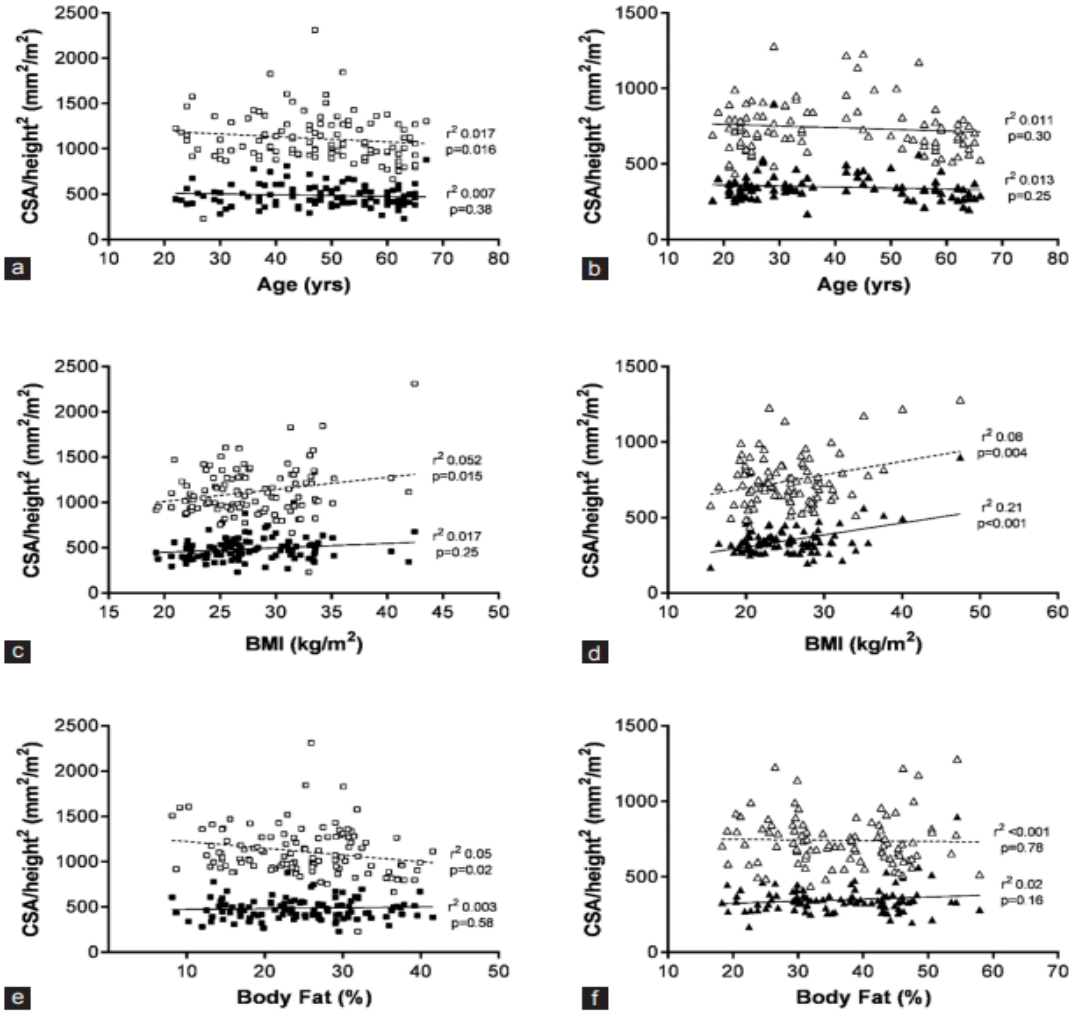

Fig 1: Gender-specific distribution of psoas and rectus abdominus muscle cross-sectional area/height² with age, body mass index, and percentage body fat. Cross-sectional area adjusted for height (cross-sectional area/height²) of psoas major (white square/circle) and rectus abdominus (black square/circle) muscles in men (a, c and e) and women (b, d, and f) by age (a and b), body mass index (c and d), and percentage body fat (e and f). Linear regression performed in GraphPad Prism with corresponding r² and P values. □: Male psoas; Δ: Female psoas; ■: Male rectus abdominus; ▲: Female rectus abdominus

Further investigation in a smaller, older subset of the cohort for which VO_{2max} was available (n = 105 (72M), age 54.5 ± 8.5 years) was carried out to assess the validity of psoas major and RA muscle CSA as a marker for cardiorespiratory fitness. Baseline characteristics for this cohort are shown in Supplementary Figure 3. Average VO_{2max} was 2523 ± 1091 ml/min, with female VO_{2max} lower (1520 ± 332 ml/min) than male (3002 ± 998 ml/min). After correction for weight, male VO_{2max} was 32.2 ± 12.1 ml/kg/min, while female was 19.9 ± 4.3 ml/kg/min. Correlation analysis between VO_{2max} (adjusted for weight) and study outcomes is shown in Table 2. Psoas major muscle CSA/height2 (mm² /m²) correlated strongly with VO_{2max}

(ml/kg/min) (r = 0.56, P < 0.01), with no association observed with RA CSA/height² (r = 0.17, P = NS). Both age (r = -0.64) and height (r = 0.49) correlated strongly with VO_{2max} to a similar degree of significance (P < 0.01). Gender-specific analysis revealed a significant correlation between psoas major CSA/height2 and VO_{2max} (ml/kg/min) (r = 0.33, P < 0.01) in males. In female volunteers, VO_{2max} (ml/kg/min) correlated strongly with individual adipose compartments but no associations were observed with anthropometric or core muscle group measurements [Table 2]. Gender-specific distribution of psoas major and RA CSA/height² with VO_{2max} (ml/kg/min) is shown in Figure 3. Linear regression revealed psoas major CSA/height² which were significant predictors of VO_{2max} in male participants [P < 0.001, Figure 3a], with no effect in women [Figure 3b]. RA muscle was not found to be a significant predictor of VO_{2max} in either men or women [Figure 3].

Discussion

In the present study, we characterize how the CSA of psoas major and RA muscles varies with age, gender, and BMI in a cross-sectional population. The CSA of the psoas major strongly correlated with and was a significant predictor of VO_{2max} in a male subset of our cohort, with no such relationship observed with RA. Physical inactivity is a leading cause of most chronic illness and practical methods to determine fitness levels are needed to enable effective assessment of lifestyle interventions and public health planning [17,18]. The use of MRI and computerized tomography (CT) scans to measure the content and distribution of body fat is increasingly common in both research and clinical fields, with cross-sectional abdominal imaging a common procedure in a diagnostic setting. Postprocessing of abdominal region scans enables an in-depth investigation of tissue morphology, including the CSA of different muscles. Muscle size represents a quantitative index, reflecting general health and intervention risk [19]. While obtaining whole-body images can be time-consuming and expensive, studies have shown that the CSA of abdominal skeletal muscle provides a reliable surrogate of whole body muscle mass [10]. Within this region lies the psoas major muscle, a component of the core muscle group and a surrogate marker for sarcopenia and surgical outcomes [9,12,20]. The RA muscle, often referred to as the abdominals, is another component of the core muscle group that lies within the L4 region and was included in our analysis as a comparator. The psoas major is easily identified on axial images in both MRI and CT scan, and analysis of muscle CSA can be easily translated into any research institute where cross-sectional imaging of the

abdominal region is available using this simple and straightforward method. Our data indicate psoas major CSA predicts VO_{2max}, albeit in men only, with no such effect observed with RA. Correlation analyses of RA and psoas major CSA adjusted for height revealed comparable degrees of association for the majority of study outcomes. There was however a significant inverse correlation between psoas major CSA and age, a relationship not observed with RA. In addition, while the psoas was negatively correlated with total, subcutaneous, and subcutaneous abdominal fat, RA also showed a positive correlation with metabolically adverse visceral and internal fat stores [21]. Cardiorespiratory fitness is known to be a significant predictor of fat mass and together these data indicate that of the two core muscles, the psoas major is the more viable marker for metabolic and cardiovascular health. Ethnic differences exist regarding muscle mass distribution [22] and to avoid these potentially confounding effects, study recruitment was limited to Caucasians. Further research is therefore warranted to determine the influence of broader participant demographics on the positive associations between psoas major CSA, cardiorespiratory fitness, adiposity, and fat-free mass. As expected, the CSA of both psoas major and RA muscles was significantly smaller in women compared to men, necessitating gender-specific analysis. The inverse relationship observed between psoas and age in men was expected and reflects an established association [22]. However, in women, we failed to see a reduction in either psoas major or RA size as age increased, or indeed any correlation between VO_{2max} and other outcomes. Indeed, it is clear that the significant associations we did observe between VO_{2max} and study outcomes were driven by the relationship in men. Several factors may have contributed to this; first, the number of women for which VO2max data were available was considerably smaller (n = 33) compared to men (n = 72). Second, the range of VO_{2max} values was more limited in women (511–1175 ml/min) than men (663–2312 ml/min), perhaps reflecting the reduced levels of reported physical activity in women who participated; 24% reported “fit” (corresponding to >5 h exercise per week), compared to 42% of the men. Interventional studies which employ exercise and subsequently measure the effects on VO_{2max} and core muscle size will be required to eliminate the confounding effects of age and determine the efficacy of psoas as a marker of metabolic fitness.

Limitations of the Study

Sample size in the present study was less.

Conclusion

Our findings indicate that psoas major CSA measured at L4 is strongly associated with cardiorespiratory fitness, adiposity, and fat-free mass. Hence, psoas major is a potential marker of cardiorespiratory fitness. Additional work in a larger, racially diverse population with a more expansive range of fitness levels will be required to confirm its utility.

Financial support and sponsorship

GF, JB, and ELT were all funded through the Nutritech study (FP7-KBBE-289511).

Conflicts of Interest

There are no conflicts of interest.

References

1. World Health Organisation. Global Strategy on Diet, Physical Activity and Health: Physical Activity and Adults. World Health Organisation; 2015. Available from: http://apps.who.int/gb/ebwha/pdf_files/WHA57/A57_9-en.pdf?ua=1.
2. Physical Activity Guidelines for Adults – Live Well – NHS Choices. Department of Health, NHS; 2013.
3. Dunn AL, Marcus BH, Kampert JB, Garcia ME, Kohl HW, Blair SN. Comparison of lifestyle and structured interventions to increase physical activity and cardiorespiratory fitness: A randomized trial. JAMA 1999; 281:327-34.
4. Kuipers H, Verstappen FT, Keizer HA, Geurten P, van Kranenburg G. Variability of aerobic performance in the laboratory and its physiologic correlates. Int J Sports Med 1985; 6:197-201.
5. Wei M, Gibbons LW, Mitchell TL, Kampert JB, Lee CD, Blair SN. The association between cardiorespiratory fitness and impaired fasting glucose and type 2 diabetes mellitus in men. Ann Intern Med 1999; 130:89-96.
6. Myers J, Prakash M, Froelicher V, Do D, Partington S, Atwood JE. Exercise capacity and mortality among men referred for exercise testing. N Engl J Med 2002; 346:793-801.
7. Englesbe MJ, Lee JS, He K, Fan L, Schaubel DE, Sheetz KH, et al. Analytic morphomics, core muscle size, and surgical outcomes. Ann Surg 2012; 256:255-61.

8. Bogdanis GC. Effects of physical activity and inactivity on muscle fatigue. Front Physiol 2012; 3:142.
9. Regev GJ, Kim CW, Tomiya A, Lee YP, Ghofrani H, Garfin SR, et al. Psoas muscle architectural design, in vivo sarcomere length range, and passive tensile properties support its role as a lumbar spine stabilizer. Spine (Phila Pa 1976) 2011; 36:E1666-74.
10. Shen W, Punyanitya M, Wang Z, Gallagher D, St-Onge MP, Albu J, et al. Total body skeletal muscle and adipose tissue volumes: Estimation from a single abdominal cross-sectional image. J Appl Physiol 2004; 97:2333-8.
11. Jones KI, Doleman B, Scott S, Lund JN, Williams JP. Simple psoas cross-sectional area measurement is a quick and easy method to assess sarcopenia and predicts major surgical complications. Colorectal Dis2015; 17:O20-6.
12. Durand F, Buyse S, Francoz C, Laouénan C, Bruno O, Belghiti J, et al. Prognostic value of muscle atrophy in cirrhosis using psoas muscle thickness on computed tomography. J Hepatol 2014; 60:1151-7.
13. Englesbe MJ, Patel SP, He K, Lynch RJ, Schaubel DE, Harbaugh C, et al. Sarcopenia and mortality after liver transplantation. J Am Coll Surg 2010; 211:271-8.
14. Thomas EL, Parkinson JR, Frost GS, Goldstone AP, Doré CJ, McCarthy JP, et al. The missing risk: MRI and MRS phenotyping of abdominal adiposity and ectopic fat. Obesity (Silver Spring) 2012; 20:76-87.
15. Thomas EL, Hamilton G, Patel N, O'Dwyer R, Dore CJ, Goldin RD, et al. Hepatic triglyceride content and its relation to body adiposity: A magnetic resonance imaging and proton magnetic resonance spectroscopy study. Gut 2005; 54:122-7.
16. Bhamidipati PK, Carson KR, Wildes TM. Psoas cross-sectional area as radiographic measure of sarcopenia does not predict overall survival in multiple myeloma. Blood 2013; 122:5236.
17. Booth FW, Roberts CK, Laye MJ. Lack of exercise is a major cause of chronic diseases. Compr Physiol 2012; 2:1143-211.
18. Lee IM, Shiroma EJ, Lobelo F, Puska P, Blair SN, Katzmarzyk PT. Effect of physical inactivity on major non-communicable diseases worldwide: An analysis of burden of disease and life expectancy. Lancet 2012; 380:219-29.

19. Lee JS, He K, Harbaugh CM, Schaubel DE, Sonnenday CJ, Wang SC, et al. Frailty, core muscle size, and mortality in patients undergoing open abdominal aortic aneurysm repair. J Vasc Surg 2011; 53:912-7.
20. Sheetz KH, Zhao L, Holcombe SA, Wang SC, Reddy RM, Lin J, et al. Decreased core muscle size is associated with worse patient survival following esophagectomy for cancer. Dis Esophagus 2013; 26:716-22.
21. Bergman RN, Kim SP, Catalano KJ, Hsu IR, Chiu JD, Kabir M, et al. Why visceral fat is bad: Mechanisms of the metabolic syndrome. Obesity (Silver Spring) 2006;14 Suppl 1:16S-9S.
22. Silva AM, Shen W, Heo M, Gallagher D, Wang Z, Sardinha LB, et al. Ethnicity-related skeletal muscle differences across the lifespan. Am J Hum Biol 2010; 22:76-82.

Paper 8

Advancing Pancreas Segmentation in Multi-protocol MRI Volumes using Hausdorff-Sine Loss Function

Hykoush Asaturyan[1], E. Louise Thomas, ***Julie Fitzpatrick***[2], Jimmy Bell[2], and Barbara Villarini[1]

Abstract

Computing pancreatic morphology in 3D radiological scans could provide significant insight about a medical condition. However, segmenting the pancreas in magnetic resonance imaging (MRI) remains challenging due to high inter-patient variability. Also, the resolution and speed of MRI scanning present artefacts that blur the pancreas boundaries between overlapping anatomical structures. This paper proposes a dual-stage automatic segmentation method: 1) a deep neural network is trained to address the problem of vague organ boundaries in high class-imbalanced data. This network integrates a novel loss function to rigorously optimise boundary delineation using the modified Hausdorff metric and a sinusoidal component; 2) Given a test MRI volume, the output of the trained network predicts a sequence of targeted 2D pancreas classes that are reconstructed as a volumetric binary mask. An energy-minimisation approach fuses a learned digital contrast model to suppress the intensities of non-pancreas classes, which, combined with the binary volume performs a refined segmentation in 3D while revealing dense boundary detail. Experiments are performed on two diverse MRI datasets containing 180 and 120 scans, in which the proposed approach achieves a mean Dice score of 84.1 ± 4.6% and 85.7 ± 2.3%, respectively. This approach is statistically stable and outperforms state-of-the-art methods on MRI.

Introduction

Segmenting the pancreas in 3D radiological scans (e.g. an MRI volume) could provide significant insight into the severity or progression of type 2 diabetes [1] and ductal adenocarcinoma [2]. However, pancreas segmentation presents several challenges due to high structural and inter-patient variability in size and location. The greyscale intensity of the

pancreas can be very similar to neighbouring tissue, and the boundary contrast can vary depending on the level of surrounding visceral fat. Differing from computer tomography (CT), the low resolution and slower imaging speed of MRI presents edge-based artefacts that blur the imaging boundaries between the pancreas and surrounding organs [3]. In existing research literature, pancreas segmentation tasks have been driven by two major methodologies: multi-atlas based [4, 5] coupled with statistical shape modeling [6], and in more recent years, convolutional neural networks (CNNs) or deep learning [7, 3, 8]. While CNNs have achieved higher quantitative accuracy scores in 2D medical image segmentation, such methods can exhibit discontinuity in predicting pancreatic regions between consecutive slices for an input volume. This paper presents a novel approach for automatic pancreas segmentation in MRI. As illustrated in Figure 1, the proposed method consists of two successive stages. First, a CNN specialising in blurred boundary detection is trained to predict targeted pixel-wise pancreas tissue. This deep learning stage firstly identifies the main pancreas region (ROI) in a dataset of MRI volumes [8] by training a random forest on extracted texture and probability-wise features on image patches of 25 × 25 pixels. Next, inspired by the encoder-decoder architecture of SegNet [9] a new model termed Hausdorff Sine SegNet (HSSN) is developed using the ROI data. A novel loss function incorporates the modified Hausdorff distance metric and a sinusoidal component to capture local boundary information, enforce edge detection and thus raise the true pancreas prediction rate on a 2D (slice-by-slice) basis. The testing stage consists of two phases. First, the output of the trained HSSN for a given test MRI volume encodes spatial information to classify every pixel in each slice, thus forming a volumetric binary mask (VBM). The second phase generates dense contouring by further tackling the low dissimilarity between organ boundaries: a digital contrast enhancement model is utilised to improve the greyscale variation between surrounding background classes within close proximity to the pancreas. A 3D energy-minimising algorithm performs refined segmentation on the enhanced pancreas that is fused with the VBM, producing greater consistency in spatial smoothness and prediction among successive slices. The proposed method, which is evaluated on two MRI datasets with varying noise, outperforms the state-of-the-art approaches [8, 10–12], and moreover, surpasses the performance of readily employed deep learning-based loss functions. Although this approach has been tested on pancreas segmentation, the methodology is reproducible, scalable and generalisable to other organ segmentation tasks. The implementation is available at https://github.com/med-seg/p.

Materials and methods

Training the HSSN

The proposed HSSN model has an encoder-decoder topology, as illustrated in Figure 2. The decoder network uses max-pooling indices to upsample low-resolution feature maps, consequently retaining high-frequency details to improve pancreatic boundary delineation, and reducing the total number of trainable parameters in the decoders. Unlike other models that have been fine-tuned from pre-trained CNNs using a large number of natural images [3, 13], this network is trained from scratch using exclusively pancreas datasets. Since this organ accounts for ~1% in a scan, there is a need to weight the loss differently based on the true class: Median frequency balancing [14] is utilised, in which the weight assigned to a class in the loss function is the ratio of the median of class frequencies computed on the entire training set divided by the class frequency. The HSSN also employs data augmentation of random reflections and translations to reduce overfitting [15], and further address problems caused by high shape variability.

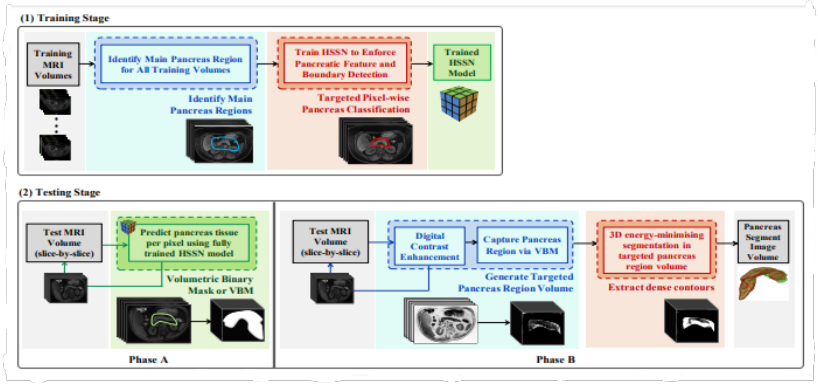

Fig. 1. Overview of proposed approach. (1) develop the HSSN deep learning model using training MRI; and (2) apply the test MRI to generate segmented pancreas volume.

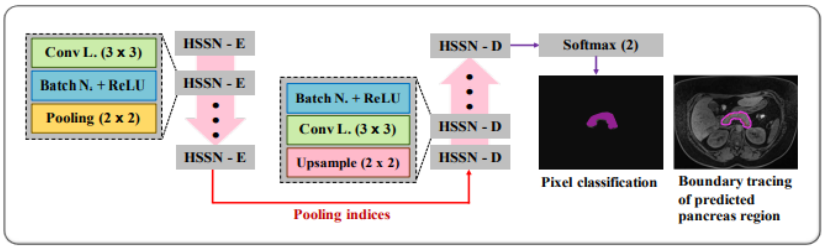

Fig. 2: Overview of HSSN model. An encoder stage (5 blocks of HSSN-E) downsamples the MRI input through convolution, batch normalisation and ReLU. A decoder stage (5 blocks of HSSN-D) upsamples its input using the transferred pooling indices from its corresponding encoder to generate sparse feature maps. From here, convolution is performed with a trainable filter of weights to density the feature map. Resulting decoder output

feature maps are fed to soft-max classifier for 2-channel pixel-wise classification of the input image as "pancreas" or "non-pancreas".

Integrated Hausdorff-Sine Loss Function

A novel loss function is proposed for training the segmentation neural network. The optimisation of the modified Hausdorff distance and a sinusoidal functionality serves to reduce the boundary matching error and "enhance" a resulting pixel-wise pancreas prediction. Let T_H and Y_H represent the ground-truth and network boundary predictions respectively, where T_H, $Y_H \subset \mathbb{R}^n$ such that $|T_H|, |Y_H| < \infty$. Furthermore, t_j and $y_j \in \{0, 1\}$ are indexed pixel values in T_H, and Y_H respectively, and can be viewed as boundary points. The Euclidean distance between a point t_j and set of points, Y_H is $s(t_j, Y_H) = \min_{y_j \in Y_H} \|t_j - y_j\|$, and the distance between a point y_j and set of points, T_H, is $s(y_j, T_H,) = \min_{t_j \in T_H} \|y_j - t_j\|$. If $\varepsilon_y = \frac{1}{|Y_H|} \sum_{y_j \in Y_H} s(t_j, Y_H)$ and $\varepsilon_T = \frac{1}{|T_H|} \sum_{t_j \in T_H} s(y_j, T_H)$, the modified Hausdorff distance loss, L_{mhd} is:

$$L_{mhd} = \text{MAX}\ \{\varepsilon_Y, \varepsilon_T\} \tag{1}$$

Thus, computing the gradient yields:

$$\frac{\partial L_{mhd}}{\partial Y_H} \begin{cases} \frac{\partial}{\partial Y_H}(\varepsilon_Y) & if\ \varepsilon_Y > \varepsilon_T \\ \frac{\partial}{\partial Y_H}(\varepsilon_T) & if\ \varepsilon_T < \varepsilon_Y \\ \text{undefined} & if\ \varepsilon_Y = \varepsilon_T \end{cases} \tag{2}$$

An additional sinusoidal component increases non-linearity during network training and empirically evaluated, raises the true positive predictions. If *T* and *Y* represent the ground-truth and network predictions, the loss L_{sine} is defined:

$$L_{sine} = -\frac{1}{|Y|} \sum_{i=1}^{nC} \sin(T_i) \log_2(Y_i) \tag{3}$$

where *n*C = 2 is the number of classes (e.g., Y_1, refers to "pancreas" and Y_2 refers to "non-pancreas"). From here, computing the gradient yields:

$$\frac{\partial L_{sine}}{\partial Y_i} = -\frac{1}{|Y|} \frac{\sin(T_i)}{Y_i log_{10}(2)} \tag{4}$$

The model is updated via the combined gradients of L_{sine} and L_{mhd}.

Testing Stage

(A) Targeted Pancreas Binary Mask

The trained HSSN model performs pixel-wise prediction on each slice in a test MRI volume to generate a resulting volumetric binary mask (VBM). Columns (a) and (b) in Figure 3 displays three sample input slices in three different image volumes, and the corresponding positive pancreas region (white mask) as predicted by the HSSN model. The red contouring in each image in column (b) is the ground-truth.

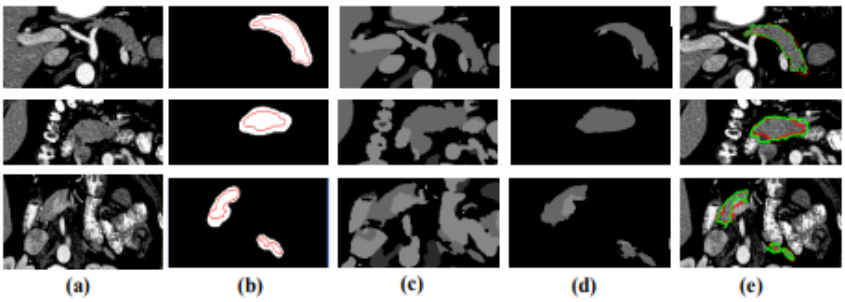

Fig. 3: Visualising proposed approach.

(B) Achieve Dense Contouring

The test MRI volume undergoes non-local means for denoising, after which a learned intensity model incorporates a sigmoid function to exhaustively differentiate pancreatic tissue against background classes. Every S_i-th slice transforms to $C(s_i) = 1/(1 + \exp[g(c - s_i)])$, where g controls the actual contrast, and c is the cut-off value representing the (normalised) greyscale value about which g is changed [12, 16]. The VBM is applied to the enhanced image volume and processed through a 3D unsupervised energy minimisation method via continuous max-flow [17], revealing detailed contouring as highlighted in Figure 3, column (c). The accurate HSSN predictions reduce the level of non-pancreatic tissue carried into the max-flow segmentation stage, as shown in Figure 3, column (d), eliminating the need for post-processing.

Experimental Results and Analysis

Datasets and Evaluation

Two expert-led annotated pancreas datasets are utilised. MRI-A and MRI-B contain 180 and 120 abdominal MRI scans (T2-weighted, fat suppressed), which have been obtained using a Philips Intera 1.5T and a Siemens Trio 3T scanner, respectively. Every MRI-A scan has 50 slices, each of size 384 × 384 with spacing $2mm$, and $0.9766mm$ pixel interval in the axial and sagittal direction. Every MRI-B scan has 80 slices, each of size 320 × 260 with $1.6mm$ spacing,

and 1.1875*mm* pixel interval in the axial and sagittal direction. The proposed approach is evaluated using the Dice Similarity Coefficient (DSC), precision (PC), recall (RC) and the Hausdorff distance (HSD) representing the maximum boundary deviation between the segmentation and ground-truth.

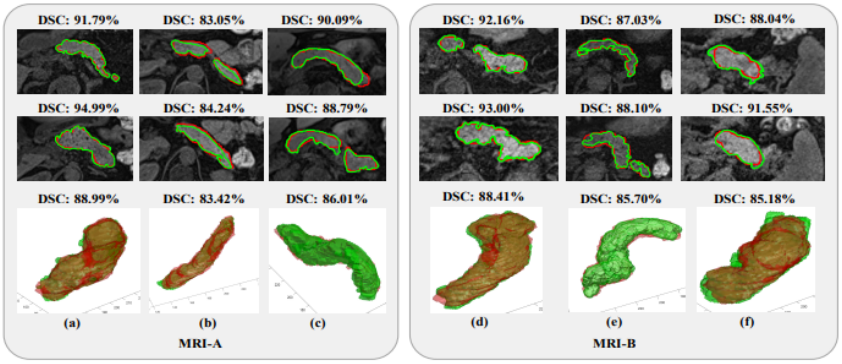

Fig. 4: Segmentation results in six different MRI scans (volumes). Every column corresponds to a single MRI volume. From left, first row displays sample MRI axial slices with segmentation outcome (green) against ground-truth (red), and computed DSC. Second row displays 3D reconstruction of entire pancreas with computed DSC.

Network Implementation

The training and testing data are randomly split into 160 and 20 (MRI-A) and 100 and 20 (MRI-B). The HSSN model employs stochastic gradient descent with parameters momentum (0.9), initial learning rate (0.001), maximum epochs (300) and mini-batch size (10). The mean time for model training is ~11 hours and the testing phase is ~7.5 minutes per MRI volume using an i7-59-30k-CPU at 3.50 Ghz. Future work can potentially reduce these run-times by a factor of 10 via multiple GeForce Titan X GPUs.

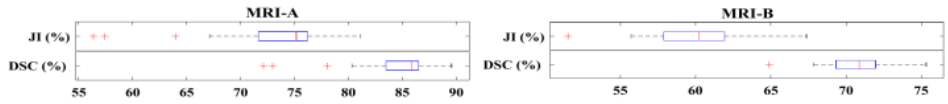

Fig. 5: Box plots of DSC and JI.

Analysis of Proposed Approach

Figure 4 displays the final segmentation results in six MRI scans, equally split between MRI-A and MRI-B. Columns (a, b, c) are part of MRI-A, yet there is high variation between intensity and contrast in the original axial MRI slices. Columns (d, e, f) corresponds to exemplars from MRI-B. As reflected in Figure 5, 85% of MRI-A compared to 95% in MRI-B segmentations score above 80% in DSC, demonstrating the robust performance of the approach with respect to poor image quality, intensity distribution and spatial dimensions.

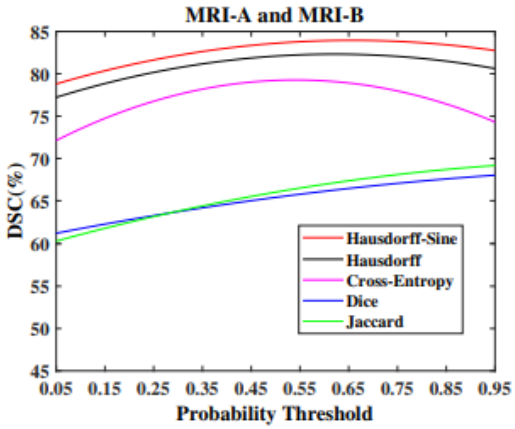

Fig. 6: DSC across threshold ranges [0.05, 0.95] via multiple loss functions:

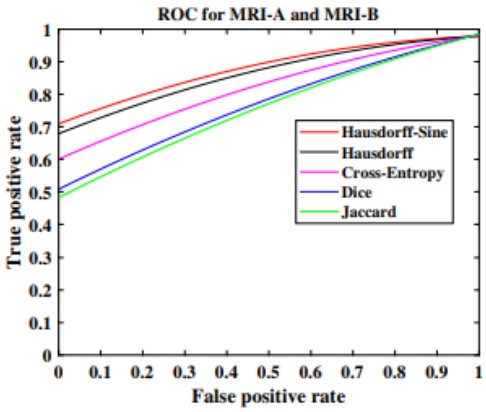

Fig. 7: Averaged ROC curves via multiple loss functions.

Hausdorff-Sine Loss

Figure 6 compares the segmentation results (in DSC) using Hausdorff-Sine and the loss functions, Hausdorff, Cross-entropy, Dice [18] and Jaccard [19] in the probability range [0.05,0.95]. The cross-entropy penalises true positive predictions, forcing the "optimum" probability to approximately 0.5. Although the Dice loss minimises the class distribution distance, squaring the weights in the backpropagation stage causes instability and a higher rate of false negative predictions. Similarly, the Jaccard loss suffers from low true positive predictions. Empirically tested, the Hausdorff loss minimises the maximum deviation between a prediction and desired outcome; however, the addition of a sinusoidal component increases non-linearity during training, and thus Hausdorff-Sine achieves improved true positive predictions across differing thresholds while delivering strong discrimination of true negatives. The ROC curves in Figure 7 highlight the inferior performance of other loss functions in the

extremely unbalanced segmentation, whereas Hausdorff-Sine generally improves the true positive accuracy results.

Phase B of Testing Stage

Integrating the second phase (B) produces contextual boundary information that is essential for accurate segmentation in biomedical imaging. Figure 3, column (b) and column (e) visibly highlights the differences in segmentation boundary delineation against the ground-truth before and after this phase. Thus, the mean HSD metric confirms less deviation from the ground-truth (see Table 1 and 2) by approximately 1 mm, and furthermore, the mean DSC raises by approximately 4% in both MRI-A and MRI-B.

Table 1: Deep learning model performance using state-of-the-art loss functions versus the integrated novel Hausdorff and Hausdorff-Sine loss. Datasets MRI-A and MRI-B are evaluated in 9-fold and 6-fold cross-validation (FCV), respectively. DSC, PC, RC and HSD are presented as mean ± standard deviation.

MRI-A: Train/Test (160/20) 9-FCV				
Loss	DSC(%)	PC(%)	RC(%)	HSD(mm)
CE	77.9±3.6	88.4±6.18	95.6±2.26	12.4±5.5
Dice	63.5±9.1	63.8±20.0	86.8±10.5	16.8±5.3
Jac	63.2±9.6	62.5±19.8	87.1±10.0	17.0±5.4
Haus	78.4±6.1	89.5±9.11	96.2±4.06	12.7±4.9
Haus-Sin	**79.7±4.0**	**93.2±7.46**	**97.2±2.67**	**11.2±3.6**

MRI-B: Train/Test (100/20) 6-FCV				
Loss	DSC(%)	PC(%)	RC(%)	HSD(mm)
CE	79.9±4.33	92.6±6.89	96.3±2.76	10.5±3.34
Dice	67.1±12.8	77.2±15.1	85.2±16.8	21.4±12.3
Jac	68.6±6.96	68.3±16.9	88.5±8.34	17.9±7.58
Haus	81.0±4.25	94.8±3.84	98.3±2.28	10.2±4.17
Haus-Sin	**82.1±2.99**	**97.7±2.50**	**99.1±0.78**	**10.0±6.63**

Table 2: DSC, PC, RC and HSD as mean ± standard deviation [lowest, highest] for automatic segmentation methods. Datasets MRI-A and MRI-B are evaluated in 9-fold and 6-fold cross-validation (FCV), respectively.

MRI-A: Train/Test (160/20) 9-FCV				
Method	DSC(%)	PC(%)	RC(%)	HSD (mm)
U-Net [10]	66.8±8.8 [42.3, 77.3]	71.3±4.4 [62.9, 80.5]	85.1±4.8 [76.9, 88.16]	16.9±5.8 [8.22, 24.1]
Cascaded-CNN [8]	52.7±6.9 [34.4, 60.7]	64.0±4.1 [50.4, 68.0]	75.2±4.6 [68.1, 78.25]	21.5±9.3 [15.7, 38.6]
Dense V-Net [11]	73.6±6.1 [49.6, 78.8]	86.1±3.3 [78.5, 88.5]	94.6±3.4 [82.8, 96.37]	14.4±7.2 [6.63, 20.5]
Geo-Desc [12]	78.2 ±5.8 [67.1, 86.3]	85.3±9.7 [70.8, 98.9]	93.9±9.5 [52.5, 99.13]	13.8±4.4 [6.11, 18.4]
Proposed	**84.1±4.6 [72.1, 89.6]**	**95.5±6.3 [71.7, 99.7]**	**97.6±3.0 [89.9, 100.0]**	**10.6±3.7 [6.184, 18.4]**
MRI-B: Train/Test (100/20) 6-FCV				
Method	DSC(%)	PC(%)	RC(%)	HSD (mm)
U-Net [10]	72.8±6.0 [58.9, 80.8]	83.8±3.1 [74.2, 87.46]	94.6±3.5 [82.8, 95.72]	14.0±8.1 [6.82, 21.7]
Cascaded-CNN [8]	54.8±5.1 [44.4, 65.7]	64.3±3.5 [59.5, 67.91]	76.2±3.7 [69.9, 79.64]	22.3±8.6 [16.0, 37.5]
Dense V-Net [11]	74.0±5.3 [65.1, 80.3]	85.4±3.1 [78.5, 89.74]	93.0±3.8 [84.9, 96.35]	16.7±7.0 [8.46, 19.8]
Geo-Desc [12]	81.2±5.0 [72.6, 85.8]	84.7±5.8 [73.1, 93.64]	84.6±8.2 [69.2, 97.28]	14.7±4.1 [8.13, 17.6]
Proposed	**85.7±2.3 [79.9, 90.3]**	**96.1±3.6 [86.7, 100.0]**	**99.3±0.7 [99.9, 100.0]**	**9.08±2.0 [4.87, 14.8]**

Comparison with the State-of-the-art

Table 2 highlights the proposed approach outperforming state-of-the-art methods [8, 10–12] in terms of accuracy and statistical stability despite employing non-organ optimised protocol data.

Conclusion

This paper presents a novel approach for automatic pancreas segmentation in MRI volumes generated from different scanner protocols. Combined with the proposed Hausdorff-Sine loss, an encoder-decoder network reinforces pancreatic boundary detection in MRI slices, outperforming the rate of true positive predictions compared to multiple loss functions. In the later stage, a 3D hybrid energy-minimisation algorithm addresses the intensity consistency problem that is often the case when segmenting image volumes on a 2D basis. The proposed approach generates quantitative accuracy results that surpass reported state-of-the-art methods, and moreover, preserve detailed contouring.

References

1. Mavin Macauley, Katie Percival, Peter E. Thelwall, Kieren G. Hollingsworth, and Roy Taylor. Altered Volume, Morphology and Composition of the Pancreas in Type 2 Diabetes. PLOS ONE, 10(5):1–14, 2015.

2. Ahmad Omeri, Shunro Matsumoto, Maki Kiyonaga, Ryo Takaji, Yasunari Yamada, Kazuhisa Kosen, Hiromu Mori, and Hidetoshi Miyake. Contour variations of the body and tail of the pancreas: evaluation with mdct. J Radiol, 35(6):310–318, 2017.

3. Jinzheng Cai, Le Lu, Zizhao Zhang, Fuyong Xing, Lin Yang, and Qian Yin. Pancreas Segmentation in MRI Using Graph-Based Decision Fusion on Convolutional Neural Networks, pages 442–450. Springer International Publishing, 2016.

4. Toshiyuki Okada, Marius George Linguraru, Yasuhide Yoshida, Masatoshi Hori, Ronald M. Summers, Yen-Wei Chen, Noriyuki Tomiyama, and Yoshinobu Sato. Abdominal multi-organ segmentation of ct images based on hierarchical spatial modeling of organ interrelations. In Abdom Radiol, pages 173–180. Springer Berlin Heidelberg, 2012.

5. Akinobu Shimizu, Tatsuya Kimoto, Hidefumi Kobatake, Shigeru Nawano, and Kenji Shinozaki. Automated pancreas segmentation from three-dimensional contrast-enhanced computed tomography. Int J Comput Assist Radiol Surg, 5(1):85–98, 2010.

6. Toshiyuki Okada, Marius George Linguraru, Masatoshi Hori, Ronald Summers, Noriyuki Tomiyama, and Yoshinobu Sato. Abdominal multi-organ segmentation from CT images using conditional shape–location and unsupervised intensity priors. Med Image Anal, 26:1–18, 2015.

7. Jinzheng Cai, Le Lu, Yuanpu Xie, Fuyong Xing, and Lin Yang. Improving deep pancreas segmentation in CT and MRI images via recurrent neural contextual learning and direct loss function. CoRR, abs/1707.04912, 2017.
8. Amal Farag, Le Lu, Holger R Roth, Jiamin Liu, Evrim Turkbey, and Ronald M Summers. A bottom-up approach for pancreas segmentation using cascaded superpixels and (deep) image patch labeling. IEEE Trans. Image, 26(1):386–399, 2017.
9. Vijay Badrinarayanan, Alex Kendall, and Roberto Cipolla. Segnet: A deep convolutional encoder-decoder architecture for image segmentation. arXiv:1511.00561, 2015.
10. Olaf Ronneberger, Philipp Fischer, and Thomas Brox. U-Net: Convolutional Networks for Biomedical Image Segmentation, pages 234–241. Springer International Publishing, Cham, 2015.
11. Eli Gibson, Francesco Giganti, Yipeng Hu, Ester Bonmati, Steve Bandula, Kurinchi Gurusamy, Brian Davidson, Stephen P Pereira, Matthew J Clarkson, and Dean C Barratt. Automatic multi-organ segmentation on abdominal CT with dense VNetworks. IEEE Trans Med Imaging, 2018.
12. Hykoush Asaturyan, Antonio Gligorievski, and Barbara Villarini. Morphological and multi-level geometrical descriptor analysis in ct and mri volumes for automatic pancreas segmentation. Comput Med Imaging Graph, 75:1–13, 2019.
13. Saining Xie and Zhuowen Tu. Holistically-nested edge detection. In Proc IEEE ICCV, pages 1395–1403, 2015.
14. David Eigen and Rob Fergus. Predicting depth, surface normals and semantic labels with a common multi-scale convolutional architecture. In Proc IEEE Int Conf Comput Vis, pages 2650–2658, 2015.
15. Luis Perez and Jason Wang. The effectiveness of data augmentation in image classification using deep learning. arXiv:1712.04621, 2017.
16. Asaturyan Hykoush and Barbara Villarini. Hierarchical framework for automatic pancreas segmentation in MRI using continuous max-flow and min-cuts approach. In Image Analysis and Recognition, pages 562–570. Springer International Publishing, 2018.
17. Jing Yuan, Egil Bae, and Xue-Cheng Tai. A study on continuous max-flow and min-cut approaches. In Proc IEEE Comput Soc Conf Comput Vis Pattern Recognit, pages 2217–2224, 2010.

18. F. Milletari, N. Navab, and S. A. Ahmadi. V-Net: Fully convolutional neural networks for volumetric medical image segmentation. In Fourth Int. Conf. 3DV, pages 565–571, 2016.
19. Md Atiqur Rahman and Yang Wang. Optimizing intersection-over-union in deep neural networks for image segmentation. In ISVC, pages 234–244. Springer, 2016.

Paper 9

Largescale analysis of iliopsoas muscle volumes in the UK Biobank

Julie Fitzpatrick[13], Nicolas Basty[13]*, Madeleine Cule[2], Yi Liu[2], Jimmy Bell[1], E. Louise Thomas[1] & Brandon Whitcher[1].

Abstract

Psoas muscle measurements are frequently used as markers of sarcopenia and predictors of health. Manually measured cross-sectional areas are most commonly used, but there is a lack of consistency regarding the position of the measurement and manual annotations are not practical for large population studies. We have developed a fully automated method to measure iliopsoas muscle volume (comprised of the psoas and iliacus muscles) using a convolutional neural network. Magnetic resonance images were obtained from the UK Biobank for 5000 participants, balanced for age, gender and BMI. Ninety manual annotations were available for model training and validation. The model showed excellent performance against out-of-sample data (average dice score coefcient of 0.9046 ± 0.0058 for six-fold cross-validation). Iliopsoas muscle volumes were successfully measured in all 5000 participants. Iliopsoas volume was greater in male compared with female subjects. There was a small but signifcant asymmetry between left and right iliopsoas muscle volumes. We also found that iliopsoas volume was signifcantly related to height, BMI and age, and that there was an acceleration in muscle volume decrease in men with age. Our method provides a robust technique for measuring iliopsoas muscle volume that can be applied to large cohorts.

Introduction

The iliopsoas muscles, predominantly made up of slow-twitch fibers, are a composite of the psoas major and iliacus muscles; they are anatomically separate in the abdomen and pelvis but are merged together in the thigh. The iliopsoas is engaged during most day to day activities, including posture, walking and running. Together these muscles serve as the chief flexor of the hip and a dynamic stabilizer of the lumbar spine [1] , with the psoas uniquely having role in

the movement of both the trunk and lower extremities [2]. Given the key involvement of the iliopsoas muscles in daily activities, there is increasing interest in its potential as a health biomarker. This has most commonly taken the form of a cross-sectional area (CSA) through one (generally the right) or both iliopsoas muscles, with the most common measurement taken through the psoas muscle. This CSA can be used either as an independent measurement or as a ratio to vertebral body size [3,4] or in the form of the psoas muscle index, calculated as the psoas muscle major CSA divided by the height squared [5]. Indeed, psoas CSA has been suggested as a predictor of sarcopenia [6] , surgical outcome and length of hospital stay post surgery [7–9] , poor prognosis in response to cancer treatment [10], morbidity following trauma4 , a surrogate marker of whole body lean muscle mass [11], cardiovascular fitness [12], changes in cardiometabolic risk variables following lifestyle intervention [13] and even risk of mortality [14,15]. Measurements of the psoas major muscle are most commonly made from CSA of axial MRI or CT images [7,12], with most studies generally relying on manual annotation of a single slice, through the abdomen, these tend to be retrospectively repurposed from clinical scans rather than a specific acquisition [16–18]. However, the CSA of the psoas muscle varies considerably along its length [2] therefore small differences in measurement position can potentially have a significant effect on its overall measured size. Moreover, there is a lack of consistency within the literature regarding the precise location at which measurement of the psoas CSA should be made, with researchers using a variety of approaches including: the level of the third lumbar vertebrae (L3) [6,9,10,17,18], L4 [3,4,14,16], between L4-L5 [11,13], as well at level of the umbilicus [7,8,19] the precise position of which is known to vary with obesity/ascites. There is further discrepancy between studies regarding whether the measurements should comprise of one single [10] or both psoas muscles [17], with the majority of publications combining the areas of both muscles. This lack of consistency together with the relatively low attention given to robustness and reproducibility of its measurement, and the reliance on images from retrospective clinical scans have led many to question its validity as a biomarker [20]. A more objective proposition may be to measure total psoas muscle volume [21–25], from dedicated images. A variety of approaches have been used thus far: inclusion of muscle between L2-L5 [21], psoas muscle volume from L3 and approximately the level of the iliopectineal arch (end point estimated from images in publications) [22,23], from the origin of the psoas at lumbar vertebrae (unspecified) to its insertion in the lesser trochanter [24], or with no anatomical information provided at all [25]. Whilst all of these

approaches include substantially more muscle than is included in simple CSA measurements, these are still incomplete volume measurements. Moreover, measuring the entire psoas muscle volume as a single entity is challenging, since even with 3D volumetric scans it is difficult to differentiate between composite iliacus and psoas muscles once they merge at the level of the inguinal ligament. Therefore, to measure psoas volume as an independent muscle it is necessary to either assign an arbitrary cutoff and not include a considerable proportion of the psoas muscle (estimated to be approximately 50% in some studies [22]) or simply include the iliacus muscle and measure the iliopsoas muscle volume in its entirety Convolutional Neural Networks (CNNs) have become a strong tool for automated image segmentation, especially architectures such as the U-Net [26] for two-dimensional (2D) data or the V-Net [27] for three-dimensional (3D) data. These techniques owe their popularity to the modest amount of training data required, robustness and fast execution speed. CNNs have been applied for automated muscle segmentation in computed tomography [28–30], specifically for 2D segmentation of the psoas major muscle [29], as well as MRI31, [32]. The increasing use of whole body imaging [33] in large cohort studies such as the UK Biobank (UKBB), which plans to acquire MRI scans from the neck to the knee in 100,000 individuals [34], requires different approaches to image analysis. Manual image segmentation is time consuming and infeasible in a cohort as large as the UKBB. However, this dataset provides a unique opportunity to measure iliopsoas muscles volume in a large cross-sectional population. Therefore, development of a robust and reliable automated method is essential. In this paper, we present an automated method to segment iliopsoas muscle volume using a CNN and discuss results arising from 5000 participants from the UKBB imaging cohort, balanced for BMI, age, and gender.

	Female	**Male**
Participants	2496 (49.9)	2504 (50.1)
Ethnicity of total cohort		
White European	2422 (48.44)	2416 (48.32)
Asian	18 (0.36)	35 (0.70)
Black	17 (0.34)	12 (0.24)
Other	15 (0.30)	9 (0.18)
Chinese	11 (0.22)	10 (0.20)
Not reported	7 (0.14)	12 (0.24)
Mixed	6 (0.12)	10 (0.20)
Age (years)	63.3 ± 8.3	63.3 ± 8.4
BMI (kg/m^2)	26.2 ± 4.7	27.0 ± 3.9
Height (cm)	162.5 ± 6.1	176.2 ± 6.8
Weight (kg)	69.3 ± 13.3	83.9 ± 13.5

Table 1. Demographics of the subjects (n = 5000). Reported values are counts with percentage (%) for categorical variables and average ± standard deviation (SD) for continuous variables.

Materials and methods

Data

A total of 5000 subjects were randomly selected for this study, while controlling for BMI, age, and gender from the UKBB imaging cohort. Age was discretised into four groups: 44–53, 54–63, 63–72 and 73–82 years. The eight strata were defined to cover both age and gender. Weights were used to maintain the proportion of subjects within each age group to match that of the larger UKBB population. Demographics for the study population (Table 1) were balanced for gender (female: male ratio of 49.9:50.1). The average age of the male subjects was 63.3 ± 8.4 years and the female subjects was 63.3 ± 8.3 years. The average BMI of the male subjects was 27.0 ± 3.9 kg/m² (range 17.6–50.9 kg/m²) and for female subjects 26.2 ± 4.7 kg/m² (range 16.1–55.2 kg/m²), with the mean for both groups being categorised as overweight. The self-reported ethnicity was predominantly White European (96.76%). As per the whole UKBB population, the sub-cohort in the current study was significantly healthier than the UK general population. The most common ailment were related to arthropathies, with smaller proportion reporting a variety of neoplasms, ranging from skin melanomas to benign neoplasms (Supplementary Table S1). Participant data from the UKBB cohort was obtained as previously described [34] through UKBB Access Application number 23889. The UKBB has approval from the North West Multi-Centre Research Ethics Committee (REC reference: 11/NW/0382). All methods were performed in accordance with the relevant guidelines and regulations, and informed consent was obtained from all participants. Researchers may apply to use the UKBB data resource by submitting a health-related research proposal that is in the public interest. More information may be found on the UKBB researchers and resource catalogue pages (https://www.ukbiobank.ac.uk/). Raw MR images were obtained from the UKBB Abdominal Protocol [35] and preprocessed as previously reported [36,37]. The data were acquired on the same model, a Siemens Aera 1.5 T scanner (Syngo MR D13) (Siemens, Erlangen, Germany), across three sites (Stockport, Newcastle, Reading, UK). Te Dixon sequence involved six overlapping series that were acquired using a common set of parameters: TR = 6.67 ms, TE = 2.39/4.77 ms, in-plane voxel size 2.232 × 2.232 mm, FA = 10° and bandwidth = 440 Hz. The first series, over the neck, consisted of 64 slices, slice thickness 3.0 mm and 224 × 168 matrix;

series two to four (covering the chest, abdomen and pelvis) were acquired during 17 second expiration breath holds with 44 slices, slice thickness 4.5 mm and 224 × 174 matrix; series five, covering the upper thighs, consisted of 72 slices, slice thickness 3.5 mm and 224 × 162 matrix; series six, covering the lower thighs and knees, consisted of 64 slices, slice thickness 4 mm and 224 × 156 matrix. During preprocessing the data were resampled to voxel size 2.232 × 2.232 × 3.0 mm.

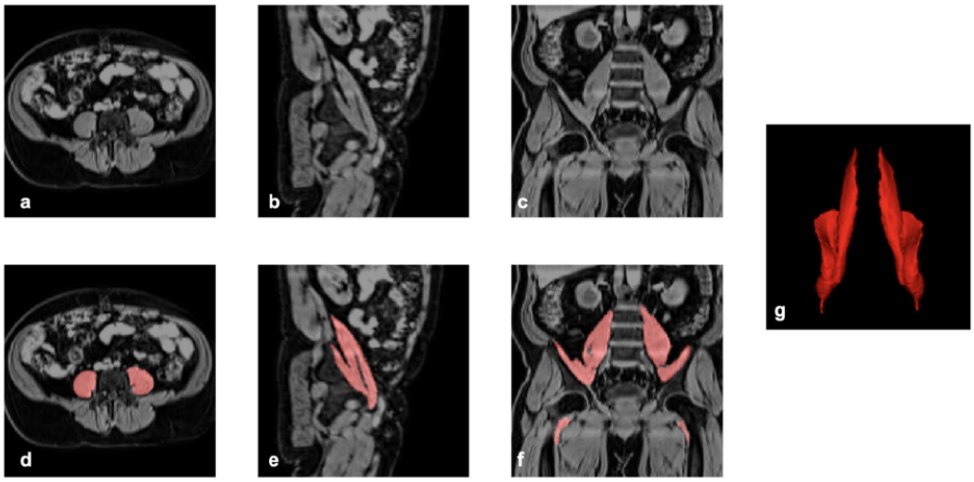

Fig 1. Iliopsoas muscle manual annotations: (a) axial, (b) sagittal, and (c) coronal views, (d–f) showing of the segmentation (red) overlaid on the anatomical reference data, and (g) 3D rendering of manual segmentation.

Manual Annotation

A single expert radiographer manually annotated both iliopsoas muscles for 90 subjects using the open-source software MITK [38]. Each axial slice of the water images was examined, the iliopsoas identified, and the borders of the psoas and iliopsoas manually drawn for 90 subjects. On average, manual annotation of both muscles took five to seven hours per subject. The annotated data covered a broad range of age and BMI from male and female UKBB participants. A typical Dixon abdominal dataset, centered on the iliopsoas muscles, is shown in Fig. 1, manual iliopsoas muscle annotations are overlaid on the anatomical reference volume in red and a 3D rendering of the manual annotation.

Model

We trained a model able to predict both muscles individually. The preprocessing steps for the training data, where the cropping is also needed for applying the model to unseen data, are as follows. Two arrays of size 96 × 96 × 192 were cropped around the hip landmarks [36], to

approximate the location of the muscles in order to perform the segmentation (an example of the cropped regions may be found in Supplementary Fig. S1). After cropping, each volume was normalised such that the signal intensities lie between zero and one, where the 99th percentile was used instead of the maximum to avoid possible spikes in signal intensity. That is, all signal intensities above the 99th percentile were mapped to one. Two sets of 16 training samples were generated for every subject by separating the right and the left muscles, introducing reflections exploiting the symmetry of the structures. Further data augmentation included seven random transformations consisting of translations by up to six voxels in-plane, up to 24 voxels out-of-plane, and random scaling ranging from −50 to +50% out-of-plane and from −25 to +25% in-plane, in addition to the original data. We chose larger factors for out-of-plane transformations to account for the skewed variability in shape and position of the muscles, reflecting the fact that there is more variation in height than width in the population. After data augmentation, 2880 training samples were produced from the original 90 manually annotated pairs of iliopsoas muscles. The model used for 3D iliopsoas muscle segmentation closely follows a similar architecture to the U-Net [26] and the V-Net [27], with a contracting path and an expansive path connected by skip connections at each resolution level. These network architectures have been established as the gold standard for image segmentation over the last few years, as they require modest amounts of training data as a consequence of operating at multiple resolution levels while providing excellent results within seconds. Several convolution blocks are used in our model architecture. An initial block (I) contains a 5 × 5 × 5 convolution with eight filters followed by a 2 × 2 × 2 convolution with 16 filters and stride two. The down-sampling blocks in the contraction ($D_{i,m}$) consist of i successive 5 × 5 × 5 convolutions with m filters followed by a 2 × 2 × 2 convolution of stride with stride two, used to decrease the resolution. In the expansion, the up-sampling blocks ($U_{j,n}$) mirror the ones in the contraction where there are transpose convolutions instead of stride two convolutions. The block (L) at the lowest resolution level of the architecture consist of three successive 5 × 5 × 5 convolutions with 128 filters followed by a 2 × 2 × 2 transpose convolution of stride two and 64 filters. The final block (F) contains a 5 × 5 × 5 convolution with 16 filters followed by a single 1 × 1 × 1 convolution and a final sigmoid activation classification layer. All blocks incorporate skip connections between their input and output, resulting in residual layers. The architecture follows: I $\rightarrow D_{2,32} \rightarrow D_{3,64} \rightarrow D_{3,128} \rightarrow$ L $\rightarrow U_{3,128} \rightarrow U_{3,64} \rightarrow U_{3,32} \rightarrow$ F with skip connections between blocks at equivalent resolution levels. Padding is used for the

convolutions throughout the network and a stride of one, unless otherwise specified, when moving between the resolution levels. Other than the final sigmoid activation, scaled exponential linear units (SELU) are used throughout the network. The SELU activation function has recently been proposed [39], where the self-normalising properties allow it to bypass batch normalisation layers enabling higher learning rates that lead to more robust and faster training. The model was trained minimising the Dice score coefficient (DSC) loss [27] with a batch size of three using the Adam optimiser and a learning rate of 1e−4 until convergence at 100 epochs. The learning rate was determined through a parameter sweep (1e−1 to 1e−6). We performed all of the CNN development, learning, and predictions using Keras (TensorFlow backend) [40] on a NVIDIA Titan V 12 GB GPU. We limited the batch size to three due to the GPU memory.

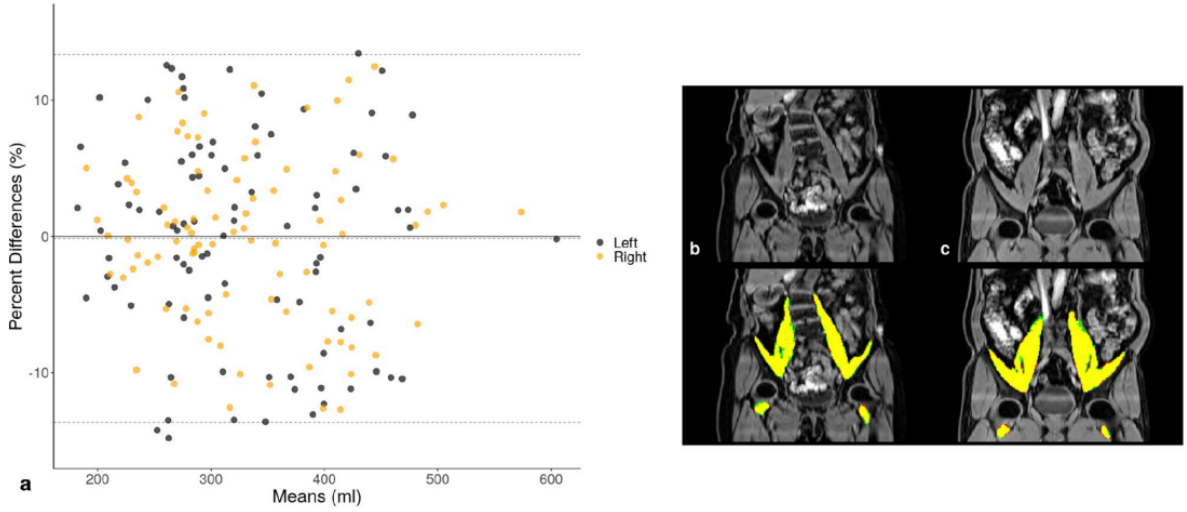

Fig 2. Bland–Altman plot (a) of iliopsoas muscle volumes determined with CNN-based and manual segmentations (n = 90), using a six-fold cross-validation experiment. Dotted lines represent the average bias (−0.2%) and the 95% limits of agreement. Overlays of the CNN-based and manual segmentations for two subjects (b, c), where the manual annotation is red, the CNN segmentation is green and the overlap is yellow.

Validation

A common metric used to evaluate segmentation performance is the DSC, also known as the F1 score. It is defined as twice the intersection of the labels divided by the total number of elements. Intersection of labels can also be seen as a True Positive (TP) outcome. The total number of elements can also be seen as the sum of all False Positives (FP), False Negatives (FN) and twice the number of TPs.

$$\mathrm{DSC} = \frac{2\,\mathrm{TP}}{\mathrm{FP} + 2\,\mathrm{TP} + \mathrm{FN}}$$

For validation of the model, we performed a six-fold cross-validation experiment, where in a single iteration 75 of the manually annotated images (approximately 83%) were used to train the model and the performance was evaluated on the remaining 15 out-of-sample images (approximately 17%).

Statistical Analysis

All summary statistics, hypothesis tests and figures have been performed using the R software environment for statistical computing and graphics [41]. Variables were tested for normality using the Shapiro–Wilk's test, the null hypothesis was rejected in all cases. Spearman's rank correlation coefficient (ρ) was used to assess monotonic trends between variables. The Wilcoxon rank-sum test was used to compare means between groups, and the Wilcoxon signed-rank test with paired observations. Methods for segmenting the iliopsoas muscle volume were compared using the Bland-Altman plot. Given the exploratory nature of the research, p-values < 0.05 were judged to be statistically significant.

Results

Validation

A summary of the cross-validation experiment may be found in Supplementary Table S2. The average bias was −0.2% with upper and lower limits of agreement being 13.3% and −13.7%, respectively (Fig. 2). The overlap between the CNN-based and manual segmentations for two subjects is also provided in Fig. 2, where the DSCs are 0.85 (left) and 0.90 (right) for (b) and 0.96 in both for (c). With consistent DSCs from the cross validation experiment showing a robust model performance on both muscles, we trained a final model using the entire 90 available manual annotations. Example segmentations from our method are provided in Fig. 3, displaying a sample of 12 subjects covering a variety of body sizes and habitus. The first three subjects (a–c) have some of the smallest iliopsoas muscles (total volume ≈ 346 ml), the next three subjects (d–f) have typical iliopsoas muscles (total volume ≈ 800 ml) and the third set of three subjects (g–i) have some of the largest iliopsoas muscles (total volume ≈ 1300 ml). The final set of three subjects represent subjects whose left and right iliopsoas muscles differ in

volume (difference in volume ≈ 93 ml for j and k, difference in volume = 182 ml for l). We can see that the model performs well for all of them, with additional details regarding model validation provided in Supplementary Fig. S2.

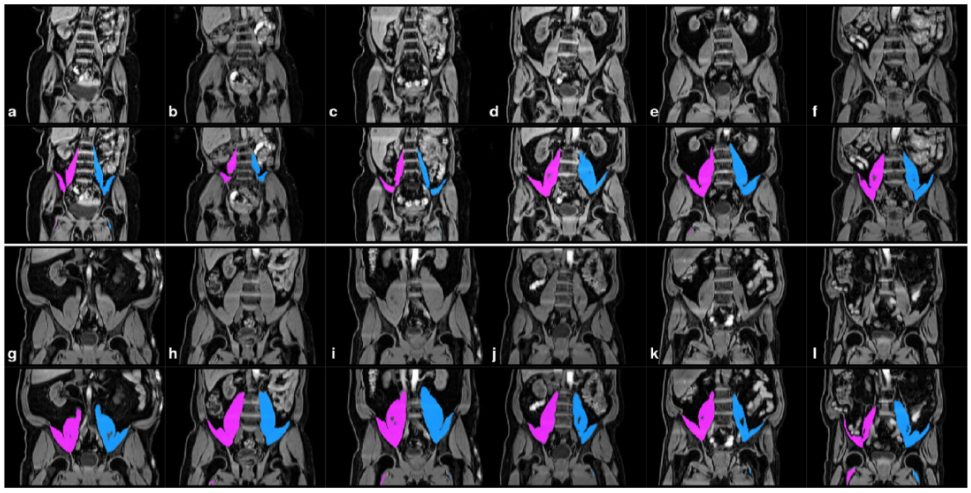

Fig 3. CNN segmentations of the left and right iliopsoas muscles overlaid in purple (right) and blue (left) from a range of body types and iliopsoas muscle volumes: (a–c) small, (d–f) average, (g–i) large and (j–l) asymmetric. The top row for each subject displays the signal intensities without the segmentation result, the bottom row includes the iliopsoas muscle segmentations.

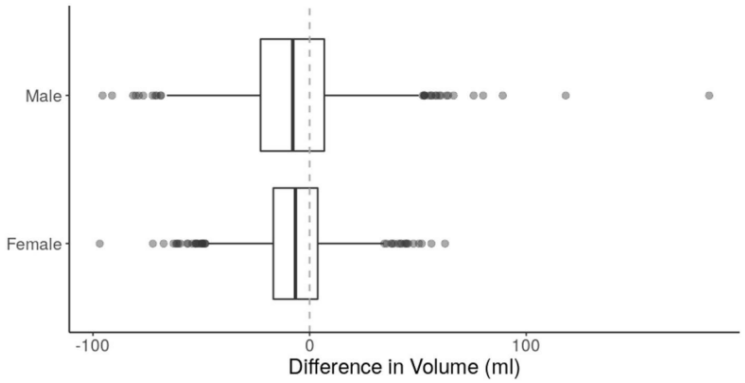

Fig 4. Difference in volume (ml) between the left and right iliopsoas muscles, separated by gender. Negative values indicate the right iliopsoas muscle is larger than the left.

Iliopsoas muscle volume

In each gender there was a small (approximately 2%) yet statistically signifcant asymmetry between lef and right iliopsoas muscles (Wilcoxon signed-rank test; male: $d = -7.3$ ml; female: $d = -6.5$ ml; both $p < 10^{-15}$) (Fig. 4). These differences were not significantly associated with the handedness of the participants. Significantly larger iliopsoas muscle volumes were measured in male compared with female subjects (Table 2).

	Female		Male		
	Mean ± SD	Range	Mean ± SD	Range	Significance
Total volume (ml)	542.3 ± 72.1	307.5, 904.2	814.5 ± 125.4	467.3, 1311.5	$p < 10^{-15}$
Average volume (ml)	271.2 ± 36.0	153.8, 452.1	407.2 ± 62.7	233.7, 655.8	$p < 10^{-15}$
Left volume (ml)	267.9 ± 36.8	134.5, 457.2	403.6 ± 63.5	247.0, 639.2	$p < 10^{-15}$
Right volume (ml)	274.4 ± 37.0	159.4, 447.0	410.9 ± 64.0	220.3, 675.1	$p < 10^{-15}$
L-R volume difference (ml)	−6.5 ± 16.1	−96.9, 62.5	−7.3 ± 22.8	−95.6, 184.4	$p = 0.040$
Iliopsoas muscle index (ml/cm^2)	205.1 ± 22.6	124.2, 304.1	261.8 ± 34.2	157.6, 417.2	$p < 10^{-15}$

Table 2. Iliopsoas muscle volumes (n = 5000). Significance refers to the p-value for a Wilcoxon rank-sums test, where the null hypothesis is the medians between the two groups (male and female subjects) being equal.

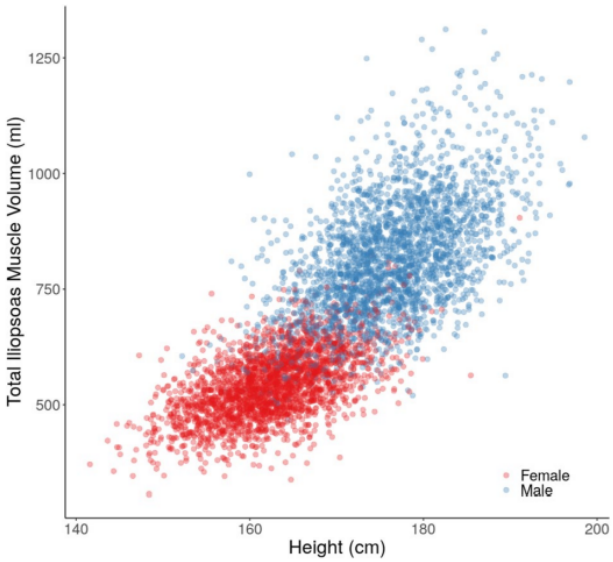

Fig 5. Scatterplot of total iliopsoas muscle volume (ml) by height (cm), separated by gender.

Relationship between iliopsoas muscle volume and physical characteristics

Significant correlations were observed between the total iliopsoas muscle volume and height in both genders (male: $\rho = 0.51$; female: $\rho = 0.54$, both $p < 10^{-15}$) (Fig. 5). To account for the

potential confounding efect of height on iliopsoas muscle volume, an iliopsoas muscle index (IMI) was defined

$$\mathrm{IMI} = \frac{\text{total iliopsoas muscle volume}}{\text{height}^2},$$

with units ml/m². Significant correlations were observed between the IMI and BMI in both genders (male: ρ = 0.48; female: ρ = 0.47, both $p < 10^{-15}$) (Fig. 6). A significant negative correlation was observed between IMI and age in both genders (male: ρ = −0.31, p < 10−15; female: ρ = −0.11, $p < 10^{-7}$). However, the relationship could not be easily explained by a simple linear method (Fig. 7). In fact the decrease in IMI as a function of age accelerates for men, starting in their early 60s, while for women it remains relatively constant

Discussion

There is considerable interest in measuring psoas muscle size, primarily related to its potential as a sarcopenic marker, thereby making it an indirect predictor of conditions influenced by sarcopenia and frailty, including health outcomes such as morbidity, and mortality [4,6–10,14,15]. The complexity in measuring total muscle directly, particularly in a frail population has necessitated the reliance on easily measured surrogates and the psoas muscle CSA is increasingly used for this purpose. However there is little consistency in the field regarding how the psoas muscle is measured, with considerable variation between publications. An automated approach to analysis will reduce the need for manual annotation, allowing more of the muscle to be measured and enable much larger cohorts to be studied, this is particularly important as large population based biobanks are becoming more common. In this paper we have described a CNN-based method to automatically extract and quantify iliopsoas muscle volume from MRI scans for 5000 participants from the UKBB. Excellent agreement was obtained between automated measurements and the manual annotation undertaken by a trained radiographer as demonstrated by the extremely high DSC with testing data. CNNs have been established as the gold standard in automated image segmentation. Te results, which can be produced with a modest amount of manual annotations as training data and smart data augmentation, are highly accurate, fast, and reproducible. Manual annotations become a bottleneck for large-scale population studies, when the number of participants exceeds many thousand such as with the UKBB. Applying automated methods to vast amounts of data

requires a thorough set of quality-control procedures beyond just out-of-sample testing data, which is often used to validate new methods in machine learning studies. Large-scale quality control can be done by steps such as looking at maximum and minimum values, asymmetric values (for symmetric structures such as the iliopsoas muscles), outliers, and overall behavior of the results. The vast majority of previous studies investigating psoas muscle size have relied on CSA measurements primarily because of data availability and time constraints [3,4,6–11,13,14,16–19]. Analysis of CSA is considerably less labour intensive than manually measuring tissue volumes, furthermore, many studies have repurposed clinical CT or MRI scans [16–18] which typically will not have been acquired in a manner to enable volume measurements. This has led to psoas muscle CSA being measured at a variety of positions relating to lumbar landmarks including L3, L4 and between L4-5, as well as more unreliable soft tissue landmarks such as the umbilicus, with the CSA measurements used alone, relative to lumbar area, height, height squared or total abdominal muscle within the image at the selected level. While lumber landmarks should provide a relatively consistent CSA in longitudinal studies, comparison between studies and cohorts becomes almost impossible. This is further compounded by studies that have shown considerable variation in psoas CSA along its length [2,42], and that regional differences in psoas CSA have been observed in athletes [43], following exercise training or inactivity [44]. This appears to suggest that CSA at a fixed position may not accurately reflect changes in the psoas size elsewhere in response to health related processes. It is clear that to overcome these confounding factors, it is essential to measure total psoas volume. In this study, we have trained a CNN to segment iliopsoas muscles, applied it to 5000 UKBB subjects and measured their total volume. Tis measurement includes the psoas major and iliacus muscles, and as mentioned in the proceeding section, the psoas minor muscle (if present). This reflects the practical difficulties of isolating the entire psoas muscle in images in a consistent and robust manner. The merging of the iliacus and psoas muscles below the inguinal ligament makes their separation not only impractical, but unachievable with standard imaging protocols. Similarly, it is not possible to separate the psoas major and minor muscles under these conditions, even if CSA measurements were to be made. Therefore, a standard operating procedure was required, either measure a partial psoas volume, selecting an anatomical cut-of before the junction with the iliacus muscle, or to include the iliacus and measure the iliopsoas muscle volume in its entirety. In this study we have opted for the latter, as selecting an arbitrary set point would clearly introduce a significant confounding

factor with unforeseeable impact on the subsequent results. Tus, we have measured the entire iliopsoas muscle, and although literature comparisons are limited, as there is a paucity of comparable volumetric studies within the general population, our average reported values for male subjects (407.2 ± 62.7 ml) were within the range 351.1–579.5 ml in a cohort which included male athletes and controls [43] Furthermore, our CNN-based method performs very well, with a small but systematic underestimation of −0.2% when compared with manual annotations. Incremental improvement of the model is possible using straightforward techniques, such as increasing the number and variety of training data or expanding the breadth of data augmentation [45]. These are currently under investigation. We observed a small (approximately 2%) but significant asymmetry in iliopsoas muscle volume, with the right muscle being larger in both male and female subjects. Previous studies have looked at the muscle asymmetry in tennis players, and found that the iliopsoas muscle was 13% smaller on the non-dominant compared with the dominant side of the body, whereas inactive controls the dominant size was 4% larger than the non-dominant [43]. Similarly footballers players have significantly larger psoas CSA on their dominant kicking side [46]. The best equivalent to this within the UKBB phenotyping data was handedness, which we found not to be related to left right differences in iliopsoas volume in the current study. An additional factor which may contribute towards iliopsoas asymmetry relates to the presence or absence of the psoas minor muscle, a long slim muscle typically found in front of the psoas major. Tis muscle can often fail to develop during embryonic growth [2] and there can be considerable differences in the incidence of agenesis which can be unilateral or bilateral with ethnicity thought to be a factor [47]. Further work is required to understand whether this contributes to the left-right asymmetry observed in the present study, since it is not possible to resolve this muscle on standard MRI images. In line with previous studies of psoas CSA, male subjects had significantly larger iliopsoas muscles compared to females [6]. This is unsurprising since gender differences in both total muscle and regional muscle volumes are well established [48,49]. Indeed some studies have suggested using gender specific cut-offs of either psoas CSA alone or psoas muscle index to identify patients at risk of poorer health outcomes [10]. Furthermore, some studies have suggested that the magnitude of gender differences in trunk muscle CSA vary depending where are measured. This adds weight to the argument that volumetric measurements are perhaps more robust than CSA measures for this comparison [50]. It has been proposed that the gender differences in psoas volume could in part relate to the

impact of height on psoas volume [12]. Indeed, we found a significant correlation between iliopsoas muscle volume and height similar to those previously reported by earlier studies [49]. However, the gender differences observed in our study were still present when correcting for height. Interestingly, it has been reported that the relationship between muscle volume and body weight is curvilinear, since increases in body weight often reflect gain in fat, as well as muscle mass. In the present study we observe a significant correlation between IMI and BMI. This is in agreement with previous studies of psoas CSA which have also shown a significant correlation with BMI [6], indeed some studies combined both metrics as a prognostic marker [17]. We also found a significant correlation between IMI and age. It is widely reported that muscle mass declines with age, particularly beyond the fifth decade, a fundamental characteristic of sarcopenia [51]. The magnitude of this decline was relatively small, but this may arise by the limited age range within the UKBB data set (44–82 years), compared to other studies that have investigated the impact of age on muscle volume across the entire adult age span (18–88 years), which usually tend to reveal a more dramatic decline in muscle volume [49]. In conclusion, we have developed a robust and reliable model using a CNN to automatically segment iliopsoas muscles and demonstrated the applicability of this methodology in a large cohort, which will enable future population-wide studies of the utility of iliopsoas muscle as a predictor of health outcomes.

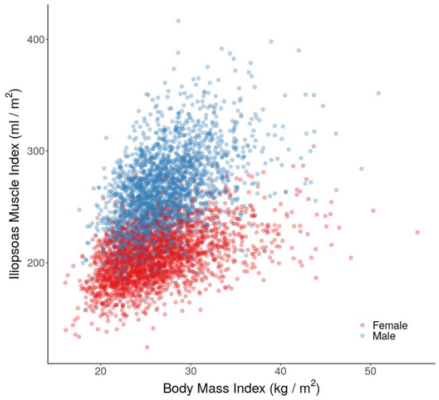

Fig 6. Scatterplot of iliopsoas muscle index (ml/m²) by BMI (kg/m²), separated by gender.

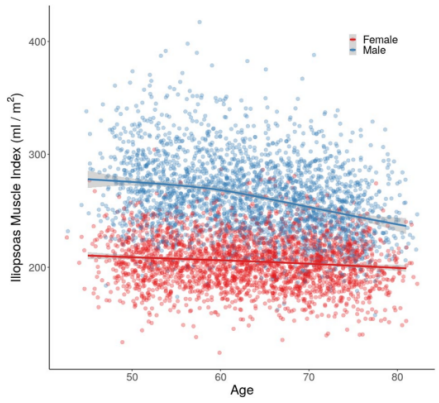

Figure 7. Scatterplot of iliopsoas muscle index (ml/m2²) by age at recruitment (years), separated by gender. The curves are ft to the data using a generalised additive model with cubic splines.

Code availability

Model weights and instructions for use are available at https://github.com/recoh/iliopsoas_muscle.

References

1. Regev, G. J. et al. Psoas muscle architectural design, in vivo sarcomere length range, and passive tensile properties support its role as a lumbar spine stabilizer. Spine 36, E1666–E1674 (2011).

2. Hanson, P., Magnusson, S. P., Sorensen, H. & Simonsen, E. B. Anatomical diferences in the psoas muscles in young black and white men. J. Anat. 194, 303–307 (1999).

3. Swanson, S. & Patterson, R. B. Te correlation between the psoas muscle/vertebral body ratio and the severity of peripheral artery disease. Ann. Vasc. Surg. 29, 520–525 (2015).

4. Ebbeling, L. et al. Psoas: lumbar vertebra index: central sarcopenia independently predicts morbidity in elderly trauma patients. Eur. J. Trauma Emerg. Surg. 40, 57–65 (2014).

5. Mourtzakis, M. et al. A practical and precise approach to quantifcation of body composition in cancer patients using computed tomography images acquired during routine care. Appl. Physiol. Nutr. Metab. 33, 997–1006 (2008).

6. Jones, K., Doleman, B., Scott, S., Lund, J. N. & Williams, J. P. Simple psoas cross-sectional area measurement is a quick and easy method to assess sarcopenia and predicts major surgical complications. Colorectal Dis. 17, O20–O26 (2015).
7. Durand, F. et al. Prognostic value of muscle atrophy in cirrhosis using psoas muscle thickness on computed tomography. J. Hepatol. 60, 1151–1157 (2014).
8. Saitoh-Maeda, Y. et al. A low psoas muscle volume correlates with a longer hospitalization afer radical cystectomy. BMC Urol. 17, 87 (2017).
9. Delitto, D. et al. A clinically applicable muscular index predicts long-term survival in resectable pancreatic cancer. Surgery 161, 930–938 (2017).
10. Kasahara, R. et al. A low psoas muscle index before treatment can predict a poorer prognosis in advanced bladder cancer patients who receive gemcitabine and nedaplatin therapy. BioMed Res. Int. 2017, (2017).
11. Morrell, G. R. et al. Psoas muscle cross-sectional area as a measure of whole-body lean muscle mass in maintenance hemodialysis patients. J. Renal Nutr. 26, 258–264 (2016).
12. Fitzpatrick, J. et al. Psoas major cross-sectional area: a potential marker of cardiorespiratory ftness. Int. J. Clin. Exp. Physiol. 4, 15–20 (2017).
13. Maltais, A. et al. One-year lifestyle intervention, muscle lipids, and cardiometabolic risk. Med. Sci. Sports Exerc. 51, 2156–2165 (2019).
14. Drudi, L. et al. Psoas muscle area predicts all-cause mortality afer endovascular and open aortic aneurysm repair. Eur. J. Vasc. Endovasc. Surg. 52, 764–769 (2016).
15. Huber, T. C. et al. Predictors of all-cause mortality afer endovascular aneurysm repair: Assessing the role of psoas muscle crosssectional area. J. Vasc. Interv. Radiol. 30, 1972–1979 (2019).
16. Lee, J.S.-J. et al. Frailty, core muscle size, and mortality in patients undergoing open abdominal aortic aneurysm repair. J. Vasc. Surg. 53, 912–917 (2011).
17. Hervochon, R. et al. Body mass index and total psoas area afect outcomes in patients undergoing pneumonectomy for cancer. Ann. Torac. Surg. 103, 287–295 (2017).
18. Bukvić, M. et al. Psoas muscle index as indicator of sarcopenia in patients with colorectal carcinoma during oncological treatment. Int. J. Sci. Eng. Res. 10, 599–602. https://doi.org/10.14299/ijser.2019.07.01 (2019).
19. Gu, D. H. et al. Clinical usefulness of psoas muscle thickness for the diagnosis of sarcopenia in patients with liver cirrhosis. Clin. Mol. Hepatol. 24, 319 (2018).

20. Baracos, V. E. Psoas as a sentinel muscle for sarcopenia: a fawed premise. J. Cachexia Sarcopenia Musc. 8, 527–528 (2017).
21. Modesto, A. E. et al. Psoas muscle size as a magnetic resonance imaging biomarker of progression of pancreatitis. Eur. Radiol. 1–10, (2020).
22. Valero, V. et al. Sarcopenia adversely impacts postoperative complications following resection or transplantation in patients with primary liver tumors. J. Gastrointestinal. Surg. 19, 272–281 (2015).
23. Amini, N. et al. Impact total psoas volume on short-and long-term outcomes in patients undergoing curative resection for pancreatic adenocarcinoma: a new tool to assess sarcopenia. J. Gastrointestinal Surg. 19, 1593–1602 (2015).
24. Zargar, H. et al. Change in psoas muscle volume as a predictor of outcomes in patients treated with chemotherapy and radical cystectomy for muscle-invasive bladder cancer. Bladder Cancer 3, 57–63 (2017).
25. Suh, J. W. et al. Efect of sarcopenic overweight on lung transplant based in three-dimensional reconstructed psoas muscle mass. Ann. Torac. Surg. 107, 1626–1631 (2019).
26. Ronneberger, O., Fischer, P. & Brox, T. U-net: Convolutional networks for biomedical image segmentation. In International conference on medical image computing and computer-assisted intervention, 234–241 (Springer, 2015).
27. Milletari, F., Navab, N. & Ahmadi, S.-A. V-net: Fully convolutional neural networks for volumetric medical image segmentation. In 2016 Fourth International Conference on 3D Vision (3DV), 565–571 (IEEE, 2016).
28. Hiasa, Y. et al. Automated muscle segmentation from clinical ct using bayesian u-net for personalized musculoskeletal modeling. IEEE Trans. Med. Imaging 39, 1030–1040 (2019).
29. Hashimoto, F., Kakimoto, A., Ota, N., Ito, S. & Nishizawa, S. Automated segmentation of 2d low-dose ct images of the psoas-major muscle using deep convolutional neural networks. Radiol. Phys. Technol. 12, 210–215 (2019).
30. Kamiya, N. et al. Surface muscle segmentation using 3d u-net based on selective voxel patch generation in whole-body ct images. Appl. Sci. 10, 4477 (2020).
31. Ghosh, S., Boulanger, P., Acton, S. T., Blemker, S. S. & Ray, N. Automated 3d muscle segmentation from mri data using convolutional neural network. In 2017 IEEE International Conference on Image Processing (ICIP), 4437–4441 (IEEE, 2017).

32. Weber, K. A. et al. Deep learning convolutional neural networks for the automatic quantifcation of muscle fat infltration following whiplash injury. Sci. Rep. 9, 1–8 (2019).
33. Borga, M. et al. Validation of a fast method for quantifcation of intra-abdominal and subcutaneous adipose tissue for large-scale human studies. NMR Biomed. 28, 1747–1753 (2015).
34. Sudlow, C. et al. UK Biobank: An open access resource for identifying the causes of a wide range of complex diseases of middle and old age. PLoS Med. 12, e1001779 (2015).
35. Littlejohns, T. J. et al. Te UK Biobank imaging enhancement of 100,000 participants: Rationale, data collection, management and future directions. Nat. Commun.https://doi.org/10.1038/s41467-020-15948-9 (2020).
36. Basty, N. et al. Image processing and quality control for abdominal magnetic resonance imaging in the UK Biobank (2020). arXiv :2007.01251.
37. Liu, Y. et al. Systematic quantifcation of health parameters from UK Biobank abdominal MRI using deep learning. bioRxivhttps ://doi.org/10.1101/2020.07.14.187070 (2020).
38. Nolden, M. et al. Te Medical Imaging Interaction Toolkit: challenges and advances. Int. J. Comput. Assist. Radiol. Surg. 8. https ://doi.org/10.1007/s11548-013-0840-8 (2013). 10 Vol:.(1234567890) Scientifc Reports|(2020)10:20215|https://doi.org/10.1038/s41598-020-77351-0 www.nature.com/scientificreports/
39. Klambauer, G., Unterthiner, T., Mayr, A. & Hochreiter, S. Self-normalizing neural networks. Adv. Neural Inf. Process. Syst. 971–980 (2017).
40. Chollet, F. et al. Keras. https://github.com/fchollet/keras (2015).
41. R Core Team. R: A Language and Environment for Statistical Computing. R Foundation for Statistical Computing, Vienna, Austria (2020).
42. Reid, J. G., Livingston, L. A. & Pearsall, D. J. Te geometry of the psoas muscle as determined by magnetic resonance imaging. Arch. Phys. Med. Rehabil. 75, 703–708 (1994).
43. Sanchis-Moysi, J., Idoate, F., Izquierdo, M., Calbet, J. A. L. & Dorado, C. Iliopsoas and gluteal muscles are asymmetric in tennis players but not in soccer players. PLoS ONE 6, e22858 (2011).
44. Hides, J. A. et al. Magnetic resonance imaging assessment of trunk muscles during prolonged bed rest. Spine 32, 1687–1692 (2007).

45. Lundervold, A. S. & Lundervold, A. An overview of deep learning in medical imaging focusing on MRI. Zeitschrif für Medizinische Physik 29, 102–127. https://doi.org/10.1016/j.zemedi.2018.11.002 (2019).
46. Stewart, S., Stanton, W., Wilson, S. & Hides, J. Consistency in size and asymmetry of the psoas major muscle among elite footballers. Br. J. Sports Med. 44, 1173–1177 (2010).
47. Ojha, P., Prakash, S. & Jain, A. Morphology of psoas minor muscle-a cadaveric study. Int. J. Curr. Res. Rev. 8, 35 (2016).
48. Gallagher, D. & Heymsfeld, S. B. Muscle distribution: variations with body weight, gender, and age. Appl. Radiat. Isot. 49, 733–734 (1998).
49. Janssen, I., Heymsfeld, S. B., Wang, Z. M. & Ross, R. Skeletal muscle mass and distribution in 468 men and women aged 18–88 years. J. Appl. Physiol. 89, 81–88 (2000).
50. Abe, T., Kearns, C. F. & Fukunaga, T. Sex diferences in whole body skeletal muscle mass measured by magnetic resonance imaging and its distribution in young Japanese adults. Br. J. Sports Med. 37, 436–440 (2003).
51. Rosenberg, I. H. Sarcopenia: origins and clinical relevance. J. Nutr. 127, 990S-991S (1997).

Author contributions

J.A.F., J.D.B. and E.L.T. conceived the study. J.D.B., E.L.T., N.B. and B.W. designed the study. J.A.F. performed the manual annotations. N.B. implemented the methods and performed data analysis. B.W. performed statistical analysis of the data. E.L.T. and N.B. drafed the manuscript. J.D.B., E.L.T., N.B., Y.L, M.C. and B.W. participated in data preprocessing and editing the manuscript. All authors read and approved the manuscript.

Competing interests

MC and YL are employees of Calico Life Sciences LLC. NB, JAF, JDB, ELT and BW declare no competing interests.

Evaluation of Papers

Paper 1 (P1): Cardiac T2* and lipid measurement at 3.0 T-initial experience

Cardiac T2* and lipid measurement at 3.0 T-initial experience published in 2008 in *European Radiology*, journal of the European Society of Radiology (ESR). Founded in 1991, European Radiology is one of the leading European journals in the field of medical imaging, owned by the European Society of Radiology. European Radiology (ER) continuously updates scientific knowledge in radiology by publication of strong original articles and state-of-the-art reviews written by leading radiologists. A well-balanced combination of review articles, original papers, short communications from European radiological congresses and information on society matters makes ER an indispensable source for current information in this field. The journal is subscribed to by a regular audience of several thousands of readers worldwide (+ 100.000), making it one of the most widely disseminated journals in Radiology. (*European Radiology*, 2023)
https://www-springer-com.salford.idm.oclc.org/journal/330/
ISSN-Electronic 1432-1084

Influence

Paper 1 have been cited 19 times in the literature with Meloni et al. (2014) supporting the feasibility of performing this technique at a field strength of 3T. Further citations publish their own T2* values which agree with those published in Paper 1 (Cobb & Paschal, 2009; Heinrichs et al., 2009; Hezel et al., 2012; Manka et al., 2010; Meloni et al., 2012; Niendorf et al., 2016; Yamamura et al., 2010).
Thus, initial normative values for cardiac T2* were presented in P1 and subsequently confirmed by other researcher groups has subsequently been published in peer reviewed journals. This works is now part of the seminal research that established the use of T2* values in clinical research.

Personal Contribution

- All the MR imaging of the complex and demanding procedure that is CMR, including patient preparation.
- Ensuring compliance with the project's governance and ethics.
- Compliance, documentation, and record-keeping to maintain good clinical practice along with ensuring that exposure times were not exceeded, the protocol to which the subject has consented to was followed precisely.
- Ensure that aquired data was fully QC so that T2* values obtained were robust and reliable.

Authors	Declan P. O'Regan Martina F. Callaghan Julie Fitzpatrick Rossi P. Naoumova Joseph V. Hajnal Stephan A. Schmitz
Title	Cardiac T * and lipid measurement at 3.0 T-initial experience
Publication Details	European Radiology 2008
Candidate Contribution	Acquisition of all imaging data Preparation and coaching of study participants Performing quality control Archiving and curating imaging data Review and feedback of final manuscript

Co-Author Confirmation

By signing the Statement of Authorship, author confirms that:

The candidate's stated contribution to the publication is accurate.

Name	Professor D.P. O'Regan
Comments	
Signed	
Date	6/3/2023

Paper 2 (P2)

Liver fat content and T2*: Simultaneous measurement by using breath-hold multiecho MR imaging at 3.0 T – Feasibility

Published in the *Radiology* in 2008
Produced by the Radiological Society of North America (RSNA), *Radiology* has long been recognised as the authoritative reference for the most current, clinically relevant, and highest quality research in the field of radiology. *Radiology* is published 12 times a year, online and in print, and it is one of the top-cited journals in the field. (*European Radiology*, 2023)
https://pubs.rsna.org/journal/radiology
ISSN: 0033-8419 (print); 1527-1315 (online)

Influence

Paper 2 has been cited 119 times most notably by esteemed researchers in the same field including Scott Reeder (Reeder et al., 2011a, 2011b, 2012; Reeder & Sirlin, 2010) Harry Hu (H. Hu et al., 2011; H. H. Hu et al., 2010), Claude B. Sirlin (Sirlin & Reeder, 2010) and Mark Bydder (Bydder et al., 2010)
In addition, Paper 2 is cited by researchers who have used data from the large cohort study DIRECT(*DIRECT - DIabetes REsearch on Patient StraTification*, 2022). DIRECT included the ME sequence originating in P2 and adapted into the imaging protocol for this study. Findings have included the discovery of glycaemic deterioration biomarkers(Koivula et al., 2019) and the role of physical activity in type 2 diabetes(Koivula et al., 2020).
This paper also served as the basis for the subsequent MRI protocol established by the Imaging Working Group of the UK Biobank, where over 68,000 participants have already. The Uk Biobak aims to scan a total of 100,000 participant in its first phase, a further 60,000 will be re-scanned as part of the second longitudinal phase.

Personal Contribution

- My role in P2 was like P1 was to ensure that examination was fully compliant with the overall objectives of the protocol and that the MR images were of sufficient quality and reproducibility to ensure best outcome.

- P2 included MRS which meant additional sequences and working alongside additional team members.
- The inclusion of patients required the input of a radiographer to ensure patient care was forthcoming.
- The person-centred care provided ensured high quality and consistent data collection along with a methodical approach to data management.

Authors	Declan P O'Regan, Martina F. Callaghan MarzenaWylezinska- Arridge, JulieFitzpatrick RossiP.Naoumova, Joseph V. Hajnal Stephan A.Schmitz
Title	**Liver Fat Content and T2*: Simultaneous Measurement by Using Breath-hold Multiecho MR Imaging at 3T-Feasibility**
Publication Details	Radiology
Candidate Contribution	Acquisition of all imaging data Preparation and coaching of study participants Performing quality control Archiving and curating imaging data Review and feedback of final manuscript

Co-Author Confirmation

By signing the Statement of Authorship, author confirms that:

The candidate's stated contribution to the publication is accurate.

Name	Professor D.P. O'Regan
Comments	
Signed	
Date	6/3/2023

Paper 3 (P3)

Reduction of total lung capacity in obese men: Comparison of total intrathoracic and gas volume

Published in the Journal of Applied Physiology in 2010
The *Journal of Applied Physiology* publishes the highest quality original research and reviews that examine novel adaptive and integrative physiological mechanisms in humans and animals that advance the field. (REF website)
https://journals-physiology-org.salford.idm.oclc.org/journal/jappl
ISSN: 8750-7587 (print); 1522-1601 (online)

Influence

After being published in the Journal of Applied Physiology in 2010 Paper 3 established that there was a reduced lung capacity in obese men. The authors followed this in 2012 with the publication '*Relation between trunk fat volume and reduction of total lung capacity in obese men'* (Watson et al., 2012). Using the whole-body imaging acquired at the same time as the thorax volumes they attempted to explain the differences comparing the abdominal fat volumes. No relationship was found but Paper 3 is cited in the methods section to convey how the MRI was performed and the images acquired.
After publication Paper 3 is cited in many literature reviews on topics such as asthma and obesity, ventilating obese patients and mechanical ventilation in obese patients(Guenette et al., 2010; Littleton, 2012; Ortiz et al., 2015; Peters, Dixon, et al., 2018; Peters, Suratt, et al., 2018; Ruppel, 2012; Silva et al., 2012; Spelta et al., 2018).
More recently however, Paper 3 has been cited more frequently due to the COVID-19 pandemic. It was established that overweight and obese men had a higher rate of death from the infection (Chawla et al., 2020; Hamer et al., 2020) and studies have cited Paper 3 as an explanation for this (Halvatsiotis et al., 2020; Khalili et al., 2021; Pérez-Cruz et al., 2021; Raeisi et al., 2022; Redwood-Brown et al., 2021; J. Wang et al., 2020; Wicaksana et al., 2021)

Personal Contribution

- First approached as adviser regarding if the imaging component was achievable and the requirements.
- Designed the MRI sequences, built them, and tested them on the scanner.
- Engaged in discussion into how to screen the patients who would not fit into the scanner.
- I then modified two hula hoops to be the same circumference as the scanner interior.
- I performed all the imaging, quality control and archiving.
- Coached the lead authors on MR image contrast and anatomy recognition and image analysis.

Authors	Watson, R. A. Pride, N. B. Thomas, E. Louise Fitzpatrick, J. Durighel, G. McCarthy, J. Morin, S. X. Ind, P. W. Bell, J. D.
Title	Reduction of total lung capacity in obese men: comparison of total intrathoracic and gas volumes
Publication Details	Journal of Applied Physiology 2010
Candidate Contribution	• Designed and optimised MRI sequences • Performed the imaging including coaching patients. • Performed quality assurance on images • Discussed and demonstrated methods of analysis and reviewed results • Reviewed final manuscript.

Co-Author Confirmation review of results

By signing the Statement of Authorship, author confirms that:

The candidate's stated contribution to the publication is accurate.

Name	Professor J.D. Bell
Comments	This project was very taxing requiring very significant input not only in the design, but also required a new acquisition modality and image analysis, all of which was undertaken by Julie. She was also key in the process of image analysis
Signed	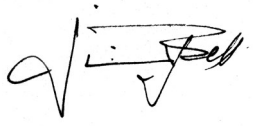

Date	15th of April 2021

Paper 4 (P4)

Whole body fat: Content and distribution

Published in Progress in Nuclear Magnetic Resonance Spectroscopy in 2013
Progress in Nuclear Magnetic Resonance Spectroscopy publishes review papers describing research related to the theory and application of NMR spectroscopy. This technique is widely applied in chemistry, physics, biochemistry, and materials science, and also in many areas of biology and medicine. The journal publishes review articles covering applications in all of these and in related subjects, as well as in-depth treatments of the fundamental theory of and instrumental developments in NMR spectroscopy.
https://www-sciencedirect-com.salford.idm.oclc.org/journal/progress-in-nuclear-magnetic-resonance-spectroscopy
ISSN: 0079-6565 (print) 1873-3301 (on-line)

Influence

Paper 4 has been cited frequently including in other literature searches (Borga, 2018; Borga et al., 2018; Bray et al., 2018; H. H. Hu et al., 2016; Kersten, 2023; Lim & Meigs, 2013; Ponti et al., 2019) and book chapters (Heymsfield et al., 2014; Thomas & Bell, 2015)
Most relevant is research which cites Paper 4 in the methods to describe the techniques to acquire data in DIRECT and the UK Biobank, the latter being the largest human cohort in the world and from where more than 8,000 paper have been already published in peer-reviewed journals. These include rational and descriptions in DIRECT (Koivula et al., 2014, 2019) along with other publications using the DIRECT data (Atabaki-Pasdar et al., 2020) and notably Wesolowska-Anderson (2022) who describes four groups of type 2 diabetes and Erikson (2020) who introduce new insight into nutrition and metabolic risk.

Using UK Biobank data Linge et al. (2018) describe body profiling but further references have used P4 to describe how the UK Biobank was set up (Littlejohns et al., 2020).
Other publications which use Paper 4 to describe their methods include studies into exercise training in NAFLD (Shojaee-Moradie et al., 2016), changes in renal sinus fat (Zelicha et al., 2018), genetic risk of adiposity (Monnereau et al., 2018).

Personal Contribution

- Conduct full literary review of ectopic fat.
- Write up work to ME procedure.
- Provide illustrations of ME and liver fat
- Prepare for publication and review all draft versions.

Authors	Thomas, E. L. Fitzpatrick, J. A. Malik, S. J. Taylor-Robinson, S. D. Bell, J. D.
Title	Whole body fat: Content and distribution
Publication Details	Progress in Nuclear Magnetic Resonance Spectroscopy 2013
Candidate Contribution	• Designed publication and content • Perform literature review of ectopic fat and methodologies • Participated in writing and editing • Review final manuscript.

Co-Author Confirmation

By signing the Statement of Authorship, author confirms that:

The candidate's stated contribution to the publication is accurate.

Name	Professor J. D. Bell
Comments	Julie made a very significant contribution to this publication, from its original design to its writing and editing. Her knowledge of existing MRI and MRS techniques and their corresponding literature were pivotal for the final outcome
Signed	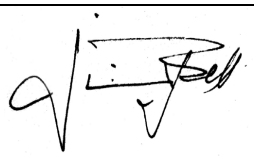
Date	15th of April 2021

Paper 5 (P5)

Validation of a fast method for quantification of intra-abdominal and subcutaneous adipose tissue for large-scale human studies

Published in NMR in Biomedicine in 2015
NMR in Biomedicine is a journal devoted to the publication of original full-length papers, rapid communications and review articles describing the development of magnetic resonance spectroscopy or imaging methods or their use to investigate physiological, biochemical, biophysical, or medical problems.
https://analyticalsciencejournals-onlinelibrary-wiley-com.salford.idm.oclc.org/journal/10991492
ISSN: 0952-3480 (print); 1099-1492 (online)

Influence

Paper 5 has been cited 48 times including test re-test reliability which was published by Newman et al. (2016) referencing the methods section of P5 and performing the protocol on a wide bore 3T scanner. The feasibility of using the protocol presented in P5 for large scale studies was published in PLoS ONE in 2016 after 3000 UKBB participants were analysed (West et al., 2016). Further evidence of the Profilers use in large scale population studies was published in Magneton FLASH magazine, a Siemens publication presenting MRI articles, application tips and technical information (Forsgren & West, 2017). Interestingly, the Profiler software has expanded beyond abdominal fat segmentation to breast fat volume analysis published in 2017 where the methods from paper 5 are cited (Petridou et al., 2017). Petridou et al. (2017) gave new insight into breast density and a robust method of measurement of fibro glandular tissue without the use of ionising radiation.

The AMRA Profiler has become part of the UK Biobank body imaging protocol and Paper 5 has been cited frequently in the methods sections of papers which have used data from the UK Biobank. Most notably was Linge et al. (Linge et al., 2018) where the first analysis of 6000 participants drawing attention to how "*Different diseases were linked to different body composition profiles (BCP), which could not be described by a single fat compartment alone*"

and that "*more targeted and effective disease treatments could be developed*". More recently the same author published further findings regarding defining sarcopenia in aging and Obesity (Linge, Heymsfield, et al., 2020) and adverse muscle composition in NAFLD which also cite Paper 5 in the methods (Linge, Ekstedt, et al., 2020). In addition, UKBB body data has been included in a publication looking at cardiovascular outcomes along with data from the Dallas Heart Study (Tejani et al., 2022).

In similar fashion other publications cite Paper 5 as their methods when using the AMRA protocol, Profiler software and slice-O-Matic software. These include a variety of findings including an investigation into the FTO gene and appetite (Reistenbach Goltz et al., 2019), comparisons between DXA and CT (Coletta et al., 2019), the use of Empagliflozin Treatment in Obesity (M. H. Lee et al., 2022; Neeland et al., 2021) and my own publication investigating Large-scale analysis of iliopsoas muscle volumes in the UK Biobank which is submitted for consideration within this PhD (J. A. Fitzpatrick et al., 2020).

Personal Contribution

- Perform all protocol set up as well as actual imaging including patient preparation.
- QC, curation and archiving of data.
- Oversaw QC of image analysis, provide feedback to inventors at every stage of analysis and publication.

Authors	Borga, Magnus Thomas, E. Louise Romu, Thobias Rosander, Johannes Fitzpatrick, Julie Dahlqvist Leinhard, Olof Bell, Jimmy D.
Title	Validation of a fast method for quantification of intra-abdominal and subcutaneous adipose tissue for large-scale human studies
Publication Details	NMR in Biomedicine 2015
Candidate Contribution	• Set up and tested acquisition protocol. Performed all the imaging acquisition and assessed quality and consistency. • Provided feedback and writing of publication • Reviewed the final manuscript.

Co-Author Confirmation

By signing the Statement of Authorship, author confirms that:

The candidate's stated contribution to the publication is accurate.

Name	Professor J. D. Bell
Comments	Julie actively participated in the designed of the study, its performance, analysis and writing of this seminal paper, which became the basis for a larger multi-centre and Biobank studies
Signed	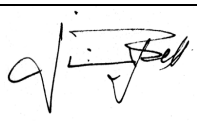
Date	15th of April 2021

Paper 6 (P6)

Changes in Liver Volume in Patients with Chronic Hepatitis C Undergoing Antiviral Therapy

Published in Journal of Clinical and Experimental Hepatology 2016.
Journal of Clinical and Experimental Hepatology (JCEH) is an international peer-reviewed journal of hepatology and publishes six issues in a year. JCEH publishes outstanding basic and clinical papers on all aspects of liver diseases, including both human and animal studies.
https://www.jcehepatology.com/
ISSN: 0973-6883 (print); 2213-3453 (online)

Influence

Paper 6 has been cited five times by other studies who have recognized the findings but interesting Wake et al. (2020) did not see the same increase in liver volume in their study though did record improved liver function tests with sustained viral response.
In their study '*Building Large-Scale Quantitative Imaging Databases with Multi-Scale Deep Reinforcement Learning: Initial Experience with Whole-Body Organ Volumetric Analyses'* which cites Paper 6, Winkle et al. (2021) draw attention to how useful organ volume measurements is and that manual techniques are not realistic due to time and resources and call for the annotation process to be automated.

Personal Contribution

- Performed the MR imaging when joining the study after it commenced.
- Curating previously acquired data.
- Identified a method to measure the liver and completed the analysis.
- Organising and performing an exercise in repeatability with a co-author.
- Wrote the first draft of the manuscript and reviewed the final draft after sharing with the co-authors.

Paper 7 (P7)

Psoas major cross-sectional area: A potential marker of cardiorespiratory fitness

Published in International Journal of Clinical and Experimental Physiology March 2017
The aim of the International Journal of Clinical and Experimental Physiology (IJCEP) is to publish peer reviewed quality research papers in Physiology that have clinical application in medicine or papers with experimental evidence having a future perspective of application in medicine.
https://www.ijcep.org/index.php/ijcep
ISSN: 2348-8832 (print); 2348-8093 (online)

Influence

Paper 7 has been cited six times with Byun et al. (2019) agreeing that the psoas CSA is a predictor of mortality after hip fracture. Hawkins et al. (2018) also cited P7 in their study which used the PM size to predict outcomes after aortic valve replacement.
Having established a link between PM CSA and CV Fitness this encouraged further work in this area and exploring the possibility of automating the process of segmentation. The original manual annotation and analysis of the MR images served as “ground-truth” for a subsequent AI-based algorithm that allow for automated analysis of abdominal images. This has now been applied to <60,000 participant in the UK Biobank and will serve as the basis for a follow up paper in this area.

Personal Contribution

- Conceived the study after a period of observation and discussion with the group head.

- A method for extracting the images was identified along with methods to measure physical activity.
- Persuaded a co-author to join me who had expertise in measuring V02 Max and statistics.
- I performed all the imaging, curation, analysis, and extraction of data.
- Created original “ground-truth” for subsequent AI training.
- Participate in writing of first draft.
- Presented poster at international conference.

Paper 8 (P8)

Advancing Pancreas Segmentation in Multi-protocol MRI Volumes using Hausdorff-Sine Loss Function

Conference paper presented at 10th International Workshop on Machine Learning in Medical Imaging (MLMI 2019) in conjunction with The Medical Image Computing and Computer Assisted Intervention Society (MICCAI) 2019 Shenzhen, China. Oct 2019
Published in book section Machine Learning in Medical Imaging. Part of the Lecture Notes in Computer Science book series (LNIP, vol. 11861).
https://link.springer.com/bookseries/558

Influence

P8 has been cited nine times including similar work by other groups in abdominal organ segmentation (Bakasa & Viriri, 2023; Chen et al., 2019; Sakai, 2021; Sánchez-Peralta et al., 2020; R. Wang et al., 2021).
First and last author of P8 presented follow up work for organ segmentation from multiple modalities and scanner protocols citing the work in P8 (Villarini et al., 2021).
Another group using UK Biobank data have cited P8 when presenting their automated pipeline for pancreas volume and shape characterization (Triay Bagur et al., 2020). While my colleagues on P9 have included P8 as a citation in measuring pancreas fat and iron content (Basty et al., 2020a).

Personal Contribution

- Provided in-depth pancreatic anatomical input to co-authors for acquisition and subsequent AI development
- Perform all segmentation for AI training data.
- Assessment and grading of all output during training of AI-based algorithm.
- QC final output from automated system prior to final data analysis and publication

Authors	Asaturyan, Hykoush Thomas, E.L. Louise Fitzpatrick, Julie Bell, Jimmy D. J.D. Villarini, Barbara Louise Thomas, E Fitzpatrick, Julie Bell, Jimmy D. J.D. Villarini, Barbara
Title	Advancing Pancreas Segmentation in Multi-protocol MRI Volumes using Hausdorff-Sine Loss Function
Publication Details	Machine Learning in Medical Imaging 2019
Candidate Contribution	• Anatomical expert who provided all the ground truth which the computer programmer used for developing learning model. • Assessed the outcomes and graded how well the computer model had segmented the pancreatic tissue • Participated in writing and review the final manuscript.

Co-Author Confirmation

By signing the Statement of Authorship, author confirms that:

The candidate's stated contribution to the publication is accurate.

Name	Professor J.D. Bell
Comments	Julie provided expert input in the designed and implementation for this project. Created all the necessary ground-truth for the machine-learning models, reviewed results and elaborated upon way to improve the outputs. She help in the writing of the manuscript and reviewed the final version
Signed	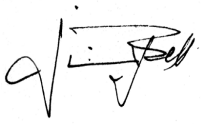
Date	15th of April 2021

Paper 9 (P9)

Large-scale analysis of iliopsoas muscle volumes in the UK Biobank

Published in Nature Scientific Reports in 2020
Scientific Reports is an online peer-reviewed open access scientific journal published by Nature Portfolio, covering all areas of the natural sciences Scientific Reports is the 6th most-cited journal in the world (*Scientific Reports*, 2023).

https://www-nature-com.salford.idm.oclc.org/srep/
ISSN: 2045-2322 (print); 2045-2322 (online)

Impact and Reach

Thus far, P9 has been cited thirteen times including in an examination of treating psoas muscle dysfunction(Shi & Han, 2022). Other researchers have also used UKBB data to measure body composition using deep regression to automate body composition analysis (Langner et al., 2020, 2021) citing both P5 and P11. Citing P11, Weber et al (2021) also used convolutional neural networks to investigate fatty infiltration into the cervical muscles. However, they used both the in and out of phase images to measure the fat content where P11 used only the derived water images.
The psoas muscle is easy to identify and conspicuous on several imaging modalities. Van Erck et al. (2022) used CT images to measure the total volume of the psoas muscle again using deep learning. Citing P11 they acknowledge that whole muscle volume is useful but go on to correlate it to clinical outcomes, concluding that fully automated whole muscle psoas assessment is a tool with great opportunities in large scale studies and clinical applications. P11 uses a technique which is prone to artifacts and up to 10% of data can be discarded due to water-fat swaps. This can be improved by using deep learning to fix these swaps and thus salvaging this data. My colleagues Basty et al (2021)have developed this citing P11 in the methods and P4 in the introduction.

Personal Contribution

- Conceived the study.
- Set up original acquisition protocol at the UK Biobank sites and QC all images.
- Generated ground truth for training data.
- Collaborated in the writing of initial draft of paper, including MR imaging methods and ground-truth validation.
- Reviewed and edited final draft.

Aims

Aim 1: to identify the processes required to enable quantification of MRI based parameters through optimised acquisition and analysis.

Aim 2: identify how these processes were undertaken in papers presented in this thesis.

Aim 3:to identify how the different processes apply from application to big data, and future technology such as AI and crowd sourcing.

Aim 4: identify areas of optimisation in terms of pipelines and resource limitations (staff) for future uses of AI.

Objectives

In the collation and analysis of this thesis, the following themes were identified: -

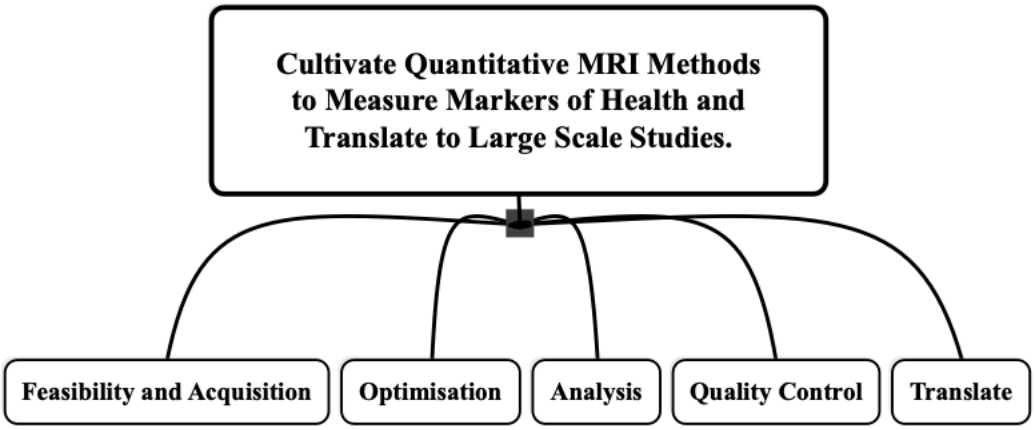

The thesis will be broken down into these chapters and sub-sections to demonstrate how this meets the aims of the research.

Feasibility and Acquisition

Medical images are created using many modalities and techniques. The information collected must be validated, relevant and achievable.

- Introduction
- Field Strength
- Ethics and Safety
- Cardiac MRI (CMRI)
- Liver MRI
- Patient experience
- Data
- DIRECT and UKBB

Optimisation

A process of optimisation is appropriate to fine tune imaging parameters to ensure efficient and effective use of resources. Limited availability of resources is considered along with the patient experience.

- Introduction
- Lung Volume
- Translate Muti-Echo to Pancreas
- Pancreas Volume
- Fast Whole Body Protocol Validation

Analysis

Information needs to be drawn out from the collected data to reach conclusions. Again, limited resources demand a straightforward and efficient method.

- Introduction
- In-House Software

- Open-Source Software
- Viewing Conditions
- Reliability
- Measuring Psoas

Quality Control

Methods to maintain and monitor quality are essential to ensure the data is fit for purpose.

- Introduction
- Pancreas Segmentation
- Machine Learning
- Quality in Large Scale Studies
- Dissemination of Imaging Protocol
- Fat Phantom

Translate

Scaling up to a large-scale study must be standardised when put into practice.

- Introduction
- Large Scale Studies- Patient Perspective
- Upscaling Body Composition Protocol
- QA in Large Scale Studies
- Psoas Muscle in Large Scale Studies

Critical Appraisal

Chapter 1

Feasibility and Acquisition

Introduction

The Scientific Method underpins the development of science, and one of the steps is to test a hypothesis through experimentation (Britanica, 2022). There are many different methods to use when conducting an experiment, and the collected data can be categorized as qualitative, non-numerical or quantitative, where the data has a unique numerical value. All methods involve collecting data for analysis to support or disprove a hypothesis. As such, the quality of acquired data must be high, and the collection method should be detailed, reproducible and free of bias. Whether gathering new data, using legacy, sharing, exchanging, or purchasing data, the manner of acquisition often remains unseen.

Papers 1, 2 and Poster Presentation A was performed at a field strength of 3 Tesla (3T). Clinical scanners of this field strength were only just starting to become available and experience at this time was described as anecdotal and unpublished (J. W. K. Lee & Shannon, 2007; Mosher, 2006) The scanner installed by the Medical Research Council imaging facility at the Hammersmith Hospital in 2003, where this research was conducted was one of the first in the UK.

Field Strength

Utilising 3T is logical because field strength has the potential to double the SNR and thus allow greater temporal and spatial resolution. In addition, there is a possibility of improved sensitivity to lower iron concentrations which may not be measurable at lower field strengths. P1 included healthy volunteers who were not expected to have abnormally high levels of iron in their livers, but it was still beneficial for obtaining accurate measurements. However, the disadvantages of 3T imaging are the increased susceptibility artefact and poor shimming, both of which are mentioned in P1. The issue of poor shimming at higher field strengths, such as 3T is addressed in P1. The use of higher-order shimming was applied routinely, as additional shimming along more directions improves homogeneity in the region under examination. Higher-order shimming reduces intravoxel dephasing and signal dropout, thus,

the images have a more uniform signal with less distortion (Zhang et al., 2009). During CMRI B0 inhomogeneity is exasperated by cardiac motion, flowing blood, and air/tissue interfaces, therefore the use of higher-order shimming was essential during the acquisition of P2. More recently, further developments have been introduced with specifically tailored and customized shimming methods, resulting in more efficient shim times and accurate spatial encoding (Juchem., et al., 2013; Matter et al., 2016).

Ethics and Safety

In keeping with Good Clinical Practice (GCP), all the papers included in this work were approved by the relevant ethics committees. However, utilising the higher field strength brings added safety considerations as, at the time, implanted devices had not been investigated for safety as thoroughly as at 1.5T, and Specific Absorption Rates (SAR) are higher. This meant that our study limited the research participants to those with no metallic implants. This severely restricted recruitment but was believed to be prudent at the time. Since its publication, the use of 3T scanners has proliferated worldwide and has become the field strength of choice for some applications, such as musculoskeletal (MSK) (Khodarahmi & Fritz, 2021; Mosher, 2006). The testing of implants has increased, and now more implanted devices have been shown to be safe or conditional at higher field strengths. Up-to-date information is available on MRIsafety.com (Shellock, 2022).

The higher SAR may have meant restricting imaging parameters to stay within MHRA guidelines, and P1 includes that the SAR was recorded and remained within the safety limits set by the MHRA (MHRA, 2007). However, it became clear that participants felt hotter in the scanner when imaging the body (thorax, abdomen, and pelvis) was performed. Participants reported feelings of warmth during acquisition of P1 and 2 and some were clearly sweating. This phenomenon of heating is well documented, and the MHRA recommends maintaining the environment at 25^{C} or below and ensuring that atmospheric humidity is below 60%. However, to counteract any adverse effects, no blankets were offered during scanning, and the participants were alerted to be aware of excessive warming. Additional monitoring was performed to obtain verbal assurance that the participants were still at a comfortable temperature at regular intervals throughout the examination.

Another phenomenon that has been proven using MRI is Peripheral Nerve Stimulation (PNS). Rapidly changing magnetic gradients induce electrical voltage potentials in the

extremities and can range from mild (tingling) to severe (muscle contractions)(Ham et al., 1997). Although not dangerous, it should be limited as PNS can be viewed as an adverse event causing the research participant discomfort and possible pain. Any reports or observations of PNS resulted in the immediate termination of the examination.
Further caution was required when moving the participants into the bore of the magnet and the staff moving around the room. Physical movement in a static magnetic field can induce the creation of electrical potentials and the possible displacement of naturally generated currents within the body, which can manifest as vertigo, nausea, phosphenes and metallic taste (M.H.R.A., 2021). Although transient, we were encouraged not to make haste around the scan room and move the participants very slowly into the magnet bore. The extra time required to address safety concerns was required to be included in the organisation of the scanning time which was a further limitation to throughput.
Since the publication of P1 and P2 3T scanners are now common and extensive evidence of their safety has been established, but caution is always recommended in the absence of firm evidence. Had the current level of robust safety information been available at the time, then more willing participants could have been included and shorter scanning times applied.

Cardiac MRI (CMRI)

Motion is a problem in CMRI because of the long scan times (Saloner et al., 2015) therefore, when performing CMRI, both the beating heart and respiration need to be compensated for to complete a successful scan. This is addressed in P2 with the use of Vector-ECG(VCG) and performing the scan in suspended respiration. The application of VCG involves extra preparation of the subject with mild skin abrasion to minimise ECG artefacts due to skin impedance. It is not included in P1 whether skin preparation was performed but it is said that '*images of diagnostic quality were obtained'*. Regarding respiratory motion, P1 says that the multi-echo (ME) sequence was performed during a single breath-hold, but not for how long it was. Although there is a statement that '*All subjects tolerated the study*,' it is worth considering that all participants were young (mean age 39) with no history of heart disease. A prolonged breath-hold may be untenable for sick patients. These details are relevant to replicating the study and preparing the patients and are examples of the unseen role played by support staff such as radiographers, which contribute to the success of any imaging examination.

Quantitative analysis was performed by the first author of P1 and P2, a cardiac radiologist using software customised for the task. Expertise in this area is needed to ensure valid results, but there are no reports of repeatability being performed to demonstrate that the results are reproducible and correct. This is also the case for the SNR and CNR measurements which use a standard method but again, no repeatability exercise is reported in the paper. Proof of consistency of results would have been a useful addition to this feasibility study though it is noted that the sample group all had exceptionally low levels of cardiac fat. It is possible that values could be variable at different tissue iron concentrations. Upon reflection, it would have been useful to explore the repeatability of the measurements by repeating the analysis under similar conditions and by the same expert observer and with another non-expert observer.
P1 clearly states in the title it is a feasibility study, and the conclusion summarises that the results are positive and cardiac T2* is indeed feasible at this field strength. Limitations and difficulties are included in the discussion, along with a justification of the methods chosen.
Paper 1 was only performed on healthy volunteers with no history of heart disease, iron overload or fatty infiltration of the myocardium. Therefore, the results are only relevant in this healthy group, and further work is required to establish normative values in patient groups. A mixture of sexes was included (nine males and three females) within the small group of young subjects. There is always the possibility of sex differences when establishing normal values. But it is tacit that a larger study is needed to ratify the results of normal values in a broader group of subjects.

Liver MRI

Paper 2 (P2) Liver fat content and T2*: Simultaneous measurement by using breath-hold multiecho MR imaging at 3.0 T – Feasibility was also published in 2008 in *Radiology*.
P2 expanded the work of P1 translating the measurement of T2*, iron and lipid quantification into the liver at the novel field strength of 3T. However, P2 includes measurements on a lipid phantom as well as normal controls and a patient group of obese individuals with hyperlipidaemia or diabetes. Thus, a broader spectrum of subjects is included, which is a strength, however the numbers are still relatively small.
Methods are well documented in P2, including all imaging parameters, which mean that the study can be easily reproduced by other groups. A detailed explanation of the construction of the lipid phantom is beneficial as it includes the exact dose of copper sulphate used to dope

the water. Using a phantom means that measurements can be verified as the exact content is known. The use of high-order shimming is referred to again, which as mentioned before, is beneficial at higher field strengths where there could be increased inhomogeneity.
In contrast to P1, Magnetic Resonance Spectroscopy (MRS) is acquired at the same time as the ME sequences in P2. MRS has had been validated at 1.5T but not at 3T at the time of publishing, there was also no histology correlation available from the patient group as this is not indicated. The lack of histology is not necessarily a serious weakness as pathology sample assessment is semi-quantitative (Boyd et al., 2020). The results included in P2 show good agreement between ME and MRS with excellent statistical significance. The results of ME liver fat analysis have an advantage over dual echo (DE) as the DE assumes that the dominant signal is from water. This results in the underestimation of fat if it is over 50% of the sampled tissue.
Once again, Paper 2 includes that all participants tolerated the imaging well and successfully completed the examination with all the spectra demonstrating satisfactory line widths. It also includes a breakdown of each author's contribution, but again no repeatability is included. As with P1, additional time could have been assigned to perform both inter and intra operator repeatability and thus evidence if the analysis was operator dependant.
The authors acknowledge this is also a feasibility study with no other studies published at the time to quantify fat in the liver using ME and the results are impressive. This indicates that this method is promising and has the advantage of being able to correct for T2* decay without the requirement for additional sequences to be included in the imaging protocol. Thus, shorter scanning times are advantageous for patients and improve the efficient use of valuable scanner time. Value in MRI has different definitions in differing scenarios but where healthcare and research costs are escalating to unsustainable levels, increased patient throughput is favourable (van Beek et al., 2019).

Patient Experience

MRI is often poorly tolerated, with patients feeling anxiety, fear, claustrophobia, and poor endurance of the acoustic noise generated by an MRI scanner. Simple acts of presenting a hygienically clean, tidy, and organised environment have been demonstrated to lessen anxiety in subjects undergoing MRI (Törnqvist et al., 2006)

Another facet which is often not reported is any additional preparation and tutoring of the research participant when acquiring new data, which is dependent on the protocol. Paper 3 (P3) and 5 (P5) are both examples of enhanced patient preparation tailored to the requirements of the study.

P3 published a study measuring the lung volume of obese men which meant that not all willing participants could fit into the MRI. A modified hula hoop was given to the recruiters which was the same size as the scanner bore. This was used to check if the participant could fit in the scanner by placing it over their head and lowered over the whole body to the floor. In keeping with the principles of Good Clinical Practice (*ICH Official Web Site : ICH*, 2023), everyone was keen to protect our study participants from the embarrassment and discomfort of not being able to fit in the scanner so this was proposed as it could be performed discreetly in the lung function department before consent was finalised. Another aspect of enhanced preparation for the participants in P3 was the respiratory tutoring participants went through with the physiologists before the imaging, which primed them to achieve full inspiration and maintain it for the required scan time. P5 involved an extended scan time and suspension of respiration, so additional time was incorporated to explain this to the participants before imaging. If required by the participant, breath-holding was also practised in the scanner until it was deemed that a full understanding of the procedure was accomplished. It was agreed that additional time for practice and preparation was of great benefit to the successful acquisition of quality imaging.

A recent review and meta-analysis by Sukuki et al (2022) demonstrated that the use of mock MRI scanning and preparation programmes improved the success rate of scanning in children. While Nakarada-Nordic et al. (2020) used a mock scanner and virtual reality (VR) to successfully reduce anxiety in adult clinical patients. The use of VR could also be extended to research participants before giving consent and to other healthcare professionals so they could form a better understanding of the procedure and participant experience. The use of modern technology and mock scanners is clearly of use, but the role of the radiographer is still an important factor whether collecting research data or performing clinical scans. Carlsson et al. (2013) described the most crucial factor for reducing stress and anxiety as interactions with staff and how '*interaction with the radiographers helped me through'*.

Data

Thus far, the acquisition of new research data has been the focus, but legacy data can be re-examined and used in further studies. Papers 6 (P6) and 7 (P7) included pre-existing imaging. One advantage of this is that vast amounts of time, effort and resources can be saved, as any study using legacy data can exclude the acquisition process. However, there is always a possibility that the available data may not completely fulfil the requirements of a new study. During the analysis of P6, some of the images were excluded as complete coverage of the liver was not captured, or motion artefacts were present. Obviously, there is no way to repeat or re-acquire the poor data, so it is unusable. Further complications were encountered with the curation of the data set. Duplicate data and erroneous naming were discovered which further reduced the number of suitable sequences to segment. Robust quality control procedures are therefore required at the point of acquisition and during curation of the legacy data to minimise curation debt (Butters et al., 2020)

P7 imaging data were of high quality as it was performed and curated by an experienced radiographer. No data was excluded, but it had not been acquired with the CSA measurement of the psoas in mind. This, therefore, required a new method to identify the most suitable images to be included, and this is discussed later in the 'Analysis' chapter. This work served as testing of protocol for the production of ground-truth for subsequent large-scale AI-based analysis.

Another method to acquire quantitative research data is purchasing; however, there are limited repositories of medical images. Restrictions around consent and privacy also restrict the availability of suitable data. Researchers simply may not have the finances to buy data or have the time to chase funding sources.

Large-scale population studies have emerged in recent years, including the UK biobank, Dallas Heart Study, German National Cohort and 45 and Up Study. These rich resources contain sizable amounts of lifestyle, imaging, and epidemiology data from large groups of the population. Researchers are free to do research rather than collecting data, securing resources etc, as the data is available to all on the condition that it is for the public good. P5 includes the methods for the body composition protocol, which was used in the UK Biobank and Paper 4 (P4) includes the methods for the acquisition of ME imaging in the liver and pancreas which was incorporated in the DIRECT studies and the UK Biobank protocol.

DIRECT and UKBB

Two large scale studies have used the MRI techniques developed in the submitted portfolio. DIRECT, an acronym for DIabetes REsearCh on patient straTification is a pan-European consortium engaged in research on diabetes. Initially funded by the European Union's Innovative Medicines Initiative (IMI), diabetes experts from 20 academic research institutions and five pharmaceutical research organizations launched the DIRECT project in February 2012.

The overarching aims of the DIRECT consortium were to identify potential biomarkers that will help identify patients whose disease may progress more rapidly or who have a different response to diabetes treatments. Thus, developing a personalized or 'stratified' medical approach for the treatment of type 2 diabetes (T2D) using either existing or novel therapies. To date, 50 scientific papers related to DIRECT have been published (*Publications to Date*, 2023)

The UK Biobank (UKBB) is a large-scale biomedical database and research resource that contains in-depth genetic and health information from half a million participants. The imaging project aims to capture MRI data from the brain, heart, and abdomen, together with bone density and ultrasound scans of the carotid arteries of up to 100,000 participants. By capturing a vast number of images of the human body during both good and ill health and combining it with the genetic and lifestyle data already held on half a million participants, the study will improve understanding of why one person develops a life-altering disease when others do not.

P5 was optimised for a Siemens 1.5T scanner as the decision to purchase that manufacturer had already been made for the UKBB imaging centres. In contrast, the whole body and ME sequences included in P4 had to be used on a variety of manufacturer scanners and at field strengths of 1.5T and 3T. Thus, the echo times had to be adjusted, and each sequence, including the body composition sequences, was built from scratch on each scanner. Several visits to each imaging centre were required to ensure all were aligned, staff were trained, and all were producing comparable images. Thus, the initial set up of the DIRECT trial was arduous and burdensome, requiring expertise in MR imaging and people skills. There was a great deal of resistance to positioning the participants prone, for example, and this had to be explained and justified to others' satisfaction. Another cause of debate was the use of the maximum number of echoes attainable in the ME sequence. Most information is collected in

the initial echoes, so there was much disdain for using more, as it was deemed unnecessary. However, more data points will produce more accurate decay curves, and the total breath hold was not unmanageable for participants.

In this chapter, the acquisition of data for medical imaging research has been investigated with reference to the papers submitted for consideration. Reflections were explored in more detail than is usually included in the final papers with the role of the radiographer advocated as an essential part of the acquisition process.

Chapter 2

Optimisation

Introduction

In the previous chapter, it was highlighted that the speed of acquisition is beneficial for improving the subjects' experiences and maximise efficient use of valuable scanner time. Scanner manufacturers provide a library of sequences that is suitable for most imaging scenarios. Most of these have an adequate balance of SNR, CNR, resolution and reasonable acquisition time. As outlined in previous chapters, many parameters can be manipulated to tailor the sequence to provide diagnostic images but always with compromise. In 1988 McVeigh et al. (1988) reported that most sequences provided SNR far in excess of the minimum required, so attention can turn to increasing the specificity of the tissue under investigation. However, McRobbie et al.(2006) have described the signal as finite and that contrast is the most important aspect when considering image quality. Therefore, some level of optimisation must be undertaken by the operator to fine-tune the existing sequences or create new ones specifically for a clearly defined purpose.

Lung Volume

Paper 3(P3) *Reduction of total lung capacity in obese men: Comparison of total intrathoracic and gas volumes* (Watson et al., 2010) was conceived by two specialist physiologists. With no knowledge or understanding of imaging, they approached with a request to measure the physical volume of the thorax of obese men. Accurate measurements of a body cavity were required at full inspiration in a group of asymptomatic obese men to understand the mechanism of lung capacity restriction, which at the time was poorly understood (R. L. Jones & Nzekwu, 2006).

The subjects underwent the whole-body protocol described by Thomas et al. (2005). Initially it was hoped that routine whole-body images could be used for to determine thoracic volumes. However, these were acquired prone while the subject was free breathing so there would be variation in lung volumes throughout the acquisition. In addition, with subjects in the prone position, this was not comparable with the position of the subjects during lung

function measurements performed immediately prior to the MRI. The prone position is often used to minimise respiratory artefacts as it suppresses chest movement (Bright, Anne, 2011) and a slice thickness of 10mm and gap of 10mm are too coarse for the measurements to be reliable as combined with free breathing; this would easily lead to partial volume effects.

A new sequence was created to be run before the whole-body acquisition. The requirements were that the subject was in full respiration and that the fatty and lean tissues could be clearly and easily distinguished. A T1 weighted image would provide the required image contrast and could be performed while the subject held their breath. Fat is hypointense on T1 images, however, so is protein, haemorrhage, melanin, and gadolinium. Nevertheless, because these other tissues were not expected or required detection, T1 weighting was settled on as there would be good contrast between tissues. A gradient echo sequence would no doubt be a faster acquisition, there was concern about the possibility of Moiré fringe field artefacts that are only apparent in this type of pulse sequence (Murphy & Ballinger, 2020).

The imaging plane was changed to coronal to cover the entire thorax using the maximum FOV of 530mm. This produced an image that provided the greatest amount of coverage in the shortest time and included all participants. Scanning in a more conventional axial plane would require more slices and take much longer to acquire to produce the same amount of coverage.

Often, the built-in body coil of the scanner would be adequate for this acquisition, however, to maximize the SNR a surface coil was used. This increase in SNR provided more flexibility when other parameters, such as matrix were altered.

As stated in the methods of P3 each subject made five breath holds that included the survey sequences. The images used for the analysis were performed in two breath holds and a small maker was attached to the chest wall to monitor whether full inspiration was maintained. In addition, visual inspection of the images for motion artifact after the acquisition was performed.

It was not ideal to not be able to include the whole thorax in one acquisition as this meant to possibility that there could be variations in position between two acquisitions. However, a balance between coverage and time within a single breath hold was not achievable while maintaining the minimum resolution acceptable in these circumstances. To curtail this, participant underwent thorough training with the physiologists before the imaging, which prepared them to achieve full inspiration, maintain it and repeat in the required scan time.

This meant that some willing participants were excluded as they could not fulfil these requirements. In addition, performing a study on obese subjects meant that not all participants could fit into the MRI. A modified hula hoop was given to the recruiters, which was the same size as that of the scanner bore. This was used to check if the participant could fit in the scanner by placing it over their head and lowered over the whole body to the floor. In keeping with the principles of GCP (*Good Clinical Practice*, 2020), everyone was keen to protect our study participants from the embarrassment and discomfort of not being able to fit in the scanner, so this was proposed as it could be performed discreetly in the lung function department before consent was finalised.

MRI technology has advanced since P3 was published in 2010. At that time, there was no ability to use parallel imaging to accelerate the scans. If this study be repeated, the use of up-to-date acceleration techniques, which are now widely available, would allow complete coverage of the thorax in one acquisition. Thus, one breath hold could be performed covering the entire thorax. This was also touched upon in chapter 1, where the potential for parallel imaging could be used to improve temporal resolution.

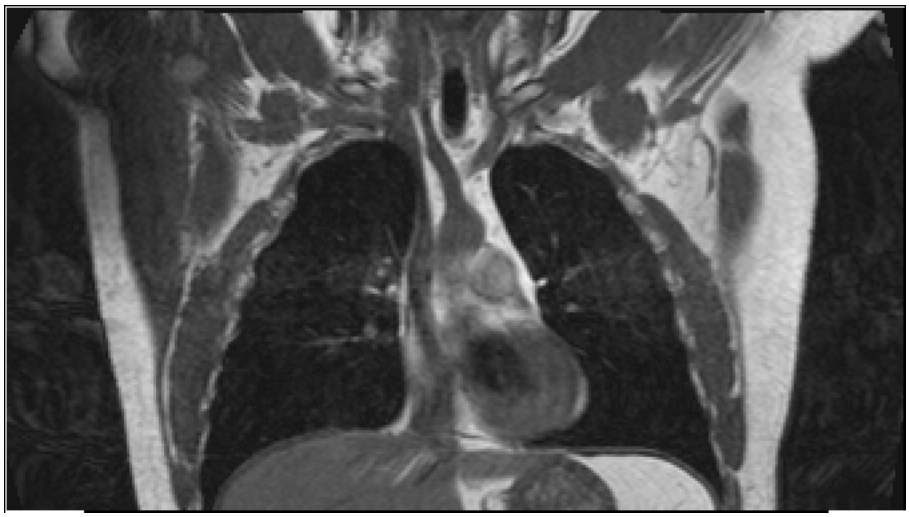

Figure 5: Example of Coronal T1 weighted image of the thorax

Inspection of the image shows that there is motion artefact from the heart contractions in the phase-encoding direction. Although conspicuous, it does not interfere with the ability to accurately segment tissues and supports the exclusion of cardiac gating. It is also noteworthy that there are few details of the lung parenchyma. MRI can produce images of exquisite detail but requires dedicated sequences tailored to specific clinical applications (Biederer et al., 2012). In this instance, resolution of small detail is sacrificed to save time.

Translate Multi-Echo to Pancreas

Paper 4 (P4) *Whole Body Fat: Content and Distribution* is a review carried out after being invited to submit to the journal NMR in Bioscience. This involved extensive searches of all major research sources (PubMed etc.) and collating the relevant papers. Also included were the descriptions of ectopic fat measurement using MRI, which were developed from P1 and P2.

The successful use of ME sequences at 3T field strength published in P1and P2 sparked interest in the technique from the molecular imaging group and to translate it into their imaging protocol. Ectopic fat in the pancreas has been linked to organ dysfunction, including type 2 diabetes (Gaborit et al., 2015). The current procedure for accurate measurement of fat content at the time-MRS-in the pancreas challenging. Indeed, it was described as '*impossible*' by Sijens et al. (2010). MRS sequences are long, and respiratory motion is inevitable when imaging the upper abdomen if not compensated for. Thus, part of the acquisition could be measuring outside the pancreas in the surrounding visceral fat. Using respiratory compensation resulted in an acquisition time that was twenty minutes, unacceptably long in this scenario. This was supported by Lingvay et al. (2009) who performed a dedicated examination of the pancreas using MRS, which took 30 minutes. In addition, Sijens et al (2010) stated in their publication that *'additional MRS examination of pancreas made the total MRI examination times 'too lengthy'*. This is in comparison with MRS in the liver which can be acquired while the participant is left to free breath. Accurate placement of the voxel within the right lobe, away from the hilum, and obvious vessels results in the voxel always measuring liver tissue despite any small respiratory motion.

Multi Echo imaging is field strength specific, and the echo times (TE) of the transferred sequences were not appropriate for the lower field strength of 1.5 Tesla (Elster, 2021). Therefore, the initial action was to update the echo times. Afterwards, a period of work-up ensued, testing the sequences on a phantom and healthy volunteer, and learning the post-processing techniques to produce quantitative results and colour maps.

As validation of ME in the pancreas is still required, MRS subsequently was denoted as the gold standard (H. H. Hu et al., 2010) and continued to be acquired despite the aforementioned limitations. To improve the likelihood of successful MRS of the pancreas being acquired the voxel shape was altered. In the liver where voxel placement is more straightforward, a cube is conventionally used. However, to better fit within the pancreas, the voxel shape was

elongated to include the same volume, but in a cuboid shape, which can be viewed in P4. The updated shape of the voxel along with instructions to continue shallow breathing provided evidence indicating good correlation between the MRS and ME of the pancreas. The first results were presented as a poster at the 11th International Congress on Obesity in Stockholm, Sweden (J. Fitzpatrick, Thomas, Durighel, O'regan, et al., 2010) Supporting Evidence ii. The poster conferred that ectopic pancreas fat increases with body mass index (BMI) and is closely related to internal adipose depots than subcutaneous stores.
As the procedure resulted in valid results and was easily integrated into the existing imaging protocol, the ME imaging of the pancreas and liver became part of the protocol in two large-scale imaging studies. The DIRECT project (*DIRECT - DIabetes REsearch on Patient StraTification*, 2022), a pan-European study identify biomarkers in type 2 diabetes and the UK Biobank (*About UK Biobank | UK Biobank*, 2022). The justification was that ME sequence could be performed on all MRI scanners regardless of manufacturer, allowing for reliable measures of ectopic fat in the liver and pancreas to be collected in these population studies. The work to optimise ME single slice pancreas, accurate acquisition, coherent analysis, and presentation of results made it an appealing technique which could be adopted in large-scale studies.

Pancreas Volume

However, large-scale studies would involve many imaging centres and different scanner operators of different capabilities. Thus, fast 3D T1 with fat saturation sequence, which would cover the pancreas, was included (Morana et al., 2017). The rationale was to allow easier positioning of the pancreas ME. However, The Principal Investigator talked about pancreatic volume with the group head since there is evidence that it is reduced in T2D. Neither felt it would be viable so was not initially included in the protocol. However, during the work-up, an interpolated sequence which was extremely fast acted as a localiser for the ME sequence. This would also cover the entire organ and using a fat saturation pulse resulted in the pancreas being easy to identify for scanner operators and allowed accurate placement of the single slice ME sequence. In addition, complete coverage of the pancreas was achieved, and therefore, the possibility of whole pancreas segmentation was accomplished. This type of sequence had been used in previous research to measure pancreatic volume in T1D and shown to be a reliable method (Williams et al., 2007).

Fast Whole-Body Protocol Validation

Validation of a fast Method for quantification of intra-abdominal and subcutaneous adipose tissue for large scale human studies (Borga et al., 2015) was published in 2015 following collaboration with the private company AMRA Medical (2023). Time is a crucial factor in MRI and the opportunity to validate a new faster sequence which could be automatically segmented was explored in Paper 5 (P5). The superior soft tissue contrast provided by MRI is a reliable way to segment lean and non-lean tissues in the body, both human and animal. In addition, the lack of ionising radiation means that MRI is more suited to research studies. However, the method described previously (Thomas et al., 2005) was too time consuming and required manual segmentation performed by trained individuals. To explore the possibility of an alternative, faster method for obtaining the same measurements meant doing a direct comparison between the two methods. Therefore, a single operator was to acquire the imaging to ensure unvarying acquisition to provide consistent, comparable, and quantifiable data.

As acknowledged in P5, the two imaging techniques were quite different, including different patient positions, supine, as opposed to the usual prone position. Thus, comparing the two techniques was not comparing like with like. This is mentioned in the discussion section along with the need for accurate positioning and identification of the anatomy.

Another difference between the two protocols was that the AMRA Profiler did not cover the entire body. In contrast to the 'whole body' sequence which covered from fingertips to toes the Profiler covered from 'neck to knees. This was deemed acceptable as the extremities did not contribute as much information regarding health in body composition in a large population study. However, the differing amounts of coverage of the two methods required accurate anatomical points to identify where the body cavities began and ended. An agreement was easily reached for the thorax, as the diaphragm is a clear border with the abdomen. Visceral fat in the abdomen is linked to health outcomes (Fox et al., 2007) however, identifying an anatomical landmark of where the abdomen transitions into the pelvis and the pelvis ends, was more challenging. Various points in the bony pelvis were discussed including the iliac crests and pubic symphysis but neither agreed upon. The possibility of excluding relevant tissues and how well the pubic symphysis could be defined on imaging made these unsuitable landmarks. Eventually, after examining some of the

images, it was agreed that the acetabulum of each hip joint would be the cut-off point thus including all the pelvis contents in the analysis.

In this section, optimisation of MRI for human research has been considered. Different scenarios have been presented and the importance of tailoring the sequence to the requirements of the study examined. The work undertaken in the submitted papers is that demonstrates there is no ‘one size fits all’ and optimisation is a requirement when undertaking research using MRI.

Chapter 3

Analysis

Introduction

An analysis is a detailed examination of the elements or structure of something. In quantitative research, the collected data can undergo some type of analysis to draw out information. However, according to Albers (2017), the analysis begins with the formulation of the research question where the type of data to be collected is considered and how it will be analysed. Thus, an understanding of the data, the relationships within it, and connecting them to understand and clarify the research question is the basis of analysis.
Previously P1 and 2 referred to a single observer; a radiologist performed all the analysis and having a single operator strengthened the reliability of data collection. It was also mentioned that there are weaknesses in having a single person do things in isolation and the absence of repeatability was touched upon. However, as P1 and 2 were both feasibility studies, this approach can expedite results, publications and boost the dissemination of knowledge. Leading the way for others to reproduce a study and share their findings.

In-House Software

The use of in-house software was mentioned in P 1, 2, and 4 to perform the analysis which means that a specific programme was created to carry out a predesignated task. Expertise in this area is required which may be available in a large research institution but may not be accessible to a smaller group or an independent researcher. The fact that in-house software for a specific task is used also means that any others, wishing to reproduce the research will not necessarily have the software available to them. There is also a risk that in-house software has not been tested thoroughly, could contain bugs, and may not be suitable for the task.
The Open Science Movement encourages the sharing of research output. In 2011, Woelfle et al. (2011) proposed that an ‘open-source’ approach can accelerate new scientific discoveries. There are many ways to share research with arguments for and against, but there now exist repositories where computer code can be shared; thus replication, re-analysis and validation of work can be performed with other researchers able to reference the original code.

Segmentation of an organ has already been introduced in P3, where lung volume was measured and shown to be reduced in obese men. Paper 6 (P6) presents the results of liver volume measurements in patients undergoing therapy for Hepatitis C infection. Commercially available equipment was used to draw contours around the borders of the whole liver on T1 weighted MR images. An image processing workstation (Philips View Forum), purchased at the same time as the scanner was freely accessible and had the required software package to perform volumetric measurements. This meant that no further financial outlay was required to purchase equipment and no specialised knowledge was required to create task-specific software. The View Forum is user-friendly and uses the international standard DICOM format; as such, it is used by many researchers for post-processing and analysis. However, the View Forum is tethered to Philips imaging equipment and therefore its use is limited to one physical location.

Open-Source Software

Open-source software is another option used in Paper 7 (P7) to measure the psoas muscle cross-sectional area. Software for many tasks can be downloaded for free which has been developed by experts and shown to be robust by its use in peer-reviewed journals. Image J (National Institutes of Health, 2023) was chosen as recommended by a trusted colleague and could be installed on a laptop making it portable. The advantage was that, unlike the View Forum, an analysis could be performed at any location where a laptop computer could be used. Thus, measurements were performed in a variety of settings which accelerated the turnaround, producing results in a favourable timeframe.

Papers 7,8 and 9 (P7, P8 and P9) used open-source software, The Medical Imaging Interaction Toolkit (MITK) (*The Medical Imaging Interaction Toolkit (MITK) - Mitk.Org*, 2022), to segment the pancreas and psoas muscle. MITK is a powerful tool for image processing with a high degree of interaction and specialised medical imaging algorithms such as segmentation. Of particular use is MITK builds a 3D rendition of the segmented structure. This image could be inspected in all imaging planes and fine-tuning was performed simultaneously. Collaboration with imaging scientists was uncomplicated and effortless, as they already used the application, and with their experience and in-depth understanding of the software its use was quickly mastered. The seamless way MITK constructed 3D images meant that it was possible to measure the volume of the psoas muscle and served as an initial

experience for all subsequent production of ground-truth for all the research programs undertake by the team at the University of Westminster. Examples of which are included in appendix D.

3D rendering was very useful as being able to appreciate the shape of an organ was a bonus. P4 includes a description of the pancreas where ectopic fat has infiltrated, and the organ outline appears irregular when compared to a pancreas without fatty infiltration. Observing this in 3D had a greater impact and encouraged more exploration into larger-scale organ segmentation and morphology (Thanaj et al., 2022, 2023).

Viewing Conditions

Having the flexibility to perform analysis on a laptop was a great advantage, but this meant that the viewing conditions were variable. Background lighting was changeable as the task was performed in a variety of situations, including while travelling, bright natural light, and at night. Perceived contrast depends on retinal adaptation to local conditions (Arenson et al., 2003) and no account was taken to measure or standardise this during the analysis of any of the publications. It would be interesting to investigate whether the results were affected by the local viewing environment. In the same vein, no attempt was made to harmonise the display of the laptop. Different computer laptops were used for P 6,7,8 and 9 and physical parameters such as screen luminance, resolution, and refresh rate were not recorded. Again, another line of investigation would be to explore different displays and any impact this has on the observer performance and results.

Reliability

Previously it was documented that the exclusion of repeatability was a possible weakness of P1 and 2. In contrast, repeatability was included in P6 and 7 and poster B. This is an important exercise as it measures the reliability of any measurement and there are various ways to estimate it. P6 and Poster B examined inter-rater/observer reliability to test whether the two different observers are consistent. P6 used an experienced radiographer, and a radiologist and the results were excellent with good agreement. In contrast, the agreement between observers in Poster B was poor where an expert and non-expert were compared. This finding supports the need for experts to perform radiological organ segmentation.

Another test of reliability, the test-retest was also performed during the analysis of P6 where both observers repeated five slices, five times. Test-retest was also included in P7 with favourable results and supports the possibility that radiographers can play a larger role in organ segmentation or other medical imaging-related tasks. Once again, much of this work was key to the subsequent protocol developed by the team at the University of Westminster to create ground-truth data set for the different projects.

Measuring Psoas

The introduction to this section discusses that analysis begins with the formulation of the research question which was necessary when developing the methods for P7 and supporting evidence iv. The project was conceived following observation of whole-body images and collection of questionnaires from research participants. It appeared that reported levels of activity did not reflect with muscle mass on MRI and there is evidence in the literature that people overestimate their physical activity (Westerterp, 2009). Furthermore, direct measurements of activity are known to be more accurate but are expensive and require time, specialised training, and equipment (Martins et al., 2017) thus they are not practical or easily accessible. At the time there was some suggestion that the total muscle mass could be estimated from a single abdominal image (Shen et al., 2004) but still required trained imaging personnel to perform the segmentation. As the psoas major muscle (PM) is easy to recognise on abdominal imaging and is engaged during multiple movements in an ambulant person the notion that it could be used as a marker of activity was proposed and developed during discussions with colleagues.

The method for measuring the psoas major was deliberated and the possibility of measuring a simple diameter was initially considered. The PM can have an irregular shape so there is not always an obvious diameter to measure. The largest measurement was considered but this would be anterior-posterior on some but more oblique on others. Therefore, a cross-sectional area was settled upon which was also used by Jones et al (2015), Lee (2011) and Stewart (2010). The literature indicates that the psoas is largest at the level of L4/5 (Jorgensen et al., 2003; Kim et al., 2013; Stewart et al., 2010) therefore this vertebral level was selected as most suited to the measurement of CSA. Although one study did measure all lumbar vertebral levels (Ranson et al., 2006).

The PM was not measured in isolation as it could be theorised that any muscle in the human body reflects physical activity. The rectus abdominus (RA) CSA was also measured at the same level and was not correlated with V02 max or fat mass. Although there is evidence that PM CSA is a useful marker of health this has been called a *'flawed premise'* by Baracos (2017). In this article, it is argued that no single muscle can be used to represent anything other than its specific function and that the psoas should not be chosen because it is '*simple and easy'* to locate. In addition, localised psoas atrophy is associated with spinal diseases/pathology which are common in older adults who are typically the subjects of this area of research. Thus, this argument appears to strengthen the need for whole-body muscle measurements, which would require automation to achieve.

One confounding factor in measuring PM CSA is the possible presence or absence of a psoas minor muscle which is significantly different in ethnic groups and can be unilateral (Hanson et al., 1999). The presence of a psoas minor muscle could potentially artificially increase CSA and impact the results. Interestingly, no evidence of an additional structure was noted during any of the analysis. This may be because the resolution of the images was insufficient to allow differentiation of psoas minor. Another reason could be that the psoas minor is not present in 50-67% of the population (Rosse et al., 1997; Sinnatamby, 2011), and the sample may not be representative and include any.

An interesting study to investigate the PM further would be to use MRS to measure fatty infiltration. The quality of the muscle could then be examined along with the size.

Several mentions have been made of a single operator, trained, and experienced in medical imaging performing manual segmentation. This is time-consuming are there simply may not be adequate resources available for this task so it is reasonable to explore other options.

During the latter part of the analysis of the ME pancreas presented in P4 and supporting evidence 11 and 111 a PhD student joined the project. With no experience in anatomy or imaging, they were required to learn the entire process of recognising the pancreas and performing the analysis. 176 subjects were analysed by two users, and which was presented as a poster at the ISMRM Scientific Meeting in Long Beach, California 2012 alongside the MRS data (supporting evidence iii). Here we demonstrated that ME compared well with MRS, but ME was more robust. A point of interest was how many pancreases each observer could identify. The experienced user could analyse 93.2% of the data, while observer 2, with no background in imaging, could only identify 71.7%. The 26% difference in pancreases

identified between the observers is unambiguous evidence that a trained observer with a background in imaging should be undertaking this type of analysis of medical images. As this was an international meeting of water/fat MRI techniques, most of the experts in this field were present including Dixon, Reeder, Sirlin, Hu, Szczepaniak and Hamilton amongst others. The poster (supporting evidence iii) was well-received and opened a conversation about the use and effectiveness of acquiring a single slice. This discussion led to the suggestion that several slices could be used to cover the whole organ. Although a valid suggestion, the time available negated additional time being allocated to cover the whole organ. This had already been considered, and it was hypothesized that at least eight slices would be required for full coverage owing to the variable size and position of the pancreas. This would result in another two minutes of scan time, and with added rest time between BH would be much longer. Measuring ectopic fat in the pancreas was already added to the body composition protocol and thus needed to be as short as possible while still producing useful results.

In this section, the analysis of research data has been discussed. Rather than being one of the final steps, analyses need to be considered at every stage of the experiment to effectively demonstrate any relationships within the acquired data.

Chapter 4

Quality Control

Introduction

The term quality assurance (QA) and quality control (QC) are clearly defined in reference to acceptance testing and monitoring of scanner performance in authoritative documents from the Institute of Physics and Engineering in Medicine (IPEM), The American Association of Physicists in Medicine (AAPM) and Medicines & Healthcare products Regulatory Agency (MHRA). In the UK the MHRA guidelines for the safe use of MRI equipment recommends "*monitoring of both signal and geometric parameters. MR units should not rely solely on the manufacturer's daily quality assurance (QA) programme*" (MHRA, 2021). A comprehensive QA programme should be regularly fulfilled in accordance with the local MR safety officer, so that the scanner functions within accepted tolerance levels and to anticipate any variations before becoming apparent in the imaging quality. Distinct from these terms, QA and QC are data quality (DQ) or information quality (IQ), which refers to whether the data/information is fit for purpose (Fadahunsi et al., 2021) although this will differ depending on the end user. For example, a patient may judge the quality of a service as how compassionate the caregiver is while a manager may use a different metric such as throughput.

The previous section highlighted that some of the imaging was not inspected for quality and curated well as such some data was not used in P6. Researchers have an ethical obligation to acquire quality data that can be trusted and archived meticulously so that it can be easily accessible (*WMA Declaration of Taipei on Ethical Considerations Regarding Health Databases and Biobanks – WMA – The World Medical Association*, 2016).

Ongoing quality checks are required to trust the data. This was the case with P5 where the newer technique was compared side by side to the established technique. The quality of the data was assured by a suitably qualified personnel-a dedicated research radiographer-preparing, acquiring, visually inspecting, curating the data, and providing feedback to the manufacturers. Consistency of the data was also assured by this method of one person doing multiple tasks, so variations were minimised. However, relying on dedicated staff to perform

tasks consistently will only work in small-scale studies where numbers are limited, or the time scale is short. As mentioned previously in the section 'Acquisition' there are weaknesses though as mistakes can be easily overlooked and bias introduced without the benefit of another observer. In the real world it is simply not possible to have a single operator performing all the imaging-related tasks. Staff take leave, may be rostered to another area, and can change jobs so it is inconceivable to have that level of continuity when undertaking larger studies over longer periods of time. Variations in the personnel are inevitable and this must be considered when undertaking larger studies.

Pancreas Segmentation

Paper 8 (P8) depended on the expert input of a single research radiographer to provide the ground truth training data and evaluation in the development and testing of an automated organ segmentation task. UK trained Radiographers are knowledgeable about anatomy and can identify the pancreas which will be only 1% of an abdominal MRI scan (Asaturyan et al., 2019a). Providing accurate ground truth for training data was a labour-intensive and time-consuming task which is acknowledged as a reason for the lack of quality data for machine learning applications. Being able to dedicate time and effort exclusively to the task of pancreas segmentation was invaluable but also somewhat unusual. It has been established that there are not enough resources and skilled people to perform this task and it is a limitation of the expansion of machine learning (Willemink et al., 2020). It is assumed that radiologists are required for accurate organ segmentation but here is an example where a radiographer was classified as the expert and was able to fulfil the required task with speed and accuracy. P8 mentions the boundary contrast of the pancreas is similar to the surrounding tissue and thus confidently identifying the border is challenging; a radiographer experienced in abdominal MRI is suitable to perform this task.

In addition to segmenting the images to produce the ground truth, the outputs were evaluated and marked on an accuracy scale. That is, the same radiographer viewed the outputs and graded the accuracy of the segmentation results to provide feedback on how the software performed. Once again, a task usually performed by a radiologist was comfortably performed by an experienced radiographer. The development of machine learning can be accelerated with the input of the radiographer workforce taking a more active role.

Machine Learning

Machine learning is a sub-field of artificial intelligence and can be defined as "*the field of study that gives computers the ability to learn without explicitly being programmed*."(Samuel, 2000). The process begins with training data which the computer uses to train itself to find patterns. This is tested on another set of training data to which the computer has not been exposed. The results are articulated as the Sorensen-Dice Coefficient show how accurate the computer is and whether the resulting algorithm can be used with different data.

The provision of training data is a bottleneck in the application to medical imaging and requires an 'expert' to appraise and annotate images in preparation for training the computer. This expert is usually a radiologist but there seems to be no reason why radiographers cannot perform this role. Radiographers are experts in imaging and anatomy and are now performing tasks previously done only by a Radiologist. Examples are reporting, administering contrast medium, and performing some interventional studies autonomously. Therefore, it seems logical that radiographers could play a more active role in producing training data sets. A further advantage would be to contribute to job satisfaction by being recognised as capable of doing this task and adding further prestige to the role of the radiographer (Chevalier et al. 2022).

P8 successfully presents a novel approach to generate accurate pancreas segmentation and can be translated to other organs. Mentioned in the conclusion is the fact that the outputs were generated from two different scanners with differing protocols. The variation in MRI scanners is significant and protocols can be variable across manufacturers. Differences in field strength, gradient strength, shimming, and coils can produce subtle but important variations in images. P8 drew attention to the differences in parameters of the training data from two different scanners in the results section and how the approach coped well despite this. Using the Dice Similarity Coefficient, a score above 80% demonstrated the robust performance of the proposed approach.

Quality in Large Scale Studies

A visual review by a suitably qualified person has so far been emphasised to assess DQ and this is an important step in the production of images. However, when scaling up research studies to larger cohorts there may be differences in the competence across geographical

regions along with different scanners. P4 and supporting evidence ii and iii document the development of the ME sequence and how it can be used to measure fat in internal organs and this technique became part of the protocol for the DIRECT project, where several imaging centres across Europe were involved. It was not possible for a single person to undertake all the imaging, but a single person could oversee and train the imaging personnel. In this way, standardisation could be accomplished which contributed to DQ by communicating the imaging requirements and having a single point of contact to advise and troubleshoot for all the centres. Standardisation activity at the beginning of a multi-centre imaging study will reduce variance which could impact the analysis and there is good evidence that robust data can be acquired in neurological studies in these circumstances (Glover et al., 2012).

In 2011, the paper '*Evaluating the role of the diagnostic research radiographer*' was published in *Radiography* where Reid and Edwards (2011) advocate the role of the research radiographer with one of the advantages being '*consistency of application'*. In large-scale studies, it is not always possible to be at all imaging centres, but it is possible to delegate the role to specified people. Although done informally, staff who were keen to be involved were identified during site visits and networks were formed thus strengthening team working and communication. This evolved during the protocol dissemination phase where protocols were shared between the same manufacturer scanners and troubleshooting was completed. In addition, a directory of staff names and contact details was distributed to encourage communication and introduce a little healthy competition too.

Dissemination of Imaging Protocol

To meet the expectations of all staff a visual presentation was given along with a written protocol. Both visual and written protocols of the imaging requirements were distributed to all the centres, included in appendix B in hard and electronic formats. Furthermore, all centres were required to provide a healthy volunteer to scan during site visits. This allowed a demonstration of the required protocol and a way to assess site understanding and compliance. Finally, when the first patient was recruited at each centre their imaging was overseen to guarantee understanding, compliance and quality before being given the go ahead to unsupervised imaging. All these initiatives were designed to deliver effective, efficient,

and consistent imaging of the study participants. It would be advantageous to document 'start-up' activities to provide formal records and templates for further studies to follow.
It is believed that all MRI machines are the same and produce identical outputs. Although working on the same principle the advice to perform QA and QC demonstrates that regular care is required to maintain the minimum standards. Performed on test objects referred to as phantoms, the evaluations prescribed by authoritative bodies mentioned earlier measure the technical specifications. All centres in the DIRECT project undertook the recommended QC programme and these were inspected at the time of site visits. With hindsight it would have been prudent to formalise this and make a record that observation had occurred and even centralised copies of the QC outcomes. Although the QA programmes were followed at all centres differences were observed which required variations to tailor the protocols at some centres. The largest field of view (FOV) acquired by each scanner was most apparent and varied from 380mm to 530mm. A visual example is included for reference.

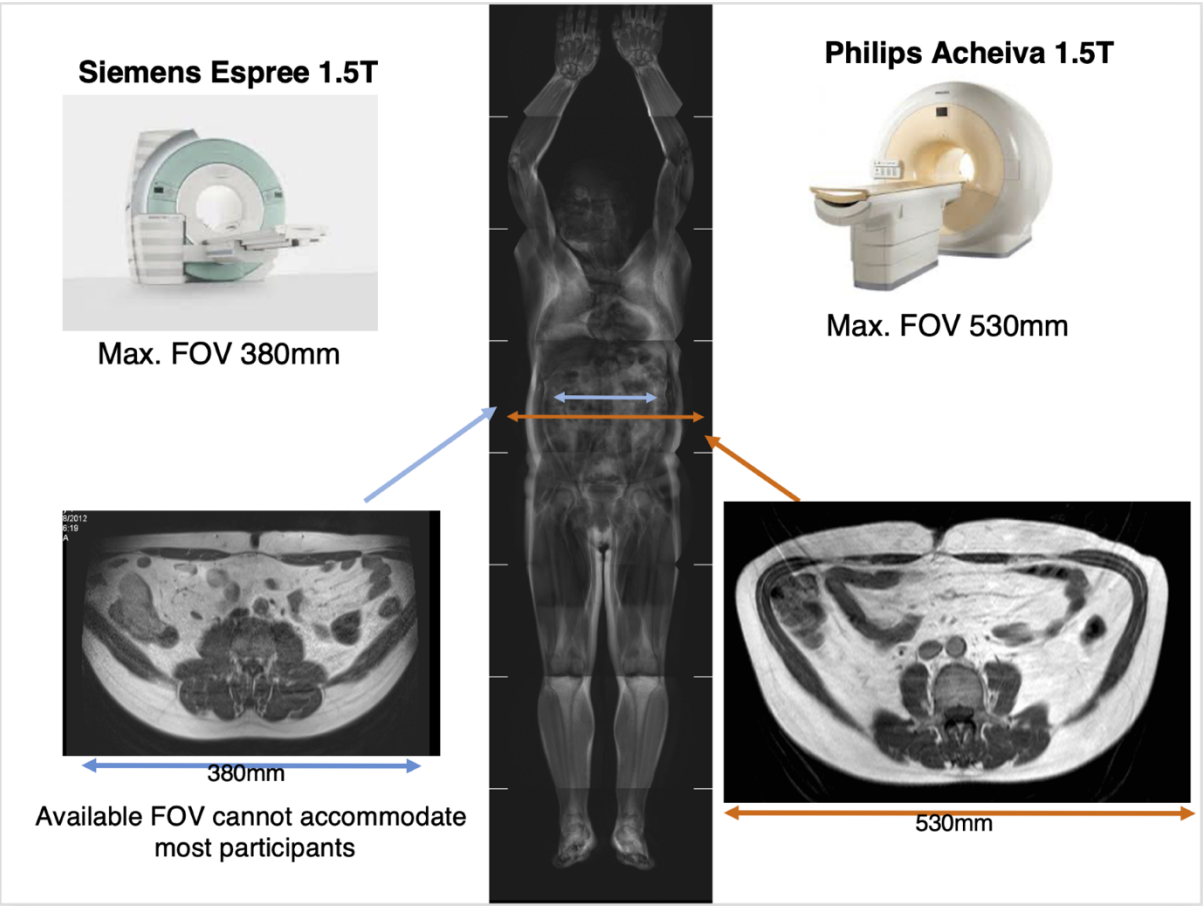

Figure 6 FOV in different MRI equipment

This was not anticipated by the sponsors of the study, who recruited the imaging sites on the basis that they had an MRI scanner. The input from a medical imaging professional at this

stage would have anticipated the extra work required to standardise the imaging with a wide variety of scanner capabilities.

Fat Phantom

The inclusion of the ME sequence to the protocol was a concern as not all scanners had the capability to perform MRS; thus, no quantitative comparisons could be undertaken to ensure consistent measures of fat were being acquired. Fat phantoms do exist but are very expensive and no budget was available, so this was ruled out. Discussions about the possibility of a food source, such as mayonnaise being used were also ruled out as even an unopened jar would change over time and eventually spoil thus not stable enough. Additionally, travelling across international borders with foodstuffs may have encountered difficulties. The lipid emulsion known by its commercial name Intralipid was next investigated as it is stable, could remain sealed, and is supplied in predefined fat concentrations. This was tested on two scanners, but the water content of Intralipid was too high to use the ME analysis software for accurate measurements. Since the T1 of water is four seconds and the T2 is 2 seconds (Elster, 2023) insufficient decay could occur during the acquisition to measure the oscillation in the signal due to fat content.

While attending the ISMRM fat/water separation meeting (supporting evidence iii) one of the delegates presented a 'home-made' fat phantom which could be easily constructed from common and cheap ingredients and would be stable for at least a year. Using Catherine Hines recipe (Hines et al., 2009) a chemist colleague helped to construct the phantom at 10% lipid with no iron content. The phantom travelled to all imaging centres during the start-up phase with ME outputs being collected along with MRS where possible. The results were satisfactory and verified that fat measurements were standardised and consistent. Interestingly, the fat phantom lasted more than a year and was used regularly in other studies and experiments. This was surprising, as it was sealed in the normal atmosphere and so was predicted to decay more rapidly. A better strategy would have been to seal it in an atmosphere of nitrogen to avoid oxygen related decay, but this option was not available at the time. Fat phantom measurements were performed on all scanners during the initial start-up phase of the DIRECT trial, and it would have been useful to repeat the measurements at regular intervals. The scanner performance regarding fat measurements using ME could then have been monitored over time and any changes noted before impacting the study. Further

investigation into repeatability would have been useful to perform at this time too. However, a commercial phantom guaranteeing consistent performance would have been required and additional travel time and expenses necessary. Alternatively, a phantom could be given to each imaging centre which would stay and become part of their regular quality control programme with the responsible person at each centre recording and responding to any diversity. Again though, additional expense would be incurred.

In this section it has been demonstrated that quality is a broad term and must be seen as specific to any task. In a similar fashion to other sections the procedures must begin early in the process of setting up any research study to be effective.

Chapter 5

Translate

Introduction

Providing determents of health has been the motivation behind the increase in large cohort-based studies. Increasing sample size increases statistical power (Desmond & Glover, 2002; Turner, 2014) so that the underlying links between clinical conditions and lifestyle can be better understood. Some large cohort studies include imaging data, and this work has so far included the cultivation of quantitative methods of organ segmentation to measure organ volume and ME imaging to measure ectopic fat in the pancreas and liver. These techniques have been included in two large-scale studies so far, the DIRECT consortium and the UKBB, both of which have resulted in new disease insights and will continue to do so as the acquired data continues to be investigated. A letter acknowledging the contribution to UKBB is included in Appendix C.

Large Scale Studies-Patient Perspective

From an imaging perspective, the biggest difference, and most challenging was standardising the imaging protocols as DIRECT used MRI scanners from different manufacturers. Fine-tuning of the protocols was required to compensate for different scanner capabilities. Something that was avoided in the UKBB, as all the imaging centres used the same scanner manufacturer who installed identical models. The imaging protocols incorporated established techniques were demonstrated to be robust and reliable. The body composition technique outlined in P4 was used in DIRECT, whereas the automated technique from P5 was selected in the UKBB. The feedback from participants indicated that the P5 technique was the most popular, as it required them to lie supine. The prone position included in P4 was uncomfortable for many, and the staff and patients found it more burdensome to accurately position.

Nevertheless, being able to continue breathing quietly was welcomed by many. In contrast, P5 technique required consecutive breath-holds, which some found tiresome and challenging

to manage. Taking a little extra time during preparation and practising the breathing technique made it more manageable, but time was limited in the UKBB.

Upscaling Body Composition Protocol

P5 demonstrated that accurate and reproducible body composition imaging was possible and well tolerated by study participants at smaller scale imaging. However, as the number of datasets increases, it may take time to maintain accurate acquisition and analysis. When the technique described in P5 was adopted int the UKBB, it was slightly modified. No localiser was performed; landmarking was positioned over the clavicles, and technical quality was assessed afterwards. This acquisition method allowed the maximum throughput, and the UKBB achieved the goal of imaging 126 participants per week at week 16. Although this method maximised throughput, it ran the risk of variations in positioning and substandard quality imaging being included. In 2016 West et al. (2016) published their investigation '*Feasibility of MR-Based Body Composition Analysis in Large Scale Population Studies'*, citing P5. The first 3000 participants in the UKBB who underwent the protocol from P5 were included in the study. One aim of the study was to investigate the feasibility of the protocol being translated into large-scale studies. 99% of scans were analysable by the AMRA profiler used in P5 with each dataset assessed on a per-subject basis. The study concluded that participants tolerated the MR body protocol very well, robust analysis was achieved and that '*the method can be readily applied in population-wide studies*.'

QA in Large Scale Studies

Translating to large-scale imaging includes sustaining the quality of imaging which would usually involve visual inspection directly after acquisition by the operator. In the UKBB, strict time constraints and a high-throughput acquisition protocol limit the visual inspection of images. However, there is still a need to identify suboptimal images and ensure the integrity of results. Automated methods have been proposed for the task of QC MR images. Tarroni et al. (2020) have published their fully automated QC pipeline for UKBB cardiac images and Alfaro-Almagro et al. (2018) have published their image processing and QC for the first 10,00 brain images. Indeed, as part of West et al. (2016) publication a QC criterion was defined for the acceptance/rejection of datasets, but visual inspection of the images was still required. In 2020 P9 co-authors Basty et al. (2020b) published '*Image processing and*

Quality Control for Abdominal Magnetic Resonance Imaging in the UK Biobank' where a fully automated analysis and pipeline for the UKBB abdominal protocol is presented. The pipeline includes the detection of water/fat swaps and the simultaneous estimation of PDFF and R2* from the single slice ME sequences. This is unlike West et al. (2016) who only presented the outcome of the analysis of the body composition portion of the protocol. Thus far, the pipeline has been used on the first 38,971 participants of the UKBB who have undergone the abdominal imaging protocol, with plans to include all 100,000 when that number is achieved. Outcomes are anticipated to boost investigations into body composition, organ volume and organ morphology and the associated diseases using the UKBB body protocol and some rudimentary images are included in Appendix D.

Psoas Muscle in Large Scale Studies

Previously P7 demonstrated a link between PM cross-section and cardiovascular fitness, and there is evidence that this muscle is indicative of sarcopenia and general frailty (Balsam, 2018). Continuing the work of P7 is Paper 9 (P9). Published in Scientific Reports 2020 presented the outcome of an investigation into the large-scale analysis of psoas volume in 5000 UKBB participants. Earlier it was discussed that Baracos (2017) questioned whether the PM is a sentinel muscle and whether the cross-sectional area of any one muscle can be used to predict anything with certainty. In 2019 Waduud et al (2019) published an article that concluded that the total volume of the psoas is represented by single-slice cross-sectional volumes at the level of L3 thus suggesting that future studies could reliably measure the CSA at L3. However, this was criticised by Flaris and Konstantinidis (2021). They pointed out that they used a non-validated linear model and questioned the validity of the claims in the Waduud paper. Subsequently, Otaki et al.(2020) published an article in which the total psoas muscle volume was measured in prostate cancer patients. 3D images of the PM were automatically generated using Synapse Vincent by Fujifilm® software. Although the authors describe the whole PM volume, it appears that the included anatomy ends at the pelvis, and the distal part of the PM is excluded. This was also the case with Davico et al. (2022), where the proximal portion of the PM was excluded due to it being '*difficult to identify'*, and the images, collected retrospectively, were not all found to cover the entire muscle. In contrast, P9 included the entire muscle, due to the imaging protocol outlined in P5, which was used for the body composition portion of the UKBB imaging protocol. 3D images were acquired from

‘neck to knees’, with a slice gap of 0mm; full uninterrupted coverage of the PM was available for analysis.

Although manual segmentation remains the gold standard for muscle segmentation, it is not feasible to use this method for large-scale studies because the human resources required do not exist. Therefore, for P9 an automated method was devised using artificial intelligence. Nonetheless, manual segmentation was still required for the training data, and 90 subjects were segmented using the open-source software MITK. It is mentioned that these were performed by an expert radiographer in the methods section of P9 and the annotation of both muscles took between five to seven hours. Hence evidence that it is not realistic to undertake this on a large scale where many thousands of imaging datasets are collected. The automated method outlined in P9 indicates that it is possible to measure whole PM volume accurately and dispenses with the lack of consistency in how the muscle is measured in other publications. However, van Erck et al. (2022) has recently published their findings when using an automated method to measure PM at L3 using computerised tomography (CT). Citing and acknowledging that P9 has correctly measured the PM volume, this study questions if whole volume measurements are predictive of clinical outcomes.

The success of automated methods relies on the fact that the training data/ground truth is correct and accurate. Recently, Davico et al. (2022) published their work testing for intraoperative repeatability of manual segmentation of the hip muscles, including the PM citing P9. Their findings were encouraging, measurements being highly repeatable though acknowledging that great care should be taken as errors could be magnified during interpolation.

Following the successful implementation of the UKBB abdominal protocol, the co-authors of P9 went on to publish ‘*Genetic architecture of 11 organ traits derived from abdominal MRI using deep learning*’ (Liu et al., 2021). Citing P9 the paper presents the quantification of abdominal organ volume, fat and iron content based on the analysis of 38.000 abdominal scans from the UKBB.

The ground-truth training data for organ volume was performed by a team of radiographers using MITK, who underwent training based on a standard operating procedure created by the author. Bearing in mind the significant bottleneck, already mentioned in producing high-quality training data for machine learning, radiographers who understand anatomy and image contrast can support this role. With its increased use, machine learning has the potential to

become a part of routine clinical care, and radiographers are ideal for supporting this progression in imaging technology.

With the publication of P9 and *'Genetic architecture of 11 organ traits derived from abdominal MRI using deep learning'* which cites P9 there is evidence that MRI markers of health, including organ volume, ectopic fat, and iron, have been cultivated and successfully translated into large-scale studies.

Future Work

So far, this work has included appropriately trained and qualified personnel, such as radiographers, medics, and physicists. Several mentions are included that there needs to be more high-quality training data and suitable people to produce it. However, this will not change in the current climate, so alternative resources require further investigation.

Crowdsourcing: 'th*e practice of obtaining information or input into a task or project by enlisting the services of a large number of people, either paid or unpaid, typically via the internet' (OED Online, 2022)* is a resource that could be an alternative to expert annotation. In 2015, Gurari et al.(2015) presented their findings evaluating the performance of experts, crowdsourced non-experts and algorithms. Both experts and crowdsourced non-experts performed consistently well, outperforming all algorithms, and so may become a valuable resource in medical imaging segmentation.

Work in crowdsourcing organ segmentation has already begun, with twenty non-experts recruited to segment the uterus using T1 weighted images from the UKBB. All participants underwent training via YouTube videos to download data and MITK, upload data to MITK, perform the segmentation, save it, and upload it to a shared folder (J. Fitzpatrick, 2021). This work will be written up after the conclusion of this thesis.

The use of crowdsourced non-experts could solve the bottleneck in producing high-quality training data. Nevertheless, several factors must be considered. Crowdsourcing can rely on altruism which could be limiting, and thus payment may be offered. However, offering money may not motivate crowd participants to produce high-quality work, as quantity will be more lucrative than quality. The source of any financing must also be considered and whether this will introduce bias. The quality of the initial data, assessment of segmentation and correct data filing are factors that need to be considered.

Career Aspirations

Having completed my PhD, I am eager to explore opportunities within industry and academic or clinical settings. My primary focus is on continuing research endeavours to contribute to advancing the radiography field. To achieve this, I plan to maintain academic connections with the University of Westminster and Salford, considering grant applications to support future research endeavours.

Additionally, I aim to broaden the impact of the 'continued professional development' group I initiated at my workplace by incorporating all European radiographers and imaging technologists within the company. With a commitment to fostering lifelong learning in the profession, I will be readily available to mentor colleagues interested in pursuing further education.

Conclusion

This thesis has been submitted to fulfil the requirements for PhD by publications. Nine peer-reviewed published papers were included, along with supporting evidence, accompanied by a critical appraisal of the papers and an overview of their impact. This PhD has focused on cultivating quantitative methods for MRI, with the goal of translating them into large-scale studies. This work describes a journey from entering a research environment to culminating in the generation of original and novel work that has endured peer review and has been translated into large-scale imaging studies.

Upon reflection on the submitted work, themes were identified that characterised the requirements when undertaking quantitative research. Rather than documenting the parameters, an entire itinerary must be identified and appropriately assigned immediately after the conception of a research project.

Four aims were identified to demonstrate how the overarching objective of the work was achieved.

A discussion is included as to how the processes are effectively undertaken. Included is how a safe and welcoming environment contributes to the acquisition of quality data, how the protocol should be achievable, relevant, and reproducible and how this is achieved through optimisation. The role of a dedicated research radiographer is also included. Choices when selecting tools for analysis are discussed as how the analysis should be part of the initial considerations when any study is conceived; in addition, giving and receiving feedback via discussion and the process of publishing and how this can contribute to the process of optimisation.

Translating the imaging methods to large-scale studies is identified as how the upscaling process differs from routine diagnostics and the requirements regarding consistency of acquisition, managing QC processes and analysis of big data.

Finally, a means to automate some of the processes required for large-scale studies are proposed to effectively generate meaningful outcomes and relevant information regarding health markers in realistic time frames.

The feasibility of using MRI to measure critical physiological parameters such as ectopic fat content and organ volume accurately and precisely, in various tissues has been demonstrated. These methods have then been shown to translate into large-scale studies. By continuing to

refine and validate these methods, we can help to pave the way for a new era of how imaging is used to influence which treatments and interventions are helpful and represents a significant step forward in our understanding of quantitative MRI methods and their potential applications in large-scale studies.

Appendix

A. **Supporting Evidence-Poster Presentations**

Ai. Quantifying hepatic lipid content and T2* decay using breath-hold mutiecho imaging at 3.0 tesla (O'Regan et al., 2007)

Presented at the 16th meeting and Exhibition of the International Society for Magnetic Resonance in Medicine: Berlin, German y 19-25th May 2007

Quantifying hepatic lipid content and T2* decay using breath-hold multiecho imaging at 3.0 tesla

Imperial College London

MRC Clinical Sciences Centre

Declan O'Regan, Martina Callaghan, Marzena Arridge, Julie Fitzpatrick, Rossi Naoumova, Jo Hajnal, Stephan Schmitz.
Imaging Sciences Department, MRC Clinical Sciences Centre, Hammersmith Hospital, Imperial College, London, United Kingdom

Introduction

Lipid quantification using gradient echo sequences relies on the chemical shift in resonant frequency between fat and water molecules. Single and dual echo techniques have previously been used to estimate lipid content within the liver and adrenals. A disadvantage of this approach is that a separate sequence needs to be acquired to allow correction for T2* decay, and potentially a third sequence with different T1-weighting to confirm whether the dominant species is fat or water.

In contrast, multiecho imaging has the potential to provide a more accurate measurement of tissue fat content in a single sequence. The signal intensity variation in a multiecho acquisition would be expected to depend on the individual T2* decays of the fat and water components, as well as a periodic oscillation of signal intensity between in-phase and out-of-phase echo times dependant on the fat:water ratio. A rapid single sequence to allow accurate tissue fat quantification, as well as T2* measurement, would be of potential value in both lipid and iron deposition disorders.

Aim

The aim of this study was to design and optimize a breath-hold in-phase and out-of-phase multiecho sequence suitable for quantifying liver fat fraction. A model was developed to derive the individual signal contributions from the fat and water components as a function of echo time and their respective T2* decay constants. The sequence was tested on fat phantoms and in humans, and compared to hepatic proton magnetic resonance spectroscopy (MRS).

Method

A model was developed to describe the signal intensity variation observed as a function of echo time in a tissue containing fat and water (Figure 1). The lipid content and T2* decay constants of fat and water could then be derived by measuring the signal intensity in a region of interest and employing an iterative curve-fitting technique to the data points (Figure 2).

The MRI studies were performed on a 3.0 tesla Philips Intera system (Best, Netherlands). Imaging was performed using a breath-hold spoiled gradient echo sequence with a seven echo readout giving a total acquisition time of 4 seconds for a single slice. The multiecho sequence parameters were flip angle 20°, field of view 320mm, slice thickness 10mm, acquired voxel size (mm) 2.5 x 2.5 x 10, TR 11 ms and 2 signal averages. Liver imaging was performed on 5 healthy volunteers and 5 patients with diabetes.

Comparison was made to a point-resolved spectroscopy sequence without water suppression corrected for T2 decay.

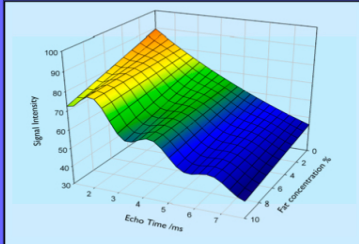

Figure 1. The protons in water molecules have a higher Larmor frequency than those in lipids. In tissues containing a mixture of fat and water the phase interference between these resonating nuclei produces a sinusoidal variation of the magnitude signal intensity. The fat and water species will each have an exponential T2* decay. Thus the standard model of magnitude signal intensity can be extended to the following biexponential equation -

$$|S| = \left| S_W e^{-t/T2^*_W} + S_F e^{-t/T2^*_F + i\Delta\omega t} \right|$$

where $T2^*_w$ and $T2^*_f$ are the decay constants for the respective water (S_w) and fat (S_f) signal components and ω the frequency difference.

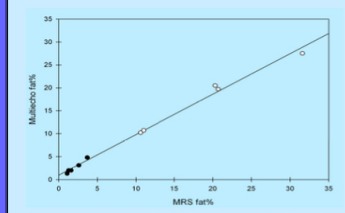

Figure 3. The relationship between fat estimation in the liver using Multiecho and Magnetic Resonance Spectroscopy techniques ($y = 0.97x + 0.15$, $r_2 = 0.99$, $p<0.0001$). Closed circles are normal volunteers and open circles are patients. An MRS spectrum of a steatotic liver is shown below with a water resonance at 4.7 ppm and lipid at 1.3 ppm.

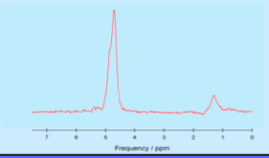

Figure 2. A plot of mean signal intensity in a region of interest of a steatotic liver in the multiecho sequence showing the biexponential model's convergence on a best-fit curve (below left). An axial breath-hold multiecho acquisition of the liver with seven readouts at alternately out-of-phase and in-phase echo times (below right).

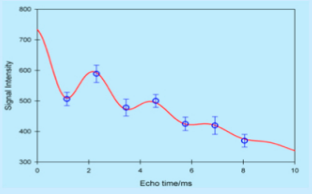

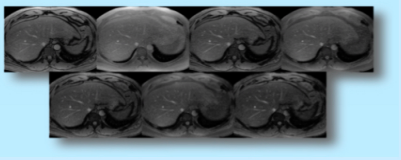

Results

The multiecho sequence modeling converged on a fit for S_w and S_f in all cases, and also individual $T2^*_w$ and $T2^*_f$ components in those with steatosis. In the patient group the mean hepatic fat fraction was 15.2% ±4.9; the mean water T2* 16.3 ±3.8 ms, and the mean lipid T2* 9.9 ±6.2 ms.

In the volunteer group the mean hepatic fat fraction was 2.0% ±0.8 and the mean global T2* 21.9 ±10 ms. Pearson's test indicated a significant correlation coefficient between multiecho and spectroscopic measurement of hepatic lipid ($y=0.97x + 0.15$, $r^2=0.99$, $p<0.0001$) (Figure 3).

Discussion

Multiecho imaging provides a rapid method of quantifying liver fat content that is highly correlated to proton spectroscopy. In contrast to dual-echo methods a single multiecho sequence overcomes the potential error due to differential T2* decay of fat and water; and enables the correct assignment of the fat and water signal components. Multiecho imaging provides an accurate and efficient method for spatially-resolved fat quantification and T2* characterization of liver tissue.

SCHERING

Aii. Measurement of Pancreatic Fat Using Muti Echo MRI

(J. Fitzpatrick, Thomas, Durighel, O'Regan, et al., 2010)

Presented at the 11th International Congress on Obesity: Stockholm, Sweden July 2010

Imperial College London

Measurement of Pancreatic Fat Using Multi Echo MRI

JA Fitzpatrick[1,2], EL Thomas[2], G Durighel[2], DP O'Regan[3], SD Taylor-Robinson[1] and JD Bell[2]

[1] Division of Diabetes, Endocrinology and Metabolism, Department of Medicine, Imperial College, London

[2] Metabolic and Molecular Imaging Group, MRC Clinical Sciences Centre, Imperial College London

3 Division of Clinical Sciences, MRC Clinical Sciences Centre, Imperial College London

MRC Clinical Sciences Centre

Objective

The purpose of this study is to develop and evaluate the use of single slice Multi-echo MRI as a robust, non-invasive tool for the assessment of pancreatic fat content and to compare to MRS.

Background

Excessive pancreatic triglyceride is thought to accumulate early in the natural course of type-2 diabetes and could be used to identify those at risk and monitor interventions[1]. ^{1}H Magnetic Resonance Spectroscopy (MRS) is currently used for liver fat quantification; however this can be challenging in the pancreas due to its size and position. Therefore we propose to use Multi-echo (ME) imaging to measure pancreatic fat[2].

Methods:

- 78 subjects (49 male, 29 female, age 21-71 years, BMI 19.8 – 40.5 kg/m^2) were recruited.
- Single slice multi-echo images were obtained during a single 15 s breath-hold, using a surface coil: parameters TR 150 ms, 20 echoes TE starting at 1.15 and then at intervals 1.15 ms.
- ^{1}H MRS of the pancreas (IPCL) and liver (IHCL) were obtained at 1.5T following an overnight fast
- Total and regional adipose tissue content was measured by whole body MRI[3].

Results:

Figure 1: Typical multi-echo images are shown in Figure 1, where A=Liver and B=Pancreas.

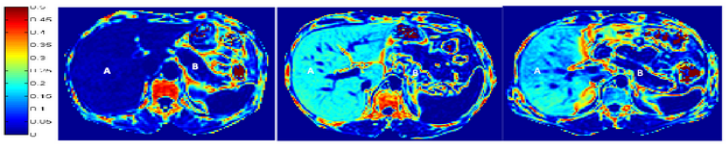

Low liver fat
Low pancreatic fat

High liver fat
High pancreatic fat

High liver fat
Low pancreatic fat

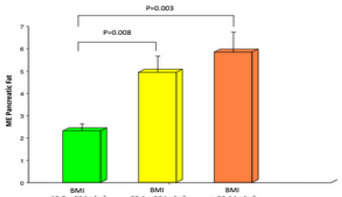

Figure 2: Pancreatic fat content increases with increasing BMI.

- Pancreatic fat increased with increasing BMI (Figure 2).
- There was a weak, but significant correlation between liver and pancreatic fat content (r=0.24, p=0.02).
- There was a stronger correlation for internal compared with subcutaneous AT depots (Table 1).

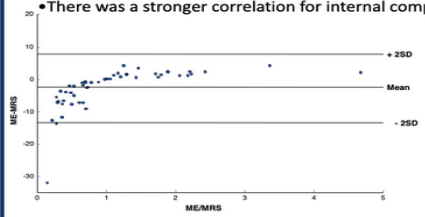

Figure 3: Bland and Altman plot to show agreement between ME and MRS measures of pancreatic fat

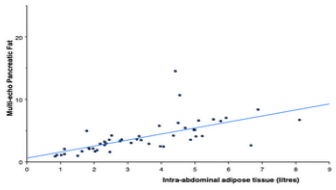

Figure 4: Relationship between ME measurement of pancreatic fat and intra-abdominal AT.

	Multi-echo pancreatic fat
Weight (kg)	**r=0.34, p=0.002**
BMI kg/m^2	**r=0.27, p=0.01**
Waist to hip ratio	**r=0.48, p<0.0001**
Total AT (litres)	r=0.19, p=0.11
SC AT (litres)	r=0.02, p=0.44
Internal AT (litres)	**r=0.63, p<0.0001**
SC abdominal AT (litres)	r=0.08, p=0.29
Intra-abdominal AT (litres)	**r=0.63, p<0.0001**

Table 1: Pearsons correlations coefficients for the relationship between pancreatic fat content anthropometry and adiposity

- There was a significant correlation between Multi-echo and ^{1}H MRS measurements of pancreatic fat (r=0.66, p<0.0001).
- Since ME could detect pancreatic fat in all subjects, it appears more a more reliable method than ^{1}H MR Spectroscopy, since pancreatic fat content was undetectable in several subjects using ^{1}H MRS.

Discussion and Conclusions

- Pancreatic fat is more closely related to internal adipose tissue depots than subcutaneous stores.
- There is good agreement between ^{1}H MRS and ME imaging, although ME has the advantage of being more reliable. Additionally from a single image acquisition it is possible to measure regional fat differences in the head and tail of the pancreas.
- It is possible to measure routinely pancreatic fat content using ME imaging as part of a standard MR examination.

References:

1. Lingvay I et al. J Clin Endocrinol Metab. 2009; 94:4070-6; 2. O'Regan DP. Radiology. 247.550-557 3. Thomas EL et al. Gut. 2005 Jan;54(1):122-7.

Aiii. Comparing Multi Echo and MRS to Measure Pancreatic Fat

(J. Fitzpatrick et al., 2012)

Presented at ISMRM SCIENTIFIC WORKSHOP ~ Fat-Water Separation: Insights, Applications & Progress in MRI: Long Beach, California, USA. February 2012

Imperial College London

MRC Clinical Sciences Centre

Comparing Multi Echo MRI and MRS to Measure Pancreatic Fat

JA Fitzpatrick[1,2], EL Thomas[2], NB Al Saud[2], G Durighel[2], DP O'Regan[3], G Frost[4], SD Taylor-Robinson[1] and JD Bell[2]

1 Division of Diabetes, Endocrinology and Metabolism, Department of Medicine, Imperial College, London
2 Metabolic and Molecular Imaging Group, MRC Clinical Sciences Centre, Imperial College London
3 Division of Clinical Sciences, MRC Clinical Sciences Centre, Imperial College London
4Nutrition and Dietetic Research Group, Department of Investigative Medicine, Imperial College London

Introduction:

- There is growing interest in understanding how pancreatic fat is implicated in β-cell dysfunction and its role in the development of type-2 diabetes.
- A variety of approaches have been used to assess pancreatic fat content non-invasively, including ^{1}H MRS and several MRI-based methods.
- ^{1}H MRS of the pancreas is technically more challenging, compared to the liver, due to its shape and location.
- Developing a fast, robust protocol that can be more universally applied is desirable.

Methods:

•176 subjects (123male, 53 female, age 20-75 years, BMI 18.9 – 40.5 kg/m^2) were recruited.

•Following an overnight fast, single slice multi-echo images were obtained during a single 15 s breath-hold, using a surface coil, parameters TR 150 ms, 20 echoes TE starting at 1.15 and then at intervals 1.15 ms.

•^{1}H MRS of the pancreas and liver were obtained during the same examination (see Figure 1). All ME images were analysed by an experienced MRI practitioner (Observer 1), and a student trained to analyse pancreas data (Observer 2).

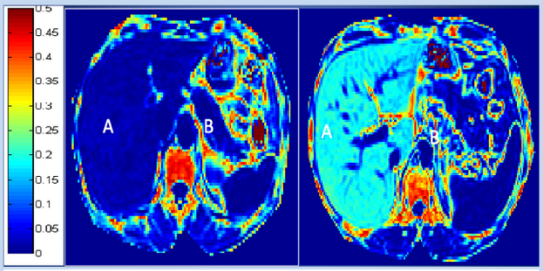

Figure 1. Typical ME images are shown in Figure 1 where A=Liver and B=Pancreas

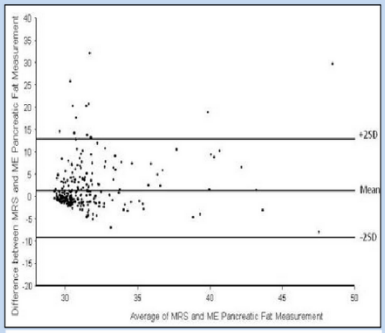

Figure 2. Bland and Altman plot showing good agreement between MRS and ME

Results:

- From the ME Images obtained, the pancreas could be identified and fat content measured in 93.2% of subjects by observer 1 and by 71.7% subjects by observer 2
- ^{1}H MR Spectra were obtained in 98% subjects, but repeated acquisition in some were necessary due to contamination from surrounding adipose tissue. Of these spectra, 10-15% were classed as unreliable after visual inspection.
- Bland and Altman showed relatively strong agreement between the 2 different methods, although agreement was less good with greater degrees of fat infiltration (>20% fat), Figure 2.
- There was a weak but highly significant correlation between fat content in the pancreas and liver ^{1}H MRS r=0.304 p<0.001; ME r=0.203 p<0.001).

Discussion and Conclusions:

- There is good agreement between ^{1}H MRS and ME imaging, although in our experience for assessment of fat infiltration, ME was a more robust method than MRS of the pancreas. MRS being less reliable, mainly owing to contamination from surrounding visceral fat.
- Additionally, ME has the advantage of being able to measure regional fat differences in the head and tail of the pancreas and the liver simultaneously from a single acquisition.
- Therefore, we conclude that ME is a robust and more reliable technique and that it is possible to measure pancreatic fat content routinely using ME, as part of a standard MR examination.

References:

1. Lingvay I et al. J Clin Endocrinol Metab. 2009; 94:4070-6; 2. O'Regan DP. Radiology. 247.550-557 3. Thomas EL et al. Gut. 2005 Jan;54(1):122-7 4. Hu HH. et al. Obesity 2010 18(4):459-67 5. Schwenzer NF. et al. Invest Radiol 2008 43(5):3306. Sijens PE et al. World J Gastroentrol 2010 16(16):1993-87. Li J et al. Pancreas 2011 40(2):295-9

Aiv. Psoas Muscle Cross Sectional Area: A Novel Marker of Physical Fitness (J. A. Fitzpatrick et al., 2013)

Presented at European Congress on Obesity: Liverpool, U.K. May 2013

Imperial College London

MRC Clinical Sciences Centre

Psoas Muscle Cross Sectional Area: A Novel Marker of Physical Fitness

JA Fitzpatrick[1,3], ES Chambers[2], EL Thomas[1], G Frost[2], SD Taylor-Robinson[3] and JD Bell[1]

1 Metabolic and Molecular Imaging Group, MRC Clinical Sciences Centre, Imperial College London

2Nutrition and Dietetic Research Group, Department of Investigative Medicine, Imperial College London

3Division of Diabetes, Endocrinology and Metabolism, Department of Medicine, Imperial College, London

Introduction

The psoas muscle of the trunk is recruited during hip joint flexion and functions as a stabilizer of the hip and lumbar region. Due to the importance of the psoas muscle in maintaining balance and stability when performing movement, we hypothesized that psoas muscle size will be strongly associated with level of physical fitness .

Methods

Thirty Caucasian men (mean ± SD age: 44 ± 6 yr; BMI: 29.4 ± 5.9 kg/m^2) underwent MRI at 1.5T following an overnight fast. Whole body T1 weighted axial images of the whole body were obtained and measurements of total and regional fat mass acquired. Cross sectional area (CSA) of the psoas, rectus abdominis and total trunk CSA at the level of L5 were calculated by an experienced Radiographer (Fig. 1). Physical fitness was measured as maximal oxygen consumption (VO_{2max}) during an incremental cycling test to exhaustion.

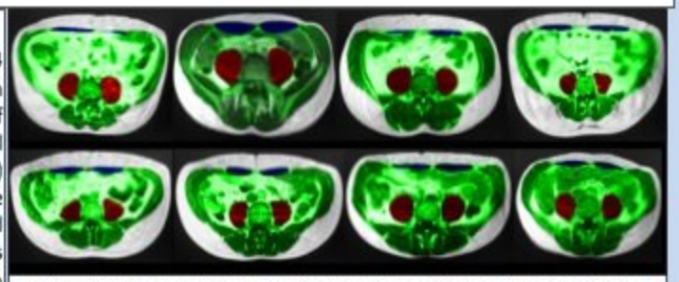

Figure 1: Magnetic resonance imaging of the trunk area obtained at L5. Psoas(red), rectus abdominis(blue) and total trunk CSA(green) were calculated.

Results

Psoas CSA and rectus abdominis CSA were calculated as a percentage of total trunk CSA. These values correlated significantly with body weight, therefore psoas CSA and rectus abdominis CSA were expressed relative to body weight. Multiple linear regression was used to investigate if measures of psoas CSA and rectus abdominis CSA could predict fitness and total and regional fat mass. The probability of F was used to retain (<0.05) or remove (>0.10) predictors in backwards elimination models. Only psoas CSA was a significant predictor of fitness (Fig.2), total fat mass (Fig.3) and regional fat mass (Table 1).

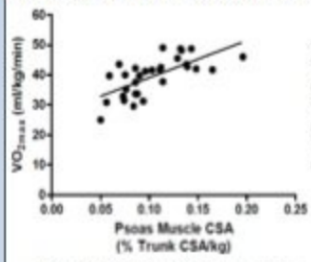

Figure 2: Relationship between psoas CSA and physical fitness ($r^2 = 0.46$, $p < 0.001$).

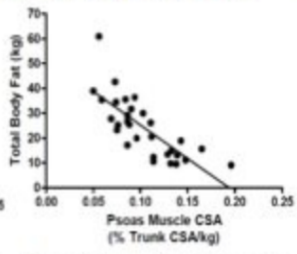

Figure 3: Relationship between psoas CSA and total body fat ($r^2 = 0.60$, $p < 0.001$).

Table 1: Psoas and rectus abdominis CSA as predictors of fitness and fat mass

	Significant Predictor Variables *			Total R^2
Outcome Variables	Constant	Psoas CSA (% Trunk CSA/kg²)	Rectus Abdominis CSA (% Trunk CSA/kg²)	
Physical Fitness (VO_{2max})	26.74 (2.77)	123.60 (25.32)	-	0.46
Total Body Fat	52.20 (4.59)	-269.68 (41.93)	-	0.60
Subcutaneous Fat	40.30 (4.13)	-205.90 (37.76)	-	0.52
Visceral Fat	11.91 (0.91)	-63.77 (8.34)	-	0.68
Subcutaneous Abdominal Fat	13.60 (1.61)	-76.49 (14.68)	-	0.49
Visceral Abdominal Fat	7.72 (0.72)	-44.15 (6.56)	-	0.62
Intrahepatocellular lipid	20.57 (4.53)	-150.35 (41.41)	-	0.32

* Values are unstandardized coefficients with standard error in parentheses. All fat mass values are kg apart from intrahepatocellular lipid (geometric mean).

Discussion and Conclusions

The CSA of the psoas muscle provides an accurate and time efficient estimate of physical fitness. The significant positive association with aerobic fitness was not observed with the CSA of the rectus abdominis, suggesting this correlation is not common to all muscles in the trunk region. Physical fitness is known to be a significant predictor of fat mass[1] and our present data provides evidence that psoas CSA is also negatively correlated with total and regional fat mass. Previous studies have shown that psoas CSA correlates strongly with patient survival rates following cancer and major surgery[2-3]. Our data would suggest that improved survival rates are due to better physical fitness. Psoas muscle CSA may therefore have the potential to be used as a predictor of outcome following surgical intervention.

References

1. G O'Donovan *et al.* (2009). *Int J Obes (London);33: 1356–62.* **2.** MJ Englesbe *et al.* (2012). *Ann Surg;256: 255–261.* **3.** MJ Englesbe *et al.* (2010). *J Am Coll Surg;211(2):271-8.*

B. DIRECT Training Presentation

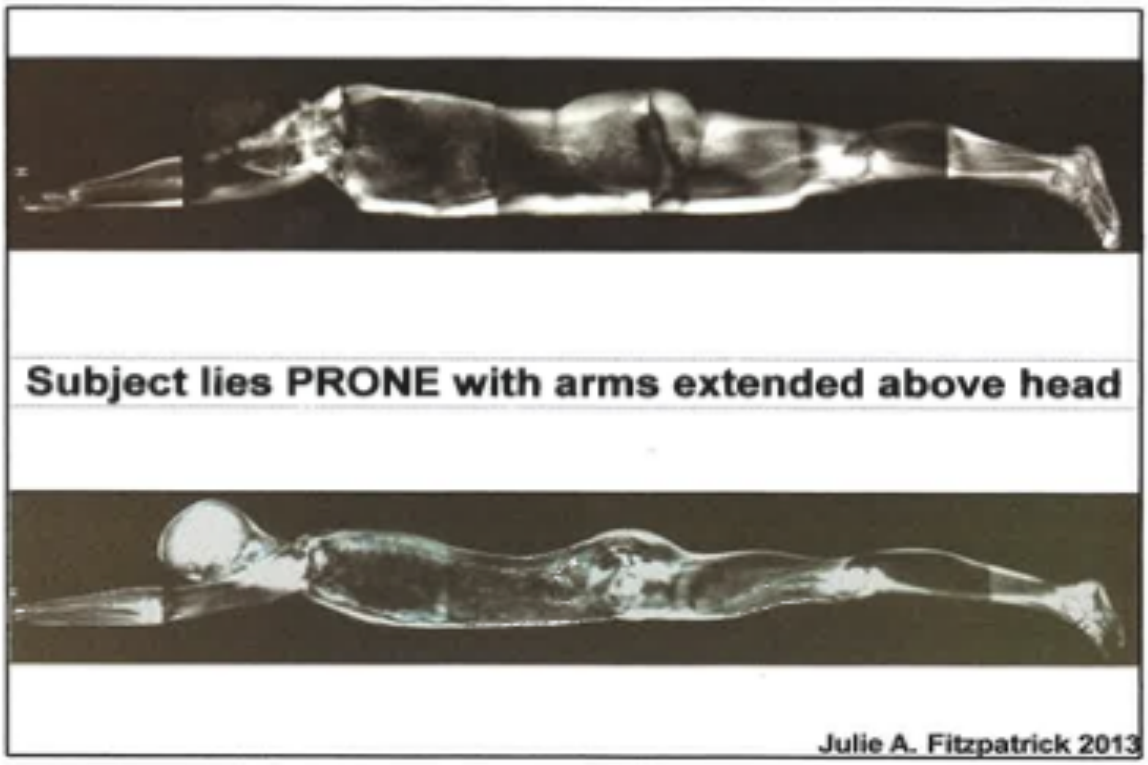
Subject lies PRONE with arms extended above head
Julie A. Fitzpatrick 2013

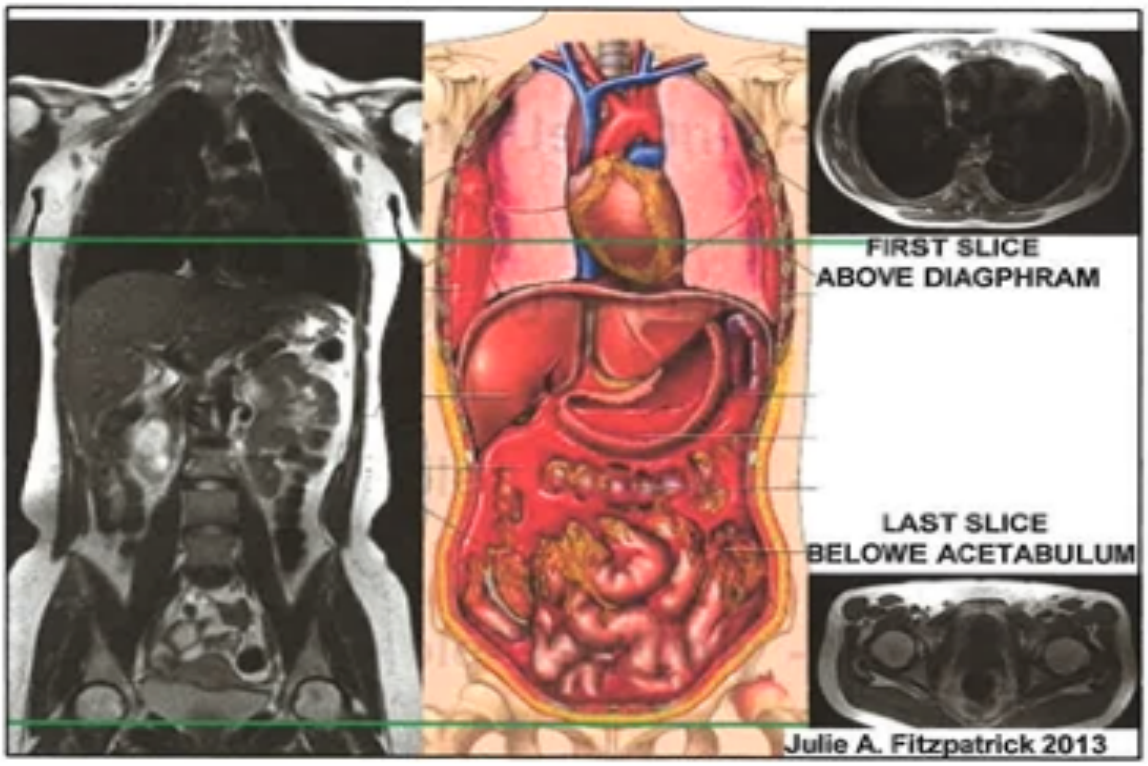
FIRST SLICE
ABOVE DIAGPHRAM
LAST SLICE
BELOWE ACETABULUM
Julie A. Fitzpatrick 2013

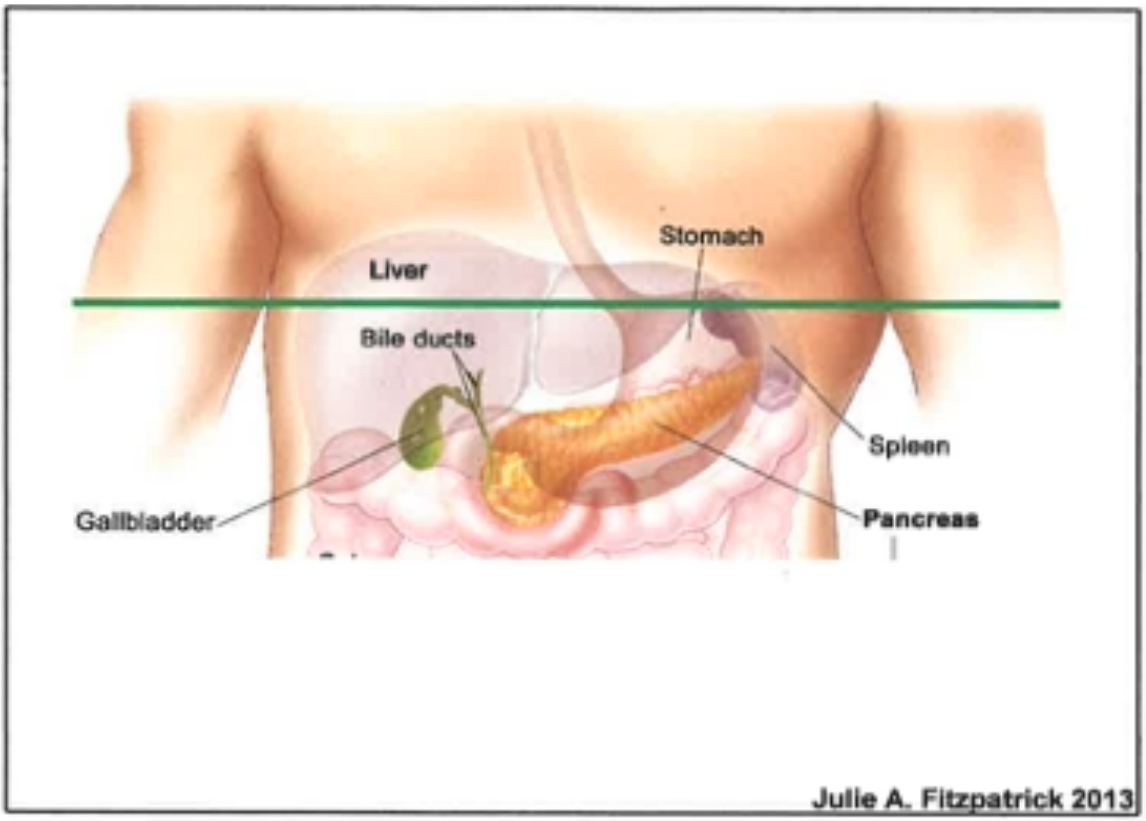
Stomach
Liver
Bile ducts
Spleen
Gallbladder
Pancreas
Julie A. Fitzpatrick 2013

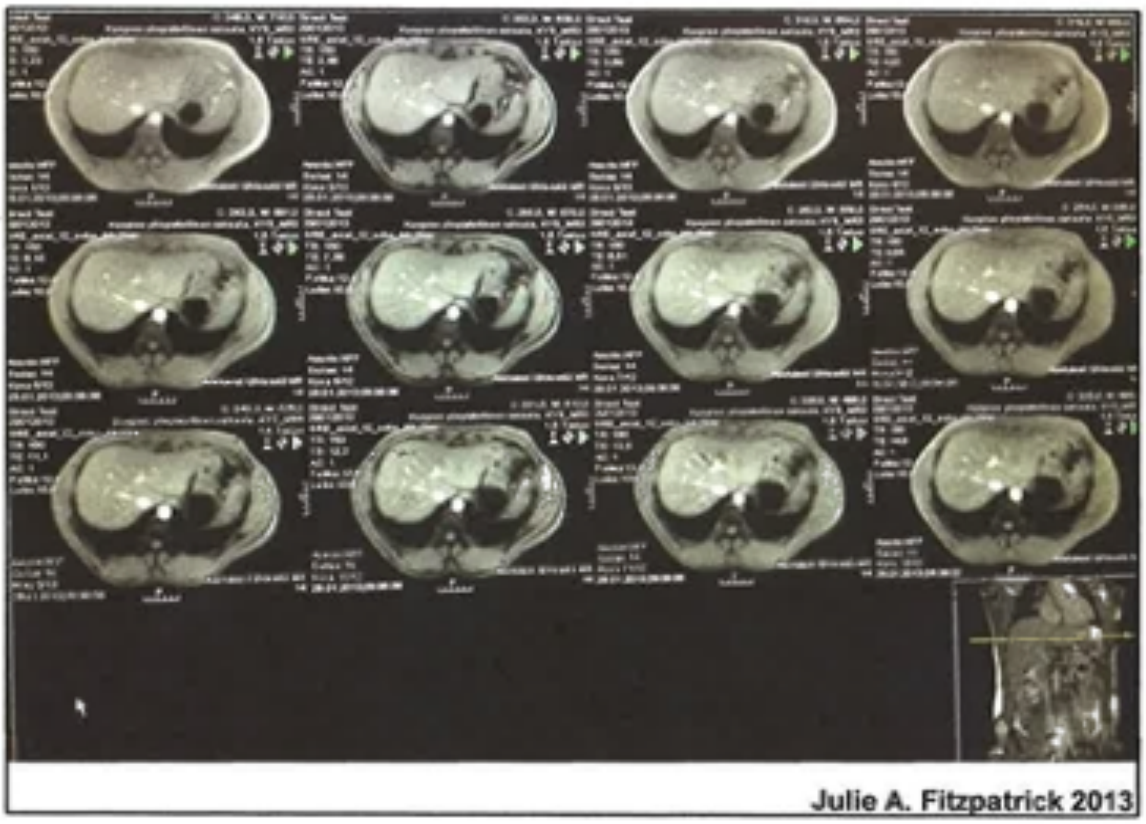
Julie A. Fitzpatrick 2013

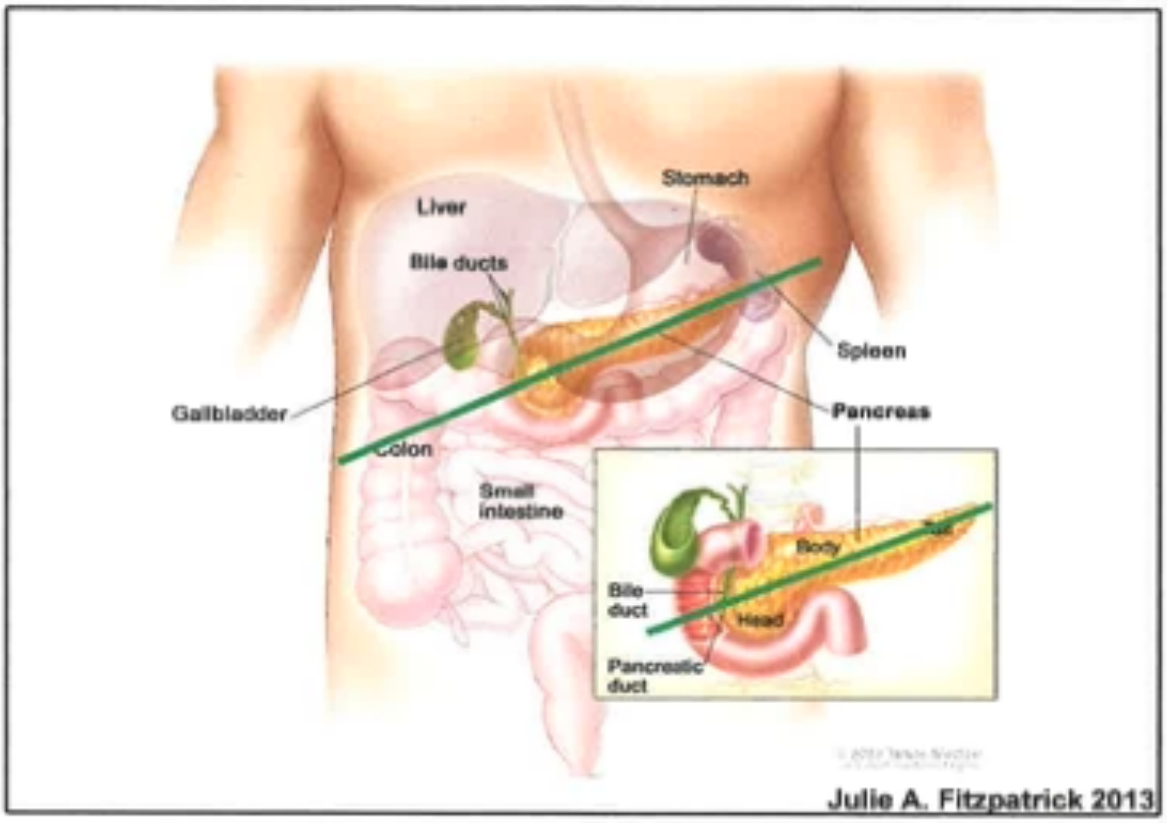
Stomach
Liver
Bile ducts
Spleen
Gallbladder
Pancreas
Colon
Small intestine
Body
Bile duct
Head
Pancreatic duct
Julie A. Fitzpatrick 2013

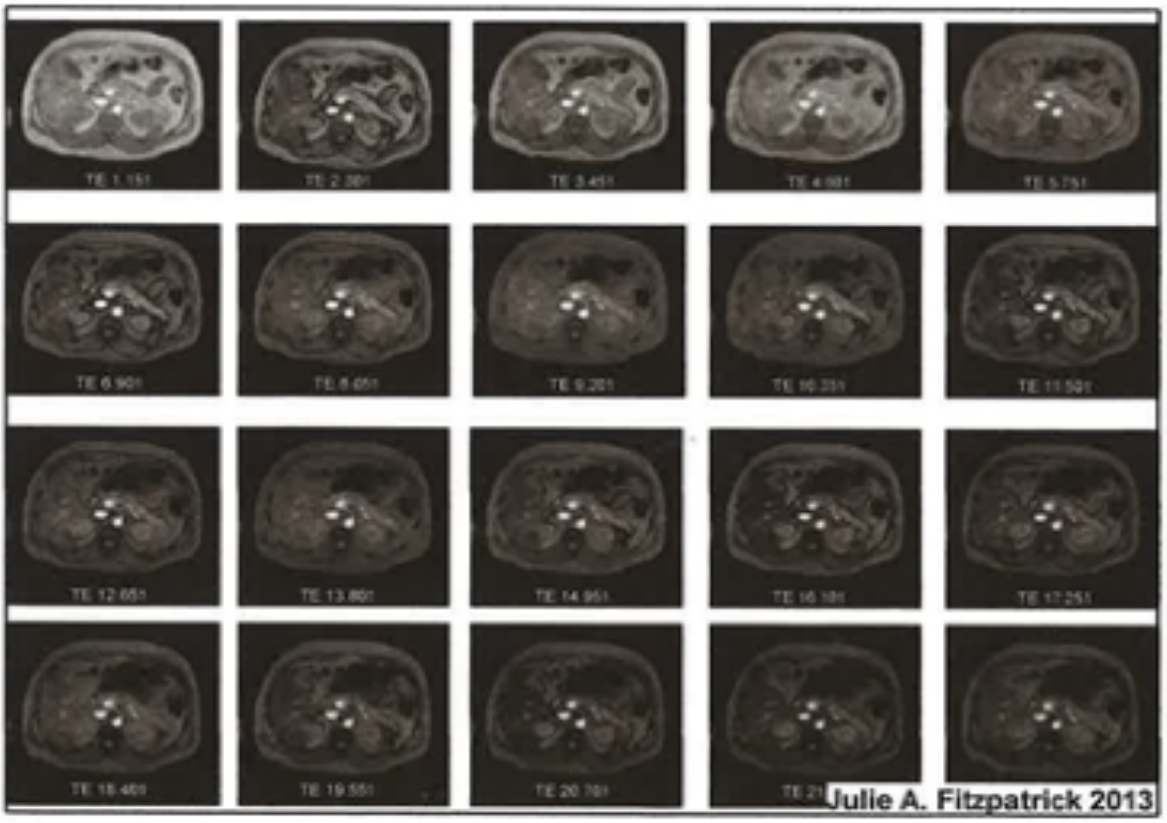
Julie A. Fitzpatrick 2013

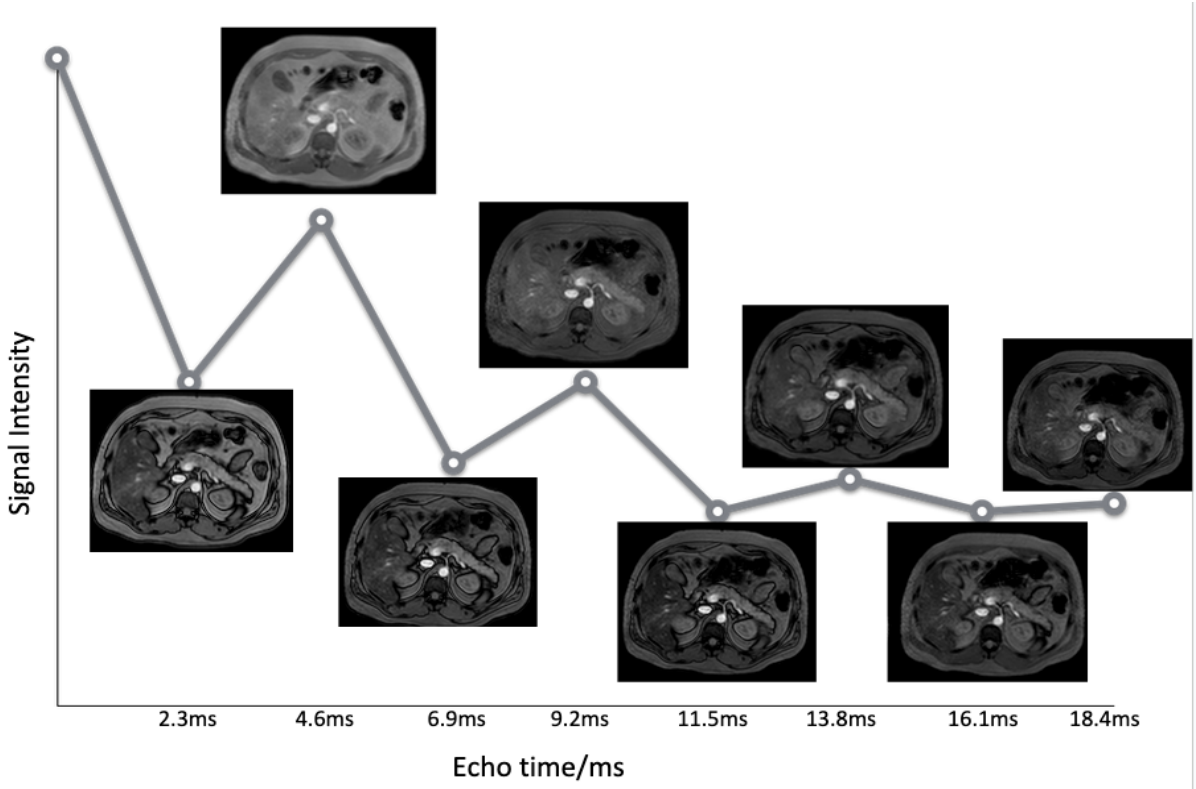
Signal Intensity
2.3ms
4.6ms
6.9ms
9.2ms
11.5ms
13.8ms
16.1ms
18.4ms
Echo time/ms

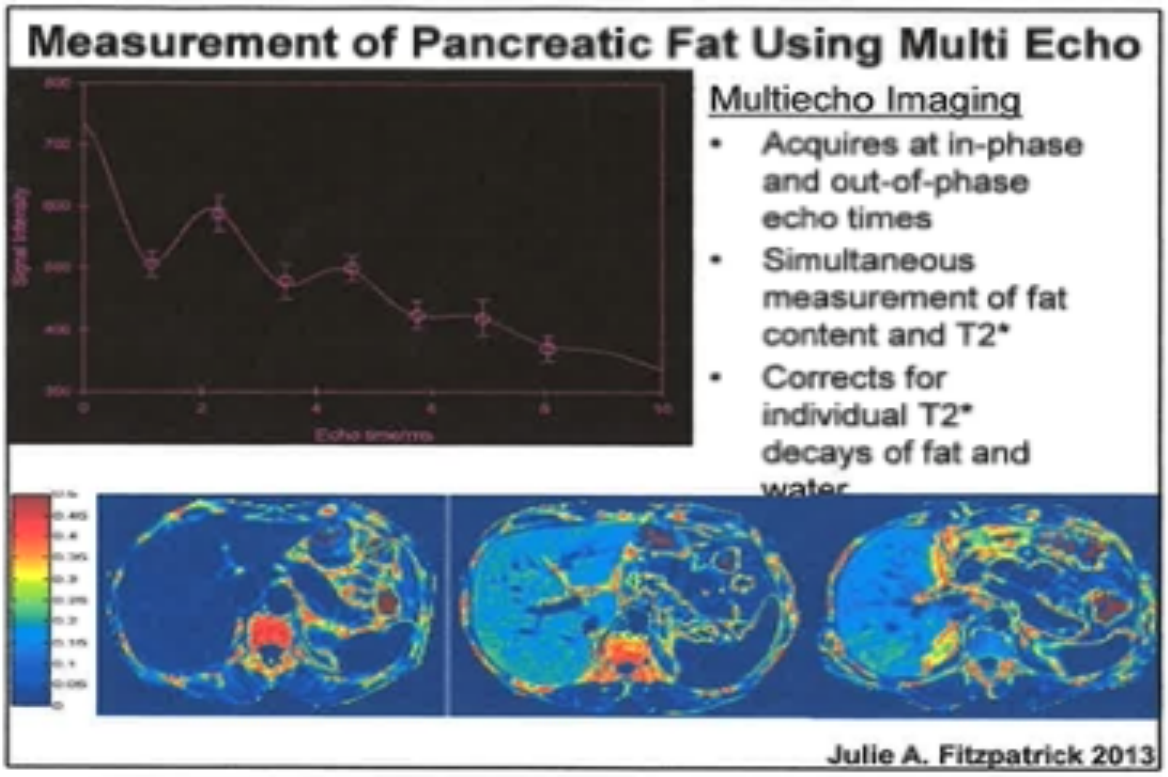
Measurement of Pancreatic Fat Using Multi Echo
Multiecho Imaging
• Acquires at in-phase and out-of-phase echo times
• Simultaneous measurement of fat content and T2*
• Corrects for individual T2* decays of fat and
Julie A. Fitzpatrick 2013

C. Biobank Letter

biobank uk
Improving the health of future generations

Ms Julie Fitzpatrick
Imperial College
Clinical Imaging Facility
Wolfson Conference Centre
Hammersmith Campus
The Hammersmith Hospital,
Du Cane Road,
London W12 0NN

30 June 2014

Dear Julie

Re: Support for the UK Biobank Imaging Enhancement

UK Biobank launched its imaging study last month. The ambitious plan to acquire state-of-the-art imaging of the brain, heart, bones and carotids of 100,000 of the people who have volunteered for the longitudinal UK Biobank study is underway! We hope that this unprecedented dataset – which will be made openly available to all researchers as it becomes available – and its potential to be linked to long-term health follow-up will make a major contribution to the understanding and treatment of a wide range of common disability and life-threatening conditions (such as dementia, diabetes, cancer and heart disease).

Despite its complexity, the project has been developed quickly and is being implemented by a small UK Biobank team in a facility dedicated entirely to the delivery of this project. This has only been possible because of the tremendous support that imaging experts from around the world have offered to the programme. Experience critical to the concept, design and implementation of this complex programme has been shared freely by leaders in the field from many countries.

On behalf of UK Biobank and the many who will benefit from this work in the future, we want to thank you for your contributions in developing the abdominal imaging protocol for UK Biobank. Without your assistance, and that of other international imaging experts, we would not have been able to get so far so fast!

Yours sincerely

Prof Sir Rory Collins FMedSci, FRCP
PI/CEO, UK Biobank
Head, Nuffield Department of Population Health
University of Oxford

Prof Paul M. Matthews OBE, MD, DPhil, FRCP, FMedSci
Chair, UK Biobank Imaging Working Group
Head, Division of Brain Sciences and
Professor of Clinical Neuroscience
Imperial College London

UK Biobank, 1-2 Spectrum Way, Adswood, Stockport, Cheshire SK3 0SA
Tel 0161 475 5360 Fax: 0161 475 5361 www.ukbiobank.ac.uk

UK Biobank Limited (company no 4978912) is a registered charity in England & Wales (1101332) and in Scotland (SC039230)

D. Current/Future Work

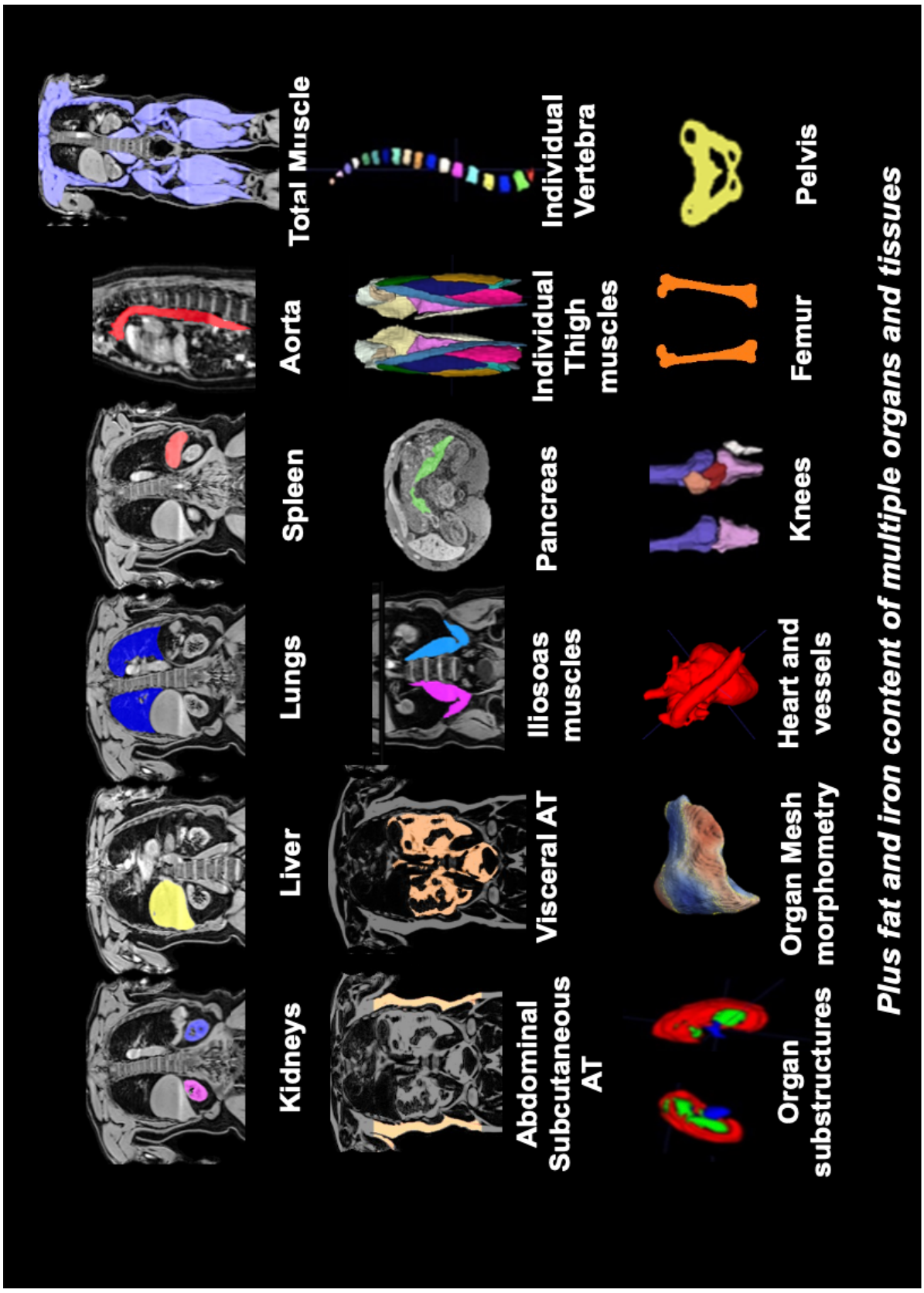

Bibliography

About FHS | Framingham Heart Study. (2022). https://www.framinghamheartstudy.org/fhs-about/

About UK Biobank | UK Biobank. (2022). http://www.ukbiobank.ac.uk/about-biobank-uk/

Albers, M. J. (2017). Quantitative Data Analysis-In the Graduate Curriculum. *Journal of Technical Writing and Communication*, *47*(2), 215–233. https://doi.org/10.1177/0047281617692067

Alfaro-Almagro, F., Jenkinson, M., Bangerter, N. K., Andersson, J. L. R., Griffanti, L., Douaud, E., Sotiropoulos, S. N., Jbabdi, S., Hernandez-Fernandez, M., Vallee, E., Vidaurre, D., Webster, M., Mccarthy, P., Rorden, C., Daducci, A., Alexander, D. C., Zhang, H., Dragonu, I., Matthews, P. M., … Smith, S. M. (2018). *Image processing and Quality Control for the first 10,000 brain imaging datasets from UK Biobank*. https://doi.org/10.1016/j.neuroimage.2017.10.034

Allisy-Roberts, Penelope, & Williams, Jerry. (2008). *Farr's Physics for Medical Imaging—2nd Edition* (2nd ed.). Elsever. https://www-elsevier-com.salford.idm.oclc.org/books/farrs-physics-for-medical-imaging/allisy-roberts/978-0-7020-2844-1

AMRA Medical | Medical Imaging and Body Composition Analysis. (2023). AMRA Medical. https://amramedical.com/

Arenson, R. L., Chakraborty, D. P., Seshadri, S. B. E. E., & Kundel, H. L. (2003). The Digital Imaging Workstation. *Journal of Digital Imaging*, *16*(1), 142–162. https://doi.org/10.1007/s10278-002-6004-y

Asaturyan, H., Thomas, E. L., Fitzpatrick, J., Bell, J. D. J. D., & Villarini, B. (2019a). Advancing Pancreas Segmentation in Multi-protocol MRI Volumes using Hausdorff-Sine Loss Function. In *Lecture Notes in Computer Science (including subseries Lecture Notes in Artificial Intelligence and Lecture Notes in Bioinformatics): Vol. 11861 LNCS*. Springer. https://doi.org/10.1007/978

Asaturyan, H., Thomas, E. L., Fitzpatrick, J., Bell, J. D., & Villarini, B. (2019b). Advancing Pancreas Segmentation in Multi-protocol MRI Volumes Using Hausdorff-Sine Loss Function. In H.-I. Suk, M. Liu, P. Yan, & C. Lian (Eds.), *Machine Learning in Medical Imaging* (pp. 27–35). Springer International Publishing. https://doi.org/10.1007/978-3-030-32692-0_4

Atabaki-Pasdar, N., Ohlsson, M., Viñuela, A., Frau, F., Pomares-Millan, H., Haid, M., Jones, A. G., Thomas, E. L., Koivula, R. W., Kurbasic, A., Mutie, P. M., Fitipaldi, H., Fernandez, J., Dawed, A. Y., Giordano, G. N., Forgie, I. M., McDonald, T. J., Rutters, F., Cederberg, H., … Franks, P. W. (2020). Predicting and elucidating the etiology of fatty liver disease: A machine learning modeling and validation study in the IMI DIRECT cohorts. *PLOS Medicine*, *17*(6), e1003149. https://doi.org/10.1371/journal.pmed.1003149

Australia's largest ongoing study of health and ageing | 45 and Up Study | Sax Institute. (2023, February 15). *Https://Www.Saxinstitute.Org.Au/*. https://www.saxinstitute.org.au/solutions/45-and-up-study/

Bakasa, W., & Viriri, S. (2023). *Pancreas Instance Segmentation Using Deep Learning Techniques* (pp. 205–223). https://doi.org/10.1007/978-3-031-25271-6_13

Balsam, L. B. (2018). Psoas muscle area: A new standard for frailty assessment in cardiac surgery? *Journal of Thoracic Disease*, *10*(Suppl 33), S3846–S3849. https://doi.org/10.21037/jtd.2018.10.96

Baracos, V. E. (2017). Psoas as a sentinel muscle for sarcopenia: A flawed premise. *Journal of Cachexia, Sarcopenia and Muscle*, *8*(4), 527–528. https://doi.org/10.1002/jcsm.12221

Barrett, D., & Noble, H. (2019). What are cohort studies? *Evidence-Based Nursing*, *22*(4), 95–96. https://doi.org/10.1136/ebnurs-2019-103183

Basty, N., Liu, Y., Cule, M., Thomas, E. L., Bell, J. D., & Whitcher, B. (2020a). Automated Measurement of Pancreatic Fat and Iron Concentration Using Multi-Echo and T1-Weighted MRI Data. *Proceedings - International Symposium on Biomedical Imaging*, *2020-April*, 345–348. https://doi.org/10.1109/ISBI45749.2020.9098650

Basty, N., Liu, Y., Cule, M., Thomas, E. L., Bell, J. D., & Whitcher, B. (2020b). *Image Processing and Quality Control for Abdominal Magnetic Resonance Imaging in the UK Biobank*.

Basty, N., Thanaj, M., Thomas, E. L., Whitcher, B., Cule, M., Sorokin, E. P., Liu, Y., Bell, J. D., & Thomas, E. L. (2021). *Swap-Free Fat-Water Separation in Dixon MRI using Conditional Generative Adversarial Networks*. https://www.researchgate.net/publication/353567511

Belsky, D. W., Caspi, A., Houts, R., Cohen, H. J., Corcoran, D. L., Danese, A., Harrington, H., Israel, S., Levine, M. E., Schaefer, J. D., Sugden, K., Williams, B., Yashin, A. I., Poulton, R., & Moffitt, T. E. (2015). Quantification of biological aging in young adults. *PNAS*. https://doi.org/10.1073/pnas.1506264112

Biederer, J., Mirsadraee, S., Beer, M., Molinari, F., Hintze, C., Bauman, G., Both, M., Van Beek, E. J. R., Wild, J., & Puderbach, M. (2012). MRI of the lung (3/3)-current applications and future perspectives. *Insights into Imaging*, *3*(4), 373–386. https://doi.org/10.1007/s13244-011-0142-z

Board of the Faculty of Clinical Radiology. (2019). Clinical Radiology UK Workforce Census Report 2018. In *The Royal College of Radiologists*. http://www.rcr.ac.uk/publications.aspx?PageID=310&PublicationID=359

Borga, M. (2018). MRI adipose tissue and muscle composition analysis-a review of automation techniques. *British Journal of Radiology*, *91*(1089). https://doi.org/10.1259/BJR.20180252/ASSET/IMAGES/LARGE/BJR.20180252.G005.JPEG

Borga, M., Thomas, E. L., Romu, T., Rosander, J., Fitzpatrick, J., Dahlqvist Leinhard, O., & Bell, J. D. (2015). Validation of a fast method for quantification of intra-abdominal and subcutaneous adipose tissue for large-scale human studies. *NMR in Biomedicine*, *28*(12), 1747–1753. https://doi.org/10.1002/nbm.3432

Borga, M., West, J., Bell, J. D., Harvey, N. C., Romu, T., Heymsfield, S. B., & Dahlqvist Leinhard, O. (2018). Advanced Body Composition Assessment: From Body Mass Index to Body Composition Profiling. *Journal of Investigative Medicine*, *66*(5), 1–9. https://doi.org/10.1136/jim-2018-000722

Bornert, P., & Norris, D. G. (2020). A half-century of innovation in technology-preparing MRI for the 21st century. *British Journal of Radiology*.

Boyd, A., Cain, O., Chauhan, A., & Webb, G. J. (2020). Medical liver biopsy: Background, indications, procedure and histopathology. *Frontline Gastroenterology*, *11*(1), 40–47. https://doi.org/10.1136/flgastro-2018-101139

Bradley, W. G., Brant-Zawadzki, M., & Cambray-Forker, J. (2001). *MRI of the Brain* (Vol. 2). Lippincott Williams & Wilkins.

Bray, T. J., Chouhan, M. D., Punwani, S., Bainbridge, A., & Hall-Craggs, M. A. (2018). Fat fraction mapping using magnetic resonance imaging: Insight into pathophysiology. *The British Journal of Radiology*, *91*(1089), 20170344. https://doi.org/10.1259/bjr.20170344

Bright, Anne. (2011). *Planning and Positioning in MRI - E-Book—Anne Bright—Google Books* (1st ed.). Churchil Livingstone. https://books.google.co.uk/books?id=VAto9pAHb8EC&q=prone#v=snippet&q=prone&f=false

Britanica. (2022, August). *Scientific method | Definition, Steps, & Application | Britannica*. https://www.britannica.com/science/scientific-method

Butters, O. W., Wilson, R. C., & Burton, P. R. (2020). Recognizing, reporting and reducing the data curation debt of cohort studies. *International Epidemiological Association International Journal of Epidemiology*, 1067–1074. https://doi.org/10.1093/ije/dyaa087

Bydder, M., Shiehmorteza, M., Yokoo, T., Sugay, S., Middleton, M. S., Girard, O., Schroeder, M. E., Wolfson, T., Gamst, A., & Sirlin, C. (2010). Assessment of liver fat quantification in the presence of iron. *Magnetic Resonance Imaging*, *28*(6), 767–776. https://doi.org/10.1016/J.MRI.2010.03.017

Byun, S.-E., Kim, S., Kim, K.-H., & Ha, Y.-C. (2019). Psoas cross-sectional area as a predictor of mortality and a diagnostic tool for sarcopenia in hip fracture patients. *Journal of Bone and Mineral Metabolism*, *37*, 871–879. https://doi.org/10.1007/s00774-019-00986-1

Candes, E., Romberg, J., & Tao, T. (2004). *Robust Uncertainty Principles: Exact Signal Reconstruction from Highly Incomplete Frequency Information*.

Canvasser, L. D., Mazurek, A. a., Cron, D. C., Terjimanian, M. N., Chang, E. T., Lee, C. S., Alameddine, M. B., Claflin, J., Davis, E. D., Schumacher, T. M., Wang, S. C., & Englesbe, M. J. (2014). Paraspinous muscle as a predictor of surgical outcome. *Journal of Surgical Research*, *192*(1), 76–81. https://doi.org/10.1016/j.jss.2014.05.057

Care Quality Commission. (2018). *Radiology review A national review of radiology reporting within the NHS in England A national review of radiology reporting within the NHS in England*. Care Quality Commission.

Carlsson, S., Carlsson, E., Appsgatan, S., & Hospi, L. (2013). 'The situation and the uncertainty about the coming result scared me but interaction with the radiographers helped me through': A qualitative study on patients' experiences of magnetic resonance imaging examinations. *Journal of Clinical Nursing*, *22*(21–22), 3225–3234. https://doi.org/10.1111/JOCN.12416

Chaleckis, R., Murakami, I., Takada, J., Kondoh, H., & Yanagida, M. (2016). Individual variability in human blood metabolites identifies age-related differences. *The Proceedings of the National Academy of Sciences*, *113*(16), 4252–4259. https://doi.org/10.1073/pnas.1603023113

Chawla, D., Rizzo, S., Zalocusky, K., Keebler, D., Chia, J., Lindsay, L., Yau, V., Kamath, T., & Tsai, L. (2020). *Descriptive epidemiology of 16,780 hospitalized COVID-19 patients in the United States*. MedRxiv. https://doi.org/10.1101/2020.07.17.20156265

Chen, Y., Ruan, D., Xiao, J., Wang, L., Sun, B., Saouaf, R., Yang, W., Li, D., & Fan, Z. (2019). *Fully Automated Multi-Organ Segmentation in Abdominal Magnetic Resonance Imaging with Deep Neural Networks*.

Chevalier, S., Colombat, P., Lejeune, J., Guglielmin, B., Bouquet, M., Aubouin-Bonnaventure, J., Coillot, H., & Fouquereau, E. (2022). Recognition of radiographers in the workplace: Why it matters. *Radiography*, *28*(3), 648–653. https://doi.org/10.1016/j.radi.2022.05.001

Cobb, J. G., & Paschal, C. B. (2009). Improved In Vivo Measurement of Myocardial Transverse Relaxation With 3 Tesla Magnetic Resonance Imaging. *J. Magn. Reson. Imaging*, *30*, 684–689. https://doi.org/10.1002/jmri.21877

Cohort directory. (2023, March). https://www.ukri.org/councils/mrc/facilities-and-resources/find-an-mrc-facility-or-resource/cohort-directory/

Coletta, A. M., Klopp, A. H., Fogelman, D., Parikh, A. M., Li, Y., Garg, N., & Basen-Engquist, K. (2019). Dual-Energy X-Ray Absorptiometry Compared to Computed Tomography for Visceral Adiposity Assessment Among Gastrointestinal and Pancreatic Cancer Survivors. *Scientific Reports*, *9*(1), 11500. https://doi.org/10.1038/s41598-019-48027-1

Creswell, J. W., & Guetterman, T. C. (2018). *Educational research: Planning, conducting, and evaluating quantitative and qualitative research*. Pearson.

Damadian, R. (1972). *United States Patent [19] Damadian*.

Davico, G., Bottin, F., Martino, A. D., Castafaro, V., Baruffaldi, F., Faldini, · Cesare, & Viceconti, · Marco. (2022). Intra-operator Repeatability of Manual Segmentations of the Hip Muscles on Clinical Magnetic Resonance Images. *Journal of Digital Imaging*. https://doi.org/10.1007/s10278-022-00700-0

Desmond, J. E., & Glover, G. H. (2002). Estimating sample size in functional MRI (fMRI) neuroimaging studies: Statistical power analyses. *Journal of Neuroscience Methods*, *118*(2), 115–128. www.elsevier.com/locate/jneumeth

Dietrich, O., Raya, J. G., Reeder, S. B., Reiser, M. F., & Schoenberg, S. O. (2007). Measurement of signal-to-noise ratios in MR images: Influence of multichannel coils, parallel imaging, and reconstruction filters. *Journal of Magnetic Resonance Imaging*, *26*(2), 375–385. https://doi.org/10.1002/jmri.20969

DIRECT - DIabetes REsearch on patient straTification. (2022). https://directdiabetes.org/

Do, C., DeAguero, J., Brearley, A., Trejo, X., Howard, T., Escobar, G. P., & Wagner, B. (2020). Gadolinium-Based Contrast Agent Use, Their Safety, and Practice Evolution. *Kidney360*, *1*(6), 561–568. https://doi.org/10.34067/KID.0000272019

Doll, R., & Hill, A. B. (1954). The mortality of doctors in relation to their smoking habits; a preliminary report. *British Medical Journal*, *1*(4877), 1451–1455. https://doi.org/10.1136/bmj.1.4877.1451

Doll, R., & Hill, S. A. B. (1964). *Mortality in Relation to Smoking: Ten Years' Observations of British Doctors*.

Ebrahim, Mohamed. (2023). *Image Contrast (TE, TR, Bandwidth) | LinkedIn*. MRI Image Quality and Procedures. https://www.linkedin.com/pulse/image-contrast-te-tr-bandwidth-mohamed-ebrahim/

Elster, A. D. (2021). *In phase/out of phase—Questions and Answers in MRI*. Questions and Answers in MRI. https://mriquestions.com/in-phaseout-of-phase.html

Elster, A. D. (2023). *Relaxation time, T1, T2*. Questions and Answers in MRI. http://mriquestions.com/why-is-t1--t2.html

Eriksen, R., Perez, I., Posma, J., Haid, M., Sharma, S., Prehn, C., Thomas, E., Koivula, R., Bizzotto, R., Mari, A., Giordano, G., Pavo, I., Schwenk, J., De Masi, F., Tsirigos, K., Brunak, S., Viñuela, A., Mahajan, A., McDonald, T., & Frost, G. (2020). Dietary metabolite profiling brings new insight into the relationship between nutrition and metabolic risk: An IMI DIRECT study. *EBioMedicine*, *58*. https://doi.org/10.1016/j.ebiom.2020.102932

European Radiology. (2023). Springer. https://www.springer.com/journal/330

Fadahunsi, K. P., O'Connor, S., Akinlua, J. T., Wark, P. A., Gallagher, J., Carroll, C., Car, J., Majeed, A., & O'Donoghue, J. (2021). Information Quality Frameworks for Digital Health Technologies: Systematic Review. *Journal of Medical Internet Research*, *23*(5). https://doi.org/10.2196/23479

Fitzpatrick, J. (2021). *Annotation Instructions—YouTube*. https://www.youtube.com/

Fitzpatrick, J. A., Basty, N., Cule, M., Liu, Y., Bell, J. D., Thomas, E. L., & Whitcher, B. (2020). Large-scale analysis of iliopsoas muscle volumes in the UK Biobank. *Scientific Reports*, *10*(1), 1–10. https://doi.org/10.1038/s41598-020-77351-0

Fitzpatrick, J. A., Chambers, E., Thomas, E. L., Frost, G., Taylor-Robinson, S. D., & Bell, J. D. (2013, May). Psoas Muscle Cross Sectional Area: A Novel Marker of Physical Fitness. *European Congress on Obesity*. https://www.researchgate.net/publication/280098360_Psoas_Muscle_Cross_Sectional_Area_A_Novel_Marker_of_Physical_Fitness

Fitzpatrick, J. A., Kim, J. U., Cobbold, J. F. L., McPhail, M. J. W., Crossey, M. M. E., Bak-Bol, A. A., Zaky, A., & Taylor-Robinson, S. D. (2015). Changes in liver volume in patients with chronic hepatitis C undergoing antiviral therapy. *Journal of Clinical and Experimental Hepatology*. https://doi.org/10.1016/j.jceh.2015.11.004

Fitzpatrick, J., Thomas, E., Durighel, G., O'Regan, D., Taylor-Robinson, S., & Bell, J. (2010). Measurement of Pancreatic Fat Using Multi Echo MRI. In J. Fitzpatrick, E. Thomas, G. Durighel, D. O'Regan, S. Taylor-Robinson, & J. Bell (Eds.), *11th International Congress on Obesity* (Vol. 94, Issue 1). https://doi.org/10.13140/RG.2.2.20860.85124

Fitzpatrick, J., Thomas, E. L., AL Saud, N. B., Durighel, G., O'Regan, D. P., Frost, G., Taylor-Robinson, S. D., & Bell, J. D. (2012). Comparing Multi Echo MRI and MRS to Measure Pancreatic Fat Introduction. *I.S.M.R.M. SCIENTIFIC WORKSHOP- Fat-Water Separation, Applications and Progress in MRI*. https://www.researchgate.net/publication/326113000_Comparing_Multi_Echo_MRI_and_MRS_to_Measure_Pancreatic_Fat_Introduction?_sg%5B0%5D=X-IVOaTx6S4rE0CgUVQk1B2NbuM3mNz4D55zd0pImJ4ToM1rcy2I0qm6pEjz_xJuXb_Onpvz4cu4ZCeKUE4gcffSqs-ArVgll0b_a-oA.2wjee0EvYQePEY1r8C_lYqo9KtOHqnTM9uFdqOIEDMkesfb2tF6k1gCLH5AB8dhBfEHxzuP-O_va-HQKKx7ywA

Fitzpatrick, J., Thomas, E. L., Durighel, G., O'regan, D. P., Taylor-robinson, S. D., & Bell, J. D. (2010). Measurement of pancreatic fat using multi-echo Mri. *Obesity Reviews*, *11*, 186–187.

Flaris, A. N., & Konstantinidis, T. (2021). Letter to the editor: Is total psoas muscle area at L3 truly representative of its volume? *Https://Doi-Org.Salford.Idm.Oclc.Org/10.1259/Bjr.20210137*, 20210137. https://doi.org/10.1259/BJR.20210137

Forsgren, M. F., & West, J. (2017). Rapid Body Composition Measurements Reveal Detailed Metabolic Changes in Large Scale Population Studies. *MAGNETOM Flash*, *69*(69). www.siemens.com/magnetom-world

Fox, C. S., Massaro, J. M., Hoffmann, U., Pou, K. M., Maurovich-Horvat, P., Liu, C.-Y., Vasan, R. S., Murabito, J. M., Meigs, J. B., Cupples, L. A., D'Agostino, R. B., & O'Donnell, C. J. (2007). Abdominal Visceral and Subcutaneous Adipose Tissue Compartments: Association With Metabolic Risk Factors in the Framingham Heart Study. *Circulation*, *116*(1), 39–48. https://doi.org/10.1161/CIRCULATIONAHA.106.675355

Gaborit, B., Abdesselam, I., Kober, F., Jacquier, A., Ronsin, O., Emungania, O., Lesavre, N., Alessi, M.-C., Martin, J. C., Bernard, M., & Dutour, A. (2015). Ectopic fat storage in the pancreas using 1 H-MRS: importance of diabetic status and modulation with bariatric surgery-induced weight loss. *International Journal of Obesity*, *39*, 480–487. https://doi.org/10.1038/ijo.2014.126

Geerts-Ossevoort, L., Elwin De Weerdt, ;, Duijndam, A., Gert Van Ijperen, ;, Peeters, H., Doneva, M., Nijenhuis, M., & Huang, A. (2018). *Compressed SENSE MR Clinical application Compressed SENSE Speed done right. Every time*.

Geraghty, E. M., Boone, J. M., McGahan, J. P., & Jain, K. (2004). Normal organ volume assessment from abdominal CT. *Abdominal Imaging*, *29*(4), 482–490. https://doi.org/10.1007/s00261-003-0139-2

German National Cohort (GNC) Consortium. (2014). The German National Cohort: Aims, study design and organization. *Eur J Epidemiol*, *29*, 371–382. https://doi.org/10.1007/s10654-014-9890-7

Glover, G. H., Mueller, B. A., Turner, J. A., Van Erp, T. G. M., Liu, T. T., Greve, D. N., Voyvodic, J. T., Rasmussen, J., Brown, G. G., Keator, D. B., Calhoun, V. D., Lee, H. J., Ford, J. M., Mathalon, D. H., Diaz, M., O'leary, D. S., Gadde, S., Preda, A., Lim, K. O., … Potkin, S. G. (2012). Function Biomedical Informatics Research Network Recommendations for Prospective Multicenter Functional MRI Studies. *Journal of Magnetic Resonance Imaging*, *36*, 39–54. https://doi.org/10.1002/jmri.23572

Good Clinical Practice. (2020). Health Research Authority. https://www.hra.nhs.uk/planning-and-improving-research/policies-standards-legislation/good-clinical-practice/

Guasch-Ferré, M., Liu, X., Malik, V. S., Sun, Q., Willett, W. C., Manson, J. E., Rexrode, K. M., Li, Y., Hu, F. B., & Bhupathiraju, S. N. (2017). *Nut Consumption and Risk of Cardiovascular Disease*.

Guenette, J. A., Jensen, D., & O'Donnell, D. E. (2010). Respiratory function and the obesity paradox. *Current Opinion in Clinical Nutrition and Metabolic Care*, *13*(6), 618–624. https://doi.org/10.1097/MCO.0b013e32833e3453

Gurari, D. (2015). *Combining crowd worker, algorithm, and expert efforts to find boundaries of objects in images* [Boston University]. https://www.proquest.com/openview/f9dc436f4c3d5f1658f39f574538ea47/1?pq-origsite=gscholar&cbl=18750&diss=y

Halvatsiotis, P., Kotanidou, A., Tzannis, K., Jahaj, E., Magira, E., Theodorakopoulou, M., Konstandopoulou, G., Gkeka, E., Pourzitaki, C., Kapravelos, N., Papoti, S., Sileli, M., Gogos, C., Velissaris, D., Markou, N., Stefanatou, E., Vlachogianni, G., Aimoniotou, E., Komnos, A., … Dimopoulos, G. (2020). Demographic and clinical features of critically ill patients with COVID-19 in Greece: The burden of diabetes and obesity.

Diabetes Research and Clinical Practice, *166*, 108331. https://doi.org/10.1016/j.diabres.2020.108331

Ham, C. L. G., Engels, J. M. L., van de Wiel, G. T., & Machielsen, A. (1997). Peripheral nerve stimulation during MRI: Effects of high gradient amplitudes and switching rates. *Journal of Magnetic Resonance Imaging*, *7*(5), 933–937. https://doi.org/10.1002/jmri.1880070524

Hamer, M., Gale, C. R., Kivimäki, M., & David Batty, G. (2020). Overweight, obesity, and risk of hospitalization for COVID-19: A community-based cohort study of adults in the United Kingdom. *PNAS*, *117*(35), 21011–21013. https://doi.org/10.1073/pnas.2011086117

Hanson, P., Magnusson, S. P., Sorensen, H., & Simonsen, E. B. (1999). Anatomical differences in the psoas muscles in young black and white men. *Journal of Anatomy*, *194 (Pt 2*, 303–307. http://www.pubmedcentral.nih.gov/articlerender.fcgi?artid=1467925&tool=pmcentrez&rendertype=abstract

Hawkins, R. B., Mehaffey, J. H., Charles, E. J., Kern, J. A., Lim, D. S., Teman, N. R., & Ailawadi, G. (2018). Psoas Muscle Size Predicts Risk-Adjusted Outcomes After Surgical Aortic Valve Replacement. *Annals of Thoracic Surgery*, *106*(1), 39–45. https://doi.org/10.1016/j.athoracsur.2018.02.010

Heinrichs, U., Utting, J. F., Frauenrath, T., Hezel, F., Krombach, G. A., Hodenius, M. A. J., Kozerke, S., & Niendorf, T. (2009). *Myocardial T * 2 Mapping Free of Distortion Using Susceptibility-Weighted Fast Spin-Echo Imaging: A Feasibility Study at 1.5 T and 3.0 T*. https://doi.org/10.1002/mrm.22054

Herate, C., Brochard, P., De Vathaire, F., Ricoul, M., Martins, B., Laurier, L., Deverre, J.-R., Thirion, B., Hertz-Pannier, L., & Sabatier, L. (2022). The effects of repeated brain MRI on chromosomal damage. *European Radiology Experimental*, *6*(1), 12. https://doi.org/10.1186/s41747-022-00264-2

Heymsfield, S., Hu, H., Wang, Z., Shen, W., & Jin, Y. (2014). Measurement of Total Adiposity, Regional Fat Depots, and Ectopic Fat. In *Handbook of Obesity* (pp. 19–36). CRC Press. https://doi.org/10.1201/b16473-4

Hezel, F., Thalhammer, C., Waiczies, S., Schulz-Menger, J., & Niendorf, T. (2012). High Spatial Resolution and Temporally Resolved T 2 * Mapping of Normal Human Myocardium at 7.0 Tesla: An Ultrahigh Field Magnetic Resonance Feasibility Study. *PLoS ONE*, *7*(12), 52324. https://doi.org/10.1371/journal.pone.0052324

Hines, C. D. G., Yu, H., Shimakawa, A., Mckenzie, C. A., Brittain, J. H., & Reeder, S. B. (2009). T 1 Independent, T 2 * Corrected MRI With Accurate Spectral Modeling for Quantification of Fat: Validation in a Fat-Water-SPIO Phantom. *J. Magn. Reson. Imaging*, *30*, 1215–1222. https://doi.org/10.1002/jmri.21957

Holmes, K., & Griffiths, M. (2016). *Image quality | Radiology Key*. Radiology Key. https://radiologykey.com/image-quality/

Hornak, J. P. (2020). *The Basics of MRI*. The Basic of MRI. https://www.cis.rit.edu/htbooks/mri/inside.htm

Hosny, A., Parmar, C., Quackenbush, J., Schwartz, L. H., & Aerts, H. J. W. L. (2018). Artificial intelligence in radiology. *Nature Reviews Cancer*, *18*(8), 500–510. https://doi.org/10.1038/s41568-018-0016-5

Hu, H. H., Chen, J., & Shen, W. (2016). Segmentation and quantification of adipose tissue by magnetic resonance imaging. *Magma (New York, N.Y.)*, *29*(2), 259–276. https://doi.org/10.1007/s10334-015-0498-z

Hu, H. H., Kim, H.-W., Nayak, K. S., & Goran, M. I. (2010). Comparison of Fat-Water MRI and Single-voxel MRS in the Assessment of Hepatic and Pancreatic Fat Fractions in Humans. *Obesity*, *18*, 841–847. https://doi.org/10.1038/oby.2009.352

Hu, H., Michael, I., & Krishna, S. (2011). Assessment of Abdominal Adiposity and Organ Fat with Magnetic Resonance Imaging. *Role of the Adipocyte in Development of Type 2 Diabetes*. https://doi.org/10.5772/20602

Huang, S. Y., Seethamraju, R. T., Patel, P., Hahn, P. F., Kirsch, J. E., & Guimaraes, A. R. (2015). Body MR imaging: Artifacts, k-space, and solutions. *Radiographics*, *35*(5), 1439–1460. https://doi.org/10.1148/rg.2015140289

ICH Official web site: ICH. (2023). https://www.ich.org/

IEC 60601-2-33:2022 Medical electrical equipment- Part 2-33 (Version 4). (2022). https://webstore.iec.ch/publication/67211

Ionizing radiation, health effects and protective measures. (2016). World Health Organization. https://www.who.int/news-room/fact-sheets/detail/ionizing-radiation-health-effects-and-protective-measures

Jones, K. I., Doleman, B., Scott, S., Lund, J. N., & Williams, J. P. (2015). Simple psoas cross-sectional area measurement is a quick and easy method to assess sarcopenia and predicts major surgical complications. *Colorectal Disease*, *17*(1), O20–O26.

Jones, R. L., & Nzekwu, M.-M. U. (2006). The Effects of Body Mass Index on Lung Volumes*. *Chest*, *130*(3), 827–833. https://www.proquest.com/docview/200480005/abstract/1D4B2BC1ED474916PQ/1

Jorgensen, M. J., Marras, W. S., & Gupta, P. (2003). Cross-sectional area of the lumbar back muscles as a function of torso flexion. *Clinical Biomechanics (Bristol, Avon)*, *18*(4), 280–286. https://doi.org/10.1016/s0268-0033(03)00027-5

Juchem, C, Green, D, & de Graaf, R.A. (2013). Multi-coil magnetic field modeling. *Journal of Magnetic Resonance*, *236*, 95–104. https://doi.org/10.1016/j.jmr.2013.08.015

Kersten, S. (2023). The impact of fasting on adipose tissue metabolism. *Biochimica Et Biophysica Acta. Molecular and Cell Biology of Lipids*, *1868*(3), 159262. https://doi.org/10.1016/j.bbalip.2022.159262

Khalili, S., Moradi, O., Kharazmi, A. B., Raoufi, M., Sistanizad, M., & Shariat, M. (2021). Comparison of Mortality Rate and Severity of Pulmonary Involvement in Coronavirus Disease-2019 Adult Patients With and Without Type 2 Diabetes: A Cohort Study. *Canadian Journal of Diabetes*, *45*(6), 524–530. https://doi.org/10.1016/j.jcjd.2020.10.014

Khodarahmi, I., & Fritz, J. (2021). The Value of 3 Tesla Field Strength for Musculoskeletal Magnetic Resonance Imaging. *Investigative Radiology*, *56*(11), 749–763. https://doi.org/10.1097/RLI.0000000000000801

Kim, J. Y., Chae, S. U., Kim, G. D., & Cha, M. S. (2013). Changes of paraspinal muscles in postmenopausal osteoporotic spinal compression fractures: Magnetic resonance imaging study. *Journal of Bone Metabolism*, *20*(2), 75–81. https://doi.org/10.11005/jbm.2013.20.2.75

Koivula, R. W., Atabaki-Pasdar, N., Giordano, G. N., White, T., Adamski, J., Bell, J. D., Beulens, J., Brage, S., Brunak, S., Mari, A., Mcdonald, T. J., Pedersen, O., Rutters, F., Schwenk, J. M., Teare, H. J. A., & Thomas, E. L. (2020). The role of physical activity in metabolic homeostasis before and after the onset of type 2 diabetes: An IMI

DIRECT study. *Diabetologia*, *63*, 744–756. https://doi.org/10.1007/s00125-019-05083-6

Koivula, R. W., Forgie, I. M., Kurbasic, A., Viñuela, A., Heggie, A., Giordano, G. N., Hansen, T. H., Hudson, M., Koopman, A. D. M., Rutters, F., Siloaho, M., Allin, K. H., Brage, S., Brorsson, C. A., Dawed, A. Y., De Masi, F., Groves, C. J., Kokkola, T., Mahajan, A., … Franks, P. W. (2019). Discovery of biomarkers for glycaemic deterioration before and after the onset of type 2 diabetes: Descriptive characteristics of the epidemiological studies within the IMI DIRECT Consortium. *Diabetologia*, *62*(9), 1601–1615. https://doi.org/10.1007/S00125-019-4906-1

Koivula, R. W., Heggie, A., Barnett, A., Cederberg, H., Hansen, T. H., Koopman, A. D., Ridderstråle, M., Rutters, F., Vestergaard, H., Gupta, R., Herrgård, S., Heymans, M. W., Perry, M. H., Rauh, S., Siloaho, M., Teare, H. J. a, Thorand, B., Bell, J., Brunak, S., … Franks, P. W. (2014). Discovery of biomarkers for glycaemic deterioration before and after the onset of type 2 diabetes: Rationale and design of the epidemiological studies within the IMI DIRECT Consortium. *Diabetologia*. https://doi.org/10.1007/s00125-014-3216-x

Koller, C. J., Eatough, J. P., Mountford, P. J., & Frain, G. (2006). A survey of MRI quality assurance programmes. *The British Journal of Radiology*, *79*(943), 592–596. https://doi.org/10.1259/bjr/67655734

Langner, T., Gustafsson, F. K., Avelin, B., Strand, R., Ahlström, H., & Kullberg, J. (2021). Uncertainty-aware body composition analysis with deep regression ensembles on UK Biobank MRI. *Computerized Medical Imaging and Graphics*, *93*, 101994. https://doi.org/10.1016/J.COMPMEDIMAG.2021.101994

Langner, T., Strand, R., Ahlström, H., & Kullberg, J. (2020). Large-scale biometry with interpretable neural network regression on UK Biobank body MRI. *Scientific Reports*, *10*(1). https://doi.org/10.1038/S41598-020-74633-5

Lee, J. S.-J., He, K., Harbaugh, C. M., Schaubel, D. E., Sonnenday, C. J., Wang, S. C., Englesbe, M. J., & Eliason, J. L. (2011). Frailty, core muscle size, and mortality in patients undergoing open abdominal aortic aneurysm repair. *Journal of Vascular Surgery*, *53*(4), 912–917. https://doi.org/10.1016/j.jvs.2010.10.111

Lee, J. W. K., & Shannon, S. P. (2007). 3 Tesla Magnetic Resonance Imaging (MRI)—Is it Ready for Prime Time Clinical Applications? *Canadian Journal of Medical Radiation Technology*, *38*(4), 37–50. https://doi.org/10.1016/S0820-5930(09)60258-9

Lee, M. H., Neeland, I. J., de Albuquerque Rocha, N., Hughes, C., Malloy, C. R., & Jin, E. S. (2022). A randomized clinical trial evaluating the effect of empagliflozin on triglycerides in obese adults: Role of visceral fat. *Metabolism Open*, *13*, 100161. https://doi.org/10.1016/j.metop.2021.100161

Lim, S., & Meigs, J. B. (2013). Ectopic fat and cardiometabolic and vascular risk. *International Journal of Cardiology*, *169*(3), 166–176. https://doi.org/10.1016/j.ijcard.2013.08.077

Linge, J., Borga, M., West, J., Tuthill, T., Miller, M. R., Dumitriu, A., Thomas, E. L., Romu, T., Tunón, P., Bell, J. D., & Dahlqvist Leinhard, O. (2018). Body Composition Profiling in the UK Biobank Imaging Study. *Obesity*, *26*(11), 1785–1795. https://doi.org/10.1002/oby.22210

Linge, J., Ekstedt, M., & Dahlqvist Leinhard, O. (2020). Adverse muscle composition is linked to poor functional performance and metabolic comorbidities in NAFLD. *JHEP*

Reports : Innovation in Hepatology, *3*(1). https://doi.org/10.1016/J.JHEPR.2020.100197

Linge, J., Heymsfield, S. B., & Leinhard, O. D. (2020). On the definition of sarcopenia in the presence of aging and obesity—Initial results from UK Biobank. *Journals of Gerontology - Series A Biological Sciences and Medical Sciences*, *75*(7), 1309–1316. https://doi.org/10.1093/GERONA/GLZ229

Lingvay, I., Esser, V., Legendre, J. L., Price, A. L., Wertz, K. M., Adams-Huet, B., Zhang, S., Unger, R. H., & Szczepaniak, L. S. (2009). Noninvasive quantification of pancreatic fat in humans. *Journal of Clinical Endocrinology and Metabolism*, *94*(10), 4070–4076. https://doi.org/10.1210/jc.2009-0584

Littlejohns, T. J., Holliday, J., Gibson, L. M., Garratt, S., Oesingmann, N., Alfaro-Almagro, F., Bell, J. D., Boultwood, C., Collins, R., Conroy, M. C., Crabtree, N., Doherty, N., Frangi, A. F., Harvey, N. C., Leeson, P., Miller, K. L., Neubauer, S., Petersen, S. E., Sellors, J., … Allen, N. E. (2020). The UK Biobank imaging enhancement of 100,000 participants: Rationale, data collection, management and future directions. *Nature Communications*, *11*(1), 1–12. https://doi.org/10.1038/s41467-020-15948-9

Littleton, S. W. (2012). Impact of obesity on respiratory function. *Respirology*, *17*(1), 43–49. https://doi.org/10.1111/j.1440-1843.2011.02096.x

Liu, Y., Basty, N., Whitcher, B., Bell, J. D., Sorokin, E. P., van Bruggen, N., Thomas, E. L., & Cule, M. (2021). Genetic architecture of 11 organ traits derived from abdominal MRI using deep learning. *ELife*, *10*. https://doi.org/10.7554/eLife.65554

Magnetic resonance imaging equipment in clinical use: Safety guidelines (p. 86). (2022). Medicines and Healthcare Products Regulatory Authority.

https://www.gov.uk/government/publications/safety-guidelines-for-magnetic-resonance-imaging-equipment-in-clinical-use

Mahmood, S. S., Levy, D., Vasan, R. S., & Wang, T. J. (2014). The Framingham Heart Study and the Epidemiology of Cardiovascular Diseases: A Historical Perspective. *Lancet*, *383*(9921), 999. https://doi.org/10.1016/S0140-6736(13)61752-3

Mäkinen, V.-P., & Ala-Korpela, M. (2016). Metabolomics of aging requires large-scale longitudinal studies with replication. *Proceedings of the National Academy of Sciences*, *113*(25), E3470–E3470. https://doi.org/10.1073/pnas.1607062113

Manka, R., Paetsch, I., Schnackenburg, B., Gebker, R., Fleck, E., & Jahnke, C. (2010). *BOLD cardiovascular magnetic resonance at 3.0 tesla in myocardial ischemia | Enhanced Reader*. Journal of Cardiovascular Magnetic Resonance.

Mann, C. J. (2003). Observational research methods. Research design II: cohort, cross sectional, and case-control studies. *Emergency Medicine Journal : EMJ*, *20*(1), 54–60. http://www.pubmedcentral.nih.gov/articlerender.fcgi?artid=1726024&tool=pmcentrez&rendertype=abstract

Manolio, T. A., & Collins, R. (2010). Enhancing the feasibility of large cohort studies. *JAMA - Journal of the American Medical Association*, *304*(20), 2290–2291. https://doi.org/10.1001/jama.2010.1686

Martins, J. C., Aguiar, L. T., Nadeau, S., Scianni, A. A., Fuscaldi Teixeira-Salmela, L., & Coelho De Morais Faria, C. D. (2017). Measurement properties of self-report physical activity assessment tools in stroke: A protocol for a systematic review. *British Medical Journal*, *7*. https://doi.org/10.1136/bmjopen-2016-012655

Matter, W., Juchem, C., Terekhov, M., & Schreiber, L. (2016). Multi-Coil B0 shimming of the Human Heart: A Theoretical Assessment. *International Society of Magnetic*

Resonance in Medicine. https://cds.ismrm.org/protected/16MProceedings/PDFfiles/1151.html

Matthews, R. (2022). *Who really invented the MRI machine? - BBC Science Focus Magazine*. Science Focus. https://www.sciencefocus.com/science/who-really-invented-the-mri-machine/

Mccormick, J. S. (1981). James Mackenzie and coronary heart disease. *Journal of the Royal College of General Practitioners*, *31*, 26–30.

McRobbie, D. W., Moore, E. A., Graves, M. J., & Prince, M. R. (2006). *MRI From Picture to Proton*. Cambridge University Press.

McVeigh, E. R., Bronskill, M. J., & Henkelman, R. M. (1988). Optimization of MR Protocols: A Statistical Decision Analysis Approach. *Magnetic Resonance in Medicine : Official Journal of the Society of Magnetic Resonance in Medicine / Society of Magnetic Resonance in Medicine*, *6*(3), 314. https://doi.org/10.1002/MRM.1910060310

Medecines and Healthcare products Regulatory Agency. (2022). *Magnetic resonance imaging equipment in clinical use: Safety guidelines* (p. 86). https://www.gov.uk/government/publications/safety-guidelines-for-magnetic-resonance-imaging-equipment-in-clinical-use

Meloni, A., Hezel, F., Positano, V., Keilberg, P., Pepe, A., Lombardi, M., & Niendorf, T. (2014). Detailing magnetic field strength dependence and segmental artifact distribution of myocardial effective transverse relaxation rate at 1.5, 3.0, and 7.0 T. *Magnetic Resonance in Medicine*, *71*(6), 2224–2230. https://doi.org/10.1002/MRM.24856

Meloni, A., Positano, V., Keilberg, P., De Marchi, D., Pepe, P., Zuccarelli, A., Campisi, S., Romeo, M. A., Casini, T., Bitti, P. P., Gerardi, C., Lai, M. E., Piraino, B., Giuffrida, G., Secchi, G., Midiri, M., Lombardi, M., & Pepe, A. (2012). Feasibility, Reproducibility, and Reliability for the T2* Iron Evaluation at 3 T in Comparison With 1.5 T. *Magnetic Resonance in Imaging*, *68*, 543–551. https://doi.org/10.1002/mrm.23236

MHRA. (2007). *Device Bulletin-* (Vol. 2007, Issue December). http://www.mhra.gov.uk/Publications/Safetyguidance/DeviceBulletins/CON2033018

MHRA. (2021). *Safety Guidelines for Magnetic Resonance Imaging Equipment in Clinical Use* (v4.3). Medicines and Healthcare products Regulatory Agency.

M.H.R.A. (2021). *Safety Guidelines for Magnetic Resonance Imaging Equipment in Clinical Use*.

Mohamed Y. Abdallah, Y., & Alqahtani, T. (2019). Research in Medical Imaging Using Image Processing Techniques. In *Medical Imaging—Principles and Applications [Working Title]*. IntechOpen. https://doi.org/10.5772/intechopen.84360

Molloy, J. C. (2011). The Open Knowledge Foundation: Open Data Means Better Science. *PLoS Biology*, *9*(12). https://doi.org/10.1371/journal.pbio.1001195

Monnereau, C., Santos, S., van der Lugt, A., Jaddoe, V. W. V., & Felix, J. F. (2018). Associations of adult genetic risk scores for adiposity with childhood abdominal, liver and pericardial fat assessed by magnetic resonance imaging. *International Journal of Obesity (2005)*, *42*(4), 897–904. https://doi.org/10.1038/ijo.2017.302

Morana, G., Faccinetto, A., Dorigo, A., Ciet, P., Venturini, S., & Fusaro, M. (2017). Imaging of the Pancreas: Technique and Clinical Applications. *MAGNETOM Flash*, *69*(3).

Moratal, D., Vallés-Luch, A., Martí-Bonmatí, L., & Brummer, M. (2008). k-Space tutorial: An MRI educational tool for a better understanding of k-space. *Biomedical Imaging and Intervention Journal*, *4*(1), e15. https://doi.org/10.2349/biij.4.1.e15

Mosher, T. J. (2006). Musculoskeletal imaging at 3T: current techniques and future applications. *Magnetic Resonance Imaging Clinics of North America*, *14*(1), 63–76. https://doi.org/10.1016/J.MRIC.2005.12.002

MRC Population Health Sciences Group (PHSG). (2014). *Maximising the value of UK population cohorts MRC Strategic Review of the Largest UK Population Cohort Studies*.

Munn, Z., & Jordan, Z. (2011). The patient experience of high technology medical imaging: A systematic review of the qualitative evidence. *Radiography*, *17*(4), 323–331. https://doi.org/10.1016/j.radi.2011.06.004

Murphy, A., & Ballinger, J. (2020). Moiré fringes. *Radiopaedia.Org*. https://doi.org/10.53347/RID-22003

Nakarada-Kordic, I., Reay, S., Bennett, G., Kruse, J., Lydon, A.-M., & Sim, J. (2020). Can virtual reality simulation prepare patients for an MRI experience? *Radiography*, *26*(3), 205–213. https://doi.org/10.1016/j.radi.2019.11.004

National Institutes of Health. (2023). *ImageJ*. http://imagej.nih.gov/ij/

Neeland, I. J., Marso, S. P., Ayers, C. R., Lewis, B., Oslica, R., Francis, W., Rodder, S., Pandey, A., & Joshi, P. H. (2021). Effects of liraglutide on visceral and ectopic fat in adults with overweight and obesity at high cardiovascular risk: A randomised, double-blind, placebo-controlled, clinical trial. *The Lancet Diabetes and Endocrinology*, *9*(9), 595–605. https://doi.org/10.1016/S2213-8587(21)00179-0

Newman, D., Kelly-Morland, C., Leinhard, O. D., Kasmai, B., Greenwood, R., Malcolm, P. N., Romu, T., Borga, M., & Toms, A. P. (2016). Test–retest reliability of rapid whole body and compartmental fat volume quantification on a widebore 3T MR system in normal-weight, overweight, and obese subjects. *Journal of Magnetic Resonance Imaging*, *44*(6), 1464–1473. https://doi.org/10.1002/JMRI.25326

Niendorf, T., Paul, K., Oezerdem, C., Graessl, A., Klix, S., Huelnhagen, T., Hezel, F., Rieger, J., Waiczies, H., Frahm, J., Nagel, A. M., Oberacker, E., & Winter, L. (2016). W(h)ither human cardiac and body magnetic resonance at ultrahigh fields? Technical advances, practical considerations, applications, and clinical opportunities. *NMR in Biomedicine*, *29*(9), 1173–1197. https://doi.org/10.1002/nbm.3268

OED Online. (2022). *Oxford English Dictionary*. OED Online. https://www-oed-com.salford.idm.oclc.org/view/Entry/163432?rskey=vaV1tu&result=1#eid

O'Regan, D. P., Callaghan, M. F., Fitzpatrick, J., Naoumova, R. P., Hajnal, J. V., & Schmitz, S. A. (2008). Cardiac T2* and lipid measurement at 3.0 T-initial experience. *European Radiology*, *18*(4), 800–805.

O'Regan, D. P., Callaghan, M. F., Schmitz, S. A., Naoumova, R. P., Fitzpatrick, J., Allsop, J., & Hajnal, J. V. (2006). Quantification of Myocardial Lipid using a Breath Hold Multiecho Technique at 3.0 Tesla. *ISMRM*. https://archive.ismrm.org/2006/1194.html

O'Regan, D. P., Callaghan, M. F., Wylezinska-Arridge, M., Fitzpatrick, J., Naoumova, R. P., Hajnal, J. V., & Schmitz, S. A. (2007). Quantifying hepatic lipid content and T2* decay using a single breath-hold multiecho sequence at 3 tesla. *Proc. Intl. Soc. Mag. Reson. Med*, *15*, 2704.

O'Regan, D. P., Callaghan, M. F., Wylezinska-Arridge, M., Fitzpatrick, J., Naoumova, R. P., Hajnal, J. V., & Schmitz, S. A. (2008). Liver fat content and T2*: Simultaneous

measurement by using breath-hold multiecho MR imaging at 3.0 T - Feasibility. *Radiology*, *247*(2), 550–557. https://doi.org/10.1148/radiol.2472070880

Ortiz, V. E., Vidal-Melo, M. F., & Walsh, J. L. (2015). Strategies for managing oxygenation in obese patients undergoing laparoscopic surgery. *Surgery for Obesity and Related Diseases : Official Journal of the American Society for Bariatric Surgery*, *11*(3), 721–728. https://doi.org/10.1016/j.soard.2014.11.021

Otaki, T., Hasegawa, M., Yuzuriha, S., Hanada, I., Nagao, K., Umemoto, T., Shimizu, Y., Kawakami, M., Nakajima, N., Kim, H., Nitta, M., Hanai, K., Kawamura, Y., Shoji, S., & Miyajima, A. (2020). Clinical impact of psoas muscle volume on the development of inguinal hernia after robot-assisted radical prostatectomy. *Surgical Endoscopy*, 1–9. https://doi.org/10.1007/s00464-020-07770-7

Pell, J., Valentine, J., & Inskip, H. (2014). One in 30 people in the UK take part in cohort studies. *The Lancet*, *383*, 1015–1016. http://www.

Pérez-Cruz, E., Castañón-González, J. A., Ortiz-Gutiérrez, S., Garduño-López, J., & Luna-Camacho, Y. (2021). Impact of obesity and diabetes mellitus in critically ill patients with SARS-CoV-2. *Obesity Research & Clinical Practice*, *15*(4), 402–405. https://doi.org/10.1016/j.orcp.2021.05.001

Peters, U., Dixon, A., & Forno, E. (2018). Obesity and Asthma. *The Journal of Allergy and Clinical Immunology*, *141*(4), 1169–1179. https://doi.org/10.1016/j.jaci.2018.02.004

Peters, U., Suratt, B. T., Bates, J. H. T., & Dixon, A. E. (2018). Beyond BMI: Obesity and Lung Disease. *Chest*, *153*(3), 702–709. https://doi.org/10.1016/j.chest.2017.07.010

Petridou, E., Kibiro, M., Gladwell, C., Malcolm, P., Toms, A., Juette, A., Borga, M., Dahlqvist Leinhard, O., Romu, T., Kasmai, B., & Denton, E. (2017). Breast fat volume measurement using wide-bore 3 T MRI: Comparison of traditional

mammographic density evaluation with MRI density measurements using automatic segmentation. *Clinical Radiology*, *72*. https://doi.org/10.1016/j.crad.2017.02.014

Ponti, F., Santoro, A., Mercatelli, D., Gasperini, C., Conte, M., Martucci, M., Sangiorgi, L., Franceschi, C., & Bazzocchi, A. (2019). Aging and Imaging Assessment of Body Composition: From Fat to Facts. *Frontiers in Endocrinology*, *10*, 861. https://doi.org/10.3389/fendo.2019.00861

Pruessmann, K. P., Weiger, M., Scheidegger, M. B., & Boesiger, P. (1999). SENSE: Sensitivity Encoding for Fast MRI. *Magnetic Resonance in Medicine*, 952–962.

Publications to date. (2023). DIRECT. https://directdiabetes.org/publications-to-date/

Quality Control and Artefacts in Magnetic Resonance Imaging. (2017). Institute of Physics and Engineering in Medicine.

Raeisi, T., Mozaffari, H., Sepehri, N., Darand, M., Razi, B., Garousi, N., Alizadeh, M., & Alizadeh, S. (2022). The negative impact of obesity on the occurrence and prognosis of the 2019 novel coronavirus (COVID-19) disease: A systematic review and meta-analysis. *Eating and Weight Disorders*, *27*(3), 893–911. https://doi.org/10.1007/s40519-021-01269-3

Ranson, C. A., Burnett, A. F., Kerslake, R., Batt, M. E., O'sullivan, P. B., Ranson, C. A., Kerslake, R., Batt, M. E., Burnett, A. F., O'sullivan, A. P. B., & Cricket Board, W. (2006). An investigation into the use of MR imaging to determine the functional cross sectional area of lumbar paraspinal muscles. *European Spine Journal*, *15*, 764–773. https://doi.org/10.1007/s00586-005-0909-3

Redwood-Brown, A., Ralston, G. W., & Wilson, J. (2021). Incidence, severity and perceived susceptibility of COVID-19 in the UK CrossFit population. *BMC Sports Science, Medicine & Rehabilitation*, *13*(1), 106. https://doi.org/10.1186/s13102-021-00318-9

Reeder, S. B., Bice, E. K., Yu, H., Hernando, D., & Pineda, A. R. (2012). On the Performance of T 2 * Correction Methods for Quantification of Hepatic Fat Content. *Magnetic Resonance in Medecine*, *67*, 389–404. https://doi.org/10.1002/mrm.23016

Reeder, S. B., Cruite, I., Hamilton, G., & Sirlin, C. B. (2011a). Quantitative assessment of liver fat with magnetic resonance imaging and spectroscopy. *Journal of Magnetic Resonance Imaging : JMRI*, *34*(4), 729–749. https://doi.org/10.1002/jmri.22580

Reeder, S. B., Cruite, I., Hamilton, G., & Sirlin, C. B. (2011b). Quantitative assessment of liver fat with magnetic resonance imaging and spectroscopy. *Journal of Magnetic Resonance Imaging*, *34*(4). https://doi.org/10.1002/JMRI.22775

Reeder, S. B., & Sirlin, C. B. (2010). Quantification of liver fat with magnetic resonance imaging. *Magnetic Resonance Imaging Clinics of North America*, *18*(3), 337–357. https://doi.org/10.1016/J.MRIC.2010.08.013

Reid, K., & Edwards, H. (2011). Evaluating the role of the diagnostic research radiographer. *Radiography*, *17*(3), 207–211. https://doi.org/10.1016/j.radi.2011.02.004

Reistenbach Goltz, F., Thackray, A., Varela Mato, V., King, J., Dorling, J., Dowejko, M., Mastana, S., Thompson, J., Atkinson, G., & Stensel, D. (2019). Exploration of associations between the FTO rs9939609 genotype, fasting and postprandial appetite-related hormones and perceived appetite in healthy men and women. *Appetite*, *142*, 104368. https://doi.org/10.1016/j.appet.2019.104368

Rosse, C., Gaddum-Rosse, P., & Hollinshead, W. H. (1997). *Hollinshead's Textbook of Anatomy*. Lippincott-Raven Publishers.

Ruppel, G. L. (2012). What is the clinical value of lung volumes? *Respiratory Care*, *57*(1), 26–38. https://doi.org/10.4187/respcare.01374

Sakai, N. (2021). *Quantitative Magnetic Resonance Imaging Techniques for the Measurement of Organ Fat and Body Composition—Validation and Initial Clinical Utility*.

Saloner, D., Liu, J., & Haraldsson, H. (2015). MR physics in practice: How to optimize acquisition quality and time for cardiac MRI. *Magnetic Resonance Imaging Clinics of North America*, *23*(1), 1–6. https://doi.org/10.1016/j.mric.2014.08.004

Samuel, A. L. (2000). Some studies in machine learning using the game of checkers. *IBM Journal of Research and Development*, *44*(1/2), 206–226. https://www.proquest.com/docview/220681210/abstract/4129CEBE9FD4F66PQ/1

Sánchez-Peralta, L. F., Picón, A., Antequera-Barroso, J. A., Ortega-Morán, J. F., Sánchez-Margallo, F. M., & Pagador, J. B. (2020). Eigenloss: Combined PCA-based loss function for polyp segmentation. *Mathematics*, *8*(8). https://doi.org/10.3390/MATH8081316

Scheek, D., Rezazade Mehrizi, Mohammad. H., & Ranschaert, E. (2021). Radiologists in the loop: The roles of radiologists in the development of AI applications. *European Radiology*, 1–9. https://doi.org/10.1007/s00330-021-07879-w

Scientific Reports. (2023, March 18). Nature. https://www.nature.com/srep/

SELECT COMMITTEE ON ARTIFICIAL INTELLIGENCE. COLLATED WRITTEN EVIDENCE VOLUME. (2017). House of Lords.

Shellock, F. G. (2022). *MRI Safety Home*. The List. https://www.mrisafety.com/

Shellock, F. G., & Crues, J. V. (2022). *MRI Bioeffects, Safety, and Patient Management: Second Edition* (2nd ed.). Biomedical Research Publishing Group.

Shen, W., Punyanitya, M., Wang, Z., Gallagher, D., St-Onge, M.-P., Albu, J., Heymsfield, S. B., Heshka, S., Gal-lagher, D., & Heyms-field, S. B. (2004). Innovative Methodology

Total body skeletal muscle and adipose tissue volumes: Estimation from a single abdominal cross-sectional image. *J Appl Physiol*, *97*, 2333–2338. https://doi.org/10.1152/japplphysiol.00744.2004.-A

Sheth, K. N., Mazurek, M. H., Yuen, M. M., Cahn, B. A., Shah, J. T., Ward, A., Kim, J. A., Gilmore, E. J., Falcone, G. J., Petersen, N., Gobeske, K. T., Kaddouh, F., Hwang, D. Y., Schindler, J., Sansing, L., Matouk, C., Rothberg, J., Sze, G., Siner, J., … Kimberly, W. T. (2021). Assessment of Brain Injury Using Portable, Low-Field Magnetic Resonance Imaging at the Bedside of Critically Ill Patients. *JAMA Neurol*, *78*(1), 41–47. https://doi.org/10.1001/jamaneurol.2020.3263

Shi, X., & Han, R. (2022). FUNCTIONAL EXERCISE ON PATIENTS' REHABILITATION WITH PSOAS MUSCLE SPORTS INJURIES. *Revista Brasileira de Medicina Do Esporte*, *28*(6), 702–704. https://doi.org/10.1590/1517-8692202228062022_0019

Shojaee-Moradie, F., Cuthberson, D. J., Barrett, M, M., Jackson, N. C., Herring, R., Thomas, E. L., Bell, J., Kemp, G. J., Wright, J., & Umpleby. (2016). Exercise Training Reduces Liver Fat and Increases Rates of VLDL Clearance But Not VLDL Production in NAFLD. *The Journal of Clinical Endocrinology & Metabolism*, *101*(11), 4219–4228. https://doi-org.salford.idm.oclc.org/10.1210/jc.2016-2353

Sijens, P. E., Edens, M. A., Jl Bakker, S., Stolk, R. P., & Maconi, G. (2010). MRI-determined fat content of human liver, pancreas and kidney. *World J Gastroenterol*, *16*(16). https://doi.org/10.3748/wjg.v16.i16.1993

Silva, P. L., Pelosi, P., & Rocco, P. R. M. (2012). Mechanical ventilation in obese patients. *MINERVA ANESTESIOLOGICA*, *78*(10).

Sinnatamby, C. S. (2011). *Last's Anatomy E-Book: Regional and Applied*. Elsevier Health Sciences. http://ebookcentral.proquest.com/lib/salford/detail.action?docID=1722067

Sirlin, C. B., & Reeder, S. B. (2010). Magnetic resonance imaging quantification of liver iron. *Magnetic Resonance Imaging Clinics of North America*, *18*(3), 359–381. https://doi.org/10.1016/J.MRIC.2010.08.014

Smith, G. D., Lawlor, D. A., Harbord, R., Timpson, N., Day, I., & Ebrahim, S. (2007). *Clustered Environments and Randomized Genes: A Fundamental Distinction between Conventional and Genetic Epidemiology*. *4*. https://doi.org/10.1371/journal

Spelta, F., Fratta Pasini, A. M., Cazzoletti, L., & Ferrari, M. (2018). Body weight and mortality in COPD: Focus on the obesity paradox. *Eating and Weight Disorders: EWD*, *23*(1), 15–22. https://doi.org/10.1007/s40519-017-0456-z

Stewart, S., Stanton, W., Wilson, S., & Hides, J. (2010). Consistency in size and asymmetry of the psoas major muscle among elite footballers. *British Journal of Sports Medicine*, *44*(16), 1173–1177. https://doi.org/10.1136/bjsm.2009.058909

Suzuki, A., Yamaguchi, R., Kim, L., Kawahara, T., & Ishii-Takahashi, A. (2022). Effectiveness of mock scanners and preparation programs for successful magnetic resonance imaging: A systematic review and meta-analysis. *Pediatric Radiology*. https://doi.org/10.1007/s00247-022-05394-8

Tarroni, G., Bai, W., Oktay, O., Schuh, A., Suzuki, H., Glocker, B., Matthews, P. M., & Rueckert, D. (2020). Large-scale Quality Control of Cardiac Imaging in Population Studies: Application to UK Biobank. *Scientific Reports*, *10*(1). https://doi.org/10.1038/s41598-020-58212-2

Tejani, S., McCoy, C., Ayers, C. R., Powell-Wiley, T. M., Després, J. P., Linge, J., Leinhard, O. D., Petersson, M., Borga, M., & Neeland, I. J. (2022). Cardiometabolic Health

Outcomes Associated With Discordant Visceral and Liver Fat Phenotypes: Insights From the Dallas Heart Study and UK Biobank. *Mayo Clinic Proceedings*, *97*(2), 225–237. https://doi.org/10.1016/j.mayocp.2021.08.021

Thanaj, M., Basty, N., Cule, M., Sorokin, E. P., Whitcher, B., Bell, J. D., & Thomas, L. (2022). Liver Shape is Associated with Disease and Anthropometric Traits. *Pre-Print*. https://doi.org/10.1101/2022.08.18.22278951

Thanaj, M., Basty, N., Whitcher, B., Sorokin, E. P., Liu, Y., Srinivasan, R., Cule, M., Thomas, E. L., & Bell, J. D. (2023). *Precision MRI phenotyping of muscle volume and quality at a population scale* [Preprint]. Radiology and Imaging. https://doi.org/10.1101/2023.03.02.23286689

The Medical Imaging Interaction Toolkit (MITK)—Mitk.org. (2022). https://www.mitk.org/wiki/The_Medical_Imaging_Interaction_Toolkit_(MITK)

Thomas, E. L., & Bell, J. D. (2015). Body Fat MRS. In *EMagRes* (Vol. 4, pp. 663–672). John Wiley & Sons, Ltd. https://doi.org/10.1002/9780470034590.emrstm1478

Thomas, E. L., Fitzpatrick, J. A., Malik, S. J., Taylor-Robinson, S. D., & Bell, J. D. (2013). Whole Body Fat: Content and Distribution. *Progress in Nuclear Magnetic Resonance Spectroscopy*.

Thomas, E. L., Hamilton, G., Patel, N., Doré, C. J., Goldin, R. D., Bell, J. D., & Taylor-Robinson, S. D. (2005). Hepatic triglyceride content and its relation to body adiposity: A magnetic resonance imaging and proton magnetic resonance spectroscopy study. *Gut*, *54*, 122–127. https://doi.org/10.1136/gut.2003.036566

Törnqvist, E., Larsson, E.-M., & Hallströ, I. (2006). It's like being in another world-patients' lived experience of magnetic resonance imaging. *Journal of Clinical Nursing*, *15*(8), 954–961. https://doi.org/10.1111/j.1365-2702.2006.01499.x

Triay Bagur, A., Ridgway, G., McGonigle, J., Brady, M., & Bulte, D. (2020). *Pancreas Segmentation-Derived Biomarkers: Volume and Shape Metrics in the UK Biobank Imaging Study* (pp. 131–142). https://doi.org/10.1007/978-3-030-52791-4_11

Turner, J. A. (2014). The rise of large-scale imaging studies in psychiatry. *GigaScience*, *3*(29). https://doi.org/10.1186/2047-217X-3-29

van Beek, E. J. R., Kuhl, C., Anzai, Y., Desmond, P., Ehman, R. L., Gong, Q., Gold, G., Gulani, V., Hall-Craggs, M., Leiner, T., Lim, C. C. T., Pipe, J. G., Reeder, S., Reinhold, C., Smits, M., Sodickson, D. K., Tempany, C., Vargas, H. A., & Wang, M. (2019). Value of MRI in Medicine: More Than Just Another Test? *Journal of Magnetic Resonance Imaging : JMRI*, *49*(7), e14–e25. https://doi.org/10.1002/jmri.26211

Van Erck, D., Moeskops, P., Schoufour, J. D., Weijs, P. J. M., Scholte Op Reimer, W. J. M., Van Mourik, M. S., Janmaat, Y. C., Planken, R. N., Vis, M., Baan, J., Hemke, R., Išgum, I., Henriques, J. P., De Vos, B. D., & Delewi, R. (2022). Evaluation of a Fully Automatic Deep Learning-Based Method for the Measurement of Psoas Muscle Area. *Frontiers in Nutrition*, *9*. https://doi.org/10.3389/fnut.2022.781860

Villarini, B., Asaturyan, H., Kurugol, S., Afacan, O., Bell, jimmy, & Thomas, E. (2021). 3D Deep Learning for Anatomical Structure Segmentation in Multiple Imaging Modalities. In *Proceedings. IEEE International Symposium on Computer-Based Medical Systems* (Vol. 2021). https://doi.org/10.1109/CBMS52027.2021.00066

Waduud, M. A., Adusumilli, P., Drozd, M., Bailey, M. A., Cuthbert, G., Hammond, C., & Scott, J. A. (2019). Volumetric versus single slice measurements of core abdominal muscle for sarcopenia. *British Journal of Radiology*. https://doi.org/10.1259/bjr.20180434

Wake, T., Tateishi, R., Fukumoto, T., Nakagomi, R., Kinoshita, M. N., Nakatsuka, T., Sato, M., Minami, T., Uchino, K., Enooku, K., Nakagawa, H., Fujinaga, H., Asaoka, Y., Tanaka, Y., Otsuka, M., & Koike, K. (2020). Improved liver function in patients with cirrhosis due to chronic hepatitis C virus who achieve sustained virologic response is not accompanied by increased liver volume. *PLoS ONE*, *15*(4). https://doi.org/10.1371/JOURNAL.PONE.0231836

Wang, J., Zhu, L., Liu, L., Zhao, X.-A., Zhang, Z., Xue, L., Yan, X., Huang, S., Li, Y., Cheng, J., Zhang, B., Xu, T., Li, C., Ji, F., Ming, F., Zhao, Y., Shao, H., Sang, D., Zhao, H., … Wu, C. (2020). Overweight and Obesity are Risk Factors of Severe Illness in Patients with COVID-19. *Obesity (Silver Spring, Md.)*, *28*(11), 2049–2055. https://doi.org/10.1002/oby.22979

Wang, R., Liu, X., Shao, H., Li, Q., & Zhong, D. (2021). *3D Dense Volumetric Network for Accurate Automated Pancreas Segmentation* (Vol. 2021, p. 3556). https://doi.org/10.1109/EMBC46164.2021.9630789

Watson, R. A., Pride, N. B., Thomas, E. L., Fitzpatrick, J., Durighel, G., McCarthy, J., Morin, S. X., Ind, P. W., & Bell, J. D. (2010). Reduction of total lung capacity in obese men: Comparison of total intrathoracic and gas volumes. *Journal of Applied Physiology*, *108*(6), 1605–1612.

Weber, K. A., Abbott, R., Bojilov, V., Smith, A. C., Wasielewski, M., Hastie, T. J., Parrish, T. B., Mackey, S., & Elliott, J. M. (2021). Multi-muscle deep learning segmentation to automate the quantification of muscle fat infiltration in cervical spine conditions. *Scientific Reports*, *11*(1). https://doi.org/10.1038/s41598-021-95972-x

Wesolowska-Andersen, A., Brorsson, C. A., Bizzotto, R., Mari, A., Tura, A., Koivula, R., Mahajan, A., Vinuela, A., Tajes, J. F., Sharma, S., Haid, M., Prehn, C., Artati, A.,

Hong, M. G., Musholt, P. B., Kurbasic, A., De Masi, F., Tsirigos, K., Pedersen, H. K., … Brunak, S. (2022). Four groups of type 2 diabetes contribute to the etiological and clinical heterogeneity in newly diagnosed individuals: An IMI DIRECT study. *Cell Reports Medicine*, *3*(1). https://doi.org/10.1016/J.XCRM.2021.100477

West, J., Leinhard, O. D., Romu, T., Collins, R., Garratt, S., Bell, J. D., Borga, M., & Thomas, L. (2016). *Feasibility of MR-Based Body Composition Analysis in Large Scale Population Studies | Enhanced Reader*. PLoS One. https://doi.org/10.1371/journal.pone.0163332

Westbrook, C., Kaut Roth, C., & Talbot, J. (2011). *MRI in Practice*. Wiley-Blackwell.

Westerterp, K. R. (2009). Assessment of physical activity: A critical appraisal. *European Journal of Applied Physiology*, *105*(6), 823–828. https://doi.org/10.1007/s00421-009-1000-2

Wicaksana, A., Hertanti, N., Pramono, R., & Hsu, Y.-Y. (2021). Are Patients with Coronavirus Disease 2019 and Obesity at a Higher Risk of Hospital and Intensive Care Unit Admissions? A Systematic Review and Meta-analysis. *Open Access Macedonian Journal of Medical Sciences*, *9*, 410–419. https://doi.org/10.3889/oamjms.2021.6585

Willemink, M. J., Koszek, W. A., Hardell, C., Wu, J., Fleischmann, D., Harvey, H., Folio, L. R., Summers, R. M., Rubin, D. L., & Lungren, M. P. (2020). Preparing Medical Imaging Data for Machine Learning. *Radiology*, *295*(1), 4–15. https://doi.org/10.1148/radiol.2020192224

Williams, A. J. K., Chau, W., Callaway, M. P., & Dayan, C. M. (2007). Magnetic resonance imaging: A reliable method for measuring pancreatic volume in Type 1 diabetes. *Diabetic Medicine*, *24*(1), 35–40. https://doi.org/10.1111/j.1464-5491.2007.02027.x

Winkel, D. J., Breit, · Hanns-Christian, Thomas, ·, Weikert, J., & Stieltjes, · Bram. (2021). Building Large-Scale Quantitative Imaging Databases with Multi-Scale Deep Reinforcement Learning: Initial Experience with Whole-Body Organ Volumetric Analyses. *Journal of Digital Imaging*, *34*, 124–133. https://doi.org/10.1007/s10278-020-00398-y

WMA Declaration of Taipei on Ethical Considerations regarding Health Databases and Biobanks – WMA – The World Medical Association. (2016). https://www.wma.net/policies-post/wma-declaration-of-taipei-on-ethical-considerations-regarding-health-databases-and-biobanks/

Woelfle, M., Olliaro, P., & Todd, M. H. (2011). Open science is a research accelerator. In *NATURE CHEMISTRY* | (Vol. 3). https://doi.org/10.1038/nchem.1149

Yamamura, J., Grosse, R., Graessner, J., Janka, G. E., Adam, G., & Fischer, R. (2010). Distribution of Cardiac Iron Measured by Magnetic Resonance Imaging (MRI)-R 2 *. *J. Magn. Reson. Imaging*, *32*, 1104–1109. https://doi.org/10.1002/jmri.22364

Zelicha, H., Schwarzfuchs, D., Shelef, I., Gepner, Y., Tsaban, G., Tene, L., Yaskolka Meir, A., Bilitzky, A., Komy, O., Cohen, N., Bril, N., Rein, M., Serfaty, D., Kenigsbuch, S., Chassidim, Y., Sarusi, B., Thiery, J., Ceglarek, U., Stumvoll, M., … Shai, I. (2018). Changes of renal sinus fat and renal parenchymal fat during an 18-month randomized weight loss trial. *Clinical Nutrition*, *37*(4), 1145–1153. https://doi.org/10.1016/j.clnu.2017.04.007

Zhang, Y., Li, S., & Shen, J. (2009). Automatic High-Order Shimming Using Parallel Columns Mapping (PACMAP). *Wiley InterScience (Www.Interscience.Wiley. Com). Magnetic Resonance in Medicine*, *62*, 1073–1079. https://doi.org/10.1002/mrm.22077

Curriculum Vitae

Julie Fitzpatrick London, England, United Kingdom

+44 (0) 7799405027

julie_7651@hotmail.com

linkedin.com/in/bitesizedmri

Summary

Accomplished and learned diagnostic radiographer with strong transitional skills. Currently undertaking a PhD by published works at University of Salford.

Experience

Visiting Researcher

University of Westminster
Dec 2016 - Present
Visiting researcher at the Research Centre for Optimal Health (ReCOH)

Ivie Image Analysis

Mar 2017 - Present
Undertaking annotation and analysis of medical images.

Imaging Technologist II

Clario
Nov 2021 - Present

Imaging Technologist II

Bioclinica
May 2018 - Nov 2021

Imaging Technologist I

BioClinica
Jul 2015 - May 2018

Research MRI Radiographer

Imperial College London
Jul 2014 - Jul 2015

Consultant

Imperial Consultants (ICON)
Apr 2011 - Jul 2015

MR Radiographer and Research Associate

Imperial College Healthcare NHS Trust
Mar 2013 - Jul 2014

MRI Radiographer-Advanced Practice

Imperial College London
Jul 2007 - Mar 2013

Senior Research Radiographer

Medical Research Council
Aug 2003 - Jul 2007

Superintendent Radiographer

Cromwell Hospital
Mar 2002 - Aug 2003

Senior I Radiographer

Cromwell Hospital
Jul 1999 - Mar 2002

Senior II Radiographer

Cromwell Hospital
Jan 1998 - Jul 1999

Senior II Radiographer

Queen Mary's University Hospital
Feb 1997 - Jan 1998

Basic Grade Radiographer

Queen Mary's University Hospital
Feb 1994 - Feb 1997

Education

The University of Salford

Doctor of Philosophy - PhD, Medical Imaging

Sep 2021 - present

City, University of London

Master's Module, Introduction to Artificial Intelligence for Radiographers

2020

Anglia Ruskin University

Master of Science (MSc), Magnetic Resonance Imaging

2013 - 2015

University of Hertfordshire

Certificate of Competence in the Administering of IV Injections

2007 - 2008

Sheffield Teaching Hospitals

Certificate of Competence, Requesting and Interpreting Intra-Orbital Foreign Bodies Prior to MRI
2006

London South Bank University

Certificate, Magnetic Resonance; Principles and Safety

2000 - 2001

Southampton School of Radiography

D.C.R.(R), Diagnostic Radiography

1990 - 1993

Courses

Introduction to Artificial Intelligence for Radiographers
City, University of London
2020

Quality Assurance in Magnetic Resonance
Institute of Physics and Engineering
2014

Introduction To Medical Statistics Course
Imperial College Faculty of Medicine
2008

The 10th International Leeds Cardiac MR Course
Leeds General Infirmary
2003

MRI In Practice
Healthsouth Training and Education
1999

Research

https://scholar.google.com/citations?hl=en&user=3oFxC3AAAAAJ&view_op=list_works&sortby=pubdate

Voluntary Positions

International Society for Magnetic Resonance in Medicine
MSK Study Group Committee Member
Jun 2018 - Jun 2019

International Society for MR Technologists
Vice-Chair Marketing Committee Society for MR Radiographers & Technologists.
Jun 2017 - Jun 2018

International Society for Magnetic Resonance in Medicine
Electro Magnetic Tissue Properties Study Group Committee Member
May 2017 - Jun 2018

International Society for Magnetic Resonance in Medicine
International Society for MR Technologists
Social Media Correspondent at ISMRM and ISMRT 2016

Professional Registration and Membership

Health and Care Professionals Council
RA 33706

Society of Radiographers
44556